

NOVEL APPROACHES TO OPTOMECHANICAL TRANSDUCTION

ONDŘEJ ČERNOTÍK

NOVEL APPROACHES TO OPTOMECHANICAL TRANSDUCTION

Von der QUEST-Leibniz-Forschungsschule
der Gottfried Wilhelm Leibniz Universität Hannover
zur Erlangung des akademischen Grades

Doktor der Naturwissenschaften
Dr. rer. nat.

genehmigte Dissertation von

Ondřej Černotík
geboren am 6. Juni 1989 in Příbram, Tschechien

Referent	Prof. Dr. Klemens Hammerer Institut für Theoretische Physik, Leibniz Universität Hannover
Korreferent	Prof. Dr. Luis Santos Institut für Theoretische Physik, Leibniz Universität Hannover
Korreferent	Dr. Claudiu Genes Max-Planck-Institut für die Physik des Lichts
Vorsitzende der Prüfungskommission	Prof. Dr. Michèle Heurs Albert-Einstein-Institut Hannover
Tag der Promotion	18. August 2017

ABSTRACT

Faithful conversion of quantum signals between microwave and optical frequencies is crucial for building quantum networks based on superconducting circuits and for detection of weak microwave signals. A promising route towards this task uses transducers based on mechanical oscillators, which interact with light via radiation pressure and with microwave fields by electrostatic forces. Existing theoretical proposals and experimental efforts focus on two avenues towards optomechanical transduction: time-independent schemes for conversion of propagating fields or state transfer via adiabatic passage. The former approach results in simple experimental setups but its applicability is limited by narrow conversion bandwidth. The latter strategy avoids this problem; nevertheless, this gain requires complex time-dependent control schemes and strong opto- and electromechanical coupling, which is out of reach for current systems. In an ideal optomechanical transducer, we would like to combine the advantages of both strategies, namely large bandwidth and simple, time-independent control.

In this dissertation, I tackle this challenge and develop two schemes for quantum networking of superconducting circuits based on two different tactics. In the first case, the transducer is optimized for a specific task: generation of entanglement between two superconducting qubits. I show how two established experimental techniques—parity measurements on superconducting qubits and optomechanical force sensing—can be combined to create a conceptually simple device, in which entanglement between the qubits is generated by measurement and postselection. Second, I demonstrate that an array of optomechanical transducers is capable of converting arbitrary input signals within a large bandwidth. The conversion process is based on adiabatic passage but, unlike existing proposals, uses spatial (and not temporal) variation of the system parameters. This approach does not require strong coupling and significantly reduces added noise. Together, these two protocols pave the way to future quantum networks with superconducting systems. The scheme for entanglement generation can be implemented with current experimental technology and is well suited for proof of principle experiments. Large quantum networks with many nodes will, on the other hand, require transducers capable of reaching high communication rates. This goal can be achieved with the large bandwidth of optoelectromechanical arrays.

Keywords: Optomechanics, hybrid quantum systems, frequency conversion

ZUSAMMENFASSUNG

Effiziente Umwandlung von Quantensignalen zwischen Mikrowellen- und optischen Frequenzen ist erforderlich für den Aufbau von Quantennetzwerken supraleitender Schaltkreise und zur Messung schwacher Mikrowellensignale. Einen vielversprechenden Weg zur Lösung dieser Aufgabe bieten Transducer auf Basis mechanischer Oszillatoren, die mit Licht durch Strahlungsdruck und mit Mikrowellenfeldern durch elektrostatische Kräfte wechselwirken. Bestehende theoretische und experimentelle Arbeiten konzentrieren sich auf zwei Vorgehensweisen zur optomechanischen Transduktion: zeitunabhängige Protokolle zur Umwandlung propagierender Felder sowie Zustandsübertragung durch adiabatischen Übergang. Ersteres führt zu einfachen experimentellen Aufbauten, deren Anwendbarkeit jedoch durch eine schmale Bandbreite begrenzt ist. Letzteres vermeidet dieses Problem, aber erfordert komplexe zeitabhängige Regelschemata und starke opto- und elektromechanische Kopplung, die mit heutigen Systemen nicht erreichbar ist. In einem idealen optomechanischen Transducer möchten wir die Vorteile beider Strategien, nämlich große Bandbreite und einfache, zeitunabhängige Steuerung, kombinieren.

In dieser Dissertation stelle ich mich dieser Herausforderung und entwickle zwei Schemata für die Vernetzung supraleitender Schaltkreise. Im ersten Falle ist der Transducer für eine bestimmte Aufgabe optimiert: Erzeugung von Verschränkung zwischen zwei supraleitenden Qubits. Ich zeige, wie zwei etablierte experimentelle Methoden – Paritätsmessungen auf supraleitenden Qubits und optomechanische Kraftmessung – kombiniert werden können, um ein konzeptionell einfaches Gerät zu schaffen, in dem die Verschränkung zwischen den Qubits durch Messung und Postselektion erzeugt wird. Zweitens zeige ich, dass beliebige Quantensignale innerhalb einer großen Bandbreite in einem Array optomechanischer Transducer konvertiert werden können. Der Prozess basiert auf adiabatischem Übergang, verwendet aber im Gegensatz zu bestehenden Strategien räumliche (und nicht zeitliche) Variation der Systemparameter. Diese Methode erfordert keine starke Kopplung und reduziert erheblich das zusätzliche Rauschen. Gemeinsam weisen diese beiden Protokolle den Weg zu zukünftigen Quantennetzwerken mit supraleitenden Systemen. Das Schema für die Verschränkungserzeugung kann mit aktueller experimenteller Technologie umgesetzt werden. Andererseits werden große Quantennetzwerke mit vielen Knoten Transducer benötigen, die hohe Kommunikationsraten erreichen können. Dieses Ziel kann mit der großen Bandbreite optoelektromechanischer Arrays erreicht werden.

Schlagwörter: Optomechanik, hybride Quantensysteme, Frequenzkonversion

SHRNUTÍ

Supravodivé elektronické obvody patří mezi nejslibnější kandidáty pro systémy umožňující kvantové zpracování informace. S využitím Josephsonových přechodů je možné vytvářet nelineární obvody, které se chovají podobně jako jednotlivé atomy a mohou tak být využity jako kvantové bity v kvantových počítačích. Kvantové počítače pak umožňují efektivně řešit problémy, které jsou neřešitelné na počítačích klasických, a měly by nám tak mimo jiné pomoci s hlubším porozuměním mnoha problémů moderní fyziky, chemie a biologie. Supravodivé obvody je s velkou přesností možné kontrolovat pomocí mikrovlnných signálů, což ale představuje zásadní problém při tvorbě kvantových komunikačních sítí, neboť efektivní kvantová komunikace vyžaduje signály o optických frekvencích, které, na rozdíl od signálů mikrovlnných, nejsou při pokojové teplotě vystaveny termálnímu šumu.

Výzkum v oblasti kvantového zpracování informace se v posledních letech zaměřuje na problematiku hybridních kvantových systémů, ve kterých jsou odlišné kvantové systémy zkombinovány tak, aby výsledné zařízení využívalo výhody jednotlivých podsystémů. Pozornosti tak neunikla ani otázka převodu elektromagnetických kvantových signálů mezi jednotlivými frekvenčními oblastmi, obzvláště mezi mikrovlnami a světlem. Jako nejperspektivnější systémy pro frekvenční konverzi se v současnosti jeví mechanické oscilátory, které interagují se světlem díky tlaku záření a s mikrovlnnými poli pomocí elektrostatických sil. Teoretické i experimentální práce se zaměřují buď na časově nezávislé protokoly založené na optomechanicky indukované transparentci, které však operují pouze v silně omezené šířce pásma, nebo strategie využívající adiabatický přechod, jež sice mohou dosáhnout výrazně větší šířky pásma, ale vyžadují složitá časově proměnná kontrolní schémata a silnou optomechanickou a elektromechanickou interakci; experimentální realizace těchto systémů je tak podstatně složitější než u protokolů využívajících časově nezávislé interakce. V ideálním konvertoru bychom přitom chtěli zkombinovat výhody obou přístupů: velkou šířku pásma a časově nezávislé kontrolní schéma.

V rámci této disertaci se věnuji tomuto problému a představuji dva nové protokoly pro stavbu kvantových komunikačních sítí se supravodivými čipy založené na časově nezávislé kontrole. První schéma využívá optomechanický konvertor, který je optimalizovaný pro jeden konkrétní účel – generaci kvantové provázanosti (entanglementu) mezi dvěma supravodivými kvantovými bity. Ukazuji, jak je možné zkombinovat dvě etablované experimentální techniky – měření parity dvou supravodivých kvantových bitů a optomechanickou detekci slabých sil – a vytvořit tak konceptuálně jednoduchý systém, v němž je kvantová provázanost generována pomocí měření a postselekce. Entanglement je pak

možno využít pro teleportaci kvantových stavů nebo pro kvantové zpracování informace distribuované přes několik izolovaných kvantových procesorů. V druhém případě se věnuji problematice konverze libovolných signálů a ukazují, že je možné zlepšit šířku pásma konverze v jednorozměrné řadě optomechanických konvertorů. Tento proces je založen na adiabatické konverzi signálu, využívá však, na rozdíl od standardních protokolů, prostorově (a nikoli časově) proměnné parametry. Adiabaticita tohoto systému současně pomáhá výrazně redukovat šum, který vstupuje do systému z termálních rezervoárů mechanických oscilátorů. Frekvenční konverzi libovolných kvantových signálů lze použít pro kvantovou komunikaci a distribuci kvantové provázanosti mezi jednotlivými uzly kvantové sítě.

Společně oba protokoly ukazují cestu k tvorbě sítí pro kvantovou komunikaci se supravodivými obvody. První zmíněný protokol pro tvorbu entanglementu mezi dvěma supravodivými kvantovými bity je možné implementovat se současnou technologií a je tak vhodný pro tvorbu prvních kvantových sítí. V delším časovém horizontu bude však třeba vyvinout protokoly umožňující rychlou a efektivní komunikaci mezi mnoha uzly. Tohoto cíle je možné dosáhnout s frekvenčním multiplexováním, podobně jako u sítí pro klasickou komunikaci. Převodníky pro tyto systémy tedy budou muset pracovat ve velké šířce pásma; tato podmínka je splněna u druhého zmiňovaného projektu – konvertoru na bázi jednorozměrných optoelektromechanických řad.

ACKNOWLEDGEMENTS

A dissertation is, by its very definition, a single-author publication but doctoral research is by no means a solitary endeavour. Many people helped me on my path in various ways, from explaining important physics concepts, to discussing physics and academic life in general, to providing emotional support in times of need. Without all these contributions, this dissertation would be very different, would have taken much longer to finish, or would not have been written at all.

First and foremost, my gratitude goes to my supervisor Klemens Hammerer. Especially at the beginning, when I was new to optomechanics and continuous measurements, Klemens always had time to explain things I did not understand and later, as my knowledge of the field deepened, to discuss and help me develop the ideas I had. He also made sure I attended my share of conferences and summer schools to discuss my work with others, learn from them, and make myself known; and he never forced me to work late into the night or during the weekends but let me have a life outside of research which, I'm led to believe, is not the case with many supervisors.

I also must not forget my teachers and mentors from my alma mater in Olomouc, particularly Jaromír Fiurášek and Radim Filip. They not only provided me with the necessary mathematical and physical background for graduate studies but also awoke my interest in the weird, fascinating world of quantum physics and its applications in information processing. Finally, Jaromír's and Radim's support was an important factor in my decision to pursue a doctorate abroad and in choosing Hannover as my new home.

I would also like to thank my colleagues from the group for creating a friendly atmosphere to work in. I am especially grateful to Denis Vasilyev for discussions on continuous measurements in Gaussian systems and for helping me to get started with numerical simulations in Python, Emil Zeuthen for discussions about optomechanical transduction, and Sahand Mahmoodian for insights into transfer matrix formalism. I also thank our secretary Birgit Gemmeke for helping me to navigate through the labyrinth of German bureaucracy and making my interaction with university administration as easy as possible.

I met many more wonderful physicists at conferences, summer schools, other universities, or when they visited Hannover. Many of them became my friends just like my colleagues in Hannover did and I am truly looking forward to all the discussions that are yet to come, about both physics and life in general. I am particularly thankful to Sebastian Hofer and Ralf Riedinger for discussions about generation of nonclassical mechanical

states, Johannes Fink for discussions about experimental aspects of optomechanical transduction, as well as to Florian Marquardt and Claudiu Genes for their hospitality during my visits in Erlangen.

The final step of my studies would not be possible without examiners and a dissertation committee to evaluate my work. I would therefore like to express my thanks to Klemens Hammerer, Luis Santos, and Claudiu Genes for taking the time to referee my dissertation and to Michèle Heurs for chairing the committee.

A lot of moral support came from one surprising place—Twitter. When I joined this social network during the first year of my PhD, I did not expect to find such a charming and supportive community of fellow graduate students, early career researchers, and post-academics. With all of you, I could grow both academically and as a person and stay motivated during hard times.

Last but not least, I am grateful for the support of my friends and family before, during, and—I hope—after my PhD studies. Thank you all for always being there for me.

I would also like to thank the cluster system team at the Leibniz University Hannover for their support in the production of this work and the European Commission for funding. Nothing shows the global nature of research and the importance of international funding programmes as a Czech completing a dissertation in Germany under the supervision of an Austrian.

CONTENTS

INTRODUCTION	1
1 HYBRID QUANTUM SYSTEMS	7
1.1 Cavity optomechanics	8
1.1.1 Optomechanical interaction	8
1.1.2 Experimental platforms	11
1.1.3 Optomechanical force sensing	13
1.1.4 Backaction evasion	15
1.2 Frequency conversion between light and microwaves	16
1.3 Circuit quantum electrodynamics	19
1.3.1 Elements of superconducting systems	19
1.3.2 Quantization of electrical circuits	20
1.3.3 Artificial atoms and microwave resonators	24
1.4 Coupling artificial atoms to mechanical oscillators	25
1.5 Other hybrid systems	27
2 CONTINUOUS MEASUREMENTS ON HYBRID QUANTUM SYSTEMS	29
2.1 Principles of continuous measurements	30
2.1.1 Quantum-optical master equation	30
2.1.2 Stochastic unravellings	32
2.2 Quantum measurements on physical systems	35
2.3 Gaussian dynamics	37
2.4 Adiabatic elimination of Gaussian subsystems	40
2.4.1 Effective equation of motion for quantum nondemolition measurement	42
2.4.2 Effective equation of motion for oscillating system–transducer interaction	45
2.5 Examples	47
2.5.1 Quantum nondemolition readout of a qubit	48
2.5.2 Two-qubit entanglement in presence of thermal noise	53
2.5.3 Single-qubit measurement using Jaynes–Cummings interaction	55

2.5.4	Qubit readout with a two-oscillator transducer	57
2.6	Summary	59
2.A	Properties of Gaussian characteristic functions	60
2.B	Positive-semidefiniteness of decay	61
2.C	Hierarchy of dynamical equations for transducer cumulants	62
3	QUANTUM FORCE SENSING WITH OPTOMECHANICAL TRANSDUCERS	65
3.1	Generation of entanglement between two superconducting qubits	66
3.1.1	Measuring qubit-state-dependent forces	66
3.1.2	Equation of motion	68
3.2	Experimental realizations	70
3.2.1	Transmon qubits	70
3.2.2	Flux qubits	75
3.2.3	Nitrogen–vacancy centres	75
3.3	Alternative schemes	77
3.3.1	Quantum nondemolition interaction	77
3.3.2	Coupling via a microwave cavity	79
3.3.3	Combining microwave cavity and modulated coupling	80
3.4	Derivation of effective equations of motion	81
3.4.1	Single-qubit readout	81
3.4.2	Two-qubit measurement	82
3.5	Analysis of stochastic master equations	84
3.6	Photocounting with optomechanical transducers	88
3.6.1	Measurement strategy	89
3.6.2	Quantum Zeno effect and the standard quantum limit	91
3.6.3	Fundamental limits on measurement precision	92
3.7	Summary	94
4	SPATIALLY ADIABATIC FREQUENCY CONVERSION IN TRANSDUCER ARRAYS	95
4.1	Single optomechanical transducer	97
4.1.1	Transduction of itinerant fields	97
4.1.2	Frequency conversion by adiabatic passage	99
4.2	Transducer array	100
4.2.1	Transfer matrix formalism	101
4.2.2	Conversion bandwidth	102
4.2.3	Numerical simulations	104
4.3	Losses and noise	105
4.3.1	Mechanical noise	106
4.3.2	Optical and microwave losses	108
4.4	Discussion	111

CONCLUSION	113
REFERENCES	115
CURRICULUM VITAE	135

INTRODUCTION

Quantum physics is set to revolutionize the way we collect, process, and transfer information. Using nonclassical states, we can make measurements with unprecedented precision, quantum parallelism promises an exponential speedup for calculations, and the impossibility of cloning of quantum states enables unconditionally secure communication. Hundred years after the birth of quantum mechanics, we are witnessing the second quantum revolution [1]—we not only understand how microscopic systems behave but we can also use this behaviour to encode and process information.

The field of quantum information matures fast and many commercial applications are already available (or will be in the near future) [2–4]. This progress goes hand in hand with increased national [5, 6] and international funding [7–10] into both basic and applied research of quantum physics and quantum information. The emerging quantum technologies can be divided into the following four categories: quantum sensing [11, 12], quantum communication [13, 14], quantum simulation [15, 16], and quantum computing [17].

One of the best platforms for quantum measurements are mechanical oscillators. Preparation of nonclassical mechanical states for quantum metrology is extremely challenging but this drawback is compensated by the large susceptibility of mechanical motion to various external forces. Additionally, mechanical oscillations can be actuated and read out using optical and microwave fields, enabling highly sensitive measurements of their position [18]. The most striking example of such a measurement is the recent detection of gravitation waves where mechanical displacement of 10^{-20} metre has been detected with massive, 40-kilogram mirrors [19]. But mechanical oscillators are not the only system suitable for quantum limited measurements. Another possibility for quantum sensing lies in using solid-state spins, such as nitrogen–vacancy centres [20, 21]. These systems are well isolated from their environment and can be addressed optically.

Light is the only medium suitable for quantum communication owing to its high propagation speed, low loss, and negligible thermal noise. Both discrete- [22] and continuous-variable [23, 24] degrees of freedom (such as polarization or time-bin encoded pulses for the former and amplitude and phase quadratures for the latter) can be used to encode and transmit information. These systems have been successfully used for quantum key distribution with increasing distance [25–27] or to distribute entanglement to two distant parties, enabling quantum teleportation [28–30] or violation of Bell inequal-

ities [31–34]. Light can also be used to construct networks of other quantum systems such as atoms and solid-state spins [35–38].

Quantum simulation enables us to study problems that cannot be simulated on classical computers. Simulators can thus bring increased understanding of various models in condensed-matter physics, lattice gauge theories, or chemical reactions. In the two common approaches, one can either create a quantum system whose dynamics closely mimic the system one wants to understand (analog quantum simulation) or encode the simulation into gates applied to quantum bits (digital quantum simulation); particularly the latter approach can be seen as an important step towards building a universal quantum computer. Among the most interesting platforms for quantum simulation are neutral atoms in optical lattices that closely resemble crystalline structure of solid-state systems, superconducting circuits [39, 40] and trapped ions [41] owing to their suitability for quantum computing (discussed below), and light where the difficulty of implementing photon–photon interactions is compensated by low losses and easy manipulation of individual qubits [42].

Finally, the most promising approaches to quantum computing rely on two-level systems, similar to classical computers. Quantum bits formed by trapped ions can be controlled by light and microwave fields [43, 44]. Nevertheless, larger systems require sophisticated trap designs, possibly with the ions being shuffled around between storage and interaction regions [45, 46]. Recently, superconducting circuits emerged as the workhorse of quantum computing [47–49]; in these systems, Josephson tunnel junctions can be used to build qubits, owing to their strongly nonlinear response to electric fields. Fabrication of these systems is well mastered and they can reach strong coupling to microwave fields that are used to control them. Experiments in recent years demonstrated quantum gates with several superconducting qubits [50–53], basic quantum algorithms [54–56], and quantum error correction [57–60].

This short overview reveals a problem with future quantum technologies: different quantum systems are suitable for different tasks. Quantum states of light can be well transmitted over macroscopic distances thanks to fast propagation, low noise, and weak interactions with the surrounding environment. Yet, it is precisely this lack of coupling that makes it virtually impossible to use light for processing of quantum information. On the other hand, superconducting circuits are extremely suitable candidates for quantum processors but their coupling to microwave fields prohibits their coupling to room-temperature quantum channels for communication across macroscopic distances (although short-distance communication is possible at microwave frequencies [61, 62]).

As a result, research in the past years started to focus on combining various quantum systems into larger, hybrid devices that combine the advantages of their subsystems [63–65]. An interface between a superconducting circuit and light, for instance, offers the possibility of fast quantum information processing and its transmission over macroscopic distances. The link between microwave and optical frequencies can be provided by atomic, molecular, and solid-state impurity spins [66–73], magnons in ferromagnetic materials [74], electrooptic modulators [75–77], or mechanical oscillators [78–87].

Of all these hybrid devices, optomechanical transducers are the most developed. In these systems, an optical cavity and a microwave resonator couple to the same mechanical oscillator; radiation pressure and electrostatic force result in dispersive interaction in which the position of the mechanical oscillator determines the resonance frequency of the electromagnetic resonator [18]. This nonlinear interaction is typically weak but can be enhanced by a strong classical driving field. A large steady-state amplitude of the cavity field leads to linearized interaction where Stokes and anti-Stokes scattering of the pump on phonons results in creation of photon-phonon pairs or exchange of excitations between the cavity field and the mechanical motion. The relative weight of the two processes can be changed by driving the system on one of the mechanical sidebands; driving on the lower mechanical sideband results in an effective beam splitter-like interaction between the mechanical motion and cavity field. Quantum states can be transmitted between two cavity fields coupled to the same mechanical oscillator by a sequence of π -pulses [88] or using adiabatic passage with a mechanically dark mode [79, 80]; practical application of these strategies requires first storing the signal in one of the cavities, which can be technically challenging.

This problem can be avoided by using the mechanically dark mode for conversion of propagating fields using interference effects similar to optomechanically induced transparency [79, 80, 82]. The bandwidth of this conversion process, however, is limited to the optomechanically broadened mechanical linewidth which is, in any practical application, just a small fraction of the linewidth of the electromagnetic resonator. For applications in quantum information processing, the issue of storage can also be partially avoided by coupling a superconducting qubit directly to the mechanical oscillator [78]. In this situation, we do not need to transmit the microwave signals from the qubit to a resonator, simplifying the system and relaxing our requirements on experimental parameters. Existing schemes for coupling superconducting qubits to light—either directly [78] or via microwave resonators [89, 90]—assume adiabatic state transfer between the superconducting and optical systems. Such strategies are robust against small imperfections in pulse shapes but require limiting decoherence to levels unthinkable with current technology.

The aim of this dissertation is to address these limitations of optomechanical transduction and to develop new strategies for frequency conversion in hybrid optoelectromechanical systems. To this end, I follow two complementary approaches: optimizing transduction for a specific task and designing new devices for general-purpose frequency conversion. When we abandon the idea of a universal transducer and focus on a single application, we can find novel, surprisingly efficient strategies by combining well-known experimental techniques. I will show that entanglement between two superconducting qubits can be generated when we combine parity measurements [91, 92] with optomechanical force sensing [93, 94]. For efficient entanglement generation, only optomechanical cooperativity moderately larger than unity and sufficient qubit lifetimes are necessary [95]; both requirements can be fulfilled with current technology. On the other hand, new strategy for frequency conversion of propagating electromagnetic fields can be inspired by combining adiabatic state transfer with approach based on optomechanically induced transparency.

The resulting device enables adiabatic conversion of propagating fields in an array of optomechanical transducers. Admittedly, such a device is challenging to implement but this disadvantage is outweighed by the conversion bandwidth that grows with the array size, which also helps to suppress the added noise [96].

Outline of the dissertation The main prerequisite to developing hybrid quantum devices is a deep understanding of their individual constituents and the ways they can be coupled to each other. I therefore introduce the systems I will use throughout the dissertation in chapter 1. I start by reviewing cavity optomechanics and electromechanics and showing how these platforms can be combined to build a frequency converter between microwaves and light. The second important field I will work with is circuit quantum electrodynamics. I show how superconducting electrical circuits can be quantized and how Josephson junctions can be used to build effective two-level systems. I then discuss approaches to coupling superconducting circuits with mechanical oscillators—both with coupling to light and without it. The former can be used to build an interface between superconducting qubits and light; the latter allows for measurements and control of superconducting qubits using mechanical oscillators or using superconducting qubits as nonlinear controllers of mechanical motion. Finally, I also briefly discuss main research efforts with other kinds of hybrid systems, in which, for instance, superconducting qubits are interfaced to light using solid-state spins or where mechanical motion is coupled to electron spins. This chapter thus does not present any new results but merely reviews current state of the field.

Chapter 2 introduces the mathematical tools needed to describe hybrid quantum systems under continuous measurements. I start by developing the formalism of stochastic master equations (following the approach of Wiseman and Milburn [97]) and review applications of continuous measurements in optomechanics and circuit quantum electrodynamics. Next, I consider the special case of linear quantum dynamics, for which the description can be greatly simplified; instead of describing the system using its density matrix, the dynamics can be characterized by the first and second statistical moments of the canonical operators. I then use these results to adiabatically eliminate Gaussian dynamics from conditional quantum dynamics of systems containing both Gaussian and non-Gaussian elements. This chapter is largely (apart from the introduction of the formalism) based on reference [98] where I contributed the main analytical and numerical results; the general idea was developed together with Denis Vasilyev, who also contributed to the description of continuous measurements on Gaussian systems.

I apply these results on optomechanical force sensors in chapter 3. Force measurements to date focus on detecting classical forces through their action on the mechanical oscillator whose position is monitored using a cavity field. If the force is exerted by a quantum system, richer physics can be expected due to coherence of such objects and interference effects when measuring more such systems simultaneously. On the particular case of two superconducting qubits coupled capacitively to two mechanical oscillators, I show that a joint measurement can be used to generate entanglement between the qubits [95]. Each qubit exerts a state-dependent force on the oscillator; joint measurement of the oscillators'

motion reveals the total spin of the qubits, which leads to conditional generation of entanglement; this setup thus enables us to build quantum networks with superconducting systems. In the second part of this chapter, I consider another example, namely quantum nondemolition detection of single photons. The cavity mode, in which the photon number is measured, couples nonlinearly to a mechanical oscillator so that the resulting force depends on the number of photons. I show that such a measurement results in quantum Zeno effect if the photons arrive into the cavity from an external source and discuss fundamental detection limits for systems where the incoupling of photons into the detector can be improved by controlling their pulse shape. This chapter presents the results of reference [95] where I contributed the main analytical and numerical results; moreover, it contains alternative schemes for qubit readout and analysis of quantum nondemolition counting of photons that are not discussed in the publication [95].

Finally, I discuss frequency conversion with an array of optomechanical transducers in chapter 4. In this system, two waveguides—one for light and one for microwaves—couple to a one-dimensional array of transducers; at each site, an optical cavity and a microwave resonator couple to a common mechanical oscillator. Varying the opto- and electromechanical coupling from site to site, we can achieve efficient adiabatic frequency conversion between the propagating fields. Remarkably, the conversion bandwidth is limited only by the adiabatic condition and the error resulting from its discretization; the conversion bandwidth can be increased by using a larger array. This chapter is based on reference [96] to which I provided the main analytical and numerical results; Sahand Mahmoodian contributed to the calculation of conversion bandwidth in a transducer array. In contrast, the chapter contains an extended discussion of previously proposed schemes for optomechanical transduction.

A few words on notation Throughout the dissertation, I use hats to distinguish quantum operators from classical numbers. For instance, x can refer to the expectation value of the position operator (or to classical position) but never represents the operator itself; that is denoted by \hat{x} . Vectors and matrices are denoted using bold roman font with small letters usually (though not always) used for vectors and capital letters denoting matrices. The vector of canonical operators is thus written as $\hat{\mathbf{r}}$ (with elements \hat{r}_i) and the covariance matrix as $\mathbf{\Gamma}$ (which is easy to distinguish from a general decoherence rate Γ). The identity matrix is denoted \mathbf{I}_n (with the subscript giving the dimensionality) and the identity operator is $\hat{\mathbf{I}}$.

Time derivatives of classical numbers are denoted by a dot, \dot{x} . Since such notation would clash with the hats worn by quantum operators, those have the derivative written out either using the standard full notation in displayed equations,

$$\frac{d\hat{\rho}}{dt},$$

or using the shorthand notation $d_t \hat{\rho}$ when used in line. Finally, the differential d , the imaginary unit i , and the Euler's number e are set in roman (and not in cursive) to distinguish them from the variables d and i and from the elementary charge e . Throughout the dissertation, I work in the natural units with $\hbar = 1$ unless otherwise noted.

CHAPTER 1

HYBRID QUANTUM SYSTEMS

Development of hybrid quantum systems demands a thorough understanding of their individual constituents. Without understanding how the individual quantum systems operate, one cannot expect to find practical ways how to combine them in larger devices. This necessity goes deeper than knowing how to couple these systems; if one does not understand their internal workings, one cannot be aware of the systems' main advantages and limitations. This knowledge is crucial: one can not only find efficient ways to couple disparate quantum systems but also ensure that the resulting hybrid system will have interesting applications.

I therefore start my dissertation by giving an overview of the basic building blocks of systems for quantum networking of superconducting circuits. I start by reviewing opto- and electromechanical systems in section 1.1; in these devices, a mechanical oscillator interacts with an electromagnetic field of either optical frequency via radiation pressure or microwave frequency via electrostatic forces. Although the underlying coupling mechanism is different in both kinds of systems, the mathematical description is identical; in both cases, the mechanical position linearly shifts the resonance frequency of an electromagnetic resonator. With a strong driving field, this interaction can be linearized and result in—depending on the driving frequency—beam splitter-like, quantum nondemolition, or two-mode squeezing interaction.

In section 1.2, I show how an opto- and electromechanical system can be combined to build a frequency converter between microwaves and light. I outline existing theoretical proposals [79, 80, 99]; in this effort, I focus on the most practical approach [79, 80, 82] in which propagating optical and microwave fields can be bidirectionally converted with high efficiency and low added noise. I show the main limitations of this approach and briefly discuss how they can be alleviated in an array of such transducers.

I change topics in section 1.3 by discussing the working principles of superconducting circuits for quantum information processing. I explain how the strong nonlinearity of Josephson tunnel junctions can be used to build effective two-level systems and how such circuits can be described using quantum mechanics.

I then discuss how superconducting qubits can be coupled to mechanical motion in section 1.4. The mechanism is the same as for electromechanical systems—the mechanical oscillator forms one electrode of a parallel-plate capacitor—but, owing to the nonlinearity

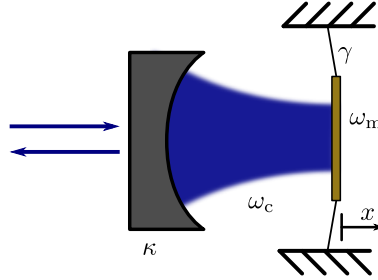


Figure 1.1: Schematic representation of an optomechanical system. The field inside a Fabry-Perot cavity exhibits radiation pressure on its mechanically compliant end mirror (shown in yellow).

of the Josephson junctions, richer dynamics can be realized. I also show how such interactions can be used to couple superconducting qubits to light and what the requirements on such systems are.

Finally, I give a brief overview of other hybrid systems for frequency conversion and for other applications in section 1.5. Together with the previous sections, this discussion shows the rich possibilities that hybrid quantum systems offer not only for applications in quantum information processing but also for investigations of fundamental physics.

1.1 CAVITY OPTOMECHANICS

1.1.1 Optomechanical interaction

We start by considering a Fabry-Perot cavity with an end mirror that is free to move; see figure 1.1. The position of the mechanical oscillator determines the length of the cavity and thus the resonance frequency for light. The light intensity, on the other hand, determines the force with which the oscillator is pushed out of its equilibrium position. As the mechanical oscillator changes position, the resonance condition for light changes. This shift results in a new light intensity inside the Fabry-Perot resonator which, in turn, changes the force acting on the mechanical oscillator and the mechanical displacement.

Mathematically, the interaction is described by the Hamiltonian

$$\hat{H} = \hbar\omega_c(x)\hat{a}^\dagger\hat{a} + \frac{p^2}{2m} + \frac{1}{2}m\omega_m^2x^2 + iE(\hat{a}e^{i\omega_L t+i\phi} - \hat{a}^\dagger e^{-i\omega_L t-i\phi}). \quad (1.1)$$

The first term describes the cavity field with annihilation operator \hat{a} and resonance frequency determined by the (classical) mechanical position x . The second and third term describe the harmonic motion of the mechanical oscillator of mass m and resonance frequency ω_m . The last term in the Hamiltonian describes driving of the cavity with a classical field E .

Next, we use the relation between cavity length and its resonance frequency,

$$\omega_c(x) = \frac{c}{L+x}, \quad (1.2)$$

where L is the equilibrium cavity length. Since the mechanical motion is typically much smaller than the cavity length, $x \ll L$, we can expand the expression (1.2) to first order in the mechanical displacement,

$$\omega_c(x) \approx \frac{c}{L} \left(1 - \frac{x}{L}\right). \quad (1.3)$$

If we now quantize the mechanical motion and introduce the annihilation operator $\hat{b} = (\hat{x} + i\hat{p}/m\omega_m)/2x_{\text{zpf}}$ with $x_{\text{zpf}} = \sqrt{\hbar/2m\omega_m}$, we can rewrite the Hamiltonian (1.1) as

$$\hat{H} = \hbar\omega_c \hat{a}^\dagger \hat{a} + \hbar\omega_m \hat{b}^\dagger \hat{b} - \hbar g_0 \hat{a}^\dagger \hat{a} (\hat{b} + \hat{b}^\dagger) + iE (\hat{a} e^{i\omega_L t + i\phi} - \hat{a}^\dagger e^{-i\omega_L t - i\phi}) \quad (1.4)$$

with the optomechanical coupling rate

$$g_0 = \omega_c \frac{x_{\text{zpf}}}{L}; \quad (1.5)$$

by ω_c , we denote the equilibrium resonance frequency.

For typical micro- and nanomechanical oscillators, the zero-point motion is extremely small: for a mechanical frequency of the order of 1 MHz and effective mass of 10 ng, the zero-point fluctuation is about 0.1 fm. With cavity length $L = 10$ mm and frequency $\omega_c \sim 10^{15} \text{s}^{-1}$, the coupling strength is $g_0 \sim 10$ Hz. Such coupling can be larger than the mechanical decay rate (mechanical oscillators can reach quality factors of several million), but optical decay by far remains the dominating process in the system.

To enhance the optomechanical coupling, we can use the classical driving of the cavity mode \hat{a} at frequency ω_L . First, we move to the rotating frame with respect to the Hamiltonian $\hbar\omega_L \hat{a}^\dagger \hat{a}$ which gets rid of the time-dependence of the driving term in the Hamiltonian (1.4),

$$\hat{H} = \hbar\Delta \hat{a}^\dagger \hat{a} + \hbar\omega_m \hat{b}^\dagger \hat{b} - \hbar g_0 \hat{a}^\dagger \hat{a} (\hat{b} + \hat{b}^\dagger) + iE (\hat{a} e^{i\phi} - \hat{a}^\dagger e^{-i\phi}) \quad (1.6)$$

with $\Delta = \omega_L - \omega_c$. Rigorous treatment of the cavity drive now requires us to write the classical equations of motion for the cavity field and the mechanical oscillator [apart from the dynamics described by the Hamiltonian (1.6), the cavity field decays at a rate κ and the mechanical motion at a rate γ] and find the new steady state [100].

In this dissertation, however, we will be interested only in the linearized optomechanical interaction that is the result of this strong driving. To understand this effect, we can follow this simplified argument: the driving results in a strong, coherent field inside the cavity with small quantum fluctuations on top of the classical field, $\hat{a} = \alpha + \delta\hat{a}$. We now have

$$\hat{a}^\dagger \hat{a} = (\alpha^* + \delta\hat{a}^\dagger)(\alpha + \delta\hat{a}) = |\alpha|^2 + \alpha^* \delta\hat{a} + \alpha \delta\hat{a}^\dagger + \delta\hat{a}^\dagger \delta\hat{a}, \quad (1.7)$$

which, upon plugging into (1.6), gives rise to three kinds of terms: the first type, proportional to $|\alpha|^2 > 1$ is a classical shift of the zero-point energy of the Hamiltonian $\Delta|\alpha|^2$ and of the mechanical equilibrium. The cross terms combining the classical amplitude and quantum fluctuations give a linearized interaction between the cavity field and the mechanical motion, $-\hbar g_0 (\alpha^* \delta\hat{a} + \alpha \delta\hat{a}^\dagger) (\hat{b} + \hat{b}^\dagger)$. The last term can be dropped from

the interaction since it is smaller than the linearized interaction. We thus obtain the Hamiltonian

$$\hat{H} = \hbar\Delta\delta\hat{a}^\dagger\delta\hat{a} + \hbar\omega_m\hat{b}^\dagger\hat{b} - \hbar g(\delta\hat{a}e^{-i\varphi} + \delta\hat{a}^\dagger e^{i\varphi})(\hat{b} + \hat{b}^\dagger) \quad (1.8)$$

with the coupling enhanced by the strong coherent component, $g = g_0|\alpha|$, and the interaction phase φ set by the phase of the cavity field $\alpha = |\alpha|e^{i\varphi}$. The phase generally depends on the phase of the driving field and the field's detuning from cavity resonance and can be found by solving the classical equation of motion for the mean field, $\alpha = \langle\hat{a}\rangle$; in the following, I put $\varphi = 0$ for simplicity. I will also use \hat{a} (and not $\delta\hat{a}$) to denote the quantum fluctuations of the cavity field.

The classical driving of the Fabry–Perot resonator that results in the linearized Hamiltonian (1.8) provides ample control over the system. Time-dependent driving amplitude can be used to modulate the optomechanical coupling, which can be used for quantum nondemolition measurement of the mechanical displacement [101] or for generation of squeezing [102, 103]. Detuning of the driving field from cavity resonance can lead to cooling of the mechanical oscillator or to amplification of the mechanical motion.

In the frame rotating with respect to the free evolution of the two oscillators, $\hat{H}_0 = \hbar\Delta\hat{a}^\dagger\hat{a} + \hbar\omega_m\hat{b}^\dagger\hat{b}$, the interaction Hamiltonian becomes

$$\begin{aligned} \hat{H}_{\text{int}} &= \hbar g(\hat{a}e^{i\Delta t} + \hat{a}^\dagger e^{-i\Delta t})(\hat{b}e^{i\omega_m t} + \hat{b}^\dagger e^{-i\omega_m t}) \\ &= \hbar g\left(\hat{a}\hat{b}^\dagger e^{i(\Delta-\omega_m)t} + \hat{b}\hat{a}^\dagger e^{-i(\Delta-\omega_m)t}\right) + \hbar g\left(\hat{a}\hat{b}e^{i(\Delta+\omega_m)t} + \hat{a}^\dagger\hat{b}^\dagger e^{-i(\Delta+\omega_m)t}\right). \end{aligned} \quad (1.9)$$

Proper choice of the detuning Δ enables three relevant regimes: By driving the cavity on the lower mechanical sideband, $\Delta = \omega_m$, we bring the first term in equation (1.9) on resonance. The cavity field and mechanical oscillator exchange excitations; the second term, describing generation and annihilation of quanta in pairs can be neglected in the rotating wave approximation (which is valid provided the mechanical sidebands can be resolved by the cavity, $\omega_m > \kappa$). The resulting coupling,

$$\hat{H}_{\text{BS}} = \hbar g(\hat{a}\hat{b}^\dagger + \hat{b}\hat{a}^\dagger), \quad (1.10)$$

describes beam splitter-like interaction between the two systems. Since the cavity is coupled to a zero-temperature bath while the mechanical oscillator is in contact with a thermal reservoir, this coupling can be used to cool the mechanical oscillator into its ground state [104–107]. The interaction also allows state transfer between the cavity field and the mechanical oscillator, which is crucial for optomechanical transduction.

If we drive the cavity on the upper sideband, $\Delta = -\omega_m$, the second term in the Hamiltonian (1.9) becomes resonant and the first term can be neglected in the rotating wave approximation. The resulting Hamiltonian

$$\hat{H}_{\text{TMS}} = \hbar g(\hat{a}\hat{b} + \hat{a}^\dagger\hat{b}^\dagger) \quad (1.11)$$

describes two-mode squeezing interaction between the field and the oscillator. This coupling can be used to generate entanglement [108], amplify the mechanical motion [109, 110], or to drive the mechanical oscillator into a limit cycle [111, 112].

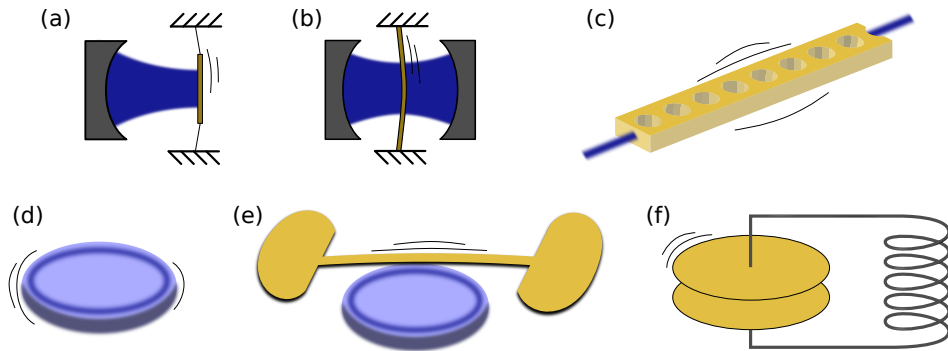


Figure 1.2: Overview of optomechanical platforms. (a) Fabry–Perot cavity with a movable end mirror. (b) Fabry–Perot resonator with a vibrating membrane in the middle. The motion of the membrane changes the optical path inside the cavity and thus affects the cavity resonance frequency. (c) An optomechanical crystal. In this nanoscale structure, even small variation of the cavity field or mechanical displacement affects the other mode, giving rise to strong optomechanical interaction. (d,e) Whispering gallery resonators. The cavity field can interact with a flexural mode of the microdisk (d) or its evanescent field couples to a nearby nanobeam via gradient force (e). (f) An LC resonator with a mechanically compliant capacitor. The mechanical motion shifts the capacitance, leading to electromechanical coupling with the microwave field stored in the resonator.

Finally, if the system is driven on resonance, $\Delta = 0$, we are left with the full linearized Hamiltonian (1.8). In this situation, the mechanical position quadrature $(\hat{b} + \hat{b}^\dagger)/\sqrt{2}$ gets imprinted onto the phase quadrature of the cavity field, $i(\hat{a}^\dagger - \hat{a})\sqrt{2}$. Homodyne detection of the output field can thus be used to infer the mechanical displacement [113]. In this regime, sideband resolution is not necessary; on the contrary, large cavity decay enables fast readout of the mechanical position.

1.1.2 Experimental platforms

The coupling between mechanical motion and light can be realized in a variety of systems; a Fabry–Perot cavity with a movable end mirror [figure 1.2(a)] is just one example. In most of these devices, the interaction is described by the Hamiltonian (1.4); this picture is valid as long as the mechanical oscillations change the optical path of light in a resonator and the leading-order correction to the resonance frequency is linear. With more complicated setups, however, other forms of coupling can be achieved; in some systems, the motion of the end mirrors results in position-dependent decay of the optical field [114].

One of the most versatile optomechanical platforms is a vibrating membrane in the middle of an optical cavity with fixed length [115]; see figure 1.2(b). The field propagating through the membrane feels a refractive index that is different from the rest of the cavity; the motion through the standing wave in the cavity changes the effective refractive index of the cavity and thus also the resonance frequency. Placing the membrane in the middle between a minimum and maximum of the standing wave results in the usual linear interaction whereas membrane placed at the minimum or maximum leads, due to mirror

symmetry of the field around the extremum, to quadratic coupling [116],

$$\hat{H}_{\text{int}} = \hbar g_0 \hat{a}^\dagger \hat{a} (\hat{b} + \hat{b}^\dagger)^2. \quad (1.12)$$

Moreover, with a highly reflecting membrane, two optical modes (with annihilation operators $\hat{a}_{\text{R,L}}$) can form in the right and left half of the cavity; the mechanical oscillator is subject to radiation pressure from both modes,

$$\hat{H}_{\text{int}} = \hbar g_0 (\hat{a}_{\text{R}}^\dagger \hat{a}_{\text{R}} - \hat{a}_{\text{L}}^\dagger \hat{a}_{\text{L}}) (\hat{b} + \hat{b}^\dagger). \quad (1.13)$$

(The minus sign is due to the opposite directions of the radiation pressure from the two modes.) For normal modes of the cavities $\hat{a}_\pm = (\hat{a}_{\text{R}} \pm \hat{a}_{\text{L}})/\sqrt{2}$, the interaction results in mechanically mediated photon hopping,

$$\hat{H}_{\text{int}} = \hbar g_0 (\hat{a}_+^\dagger \hat{a}_- + \hat{a}_-^\dagger \hat{a}_+) (\hat{b} + \hat{b}^\dagger). \quad (1.14)$$

In this setting, it is possible to reach strong nonlinear coupling if the mechanical frequency matches the detuning between the cavity fields [117] or to perform quantum nondemolition measurements of the phonon number [118]. These different forms of coupling that can be achieved with a vibrating membrane offer interesting possibilities for many experimental applications and illustrate the large variability of optomechanical systems; they are, however, not directly relevant for the rest of this dissertation where I focus on the linearized optomechanical interaction.

With cavity implementations of optomechanics, the bare optomechanical coupling is limited; much stronger coupling can be achieved with nanostructures where the field is strongly confined. The strongest optomechanical coupling to date has been achieved in optomechanical crystals. These suspended systems [shown schematically in figure 1.2(c)] have a periodic structure of holes drilled into the material, creating a band structure for photons and phonons. By creating a continuous defect in the structure (by slowly changing the shape and spacing of the holes), it is possible to trap a photonic and a phononic mode. Owing to strong confinement of both fields and changes in the effective refractive index caused by the mechanical motion, strong optomechanical coupling can be realized [119, 120].

Similar coupling rates can be achieved with microdisk optical resonators supporting whispering gallery modes of light. These structures can either support mechanical modes themselves [121]—as shown in figure 1.2(d)—or whose cavity modes are coupled to nanobeams via evanescent fields [122]; cf. figure 1.2(e). With the micrometer size of these optomechanical systems, even a small variation of the optical path length strongly affects the resonance frequency and thus gives rise to strong coupling.

Finally, optomechanical interactions are not limited to electromagnetic fields at optical frequencies. Using a superconducting microwave LC circuit with mechanically compliant capacitor [figure 1.2(f)], one can realize the same interaction. With a parallel-plate capacitor with one electrode formed by a suspended membrane, the capacitance (and thus the resonance frequency of the circuit) depends on the mechanical position. To leading order, this dependence is linear and we recover the optomechanical Hamiltonian (1.4) [113, 123].

1.1.3 Optomechanical force sensing

Mechanical oscillators are susceptible to external forces; they respond to gravitational fields and can react strongly to an electric or magnetic field if made from a conducting or magnetic material. Light can be used for precise measurements of mechanical position using interference. Combining both systems in an optomechanical device thus enables extremely sensitive measurements of external forces. Owing to the quantum mechanical nature of the interaction, the sensitivity is limited by an effect akin to Heisenberg uncertainty relation [11, 18]. Detailed understanding of the measurement sensitivity that these devices can achieve is critical for many applications, including the scheme for generating entanglement between two superconducting qubits in chapter 3.

We start by writing the Heisenberg–Langevin equations for the optomechanical system,

$$\frac{d\hat{q}_m}{dt} = \omega_m \hat{p}_m, \quad (1.15a)$$

$$\frac{d\hat{p}_m}{dt} = -\omega_m \hat{q}_m - \sqrt{2}g(\hat{a} + \hat{a}^\dagger) - \gamma \hat{p}_m + \hat{F}, \quad (1.15b)$$

$$\frac{d\hat{a}}{dt} = -i\sqrt{2}g\hat{q}_m - \frac{\kappa}{2}\hat{a} + \sqrt{\kappa}\hat{a}_{\text{in}}. \quad (1.15c)$$

The mechanical oscillator is described by its quadrature operators $\hat{q}_m = (\hat{b} + \hat{b}^\dagger)/\sqrt{2}$, $\hat{p}_m = -i(\hat{b} - \hat{b}^\dagger)/\sqrt{2}$, has a linewidth γ , and is subject to a force having a deterministic part \hat{F}_0 that we are trying to estimate and an unwanted stochastic part \hat{f}_{th} , $\hat{F} = \hat{F}_0 + \hat{f}_{\text{th}}$. The optical field is described using its annihilation operator \hat{a} and decay rate κ and is driven by quantum fluctuations \hat{a}_{in} with correlations $\langle \hat{a}_{\text{in}}(t)\hat{a}_{\text{in}}^\dagger(t') \rangle = \delta(t - t')$. In addition, we have the following input–output relation for the cavity field:

$$\hat{a}_{\text{out}} = \sqrt{\kappa}\hat{a} - \hat{a}_{\text{in}}. \quad (1.16)$$

To analyse the sensitivity of this optomechanical position measurement, we write the equations (1.15) in frequency domain,

$$-i\omega\hat{q}_m - \omega_m\hat{p}_m = 0, \quad (1.17a)$$

$$(\gamma - i\omega)\hat{p}_m + \omega_m\hat{q}_m + \sqrt{2}g(\hat{a} + \hat{a}^\dagger) = \hat{F}, \quad (1.17b)$$

$$\left(\frac{\kappa}{2} - i\omega\right)\hat{a} + i\sqrt{2}g\hat{q}_m = \sqrt{\kappa}\hat{a}_{\text{in}}; \quad (1.17c)$$

here, I use the convention $\hat{O}(\omega) = (1/\sqrt{2\pi}) \int dt e^{-i\omega t} \hat{O}(t)$ for the Fourier transform. Using the first two equations, we obtain an expression for the position quadrature

$$\hat{q}_m(\omega) = \chi_m(\omega) \left[\hat{F}(\omega) - \frac{4g\sqrt{\kappa}}{\kappa - 2i\omega} \hat{q}_{\text{in}}(\omega) \right], \quad (1.18)$$

where $\chi_m(\omega) = \omega_m/(\omega_m^2 - \omega^2 - i\gamma\omega)$ is the mechanical susceptibility and $\hat{q}_{\text{in}}(\omega) = (\hat{a}_{\text{in}}(\omega) + [\hat{a}_{\text{in}}(\omega)]^\dagger)/\sqrt{2}$ is the amplitude quadrature of the fluctuations driving the cavity.

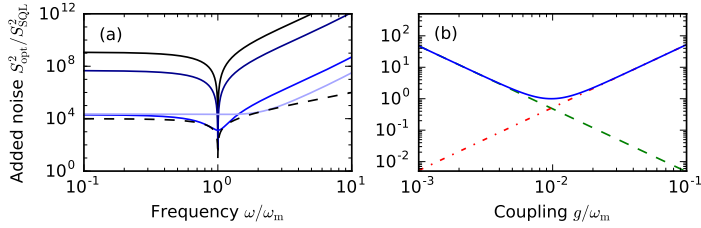


Figure 1.3: Added optical noise $S_{\text{opt}}^2 = S_{\text{add}}^2 - S_{\text{th}}^2$ in optomechanical displacement measurement. (a) Optical noise as a function of frequency for different driving powers [from dark to light $g = (0.002, 0.01, 0.5, 2)\omega_m$]. For small frequencies, $\omega < \omega_m$, the sensitivity is limited by backaction noise; sensitivity at large frequencies is limited by shot noise. The dashed line is the optimum sensitivity (1.22). (b) Added noise on mechanical resonance versus driving power. For small powers, the measurement is limited by imprecision noise (dashed green line); backaction noise (dot-dashed red line) limits sensitivity at high driving powers. The total added noise (solid blue line) is given by the sum of these two quantities and is minimized when the imprecision and backaction noise are equal.

The result (1.18) can be used to find the cavity and output field. For the phase quadrature of the output signal, we get

$$\begin{aligned} \hat{p}_{\text{out}}(\omega) &= -i \frac{\hat{a}_{\text{out}}(\omega) - \hat{a}_{\text{out}}^\dagger(\omega)}{\sqrt{2}} \\ &= \frac{\kappa + 2i\omega}{\kappa - 2i\omega} \hat{p}_{\text{in}}(\omega) + \frac{4g\sqrt{\kappa}}{\kappa - 2i\omega} \chi_m(\omega) \left[\hat{F}(\omega) - \frac{4g\sqrt{\kappa}}{\kappa - 2i\omega} \hat{q}_{\text{in}}(\omega) \right]. \end{aligned} \quad (1.19)$$

The spectrum of the output phase quadrature, $S_{p_{\text{out}}}^2(\omega) = \frac{1}{2} \int dt \langle [\hat{p}_{\text{out}}(t), \hat{p}_{\text{out}}(0)]_+ \rangle e^{i\omega t}$, is given by the expression

$$S_{p_{\text{out}}}^2(\omega) = S_{p_{\text{in}}}^2(\omega) + \frac{16g^2\kappa}{\kappa^2 + 4\omega^2} |\chi_m(\omega)|^2 \left[S_F^2(\omega) + S_{\text{th}}^2(\omega) + \frac{16g^2\kappa}{\kappa^2 + 4\omega^2} S_{q_{\text{in}}}^2(\omega) \right]; \quad (1.20)$$

here, S_F^2 is the spectrum of the signal \hat{F}_0 and $S_{\text{th}}^2 = \gamma(2\bar{n} + 1)$ of the thermal mechanical fluctuations \hat{f}_{th} . The signal on the detector has four components: the signal S_F^2 and three noise contributions coming from the thermal mechanical bath and the amplitude and phase of the input field. The measurement sensitivity is given by the noise added to the measured signal,

$$S_{\text{add}}^2(\omega) = S_{\text{th}}^2(\omega) + \frac{16g^2\kappa}{\kappa^2 + 4\omega^2} S_{q_{\text{in}}}^2(\omega) + \frac{\kappa^2 + 4\omega^2}{16g^2\kappa} \frac{1}{|\chi_m(\omega)|^2} S_{p_{\text{in}}}^2(\omega). \quad (1.21)$$

The thermal noise can be reduced by working at low temperatures but the optical noise is more difficult to combat. While the shot noise (coming from the phase uncertainty associated with $S_{p_{\text{in}}}^2$) can be reduced by increasing the coupling rate g , this simultaneously increases the backaction noise [second term in equation (1.21)]. Moreover, the amplitude and phase noise of the input field are bound by the Heisenberg uncertainty relation,

$S_{q_{in}}^2 S_{p_{in}}^2 \geq 1$ (assuming no correlations between the two). The noise is minimized when the contributions from imprecision and backaction noise are equal; the required coupling strength is $g_{\text{opt}}^2 = (\kappa^2 + 4\omega^2)/16\kappa|\chi_m(\omega)|$ and depends on the frequency component ω are optimizing for. The added noise then simplifies to

$$S_{\text{opt}}^2(\omega) = S_{\text{th}}^2(\omega) + \frac{2}{|\chi_m(\omega)|}. \quad (1.22)$$

For forces acting on mechanical resonance, $\omega = \omega_m$, the susceptibility simplifies to $\chi_m(\omega_m) = (-i\gamma)^{-1}$; the measurement sensitivity reaches the standard quantum limit and the added noise is $S_{\text{SQL}}^2 = S_{\text{th}}^2 + 2\gamma$. These relations are illustrated in figure 1.3.

1.1.4 Backaction evasion

The noise in amplitude and phase quadratures of light are bound by Heisenberg uncertainty; we cannot reduce one without increasing the other. Each of these noise sources affects a different mechanical quadrature: the uncertainty in phase limits the precision of the position measurement while the noisy amplitude quadrature disturbs the mechanical momentum. This momentum noise affects future evolution of the position [cf. equations (1.15)], reducing our knowledge of the external force.

The solution that can improve the displacement sensitivity is to measure an operator that is a constant of motion. The backaction noise will still be present but if it does not drive the measured operator, it will not disturb the measurement and reduce its sensitivity. This task can be achieved with an optomechanical cavity driven equally on both mechanical sidebands [101, 124, 125]. This driving results in modulation of the optomechanical coupling rate at the mechanical frequency,

$$\hat{H} = \hbar\omega_m \hat{b}^\dagger \hat{b} + 2\hbar g \cos(\omega_m t) (\hat{a} + \hat{a}^\dagger) (\hat{b} + \hat{b}^\dagger). \quad (1.23)$$

In the rotating frame with respect to the free mechanical oscillations, $\hat{H}_0 = \hbar\omega_m \hat{b}^\dagger \hat{b}$, we can drop the fast oscillating terms in the interaction (provided the cavity operates in the resolved-sideband regime, $\kappa < \omega_m$) and obtain the quantum nondemolition interaction

$$\hat{H} = \hbar g (\hat{a} + \hat{a}^\dagger) (\hat{b} + \hat{b}^\dagger). \quad (1.24)$$

This measurement is different from the measurement of the mechanical position in that we are measuring the operator $\hat{b} + \hat{b}^\dagger = \sqrt{2}\hat{x}_m$ in the rotating frame. From the nature of the interaction, it is clear that the measurement backaction (connected with the noise in the amplitude quadrature of the light, $\hat{a} + \hat{a}^\dagger$) affects the orthogonal mechanical quadrature, $-i(\hat{b} - \hat{b}^\dagger)$. Since the position quadrature is a constant of motion, the backaction does not affect its evolution and the measurement sensitivity is not bound by the standard quantum limit.

Driving the cavity on both sidebands is not the only possibility to beat the standard quantum limit. Improved sensitivity can also be achieved with squeezed light. The phase quadrature is squeezed (reducing the shot noise responsible for measurement insensitivity)

and sensitivity at the level of the standard quantum limit can be reached with smaller pump power [126, 127]. The strategy thus allows us to use a weaker driving field to achieve the same sensitivity; this approach can be beneficial for limiting absorption heating of the mechanical oscillator.

Another possibility is to measure a different quadrature than the phase quadrature of the output field; this strategy is known as variational measurement [128, 129]. Such an approach does not extract the maximum information about the mechanical position; this drawback is compensated by extracting information about the measurement backaction.

Finally, the standard quantum limit can be surpassed with entanglement [130–133]. In this setting, a second harmonic oscillator (an auxiliary optical cavity or an atomic cloud) is used as a reference for the measurement. This second oscillator is coupled to the probe field in the same way but has an effective negative mass; consequently, it experiences backaction force of equal size but opposite direction. Since both oscillators are measured simultaneously, the measurement backaction does not affect the joint readout and sensitivity below the standard quantum limit is possible.

1.2 FREQUENCY CONVERSION BETWEEN LIGHT AND MICROWAVES

By combining an opto- and electromechanical system in a single device, we obtain a system in which the mechanical oscillator mediates interactions between an optical cavity field and a microwave resonator; see figure 1.4(a,b). This device can serve as a link between the two frequency regimes, opening a whole plethora of applications. The linearized dynamics of such a system are given by the Hamiltonian

$$\hat{H} = \hbar\Delta_1\hat{a}_1^\dagger\hat{a}_1 + \hbar\omega_m\hat{b}^\dagger\hat{b} + \hbar\Delta_2\hat{a}_2^\dagger\hat{a}_2 + \hbar g_1(\hat{a}_1 + \hat{a}_1^\dagger)(\hat{b} + \hat{b}^\dagger) + \hbar g_2(\hat{a}_2 + \hat{a}_2^\dagger)(\hat{b} + \hat{b}^\dagger); \quad (1.25)$$

here, $\hat{a}_{1,2}$, \hat{b} are the annihilation operators for the microwave and optical cavity and the mechanical oscillator. The most straightforward approach is to drive both cavities on the red sideband, $\Delta_1 = \Delta_2 = \omega_m$, which leads to state transfer from the optical cavity to the microwave resonator via the mechanical oscillator (or vice versa),

$$\hat{H} = \hbar g_1(\hat{a}_1^\dagger\hat{b} + \hat{b}^\dagger\hat{a}_1) + \hbar g_2(\hat{a}_2^\dagger\hat{b} + \hat{b}^\dagger\hat{a}_2). \quad (1.26)$$

We can understand the dynamics best using the state space model [80, 82]; we start by writing the Heisenberg–Langevin equations and the input–output relations in the vector form

$$\frac{d\hat{\mathbf{a}}}{dt} = \mathbf{A}\hat{\mathbf{a}} + \mathbf{B}\hat{\mathbf{a}}_{\text{in}}, \quad (1.27a)$$

$$\hat{\mathbf{a}}_{\text{out}} = \mathbf{C}\hat{\mathbf{a}} + \mathbf{D}\hat{\mathbf{a}}_{\text{in}} \quad (1.27b)$$

with the vector $\hat{\mathbf{a}} = (\hat{a}_1, \hat{b}, \hat{a}_2)^T$ (with similar vectors for the input and output fields). Fourier transforming the operators, we can write the relation between the input and output fields using the scattering matrix,

$$\hat{\mathbf{a}}_{\text{out}}(\omega) = \mathbf{S}(\omega)\hat{\mathbf{a}}_{\text{in}}(\omega) = [\mathbf{D} - \mathbf{C}(\mathbf{A} + i\omega\mathbf{I}_3)^{-1}\mathbf{B}]\hat{\mathbf{a}}_{\text{in}}(\omega). \quad (1.28)$$

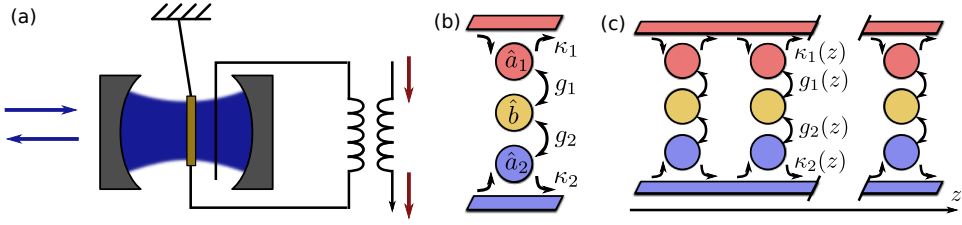


Figure 1.4: (a) Basic optomechanical transducer formed by connecting an optical cavity and a microwave resonator to a common mechanical oscillator. (b) Schematic representation of the transducer including waveguides for input and output fields. (c) Transducer array for spatially adiabatic frequency conversion.

We can find the matrix \mathbf{A} from the Hamiltonian and decay,

$$\mathbf{A} = \begin{pmatrix} -\frac{\kappa_1}{2} & -ig_1 & 0 \\ -ig_1 & -\frac{\gamma}{2} & -ig_2 \\ 0 & -ig_2 & -\frac{\kappa_2}{2} \end{pmatrix}; \quad (1.29)$$

we further have $\mathbf{B} = \mathbf{C} = \text{diag}(\sqrt{\kappa_1}, \sqrt{\gamma}, \sqrt{\kappa_2})$ and $\mathbf{D} = -\mathbf{I}_3$. We then obtain the scattering matrix

$$\mathbf{S}(\omega) = \begin{pmatrix} t_1 & n_1 & c \\ n_1 & m & n_2 \\ c & n_2 & t_2 \end{pmatrix} \quad (1.30)$$

with coefficients that are, close to cavity resonance, $\omega \approx 0$, given by

$$t_i = \frac{-C_i + C_{i \oplus 1} + 1}{C_1 + C_2 + 1}, \quad (1.31a)$$

$$c = -\frac{2\sqrt{C_1 C_2}}{C_1 + C_2 + 1}, \quad (1.31b)$$

$$m = -\frac{C_1 + C_2 - 1}{C_1 + C_2 + 1}, \quad (1.31c)$$

$$n_i = -\frac{2i\sqrt{C_i}}{C_1 + C_2 + 1}, \quad (1.31d)$$

where we defined the classical cooperativity $C_i = 4g_i^2/\kappa_i\gamma$ and \oplus denotes addition modulo 2 (i.e., $1 \oplus 1 = 2, 2 \oplus 1 = 1$).

High conversion efficiency is achieved if $|c| \sim 1$; this requires that the opto- and electromechanical cavities be impedance matched, $C_1 = C_2 > 1$. Furthermore, the noise added during conversion has to be small compared to the signal. Thermal noise is limited if $|n_i| < |c|$ which can be achieved in the strong-cooperativity regime, $\bar{C} = 4g_i^2/\kappa_i\gamma\bar{n} > 1$. Additionally, heating through the counterrotating terms is negligible in the resolved-sideband limit, $\kappa_i < \omega_m$. Under these conditions, interference prevents any signal that enters the transducer to leave through the port where it entered and the signal is effectively decoupled from the noisy mechanical motion. The conversion bandwidth is given by

the optomechanically broadened mechanical line, $\Delta\omega = \gamma(C_1 + C_2 + 1)$ [134]. I provide more detailed discussion and derivations of the conversion bandwidth and added noise in chapter 4 where I compare this basic scheme to frequency conversion in an array of optomechanical transducers.

Intracavity fields can be efficiently converted using adiabatic state transfer [79, 80]. In the strong-coupling regime, $g_i > \kappa_i$, the dynamics can be diagonalized, resulting in three normal modes

$$\hat{d}_+ = \frac{1}{\sqrt{2(g_1^2 + g_2^2)}}(g_1\hat{a}_1 + g_2\hat{a}_2) + \frac{1}{\sqrt{2}}\hat{b}, \quad (1.32a)$$

$$\hat{d}_- = \frac{1}{\sqrt{2(g_1^2 + g_2^2)}}(g_1\hat{a}_1 + g_2\hat{a}_2) - \frac{1}{\sqrt{2}}\hat{b}, \quad (1.32b)$$

$$\hat{d}_2 = \frac{1}{\sqrt{g_1^2 + g_2^2}}(-g_2\hat{a}_1 + g_1\hat{a}_2). \quad (1.32c)$$

The mode \hat{d}_2 is a dark mode of the mechanical motion and is thus insensitive to thermal mechanical noise. Frequency conversion with the dark mode uses adiabatic passage: starting with a signal in the microwave resonator and optomechanical interaction switched on, $g_1 \ll g_2$, we gradually lower the optomechanical coupling while turning the electromechanical coupling on. At the end of the process, the optomechanical coupling is completely turned off and the electromechanical coupling is switched on; we thus changed the dark mode from microwave to optical, $\hat{d}_2(t=0) = \hat{a}_1 \rightarrow \hat{d}_2(T) = -\hat{a}_2$.

Advantages of the two approaches—conversion of propagating fields and large bandwidth of adiabatic state transfer—can be combined in a single system; see figure 1.4(c). A one-dimensional array of optomechanical transducers supports a mechanically dark mode of the two propagating fields. If we slowly vary parameters from one transducer to the next (e.g., by varying the single-photon coupling of the optical and microwave cavities), the nature of the normal mode gradually changes, similar to adiabatic conversion of intracavity fields. I describe this scheme in detail in chapter 4.

When one of the systems is driven on the blue sideband, entanglement between the two cavity fields can be generated. The Hamiltonian in the rotating frame becomes

$$\hat{H} = \hbar g_1(\hat{a}_1\hat{b} + \hat{a}_1^\dagger\hat{b}^\dagger) + \hbar g_2(\hat{a}_2^\dagger\hat{b} + \hat{b}^\dagger\hat{a}_2). \quad (1.33)$$

The blue-detuned interaction between the microwave resonator field and the mechanical oscillator generates a two-mode squeezed state of the two modes; the red-detuned interaction of the mechanical oscillator and the optical cavity transfers the mechanical state onto the microwave field. It is important to keep the red-detuned interaction stronger $g_2 > g_1$ for stability; the mechanical excitations have to be transferred from the system faster than they are being created. The generated entanglement can be used to transmit signals between the two frequency domains by quantum teleportation [99], to entangle distant microwave modes by entanglement swapping [135], or for quantum illumination [136].

Once we established a link between optical and microwave domains, a window of opportunities opens. We can use the transducer to network distant superconducting chips [89, 90] or for routing of microwave and optical photons [137]. The transducer can also be used to improve detection of weak microwave signals [83, 138], including detection of individual microwave photons [139].

1.3 CIRCUIT QUANTUM ELECTRODYNAMICS

1.3.1 Elements of superconducting systems

Linearly coupled quantum harmonic oscillators—like optical cavities, microwave resonators, or mechanical oscillators—are quantum systems that can be well understood and controlled. Their main limitation, however, is that they work in the quantum–classical correspondence regime and cannot be used for universal quantum computing [140]; one can find a classical description that will give rise to the observed quantum behaviour. To truly embrace the possibilities of quantum mechanics and open all opportunities it offers, we need to include at least one nonlinear element.

The ultimate nonlinear device is a two-level system. Such systems can take a broad range of forms from fermionic spin- $\frac{1}{2}$ systems to atoms with complicated level structures; the latter can be considered two-level systems owing to the possibility of addressing a single transition. Particularly atoms and ions are interesting for many quantum experiments since they can be controlled by electromagnetic fields, giving rise to the field of cavity quantum electrodynamics [141]. The coupling in such systems is then limited by the mode volume of the field (limited, in a cavity, to the cube of the wavelength) and the dipole moment of the atom.

The coupling can be enhanced in artificial solid-state structures. In a conductor (or a superconductor), the field can be confined well below its wavelength. Artificially created atoms are mesoscopic structures and thus have largely enhanced dipole moments. Working with gigahertz-frequency fields and transitions, we can achieve coupling that is much stronger than that observed in cavity quantum electrodynamics. The nonlinearity can be provided by Josephson tunnel junctions that, together with linear inductors and capacitors, form the basic building blocks of superconducting circuits. Working at cryogenic temperatures not only enables the Josephson effect but also ensures that the circuit does not suffer from losses associated with electrical resistance and from thermal noise.

A Josephson junction is built from two superconducting electrodes sandwiching a thin layer of insulator; see figure 1.5(a,b). The superconducting layers are characterized by their respective order parameters, $\psi_i = A_i e^{i\varphi_i}$. Two additional parameters of the junction are the critical current I_0 (above which the quantum transition to normal metal occurs) and the capacitance C_J . These two parameters define the energy scale of the junction, characterized by the Josephson and charging energy [142],

$$E_J = \frac{\hbar I_0}{2e}, \quad E_c = \frac{(2e)^2}{2C_J}. \quad (1.34)$$

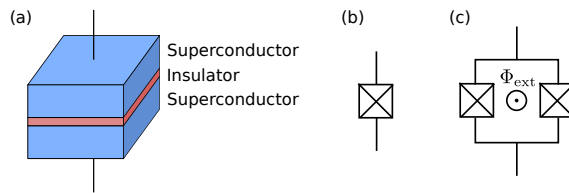


Figure 1.5: (a) Josephson junction formed by a small insulating island between two superconducting electrodes. (b) Schematic depiction of a Josephson junction. (c) A DC SQUID formed by two Josephson junctions connected in parallel.

The potential energy of the Josephson junction can be expressed in terms of the gauge-invariant phase $\varphi = \varphi_1 - \varphi_2$ [49],

$$V = -E_J \cos \varphi. \quad (1.35)$$

More intricate dynamics can be found in a DC SQUID, which is a circuit formed by two parallel Josephson junctions; see figure 1.5(c). In such a circuit, the total inductive energy is given by the sum of the inductive energies of the two junctions,

$$V = -E_{J1} \cos \varphi_1 - E_{J2} \cos \varphi_2. \quad (1.36)$$

(Here, the quantities φ_i refer to the phase difference across the i th Josephson junction.) The two phases are not independent but related through the magnetic flux threading through the loop, $\varphi_1 = \Phi_{\text{ext}}/\Phi_0 - \varphi_2$, where $\Phi_0 = \hbar/2e$ is the flux quantum. The potential energy of the DC SQUID can thus be recast as

$$\begin{aligned} V &= -(E_{J1} + E_{J2}) \cos \left(\frac{\Phi_{\text{ext}}}{2\Phi_0} \right) \sqrt{1 + \left(\frac{E_{J2} - E_{J1}}{E_{J1} + E_{J2}} \right)^2 \tan^2 \left(\frac{\Phi_{\text{ext}}}{2\Phi_0} \right)} \cos \varphi \\ &= -E_J(\Phi_{\text{ext}}) \cos \varphi \end{aligned} \quad (1.37)$$

with $\varphi = \frac{1}{2}(\varphi_1 + \varphi_2)$. Effectively, we get the same potential as for a single Josephson junction; the important distinction is that in a DC SQUID, the Josephson energy $E_J(\Phi_{\text{ext}})$ is tuneable by the external magnetic flux.

1.3.2 Quantization of electrical circuits

An electric circuit is fully characterized by the voltage $v_b(t)$ across and current $i_b(t)$ through every branch; equivalently, we can specify the branch flux and charge,

$$\Phi_b(t) = \int_{-\infty}^t d\tau v_b(\tau), \quad Q_b(t) = \int_{-\infty}^t d\tau i_b(\tau). \quad (1.38)$$

The fluxes forming a loop and charges meeting at a node follow the Kirchhoff's laws

$$\sum_{b \in \text{loop}} \Phi_b = \Phi_l, \quad \sum_{b \in \text{node}} Q_b = Q_n; \quad (1.39)$$

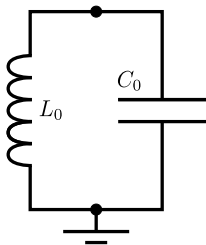


Figure 1.6: A superconducting LC circuit. Its capacitive and inductive subnetworks are formed by the branch containing the capacitor and the inductor, respectively. The circuit has two nodes (denoted by dots), both of which are active; the node at the bottom of the circuit is the ground.

therefore, not each branch gives rise to a pair of degrees of freedom.

To find the degrees of freedom—and thus the Hamiltonian—of the circuit, we follow the approach of Vool and Devoret [49]: we divide the circuit into its capacitive and inductive subnetworks and focus on the former. We now turn our attention to nodes, which we divide into active and passive—at an active node, both capacitive and inductive elements meet; passive nodes connect only capacitive (or only inductive) elements.

Although it is possible to formulate the method of nodes in full generality, I focus less on the formal aspects and more on practical applications; see reference [49] for more details. We can start with the simplest example: an LC oscillator. The circuit (shown in figure 1.6) has two active nodes; one of them—the ground—serves as a reference point and the node charge and flux are determined with respect to this node.

The electrostatic energy now plays the role of the kinetic energy and the magnetic energy corresponds to the potential energy. Owing to the linearity of the capacitor, we can express the electrostatic energy in terms of voltage (the time derivative of flux), $T = \frac{1}{2}C_0\dot{\phi}^2$. (The inductance in an LC circuit is, of course, also linear but this is no longer true for circuits containing Josephson junctions.) Together with the potential $V = \phi^2/2L_0$, the kinetic energy gives the Lagrangian $L = V - T$; the circuit obeys the Euler–Lagrange equation

$$\frac{d}{dt} \frac{\partial L}{\partial \dot{\phi}} - \frac{\partial L}{\partial \phi} = 0, \quad L = \frac{\phi^2}{2L_0} - \frac{1}{2}C_0\dot{\phi}^2. \quad (1.40)$$

We can use the Lagrangian to find the generalized momentum conjugate to the node flux,

$$q = \frac{\partial L}{\partial \dot{\phi}} = C_0\dot{\phi}. \quad (1.41)$$

Next, we apply the Legendre transformation and find the Hamiltonian

$$H = \dot{\phi}q - L = \frac{1}{2C_0}q^2 + \frac{1}{2L_0}\phi^2. \quad (1.42)$$

The equations of motion of the circuit are equivalent to the Hamilton’s equations,

$$\dot{\phi} = \frac{\partial H}{\partial q}, \quad \dot{q} = -\frac{\partial H}{\partial \phi}, \quad (1.43)$$

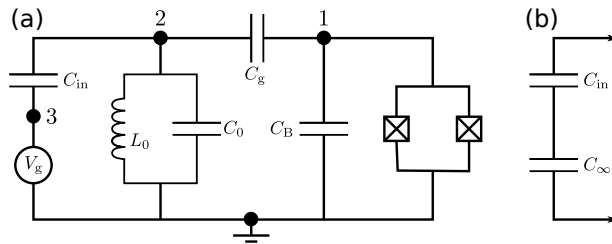


Figure 1.7: (a) Transmon qubit (right part of the circuit, formed by the DC SQUID shunted by the capacitance C_B) connected to an LC resonator (middle) and a voltage source (left). The coupling between the qubit and the resonator is provided by the capacitor C_g while the voltage is connected via the input capacitor C_{in} . The circuit has one passive three active nodes; three of these are numbered and described by the node fluxes ϕ_i . The fourth node serves as the ground. (b) Voltage source V_g replaced by a capacitor C_∞ with a large charge q_g .

and the Poisson bracket for branch flux and charge is

$$\{\Phi_b, Q_b\} = \frac{\partial \Phi_b}{\partial \phi} \frac{\partial Q_b}{\partial q} - \frac{\partial Q_b}{\partial \phi} \frac{\partial \Phi_b}{\partial q} = \pm 1. \quad (1.44)$$

The sign of the Poisson bracket depends on the nature of the branch; we get +1 for a capacitive branch and -1 for an inductive one.

Quantum mechanical variant of the Hamiltonian can be obtained by treating the flux and charge as operators and imposing the commutation relation

$$[\hat{\phi}, \hat{q}] = i\hbar. \quad (1.45)$$

If we now introduce the annihilation and creation operators via the relations

$$\hat{\phi} = \phi_{zpf}(\hat{a} + \hat{a}^\dagger), \quad \hat{q} = -i q_{zpf}(\hat{a} - \hat{a}^\dagger), \quad (1.46)$$

we recover the Hamiltonian of a quantum harmonic oscillator,

$$\hat{H} = \hbar\omega_0 \left(\hat{a}^\dagger \hat{a} + \frac{1}{2} \right). \quad (1.47)$$

Here, we introduced the resonance frequency $\omega_0 = 1/\sqrt{L_0 C_0}$ and the zero-point fluctuations $\phi_{zpf} = \sqrt{\hbar Z_0/2}$, $q_{zpf} = \sqrt{\hbar/2Z_0}$ with circuit impedance $Z_0 = \sqrt{L_0/C_0}$.

We can also consider more complicated circuits, such as the one shown in figure 1.7(a); see also reference [143]. Here, a DC SQUID shunted by a capacitor serves as a qubit. It is capacitively coupled to an LC resonator and the circuit is driven by an external voltage V_g . Before formulating the Hamiltonian, we have to understand how we can treat the voltage source. We can adopt the following approach [figure 1.7(b)]: we replace the source by a capacitor C_∞ on which a large charge q_g is stored. We treat the source as a node of its own and find the Hamiltonian of the system. In the end, we take the limit $C_\infty \rightarrow \infty$ while requiring that the ratio $q_g/C_\infty \rightarrow V_g$.

The capacitive branches give the total kinetic energy of the circuit,

$$T = \frac{1}{2}C_B\dot{\phi}_1^2 + \frac{1}{2}C_0\dot{\phi}_2^2 + \frac{1}{2}C_\infty\dot{\phi}_3^2 + \frac{1}{2}C_g(\dot{\phi}_1 - \dot{\phi}_2)^2 + \frac{1}{2}C_{\text{in}}(\dot{\phi}_2 - \dot{\phi}_3)^2. \quad (1.48)$$

The first three terms come from the branches connecting the nodes with the ground; the remaining terms stem from branches connecting the numbered nodes with each other and therefore depend on the difference of the node voltages. The magnetic potential energy has two terms,

$$V = -E_J \cos\left(\frac{\phi_1}{h}\right) + \frac{1}{2L_0}\phi_2^2. \quad (1.49)$$

This result is the consequence of the inductive branches connecting nodes only with the ground but not with each other.

We can now formulate the Lagrangian, $L = V - T$, and find the generalized momenta q_i . Writing the kinetic energy in the matrix form $T = \frac{1}{2}\dot{\boldsymbol{\phi}}^T \mathbf{C} \dot{\boldsymbol{\phi}}$ with the capacitance matrix

$$\mathbf{C} = \begin{pmatrix} C_g + C_B & -C_g & 0 \\ -C_g & C_0 + C_{\text{in}} + C_g & -C_{\text{in}} \\ 0 & -C_{\text{in}} & C_{\text{in}} + C_\infty \end{pmatrix}, \quad (1.50)$$

we have $\mathbf{q} = \mathbf{C}\dot{\boldsymbol{\phi}}$. The Hamiltonian of the circuit can be expressed as $H = \frac{1}{2}\mathbf{q}^T \mathbf{C}^{-1}\mathbf{q} + V$; taking the limit $C_\infty \rightarrow \infty$, $q_g/C_\infty \rightarrow V_g$ and imposing the commutation relation $[\hat{\phi}_i, \hat{q}_j] = i\hbar\delta_{ij}$, we get the quantum mechanical Hamiltonian

$$\begin{aligned} \hat{H} = & \frac{C_{\text{in}} + C_0 + C_g}{2C_*^2} \hat{q}_1^2 - E_J \cos\left(\frac{\hat{\phi}_1}{h}\right) + \frac{C_B + C_g}{2C_*^2} \hat{q}_2^2 + \frac{1}{2L_0} \hat{\phi}_2^2 \\ & + \frac{C_g}{C_*^2} \hat{q}_1 \hat{q}_2 + \frac{C_{\text{in}} V_g}{C_*^2} [C_g \hat{q}_1 + (C_B + C_g) \hat{q}_2], \end{aligned} \quad (1.51)$$

where $C_*^2 = C_B C_g + C_B C_{\text{in}} + C_g C_{\text{in}} + C_B C_0 + C_g C_0$.

As the next step, we assume that the capacitance forming the LC circuit is larger than any other capacitance in the circuit, $C_0 > C_g, C_B, C_{\text{in}}$. Moreover, we express the nonlinear part of the circuit in the number basis [143]: we introduce the number and phase operators $\hat{n} = \hat{q}_1/2e$, $\hat{\phi} = \hat{\phi}_1/h$ for the qubit. Together with an annihilation operator $\hat{a} = (\hat{\phi} + iZ_0\hat{q})/\sqrt{2\hbar Z_0}$ for the LC resonator, this gives the Hamiltonian

$$\hat{H} = 4E_c(\hat{n} - n_g) - E_J \cos \hat{\phi} + \hbar\omega_0 \hat{a}^\dagger \hat{a} + 2\beta e V_{\text{rms}} \hat{n}(\hat{a} + \hat{a}^\dagger). \quad (1.52)$$

Here, we have the charging energy $E_c = e^2/2C_\Sigma$ with $C_\Sigma = C_g + C_B$, $n_g = C_g V_g/2e$ is the energy offset induced by the voltage, $\beta = C_g/C_\Sigma$ gives the ratio of the gate capacitance to the total qubit capacitance, and $V_{\text{rms}} = \sqrt{\hbar\omega_0/2C_0}$ is the root-mean-square voltage of the LC oscillator.

Finally, we diagonalize the internal transmon dynamics and—since we are dealing with a nonlinear circuit—focus on the first two levels only. We thus obtain the Hamiltonian

$$\hat{H} = \hbar \frac{\omega_q}{2} \hat{\sigma}_z + \hbar\omega_0 \hat{a}^\dagger \hat{a} + \hbar g \hat{\sigma}_x (\hat{a} + \hat{a}^\dagger), \quad (1.53)$$

which describes the dipole interaction between a transmon qubit and a harmonic oscillator. The coupling rate is given by $\hbar g = \sqrt{2e\beta V_{\text{rms}}(E_J/8E_C)^{1/4}}$ and the qubit transition frequency is $\hbar\omega_q = \sqrt{8E_J E_C}$.

1.3.3 Artificial atoms and microwave resonators

The fundamental interaction between a microwave resonator and a transmon qubit is the dipole coupling, $\hat{H}_{\text{int}} = \hbar g \hat{\sigma}_x (\hat{a} + \hat{a}^\dagger)$. If both systems are on resonance, $\omega_q = \omega_0$, we can apply the rotating-wave approximation and arrive at the Jaynes–Cummings Hamiltonian

$$\hat{H}_{\text{JC}} = \hbar\omega_0 \hat{a}^\dagger \hat{a} + \hbar \frac{\omega_q}{2} \hat{\sigma}_z + \hbar g (\hat{\sigma}_+ \hat{a} + \hat{a}^\dagger \hat{\sigma}_-). \quad (1.54)$$

These circuits can reach the strong-coupling regime where the coupling rate g is stronger than the cavity decay and qubit relaxation [144, 145], enabling the observation of various quantum optical effects such as nonlinearity of the Rabi oscillations with cavity field intensity [146–148], observation of collapse and revival of a coherent state [149], or generation of nonclassical states of microwave fields [150–153].

With novel circuit designs, it is possible to reach a situation where the coupling rate is a considerable fraction of the resonance frequency [154–156]. In this regime, the qubit and resonator hybridize and can no longer be considered as separate entities. Theoretical description of circuits in the ultrastrong regime becomes problematic since one has to take into account the full Rabi model [equation (1.53)] and the number of excitations is no longer preserved. This effect can lead to situations where the ground state of the cavity field is a Schrödinger cat state [157].

If the qubit and resonator are non-resonant, they enter the dispersive regime of the Jaynes–Cummings interaction. We start from the Jaynes–Cummings Hamiltonian \hat{H}_{JC} and transform it using the unitary transformation

$$\hat{U} = \exp \left[\frac{g}{\Delta} (\hat{\sigma}_+ \hat{a} - \hat{a}^\dagger \hat{\sigma}_-) \right], \quad (1.55)$$

where $\Delta = \omega_q - \omega_0$ is the detuning between the qubit and the resonator. We can expand the resulting Hamiltonian to second order in the parameter $g/\Delta < 1$ and obtain the dispersive Hamiltonian

$$\hat{H} = \hat{U} \hat{H}_{\text{JC}} \hat{U}^\dagger = \hbar\omega_0 \hat{a}^\dagger \hat{a} + \frac{1}{2} \hbar (\omega_q + \chi) \hat{\sigma}_z - \hbar \chi \hat{\sigma}_z \hat{a}^\dagger \hat{a} - \frac{1}{2} \hbar \chi, \quad (1.56)$$

where $\chi = g^2/\Delta$.

The interaction does not lead to exchange of excitations between the qubit and the resonator since they are off-resonant. Now, the systems experience a phase shift that depends on the state of the other subsystem: measuring the phase of the qubit can provide information on the photon number inside the resonator [158]; alternatively, phase shift of light leaving the cavity can be used to infer the state of the qubit. In circuit quantum electrodynamics, the interaction is often used for quantum nondemolition measurement of the qubit state [159–161], including joint measurement of several qubits [92, 162]; I discuss these measurements in more detail in chapter 2.

The main drawback of the dispersive coupling is its perturbative character. The quantum nondemolition interaction described by Hamiltonian (1.56) is a first order expansion in the small parameter g/Δ and is thus significantly weaker than the resonant interaction. Moreover, the underlying Hamiltonian does not commute with the free qubit Hamiltonian; the dispersive readout can be considered a quantum nondemolition measurement only in the perturbative sense and generally leads to Purcell decay.

The solution to this problem lies in using longitudinal coupling between the qubit and the resonator [163, 164],

$$\hat{H} = \hbar \frac{\omega_q}{2} \hat{\sigma}_z + \hbar \omega_0 \hat{a}^\dagger \hat{a} + \hbar \lambda \hat{\sigma}_z (\hat{a} + \hat{a}^\dagger). \quad (1.57)$$

Such interaction can be achieved in a transmon qubit coupled to an LC resonator via mutual inductance. [The transversal coupling (1.53) is achieved with the qubit and resonator coupled capacitively; cf. figure 1.7.] Initially, such interaction was proposed as a platform for quantum computing in superconducting circuits but it can also be used for qubit measurements. Fast quantum nondemolition readout of the qubit state is possible when the coupling rate is modulated at the frequency of the resonator, $\lambda = \lambda_0 + \lambda_1 \cos(\omega_0 t)$ [165]; in a frame rotating with the free qubit and resonator evolution, $\hat{H}_0 = \frac{1}{2} \hbar \omega_q \hat{\sigma}_z + \hbar \omega_0 \hat{a}^\dagger \hat{a}$, the interaction is resonantly enhanced, $\hat{H}_{\text{int}} = \frac{1}{2} \hbar \lambda_1 \hat{\sigma}_z (\hat{a} + \hat{a}^\dagger)$.

Two qubits can be coupled either via a microwave resonator serving as a bus [50, 51] or directly by mutual capacitance [53, 166]. In circuits containing more qubits, basic primitives for quantum information processing can be implemented. Quantum teleportation [167, 168], basic quantum gates [50–53] and algorithms [54–56], quantum simulation [39, 40], and quantum error correction [57–60] are among the tasks that have been demonstrated in superconducting circuits.

1.4 COUPLING ARTIFICIAL ATOMS TO MECHANICAL OSCILLATORS

Nonlinear superconducting circuits can interact with mechanical oscillators in similar way as linear LC circuits. In most cases, these systems use mechanically compliant capacitors; the displacement of the mechanical oscillator determines electric properties of the circuit. Depending on the type of the circuit, both transversal [169] and longitudinal coupling [170] between a superconducting qubit and a mechanical oscillator can be realized.

Mechanically compliant capacitors are typically built as parallel-plate capacitors. One of the electrodes can be formed by a membrane [171, 172] or a nanobridge [173], which typically results in mechanical frequencies in the megahertz range. Alternatively, the capacitor can be made from a piezoelectric material so that the electric field between the electrodes induces a change of the mechanical position [81, 169]. The mechanical frequency of these oscillators depends on the thickness of the piezoelectric material and can reach several gigahertz.

For concreteness, let us consider the circuit depicted in figure 1.8; see also reference [172]. Here, a transmon qubit is built with mechanically compliant gate capacitor. The

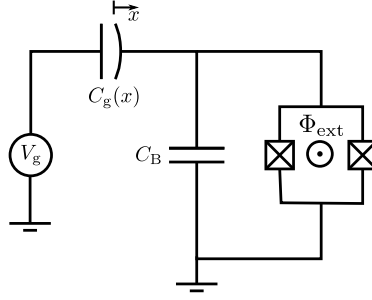


Figure 1.8: Transmon qubit with a mechanically compliant gate capacitor C_g .

Hamiltonian for the system is

$$\hat{H} = \hbar\omega_m \hat{b}^\dagger \hat{b} + 4E_c [\hat{n} - n_g(\hat{x})]^2 - E_J(\Phi_{\text{ext}}) \cos \hat{\varphi}; \quad (1.58)$$

here, the gate charge introduced by the voltage source depends on the gate capacitance and thus on the mechanical displacement. (The charging energy E_c is also affected by the mechanical motion but its effect on the qubit dynamics is much smaller and can be neglected.) The Josephson energy of the DC SQUID can be controlled using an external flux Φ_{ext} as described by equation (1.37).

Next, we linearize the gate charge,

$$n_g(\hat{x}) \approx \frac{dC_g}{dx} \frac{V_g}{2e} \hat{x} = \frac{V_g}{2e} C_g \left(1 + \frac{1}{C_g} \frac{dC_g}{dx} \Big|_{x=0} \hat{x} \right) = n_0 + n_x \hat{x}, \quad (1.59)$$

where now n_0 and n_x are independent of the mechanical position. We can now expand the Hamiltonian (1.58) to leading order in the mechanical displacement, which gives us the Hamiltonian

$$\hat{H} = 4E_c(\hat{n} - n_0)^2 - E_J(\Phi) \cos \hat{\varphi} + \hbar\omega_m \hat{b}^\dagger \hat{b} + \hbar\chi(n_0 - \hat{n})(\hat{b} + \hat{b}^\dagger). \quad (1.60)$$

The coupling rate is, for a parallel-plate capacitor, given by

$$\hbar\chi = 2E_c \frac{C_g V_g}{e} \frac{x_{\text{zpf}}}{d}; \quad (1.61)$$

here, d is the capacitor gap, that is, the distance between the static and mechanically compliant electrode. Finally, we focus only on the first two levels of the transmon; in the charge basis, we obtain the Hamiltonian

$$\hat{H} = \hbar\omega_m \hat{b}^\dagger \hat{b} + 2E_c \hat{\sigma}_z + E_J \hat{\sigma}_x + \hbar\chi(\hat{b} + \hat{b}^\dagger) \hat{\sigma}_z. \quad (1.62)$$

Hybrid nonlinear electromechanical circuits represent an interesting platform for investigating quantum optics in a solid-state system. Basic quantum optical phenomena, such as Rabi oscillations, Stark shift, or hybridization of a phonon mode and a superconducting qubit, have been observed in a transmon qubit coupled to a membrane [172]. Such

coupling can also be used to control the qubit dynamics by the mechanical oscillator or vice versa. Particularly the latter offers interesting possibilities of generating nonclassical mechanical states. It is possible to use a superconducting qubit to prepare mechanical Fock states [174, 175], squeezing [176, 177], Schrödinger-cat states [171, 178], or entanglement of two mechanical oscillators [179].

A superconducting qubit can also be used to enhance the nonlinear interaction between a mechanical oscillator and microwave resonator [173, 180–182]. In such a setup, the qubit (typically a Cooper-pair box) mediates the interaction of the two resonators. The qubit serves as a charge-dependent inductance of the microwave resonator; the gate charge controlling the Josephson inductance has a component that depends on the mechanical position. Combination of the qubit nonlinearity and large gate voltage results in an enhanced single-photon electromechanical coupling enabling us to reach the strong-coupling regime [173].

Finally, superconducting circuits coupled to mechanical oscillators can be used to realize quantum networks. In the conceptually simplest scenario, a qubit is coupled to light via an optomechanical transducer as discussed in section 1.2: the qubit is placed in a microwave cavity that interacts with a mechanical oscillator. The mechanical oscillator also interacts with an optical cavity field, enabling conversion of quantum signals between the two cavities. Existing proposals [89, 90] then suggest to use adiabatic state transfer between the qubit and the optical cavity for sending signals from one superconducting chip to another.

In these devices, the microwave resonator can be skipped and the qubit can couple directly to the mechanical oscillator. This interaction will, in practice, reduce the qubit lifetime but also eliminate decoherence due to the decay of the microwave cavity. Such a scheme can, again, be used for adiabatic state transfer between the qubit and a propagating light field [78, 183, 184] or for measurement-induced generation of entanglement between two qubits [95]. Particularly the latter approach (discussed in detail in chapter 3) is attractive for experimental implementations; by focusing on a single primitive in quantum communication, we can highly optimize the device operation. This optimization results in requirements on the system parameters that are achievable with current technology.

1.5 OTHER HYBRID SYSTEMS

Optoelectromechanical systems are not the only platform that enables efficient conversion between microwaves and light. Theoretical proposals suggest also the use of single spins [66, 67, 71, 185] (recently, the first transduction between microwaves and light using a nitrogen–vacancy centre has been reported [73]) or spin ensembles [68–70]; experimental efforts have also focused on using surface acoustic waves [84, 86], electrooptic modulators [75–77], and magnonic systems [74]. Of all these technologies, frequency conversion using localized mechanical oscillations is certainly the most mature.

Many more hybrid systems can be realized. Effective interactions between mechanical oscillators and atomic ensembles [186, 187] can be used for cooling of mechanical resonators [188, 189] or backaction-evading measurements of mechanical position [131, 133, 190].

Mechanical oscillators coupled to nitrogen–vacancy centres enable direct measurement of magnetic fields at the level of a single spin [93] or of mechanical motion [191, 192], observation of interesting effects known from quantum optics [193], or quantum information processing [194]; in these systems, the interaction is provided either by a magnetic field [195, 196] or strain [197, 198]. Surface acoustic waves can be used to couple to various systems: light and microwave signals [84, 199], to electron spins in trapped ions, nitrogen-vacancy centres, or quantum dots [200, 201], as well as to superconducting circuits [202, 203].

All in all, optoelectromechanical systems are just a small subset of hybrid quantum systems; nevertheless, already at this level, there is a broad range of interesting processes and applications. In the rest of this dissertation, I focus on a single task: improving optomechanical transduction. I consider two approaches to this problem: in the first strategy, the transducer is optimized for a specific task—generation of entanglement between two superconducting qubits. The resulting transducer is less general than in the experiment of Andrews et al. [82], which allows us to relax requirements on the experimental parameters. Nevertheless, in the context of quantum networks with superconducting circuits, long-distance entanglement between qubits is sufficient for transmitting quantum information and performing quantum gates between nodes via teleportation [204]. The other approach involves a new design for a general-purpose optomechanical transducer. By building an array of optoelectromechanical systems, we can greatly enhance the conversion bandwidth. Before diving into these topics, however, we need one more tool: an effective description of hybrid quantum systems subject to continuous homodyne measurement, which is presented in the next chapter.

CHAPTER 2

CONTINUOUS MEASUREMENTS ON HYBRID QUANTUM SYSTEMS

Quantum systems interact with their environment; the larger the system, the more pronounced this effect is. For a large part, this process is unwanted—it leads to decoherence and classical behaviour. Nonetheless, the interaction enables us to measure the dynamics of the system. For example, the photons leaving an optomechanical cavity can give us information about the state of a mechanical oscillator inside the cavity. The interplay of unitary dynamics, decoherence, and measurements requires advanced mathematical tools to describe the resulting stochastic dynamics.

In this chapter, I discuss stochastic master equations that describe dynamics of density matrices under continuous measurements. I start by developing the necessary formalism (following the approach of Wiseman and Milburn [97]) in section 2.1 before moving to its applications in circuit quantum electrodynamics and cavity optomechanics in section 2.2. In these systems, individual quantum trajectories can be observed [205] or the measurement can be used to steer the system towards a desired state with measurement-based feedback [97, 206].

Applying stochastic master equations to hybrid quantum systems requires more care. Although one can, of course, write an equation of motion for an optoelectromechanical system, numerical simulations of such systems are problematic. Hybrid systems consist of several subsystems evolving on different timescales and coupled to different environments. This problem is particularly apparent for an optomechanical transducer that is used to read out the state of a superconducting qubit (situation I discuss in detail in chapter 3): the qubit is coupled to an optomechanical system that, on its own, obeys Gaussian dynamics. Numerical simulations of such a device require truncation of its infinite-dimensional Hilbert space; the low frequency of mechanical oscillations (and correspondingly large thermal occupation) results in cutoff at extremely large Fock numbers. The size of the Hilbert space needed for efficient numerical simulations leads to memory requirements beyond current technological possibilities.

To solve this issue, I show how one can obtain an effective equation of motion for the system of interest (the superconducting qubit) by adiabatically eliminating Gaussian systems (the transducer) from conditional quantum dynamics. The precise dynamics of the transducer are irrelevant for our purposes; by deriving an effective equation of motion for the qubit, we significantly simplify the problem without discarding any crucial

information about its dynamics. Although various methods exist to adiabatically eliminate subsystems from quantum dynamics [91, 207–213], none is capable of treating thermally driven systems under continuous measurements. Here, I solve this problem and show that thermally driven systems can be adiabatically eliminated from stochastic quantum evolution if they obey Gaussian dynamics [98].

I start by considering Gaussian systems alone in section 2.3. These systems have Hamiltonians that are quadratic in the canonical operators and jump operators that are linear; moreover, they are measured using homodyne detection. Consequently, these systems possess Gaussian Wigner function and can be fully described by the first and second statistical moments of the quasi-probability density. The stochastic master equation can be used to derive equations of motion for these moments.

In section 2.4, I show how one can adiabatically eliminate Gaussian subsystems from stochastic dynamics containing both Gaussian and non-Gaussian systems. The approach uses a hybrid description where the non-Gaussian system is described by its density matrix and the Gaussian system using its statistical moments. This strategy allows straightforward elimination of systems suffering from thermal noise or consisting of several modes; these features are the main advantage compared to other adiabatic elimination methods in stochastic quantum dynamics.

I then use this approach on several examples in section 2.5. I take the model systems from circuit quantum dynamics and compare the method to the full dynamics and elimination for low-temperature thermal bath (with average number of excitations $\bar{n} \lesssim 2$). Already on this level, the new approach clearly outperforms existing methods and I argue that it can be used also for larger thermal occupations (such as those seen in cavity optomechanics).

2.1 PRINCIPLES OF CONTINUOUS MEASUREMENTS

2.1.1 Quantum-optical master equation

Consider an optical cavity. The cavity field will leak out owing to imperfect reflection on mirrors and finite mode overlap with the field outside the cavity. The field is described by the annihilation operator \hat{a} and the modes of the bath by the annihilation operators \hat{b}_k ; in full generality, k is a multi-index describing the wavenumber and polarization of the mode. The dynamics of the combined state $\hat{\rho}_{\text{SE}}$ are given by the free Hamiltonian of the cavity field and the environment and their mutual interaction,

$$\frac{d\hat{\rho}_{\text{SE}}}{dt} = -i \left[\omega \hat{a}^\dagger \hat{a} + \sum_k \omega_k \hat{b}_k^\dagger \hat{b}_k + \sum_k g_k (\hat{a}^\dagger \hat{b}_k + \hat{b}_k^\dagger \hat{a}), \hat{\rho}_{\text{SE}} \right]. \quad (2.1)$$

The master equation that describes the evolution of the state of the cavity field, $\hat{\rho} = \text{tr}_{\text{E}}\{\hat{\rho}_{\text{SE}}\}$, is best derived in the interaction picture with respect to the free Hamiltonian $\hat{H}_0 = \omega \hat{a}^\dagger \hat{a} + \sum_k \omega_k \hat{b}_k^\dagger \hat{b}_k$. The density matrix and the interaction Hamiltonian in the

interaction picture are

$$\hat{\rho}_{\text{SE}}^{\text{IP}} = e^{i\hat{H}_0 t} \hat{\rho}_{\text{SE}} e^{-i\hat{H}_0 t}, \quad (2.2a)$$

$$\hat{H}_{\text{int}}^{\text{IP}} = e^{i\hat{H}_0 t} \hat{H}_{\text{int}} e^{-i\hat{H}_0 t} = \sum_k g_k \left(\hat{a}^\dagger \hat{b}_k e^{i(\omega_k - \omega)t} + \hat{b}_k^\dagger \hat{a} e^{-i(\omega_k - \omega)t} \right). \quad (2.2b)$$

For the density operator in the interaction picture, we can write the solution generally as

$$\hat{\rho}_{\text{SE}}^{\text{IP}}(t) = \hat{\rho}_{\text{SE}}^{\text{IP}}(0) - i \int_0^t dt_1 \left[\hat{H}_{\text{int}}^{\text{IP}}(t_1), \hat{\rho}_{\text{SE}}^{\text{IP}}(t_1) \right]. \quad (2.3)$$

We can substitute this solution back to the equation of motion for $\hat{\rho}_{\text{SE}}^{\text{IP}}$ and obtain

$$\frac{d\hat{\rho}_{\text{SE}}^{\text{IP}}(t)}{dt} = -i \left[\hat{H}_{\text{int}}^{\text{IP}}(t), \hat{\rho}_{\text{SE}}^{\text{IP}}(0) \right] - \int_0^t dt_1 \left[\hat{H}_{\text{int}}^{\text{IP}}(t), \left[\hat{H}_{\text{int}}^{\text{IP}}(t_1), \hat{\rho}_{\text{SE}}^{\text{IP}}(t_1) \right] \right]. \quad (2.4)$$

Now, we trace out the environment degrees of freedom and arrive at an effective equation of motion for the system.

To enable tracing out the environment explicitly, we make the following assumptions: first, at the initial time, $t = 0$, the system and environment are uncorrelated, $\hat{\rho}_{\text{SE}}^{\text{IP}}(0) = \hat{\rho}^{\text{IP}}(0) \otimes \hat{\rho}_{\text{E}}^{\text{IP}}$. Next, we presume that the interaction Hamiltonian has no diagonal elements in the eigenbasis of the environment Hamiltonian, $\text{tr}_{\text{E}} \left\{ \hat{H}_{\text{int}}^{\text{IP}}(t) \hat{\rho}_{\text{SE}}^{\text{IP}}(0) \right\} = 0$. The equation for the system density matrix now becomes

$$\frac{d\hat{\rho}^{\text{IP}}(t)}{dt} = - \int_0^t dt_1 \text{tr}_{\text{E}} \left\{ \left[\hat{H}_{\text{int}}^{\text{IP}}(t), \left[\hat{H}_{\text{int}}^{\text{IP}}(t_1), \hat{\rho}_{\text{SE}}^{\text{IP}}(t_1) \right] \right] \right\}. \quad (2.5)$$

The last step invokes the Born–Markov approximation. The Born approximation replaces the joint state by a product state. Furthermore, the state of the environment is—owing to its large size—unaffected by the coupling, $\hat{\rho}_{\text{SE}}^{\text{IP}}(t) = \hat{\rho}^{\text{IP}}(t) \otimes \hat{\rho}_{\text{E}}^{\text{IP}}$. The Markov approximation assumes that the integrand in equation (2.5) is sharply peaked around $t_1 = t$, which enables us to replace the lower integration limit by $-\infty$ and the state $\hat{\rho}_{\text{SE}}^{\text{IP}}(t_1)$ by $\hat{\rho}^{\text{IP}}(t)$. The Born–Markov master equation then takes the form

$$\frac{d\hat{\rho}^{\text{IP}}(t)}{dt} = - \int_{-\infty}^t dt_1 \text{tr}_{\text{E}} \left\{ \left[\hat{H}_{\text{int}}^{\text{IP}}(t), \left[\hat{H}_{\text{int}}^{\text{IP}}(t_1), \hat{\rho}^{\text{IP}}(t) \otimes \hat{\rho}_{\text{E}}^{\text{IP}} \right] \right] \right\}. \quad (2.6)$$

With the interaction Hamiltonian (2.2b) and the commutation relation $[\hat{b}_k, \hat{b}_l^\dagger] = \delta_{kl}$, the Born–Markov master equation for the cavity field becomes

$$\frac{d\hat{\rho}^{\text{IP}}}{dt} = - \int_{-\infty}^t dt_1 \Gamma(t - t_1) (\hat{a} \hat{a}^\dagger \hat{\rho}^{\text{IP}} - \hat{a} \hat{\rho}^{\text{IP}} \hat{a}^\dagger - \hat{a}^\dagger \hat{\rho}^{\text{IP}} \hat{a} + \hat{\rho}^{\text{IP}} \hat{a}^\dagger \hat{a}) + \text{H.c.}, \quad (2.7a)$$

$$\Gamma(t - t_1) = \sum_k g_k^2 e^{-i(\omega_k - \omega)(t - t_1)}. \quad (2.7b)$$

The cavity field couples to a continuum of modes outside the cavity; we can replace the sum in equation (2.7b) by the integral,

$$\Gamma(t - t_1) = \int d\Omega \varrho(\Omega) g^2(\Omega) e^{-i(\Omega - \omega)(t - t_1)}, \quad (2.8)$$

where $\varrho(\Omega)$ is the density of states. The product $\varrho(\Omega)g^2(\Omega)$ is a slowly varying function of frequency and we assume it to be constant around the cavity frequency, $\Omega \sim \omega$. We can then write the master equation in the Lindblad form

$$\frac{d\hat{\rho}^{\text{IP}}}{dt} = \kappa(\bar{n} + 1)\mathcal{D}[\hat{a}]\hat{\rho}^{\text{IP}} + \kappa\bar{n}\mathcal{D}[\hat{a}^\dagger]\hat{\rho}^{\text{IP}}. \quad (2.9)$$

Here, $\bar{n} = [\exp(\hbar\omega/k_B T) - 1]^{-1}$ is the mean thermal photon number of the external field at frequency ω , $\kappa \approx 2\pi\varrho(\omega)g^2(\omega)$ is the cavity decay rate, and

$$\mathcal{D}[\hat{A}]\hat{\rho} = \hat{A}\hat{\rho}\hat{A}^\dagger - \frac{1}{2}(\hat{A}^\dagger\hat{A}\hat{\rho} + \hat{\rho}\hat{A}^\dagger\hat{A}). \quad (2.10)$$

Equation (2.9) is expressed in the rotating frame. Moving back to the laboratory frame, we just need to include a term describing the free cavity evolution, $-i[\hat{H}_S, \hat{\rho}]$. In fact, we can include other unitary dynamics, such as driving or nonlinearity of the cavity medium, in the same manner. The full Lindblad master equation for a cavity field in the laboratory frame is

$$\frac{d\hat{\rho}}{dt} = -i[\hat{H}, \hat{\rho}] + \kappa\mathcal{D}[\hat{a}]\hat{\rho}. \quad (2.11)$$

Here I used the fact that at optical frequencies, the thermal population number $\bar{n} = 0$ at room temperature.

I derived the master equation (2.11) for a cavity field but the same approach can be applied to other systems as well [97, 214]. Mechanical oscillators obey the same dynamics with Lindblad terms describing phonon loss and gain. Decay of two-level systems is described by the term $\mathcal{D}[\hat{\sigma}_-]\hat{\rho}$ and pure dephasing by $\mathcal{D}[\hat{\sigma}_z]\hat{\rho}$. Hence, the Lindblad master equation is a powerful tool in quantum optics enabling efficient treatment of all kinds of systems.

2.1.2 Stochastic unravellings

Measurement of the field leaking out of a cavity can provide useful information about the system inside the cavity. Mathematical description of such dynamics needs to go beyond the master equation approach and include the stochastic contribution of the random measurement outcomes. Such a dynamical equation can be obtained from the master equation by its stochastic unravelling. This process is not unique for a given equation; first, I will show how detecting leaked photons leads to stochastic dynamics with discrete quantum jumps. Afterwards, I will show how combining the photons leaking from the cavity with a strong laser field leads to a diffusive state evolution under homodyne detection.

We start from the master equation for a cavity field,

$$\frac{d\hat{\rho}}{dt} = -i[\hat{H}, \hat{\rho}] + \kappa\mathcal{D}[\hat{a}]\hat{\rho}. \quad (2.12)$$

Continuous monitoring of the cavity output implies that at every time infinitesimal dt we will detect either zero or one photon; since $dt \rightarrow 0$, we can neglect the probability of

detecting more photons during a single time step. The density matrix is then given by summing over the two measurement outcomes,

$$\hat{\rho}(t + dt) = \sum_{j=0}^1 \hat{M}_j(dt) \hat{\rho}(t) \hat{M}_j^\dagger(dt) \quad (2.13)$$

with measurement operators

$$\hat{M}_0(dt) = \hat{I} - \left(\frac{\kappa}{2} \hat{a}^\dagger \hat{a} + i\hat{H} \right) dt, \quad \hat{M}_1(dt) = \sqrt{\kappa dt} \hat{a}. \quad (2.14)$$

To first order in the infinitesimal dt , the operators $\hat{M}_{0,1}(dt)$ are valid measurement operators since $\sum_j \hat{M}_j^\dagger(dt) \hat{M}_j(dt) = \hat{I}$. Moreover, from the measurement operators acting on the density matrix, we obtain the master equation,

$$\hat{\rho}(t + dt) = \sum_j \hat{M}_j(dt) \hat{\rho}(t) \hat{M}_j^\dagger(dt) = \hat{\rho}(t) - i[\hat{H}, \hat{\rho}(t)]dt + \kappa \mathcal{D}[\hat{a}] \hat{\rho}(t) dt. \quad (2.15)$$

The probability of detecting a photon in the cavity output is

$$p_1(dt) = \text{tr}\{\hat{M}_1(dt) \hat{\rho} \hat{M}_1^\dagger(dt)\} = \kappa \text{tr}\{\hat{a}^\dagger \hat{a} \hat{\rho}\} dt. \quad (2.16)$$

For almost all time intervals, we have the measurement result $j = 0$ since $p_0(dt) = 1 - p_1(dt) = 1 - O(dt)$. During these time intervals, the state evolves according to $\hat{M}_0(dt)$ —infinitesimally but non-unitarily. When the outcome $j = 1$ occurs, the state changes abruptly according to $\hat{M}_1(dt)$; we call such events quantum jumps. A single quantum trajectory is then given by a series of the continuous evolutions and quantum jumps.

The number and timing of photodetections are encoded in a function $N(t)$ which gives the number of detections from time $t = 0$ to time t . For the stochastic increment $dN(t)$, we then have

$$dN^2(t) = dN(t), \quad \langle dN(t) \rangle = \langle \hat{M}_1^\dagger(dt) \hat{M}_1(dt) \rangle. \quad (2.17)$$

Assuming a pure state $|\psi(t)\rangle$, we can divide the evolution into two processes: when $dN(t) = 0$, no quantum jump took place and the system evolves according to $\hat{M}_0(dt)$. On the other hand, we observe a quantum jump if $dN(t) = 1$; then, the system evolves according to $\hat{M}_1(dt)$. These two contributions can be combined in the stochastic Schrödinger equation

$$\begin{aligned} d|\psi(t)\rangle &= dN(t) \left(\frac{\hat{a}}{\sqrt{\langle \hat{a}^\dagger \hat{a} \rangle}} - 1 \right) |\psi(t)\rangle + dt [1 - dN(t)] \left[\frac{\kappa}{2} (\langle \hat{a}^\dagger \hat{a} \rangle - \hat{a}^\dagger \hat{a}) - i\hat{H} \right] |\psi(t)\rangle \\ &= dN(t) \left(\frac{\hat{a}}{\sqrt{\langle \hat{a}^\dagger \hat{a} \rangle}} - 1 \right) |\psi(t)\rangle + dt \left[\frac{\kappa}{2} (\langle \hat{a}^\dagger \hat{a} \rangle - \hat{a}^\dagger \hat{a}) - i\hat{H} \right] |\psi(t)\rangle; \end{aligned} \quad (2.18)$$

in the second line, we used the fact that $dN(t)dt = O(dt^{3/2})$.

The stochastic Schrödinger equation can be turned into an equation for the density operator by defining the projector $\hat{\rho}(t) = |\psi(t)\rangle\langle\psi(t)|$ and using the Itô rule $d(XY) = (dX)Y + XdY + (dX)(dY)$,

$$\begin{aligned} d\hat{\rho}(t) &= (d|\psi(t)\rangle)\langle\psi(t)| + |\psi(t)\rangle(d\langle\psi(t)|) + (d|\psi(t)\rangle)(d\langle\psi(t)|) \\ &= -\mathcal{H} \left[i\hat{H} + \frac{\kappa}{2}\hat{a}^\dagger\hat{a} \right] \hat{\rho}(t)dt + \kappa\mathcal{G}[\hat{a}]\hat{\rho}(t)dN(t); \end{aligned} \quad (2.19)$$

here, I defined the superoperators

$$\mathcal{G}[\hat{A}]\hat{\rho} = \frac{\hat{A}\hat{\rho}\hat{A}^\dagger}{\text{tr}\{\hat{A}\hat{\rho}\hat{A}^\dagger\}} - \hat{\rho}, \quad (2.20a)$$

$$\mathcal{H}[\hat{A}]\hat{\rho} = (\hat{A} - \langle\hat{A}\rangle)\hat{\rho} + \hat{\rho}(\hat{A} - \langle\hat{A}\rangle). \quad (2.20b)$$

The stochastic master equation (2.19) describes the stochastic evolution of an arbitrary quantum state under photodetection. One can easily check that averaging over the ensemble reduces the stochastic master equation to the master equation $d_t\hat{\rho} = -i[\hat{H}, \hat{\rho}] + \kappa\mathcal{D}[\hat{a}]\hat{\rho}$. Finally, to fully describe the stochastic dynamics, we have to specify also the photocount function $N(t)$ or, more usually, the photocurrent

$$I(t) = \dot{N}(t). \quad (2.21)$$

The stochastic dynamics is fully described by both equations (2.19) and (2.21).

Homodyne detection is realized by mixing the output field with a strong coherent field. To derive a conditional master equation for homodyning, we start by the observation that the master equation $d_t\hat{\rho} = -i[\hat{H}, \hat{\rho}] + \kappa\mathcal{D}[\hat{a}]\hat{\rho}$ is invariant under the transformation

$$\hat{a} \rightarrow \hat{a} + \alpha, \quad \hat{H} \rightarrow \hat{H} - i\frac{\kappa}{2}(\alpha^*\hat{a} - \alpha\hat{a}^\dagger), \quad (2.22)$$

which corresponds to displacing the origin of the phase space. The new measurement operators are (assuming for simplicity that α is real)

$$\hat{M}_0(dt) = \hat{I} - \left[i\hat{H} + \frac{\kappa}{2}\alpha(\hat{a} - \hat{a}^\dagger) + \frac{\kappa}{2}(\hat{a}^\dagger + \alpha)(\hat{a} + \alpha) \right] dt, \quad (2.23a)$$

$$\hat{M}_1(dt) = \sqrt{\kappa dt}(\hat{a} + \alpha) \quad (2.23b)$$

and, for the photodetection rate, we have

$$\langle dN(t) \rangle = \langle \hat{M}_1^\dagger(dt)\hat{M}_1(dt) \rangle = \kappa \text{tr}\{[\alpha^2 + \alpha(\hat{a} + \hat{a}^\dagger) + \hat{a}^\dagger\hat{a}]\hat{\rho}(t)\}dt. \quad (2.24)$$

If the classical pump is much stronger than the output field, this expression simplifies to a strong classical field with a term proportional to $\hat{a} + \hat{a}^\dagger$. The number of photodetections approaches infinity but the effect of each photodetection becomes infinitesimal because most detections come from the classical field.

During a small time window dt with a large number of detections, $dN \sim \alpha^2 dt$, the Poissonian statistics of the pump field will be approximately Gaussian. The mean and

variance of the Gaussian-distributed photocounts are

$$\mu = \kappa \text{tr}\{[\alpha^2 + \alpha(\hat{a} + \hat{a}^\dagger) + \hat{a}^\dagger \hat{a}]\hat{\rho}(t)\}dt \approx \kappa[\alpha^2 + \alpha\langle\hat{a} + \hat{a}^\dagger\rangle]dt, \quad (2.25a)$$

$$\sigma^2 = \kappa\alpha^2 dt. \quad (2.25b)$$

We can thus write

$$dN = \kappa[\alpha^2 + \alpha\langle\hat{a} + \hat{a}^\dagger\rangle]dt + \sqrt{\kappa}\alpha dW; \quad (2.26)$$

here, dW is Wiener increment with mean $\langle dW \rangle = 0$ and variance $dW^2 = dt$.

If we use these results—the displaced frame (2.22) and the Gaussian-distributed photocounts (2.26)—in the stochastic master equation (2.19), we obtain the stochastic master equation for homodyne detection,

$$d\hat{\rho}(t) = -i[\hat{H}, \hat{\rho}(t)]dt + \kappa\mathcal{D}[\hat{a}]\hat{\rho}(t)dt + \sqrt{\kappa}\mathcal{H}[\hat{a}]\hat{\rho}(t)dW(t), \quad (2.27a)$$

$$\mathcal{D}[\hat{A}]\hat{\rho} = \hat{A}\hat{\rho}\hat{A}^\dagger - \frac{1}{2}(\hat{A}^\dagger\hat{A}\hat{\rho} + \hat{\rho}\hat{A}^\dagger\hat{A}), \quad (2.27b)$$

$$\mathcal{H}[\hat{A}]\hat{\rho} = (\hat{A} - \langle\hat{A}\rangle)\hat{\rho} + \hat{\rho}(\hat{A}^\dagger - \langle\hat{A}^\dagger\rangle). \quad (2.27c)$$

Additionally, the equation for photocurrent becomes

$$I(t)dt = \sqrt{\kappa}\langle\hat{a} + \hat{a}^\dagger\rangle dt + dW. \quad (2.28)$$

2.2 QUANTUM MEASUREMENTS ON PHYSICAL SYSTEMS

Originally, quantum trajectories have been introduced as an interesting and efficient method to solve master equations numerically [215]. At that time it was difficult to imagine that control of individual quantum systems would reach such a level where their monitoring in real time would become possible. Nowadays—only 25 years later—quantum trajectories are routinely observed in laboratories the world over and continuous measurements and measurement-based feedback are important tools for control of quantum systems.

Probably the most famous example of observation of quantum trajectories are the experiments with microwave cavities and Rydberg atoms performed by the group of Serge Haroche [216–218]. In these experiments, the atoms are used to perform Ramsey interferometry on the cavity field; the atoms are sent individually through the cavity and their dispersive interaction with the cavity field encodes the field intensity in the phase the atomic state acquires. Measurement of the atomic state after the interaction thus reveals the photon population in the cavity and enables observation of its jumps between different photon numbers.

In circuit quantum electrodynamics, individual quantum trajectories have also been observed [159, 219]. In the simplest scenario, a single superconducting qubit dispersively interacts with a cavity mode,

$$\hat{H}_{\text{int}} = \chi\hat{a}^\dagger\hat{a}\hat{\sigma}_z, \quad (2.29)$$

which is followed by a measurement of the phase quadrature of the output field. Through the interaction, the field acquires a phase shift that depends on the qubit state. If the

measurement is weak, the qubit state slowly drifts towards one of the pointer states; with a strong measurement, the qubit jumps between the ground and excited states.

With more intricate circuits, more complex dynamics can be studied. For instance, simultaneous measurement and Rabi drive can result in quantum Zeno effect [209, 220]; the measurement process counteracts the driving and the transitions between the two qubit states are suppressed. Other interesting concepts studied in circuit quantum electrodynamics include simultaneous measurements of non-commuting observables [221] and continuous measurement of the transverse component of the qubit state [222].

Continuous measurements also open new possibilities for state manipulation, especially when followed by postselection. In such a scenario, the measurement signal is used to determine whether the system reached a desired state; if that is not the case, the protocol is repeated. It is possible to use postselection to initialize the state of a superconducting qubit [160, 223]. Here, the dispersive interaction and homodyne detection are used to determine whether the qubit is in the ground or excited state; if it is found in the excited state, a single π -pulse can be applied to bring it to the ground state.

One can also generate entanglement between two superconducting qubits by measuring their total spin [91, 92]. For this task, dispersive coupling of a cavity mode to two qubits is used,

$$\hat{H}_{\text{int}} = \chi_1 \hat{a}^\dagger \hat{a} \hat{\sigma}_z^1 + \chi_2 \hat{a}^\dagger \hat{a} \hat{\sigma}_z^2. \quad (2.30)$$

If the coupling to both qubits is equally strong, $\chi_1 = \chi_2$, the phase quadrature carries information about the total spin of the two qubits, $\hat{\sigma}_z^1 + \hat{\sigma}_z^2$. For qubits initially prepared in the state $|\psi_0\rangle = \frac{1}{2}(|0\rangle + |1\rangle)(|0\rangle + |1\rangle)$, the qubits collapse onto the Bell state $|\Psi_+\rangle = (|01\rangle + |10\rangle)/\sqrt{2}$ with probability of 50 %. The greatest advantage of this approach is that the qubits do not have to be placed in the same cavity; the scheme works also when the qubits are in separate cavities and the output of one cavity is fed into the second one.

Even more applications are possible when continuous measurements are accompanied by measurement-based feedback [97, 206]. In such a scenario, the measurement signal is used to apply a feedback operation on the system. This approach is experimentally more demanding since it requires instantaneous correction of the dynamics based on the measurement outcome in each time step; it enables, however, deterministic entanglement generation [162]. Feedback can also be used to counteract backaction of the measurement [224, 225], thus stabilizing quantum trajectories [161, 226–228]. State stabilization is also possible using stroboscopic measurements and feedback [229]. Here, a strong projective measurement is applied periodically at times when the system is assumed to be in a specific eigenstate of the measurement; if it is not, feedback is used to bring it to this state.

In optomechanics, measurement feedback can be used to cool a mechanical oscillator to its ground state [126, 230–232]. Homodyne detection of light provides information about the position of the mechanical oscillator; a second laser uses this information to counteract the thermal fluctuations and confine the mechanical motion to a small region around its equilibrium position.

Another interesting approach to feedback control in optomechanics involves systems driven on the blue sideband [233]. The blue-detuned optomechanical interaction generates

entanglement between the mechanical oscillator and the light field and can be combined with time-continuous Bell measurements [234]. With these tools, it is possible to teleport an arbitrary quantum state onto the mechanical oscillator or to entangle two mechanical oscillators.

2.3 GAUSSIAN DYNAMICS

Stochastic master equations are a crucial tool for describing quantum dynamics under continuous measurements; their weakness lies in the difficulty of their simulation. One needs to generate many quantum trajectories to be able to understand the statistical properties of the physical processes. In addition, when not all decay channels are monitored, one usually has to work with density matrix—and not the wavefunction—which significantly limits the size of problems that can be simulated numerically.

One can avoid the necessity of generating many trajectories for Gaussian systems, that is, systems characterized by a Gaussian quasi-probability distribution in phase space [235]. Such systems can be fully described using the first and second statistical moments of the quasi-probability distribution, for which algebraic equations of motion can be derived. A Gaussian system is described by continuous-variable operators with linear dynamics; the canonical operators can be collected in a vector $\hat{\mathbf{r}} = (\hat{q}_1, \hat{p}_1, \dots, \hat{q}_N, \hat{p}_N)^T$ with commutation relations defining the symplectic matrix

$$[\hat{r}_i, \hat{r}_j] = i\sigma_{ij}, \quad \sigma = \begin{pmatrix} 0 & 1 \\ -1 & 0 \end{pmatrix} \oplus \dots \oplus \begin{pmatrix} 0 & 1 \\ -1 & 0 \end{pmatrix}. \quad (2.31)$$

In terms of the canonical vector $\hat{\mathbf{r}}$, the unitary dynamics is bilinear and jump and measurement operators are linear,

$$d\hat{\rho} = -i[\hat{H}, \hat{\rho}]dt + \sum_n \mathcal{D}[\hat{j}_n]\hat{\rho}dt + \sum_m \mathcal{H}[\hat{\lambda}_m]\hat{\rho}dW_m, \quad (2.32a)$$

$$\hat{H} = \frac{1}{2}\hat{\mathbf{r}}^T \mathbf{R} \hat{\mathbf{r}}, \quad \mathbf{R} = \mathbf{R}^T \in \mathbb{R}^{2N} \times \mathbb{R}^{2N}, \quad (2.32b)$$

$$\hat{j}_n = \xi_n^T \hat{\mathbf{r}}, \quad \xi_n \in \mathbb{C}^{2N}, \quad (2.32c)$$

$$\hat{\lambda}_m = (\mathbf{c}_m + i\mathbf{m}_m)^T \hat{\mathbf{r}}, \quad \mathbf{c}_m, \mathbf{m}_m \in \mathbb{R}^{2N}. \quad (2.32d)$$

[In equation (2.32b), we do not include linear terms to the Hamiltonian, which would only result in a displacement with respect to the origin of the phase space.] Since the system is Gaussian, it is fully described by the first and second statistical moments of the canonical operators,

$$\mathbf{x} = \langle \hat{\mathbf{r}} \rangle = \text{tr}\{\hat{\rho}\hat{\mathbf{r}}\}, \quad \Gamma_{ij} = \langle [\hat{r}_i, \hat{r}_j]_+ \rangle - 2x_i x_j. \quad (2.33)$$

In the following, I show how to derive equations governing the dynamics of the statistical moments which fully characterise the evolution of the Gaussian system.

We start by considering the master equation

$$\frac{d\hat{\rho}}{dt} = -i[\hat{H}, \hat{\rho}] + \sum_n \mathcal{D}[\hat{j}_n]\hat{\rho}, \quad (2.34)$$

from which we first derive the equation of motion for the mean vector \mathbf{x} . For the i th mean value, we have

$$\begin{aligned}\dot{x}_i &= \text{tr} \left\{ \frac{d\hat{\rho}}{dt} \hat{r}_i \right\} \\ &= -i \text{tr} \{ [\hat{H}, \hat{\rho}] \hat{r}_i \} + \sum_n \text{tr} \{ \mathcal{D}[\hat{J}_n] \hat{\rho} \hat{r}_i \} \\ &= -i \text{tr} \{ \hat{\rho} [\hat{r}_i, \hat{H}] \} + \text{tr} \left\{ \hat{\rho} \left(\hat{J}_n^\dagger \hat{r}_i \hat{J}_n - \frac{1}{2} [\hat{J}_n^\dagger \hat{J}_n, \hat{r}_i]_+ \right) \right\};\end{aligned}\quad (2.35)$$

in the last line and in the following, I use the Einstein summation convention. The commutator in the first term can be rewritten as

$$[\hat{r}_i, \hat{H}] = \frac{1}{2} R_{jk} [\hat{r}_i, \hat{r}_j \hat{r}_k] = \frac{1}{2} R_{jk} ([\hat{r}_i, \hat{r}_j] \hat{r}_k + \hat{r}_j [\hat{r}_i, \hat{r}_k]) = i\sigma_{ij} R_{jk} \hat{r}_k, \quad (2.36)$$

where I used the fact that the Hamiltonian matrix is symmetric, $\mathbf{R} = \mathbf{R}^T$. For the Lindblad terms, we have

$$\begin{aligned}\text{tr} \{ \mathcal{D}[\hat{J}_n] \hat{\rho} \hat{r}_i \} &= \xi_{nj} \xi_{nk}^* \text{tr} \left\{ \hat{\rho} \left(\hat{r}_k \hat{r}_i \hat{r}_j - \frac{1}{2} [\hat{r}_k \hat{r}_j, \hat{r}_i]_+ \right) \right\} \\ &= \frac{1}{2} \xi_{nj} \xi_{nk}^* \text{tr} \{ \hat{\rho} (\hat{r}_k [\hat{r}_i, \hat{r}_j] - [\hat{r}_i, \hat{r}_k] \hat{r}_j) \} \\ &= -\frac{i}{2} \sigma_{ij} (\xi_{nj}^* \xi_{nk} - \xi_{nj} \xi_{nk}^*) x_k.\end{aligned}\quad (2.37)$$

Combining everything, we can write

$$\dot{x}_i = \sigma_{ij} R_{jk} x_k - \frac{i}{2} \sigma_{ij} (\xi_{nj}^* \xi_{nk} - \xi_{nj} \xi_{nk}^*) x_k, \quad (2.38)$$

or, in the matrix form,

$$\dot{\mathbf{x}} = \mathbf{A}\mathbf{x}, \quad \mathbf{A} = \boldsymbol{\sigma}\mathbf{R} - \frac{i}{2} \boldsymbol{\sigma} \sum_n (\boldsymbol{\xi}_n^* \boldsymbol{\xi}_n^T - \boldsymbol{\xi}_n \boldsymbol{\xi}_n^\dagger). \quad (2.39)$$

For the covariance matrix, we need to evaluate the expression

$$\dot{\Gamma}_{ij} = \text{tr} \left\{ \frac{d\hat{\rho}}{dt} [\hat{r}_i, \hat{r}_j]_+ \right\} - 2(\dot{x}_i x_j + x_i \dot{x}_j). \quad (2.40)$$

We start with the coherent evolution. The commutator

$$[\hat{r}_i \hat{r}_j, \hat{H}] = \frac{1}{2} R_{kl} (\hat{r}_i [\hat{r}_j, \hat{r}_k] \hat{r}_l + \hat{r}_k [\hat{r}_i, \hat{r}_l] \hat{r}_j + [\hat{r}_i, \hat{r}_k] \hat{r}_j \hat{r}_l + \hat{r}_k \hat{r}_i [\hat{r}_j, \hat{r}_l]), \quad (2.41)$$

which, combined with $[\hat{r}_i \hat{r}_j, \hat{H}]$, gives

$$[[\hat{r}_i, \hat{r}_j]_+, \hat{H}] = i(\sigma_{ik} R_{kl} [\hat{r}_j, \hat{r}_l]_+ - [\hat{r}_i, \hat{r}_l]_+ R_{lk} \sigma_{kj}). \quad (2.42)$$

For the decay terms, we have

$$\begin{aligned}\mathcal{D}^\dagger[\hat{j}_n]\hat{r}_i\hat{r}_j &= \hat{j}_n^\dagger\hat{r}_i\hat{r}_j\hat{j}_n - \frac{1}{2}[\hat{j}_n^\dagger\hat{j}_n, \hat{r}_i\hat{r}_j]_+ \\ &= \frac{1}{2}\xi_{nk}^*\xi_{nl}([\hat{r}_k, \hat{r}_i\hat{r}_j]\hat{r}_l + \hat{r}_k[\hat{r}_i\hat{r}_j, \hat{r}_l]) \\ &= \frac{i}{2}\xi_{nk}^*\xi_{nl}(\sigma_{jl}\hat{r}_k\hat{r}_i + \sigma_{il}\hat{r}_k\hat{r}_j - \sigma_{jk}\hat{r}_i\hat{r}_l - \sigma_{ik}\hat{r}_j\hat{r}_l),\end{aligned}\quad (2.43)$$

where we used

$$[\hat{r}_i\hat{r}_j, \hat{r}_k] = \hat{r}_i[\hat{r}_j, \hat{r}_k] + [\hat{r}_i, \hat{r}_k]\hat{r}_j = i\sigma_{jk}\hat{r}_i + i\sigma_{ik}\hat{r}_j. \quad (2.44)$$

Combined with $\mathcal{D}^\dagger[\hat{j}_n]\hat{r}_j\hat{r}_i$ and summed over n , this expression gives

$$\sum_n \mathcal{D}^\dagger[\hat{j}_n][\hat{r}_i, \hat{r}_j]_+ = [\beta_{kl}(\sigma_{jk}[\hat{r}_i, \hat{r}_l]_+ + \sigma_{ik}[\hat{r}_j, \hat{r}_l]_+) - 2\alpha_{kl}\sigma_{jk}\sigma_{li}], \quad (2.45)$$

where

$$\alpha_{kl} = \frac{1}{2}(\xi_{nk}^*\xi_{nl} + \xi_{nk}\xi_{nl}^*), \quad \beta_{kl} = \frac{i}{2}(\xi_{nk}\xi_{nl}^* - \xi_{nk}^*\xi_{nl}). \quad (2.46)$$

Plugging everything into (2.40), using $\dot{x}_i x_j = A_{ik}x_k x_j$, and writing the resulting expression in matrix form, we get the Lyapunov equation

$$\dot{\mathbf{\Gamma}} = \mathbf{A}\mathbf{\Gamma} + \mathbf{\Gamma}\mathbf{A}^T + 2\mathbf{N}, \quad (2.47)$$

where \mathbf{A} is given in equation (2.39) and

$$\mathbf{N} = \frac{1}{2}\boldsymbol{\sigma} \sum_n (\boldsymbol{\xi}_n^* \boldsymbol{\xi}_n^T + \boldsymbol{\xi}_n \boldsymbol{\xi}_n^\dagger) \boldsymbol{\sigma}^T. \quad (2.48)$$

When the dynamics are described by the conditional master equation

$$d\hat{\rho} = -i[\hat{H}, \hat{\rho}]dt + \sum_n \mathcal{D}[\hat{j}_n]\hat{\rho}dt + \sum_m \mathcal{H}[\hat{\lambda}_m]\hat{\rho}dW_m, \quad (2.49)$$

we also need to evaluate the contributions from the measurement terms $\mathcal{H}[\hat{\lambda}_m]\hat{\rho}$. We start by splitting the measurement operator in its Hermitian and anti-Hermitian part, $\hat{\lambda}_m = (\mathbf{c}_m + i\mathbf{m}_m)^T \hat{\mathbf{r}} = \sum_k (c_{mk} + im_{mk})\hat{r}_k$, so we can write

$$\mathcal{H}[\hat{\lambda}_m]\hat{\rho} = [\mathbf{c}_m^T(\hat{\mathbf{r}} - \mathbf{x}), \hat{\rho}]_+ + i[\mathbf{m}_m^T \hat{\mathbf{r}}, \hat{\rho}]. \quad (2.50)$$

For the mean values, this gives the contribution

$$\begin{aligned}\text{tr}\{\hat{r}_i \mathcal{H}[\hat{\lambda}_m]\hat{\rho}\}dW_m &= \text{tr}\{c_{mk}\hat{\rho}([\hat{r}_i, \hat{r}_k]_+ - 2x_k\hat{r}_i) + im_{mk}\hat{\rho}[\hat{r}_i, \hat{r}_k]\}dW_m \\ &= (\Gamma_{ik}c_{mk} - \sigma_{ik}m_{mk})dW_m.\end{aligned}\quad (2.51)$$

The mean vector thus obeys the equation

$$d\mathbf{x} = \mathbf{A}\mathbf{x}dt + \sum_m (\mathbf{\Gamma}\mathbf{c}_m - \boldsymbol{\sigma}\mathbf{m}_m)dW_m. \quad (2.52)$$

For the covariance matrix, we need to evaluate the term

$$\text{tr}\{[\hat{r}_i, \hat{r}_j]_+ \mathcal{H}[\hat{\lambda}_m] \hat{\rho}\} dW_m - 2[(dx_i)x_j + x_i(dx_j) + (dx_i)(dx_j)],$$

where we used the Itô rule for the mean values. In the following, we concentrate on the stochastic contribution in the increments dx_j [second term on the right-hand side of equation (2.52)] as the deterministic contribution is the same as in equation (2.47). We start by considering

$$\begin{aligned} \text{tr}\{[\hat{r}_i, \hat{r}_j]_+ d\hat{\rho}\} &= c_{mk} \text{tr}\{\hat{\rho}([\hat{r}_k, [\hat{r}_i, \hat{r}_j]_+]_+ - 2x_k[\hat{r}_i, \hat{r}_j]_+)\} + im_{mk} \text{tr}\{\hat{\rho}[\hat{r}_i \hat{r}_j + \hat{r}_j \hat{r}_i, \hat{r}_k]\} \\ &= 2c_{mk}(\Gamma_{ik}x_j + \Gamma_{jk}x_i) - 2m_{mk}(x_i\sigma_{jk} + x_j\sigma_{ik}). \end{aligned} \quad (2.53)$$

In the first sum on the right hand side, we used the identity

$$([\hat{r}_i, [\hat{r}_j, \hat{r}_k]_+]_+) = 2(\Gamma_{ij}x_k + \Gamma_{jk}x_i + \Gamma_{ki}x_j + 2x_i x_j x_k) \quad (2.54)$$

which I prove in appendix 2.A. We further use

$$\begin{aligned} d(x_i x_j) &= (dx_i)x_j + x_i(dx_j) + (dx_i)(dx_j) \\ &= x_i(\Gamma_{jk}c_{mk} - \sigma_{jk}m_{mk})dW_m + x_j(\Gamma_{ik}c_{mk} - \sigma_{ik}m_{mk})dW_m \\ &\quad + (\Gamma_{ik}c_{mk} - \sigma_{ik}m_{mk})(\Gamma_{jl}c_{ml} - \sigma_{jl}m_{ml})dt. \end{aligned} \quad (2.55)$$

Combined together, the stochastic contributions to the covariance matrix cancel out, and we are left with the term $-2(\mathbf{\Gamma}c_m - \mathbf{\sigma}m_m)(\mathbf{\Gamma}c_m - \mathbf{\sigma}m_m)^T dt$. The dynamics of the covariance matrix are thus given by the Riccati equation

$$\dot{\mathbf{\Gamma}} = \mathbf{A}\mathbf{\Gamma} + \mathbf{\Gamma}\mathbf{A}^T + 2\mathbf{N} - 2 \sum_m (\mathbf{\Gamma}c_m - \mathbf{\sigma}m_m)(\mathbf{\Gamma}c_m - \mathbf{\sigma}m_m)^T. \quad (2.56)$$

Remarkably, the covariance matrix of the conditional state obeys a deterministic equation. This result further accentuates the significance of the statistical moments for stochastic quantum dynamics of Gaussian systems; the mean vector is often irrelevant and the covariance matrix carries all important information about the state.

2.4 ADIABATIC ELIMINATION OF GAUSSIAN SUBSYSTEMS

The description of Gaussian systems using the statistical moments of their canonical operators is practical not only for standalone systems but also when they are coupled to other, non-Gaussian systems. Such a scenario is common to many measurement settings: a system of interest (e.g., a superconducting qubit, see figure 2.1) is coupled to an auxiliary system; measurement on the second, readout system gives information about the state of the first system. In many situations, the second system is a harmonic oscillator (or consists of several harmonic oscillators), is subject to homodyne measurement, and hence obeys Gaussian evolution. Since the exact dynamics of the transducer is irrelevant, we would like to eliminate its evolution from the conditional master equation that describes the measurement. Describing the Gaussian transducer using its statistical moments enables its

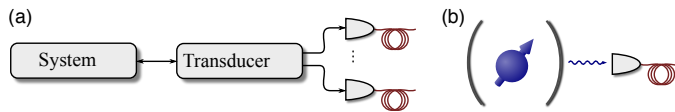


Figure 2.1: (a) Schematic of the considered setup: a quantum system is monitored by an ancillary system—a transducer—whose continuously emitted light field is detected. The simplest example of such a setup—a qubit coupled to a cavity mode with monitored output—is shown in (b). The transducer can also be a much more complex device, such as an optomechanical transducer for frequency conversion of electromagnetic fields.

elimination, provided the coupling between the system and the transducer is weak and the transducer quickly reaches a Gaussian steady state. We thus reduce the dimension of the problem and overcome the memory requirements of Monte Carlo simulations in stochastic dynamics.

In the measurement, the system of interest (e.g., a qubit) couples to the transducer (e.g., a cavity mode) whose output fields are continuously measured in a homodyne detection. The conditional dynamics of the overall system, including losses, noise, and the effect of the continuous diffusive measurement, are described by the stochastic master equation

$$d\hat{\rho} = \mathcal{L}_S \hat{\rho} dt + \mathcal{L}_T \hat{\rho} dt + \mathcal{L}_{\text{int}} \hat{\rho} dt + \sum_m \mathcal{H}[\hat{\lambda}_m] \hat{\rho} dW_m. \quad (2.57)$$

Here, \mathcal{L}_S is the system Liouvillian that contains, in general, coherent dynamics given by a system Hamiltonian \hat{H}_S and Lindblad operators describing decoherence. The Liouvillian for the transducer is

$$\mathcal{L}_T \hat{\rho} = -i[\hat{H}_T, \hat{\rho}] + \sum_n \mathcal{D}[\hat{j}_n] \hat{\rho} \quad (2.58)$$

with $\hat{H}_T = \frac{1}{2} \hat{\mathbf{r}}^T \mathbf{R} \hat{\mathbf{r}}$ and $\hat{j}_n = \xi_n^T \hat{\mathbf{r}}$. Furthermore, we assume the interaction between system and transducer linear in the transducer operators

$$\mathcal{L}_{\text{int}} \hat{\rho} = -i\epsilon[\hat{H}_{\text{int}}, \hat{\rho}], \quad \hat{H}_{\text{int}} = \hat{\mathbf{s}}^T \hat{\mathbf{r}}, \quad (2.59)$$

where $\hat{\mathbf{s}}$ is a $2N$ -dimensional vector of Hermitian operators acting on the system S . We use the small parameter ϵ to remind us that the interaction is weak and can be treated perturbatively. Finally, the measurement terms correspond to a homodyne detection, that is, the measurement operators $\hat{\lambda}_m = (\mathbf{c}_m + i\mathbf{m}_m)^T \hat{\mathbf{r}}$. The measurements also give rise to classical measurement currents that take the form

$$I_m dt = \langle \hat{\lambda}_m + \hat{\lambda}_m^\dagger \rangle dt + dW_m. \quad (2.60)$$

To zeroth order in the coupling parameter ϵ , the transducer dynamics are Gaussian and can be fully described using the first and second statistical moments of the canonical operators, now defined with respect to the reduced state of the transducer, $\hat{\rho}_T = \text{tr}_S\{\hat{\rho}\}$. The covariance matrix of the conditional state $\mathbf{\Gamma}^c$ obeys the Riccati equation (2.56); the dynamics of the covariance matrix of the unconditional state $\mathbf{\Gamma}^u$ (obtained by averaging

over the measurement result) are governed by the Lyapunov equation (2.47). (I use the superscripts c, u to distinguish the covariance matrices describing the conditional and unconditional state.)

Our goal is to derive a closed, effective equation of motion for the conditional state of the system $\hat{\rho}_S = \text{tr}_T\{\hat{\rho}\}$ which is correct to leading order of ϵ based on the assumption that transducer dynamics \mathcal{L}_T is fast on the time scale of the system–transducer interaction \hat{H}_{int} . Under this condition, the state of the system will be given by $\hat{\rho} = \hat{\rho}_S \otimes \hat{\rho}_T + O(\epsilon)$. The strategy now is to determine equations of motion for the order- ϵ correction to this approximation, solve them formally, and substitute the solution into the equation of motion for $\hat{\rho}_S$. In this way, we arrive at a closed, effective equation of motion for $\hat{\rho}_S$, which will be of second order in ϵ in the deterministic and of first order in the stochastic part.

So far, I have left the system dynamics \mathcal{L}_S unspecified. For the adiabatic elimination, we will have to make an assumption regarding \mathcal{L}_S relative to \hat{H}_{int} and \mathcal{L}_T . We will consider two main regimes: in the first case (section 2.4.1), the system dynamics are trivial, $\mathcal{L}_S = 0$. Such a situation arises in an interaction picture when the system operators \hat{s}_j in \hat{H}_{int} are constants of motion and covers, in particular, the important case of a quantum nondemolition measurement. Otherwise, $\mathcal{L}_S = 0$ can be fulfilled approximately if the time scales of \mathcal{L}_S are much slower than those of \hat{H}_{int} . When the interaction and system Hamiltonians do not commute, moving to the interaction picture with respect to the system Liouvillian \mathcal{L}_S results in a time-dependent interaction. In the simplest and most common case, the system operators oscillate at a particular frequency $\pm\omega$; this situation is described in section 2.4.2.

2.4.1 Effective equation of motion for quantum nondemolition measurement

We start the adiabatic elimination by tracing out the transducer dynamics from the stochastic master equation (2.57),

$$d\hat{\rho}_S = \text{tr}_T\{d\hat{\rho}\} = -i\epsilon[\hat{s}_i, \hat{\eta}_i]dt + 2c_{mi}\hat{\mu}_i dW_m, \quad (2.61)$$

where we defined

$$\hat{\eta}_i = \text{tr}_T\{\hat{r}_i\hat{\rho}\}, \quad \hat{\mu}_i = \hat{\eta}_i - x_i\hat{\rho}_S. \quad (2.62)$$

In view of the definition $\hat{\mu}_i = \text{tr}_T\{\hat{r}_i(\hat{\rho} - \hat{\rho}_S \otimes \hat{\rho}_T)\}$, we can give a simple physical meaning to the quantities $\hat{\mu}_i$: they measure the deviation of the exact state $\hat{\rho}$ from the tensor product state $\hat{\rho}_S \otimes \hat{\rho}_T$ with respect to the first order moments of the transducer's canonical variables \hat{r}_i . Accordingly, for the tensor product state $\hat{\rho} = \hat{\rho}_S \otimes \hat{\rho}_T$, we have $\hat{\mu}_i = 0$, and, as we will see, the $\hat{\mu}_i$ are of first order in ϵ . Next, we derive equations governing the evolution of $\hat{\eta}_i$ and $\hat{\mu}_i$, solve them formally to first order in ϵ , and plug the solutions into equation (2.61).

To obtain an equation for $\hat{\eta}_i$, we need to evaluate the expression

$$\begin{aligned}
d\hat{\eta}_i &= \text{tr}_T\{\hat{r}_i d\hat{\rho}\} \\
&= \text{tr}_T\{\hat{r}_i \mathcal{L}_T \hat{\rho}\} dt - i \epsilon \text{tr}_T\{\hat{r}_i [\hat{s}_j \hat{r}_j, \hat{\rho}]\} dt + c_{mj} \text{tr}_T\{\hat{r}_i [\hat{r}_j - x_j, \hat{\rho}]_+\} dW_m \\
&\quad + i m_{mj} \text{tr}_T\{\hat{r}_i [\hat{r}_j, \hat{\rho}]\} dW_m \\
&= A_{ij} \hat{\eta}_j dt - \frac{i}{2} \epsilon (\Gamma_{ij}^c + 2x_i x_j) [\hat{s}_j, \hat{\rho}_S] dt + \frac{1}{2} \epsilon \sigma_{ij} [\hat{s}_j, \hat{\rho}_S]_+ dt \\
&\quad + c_{mj} (\hat{U}_{ij} + 2x_i \hat{\mu}_j) dW_m - \sigma_{ij} m_{mj} \hat{\rho}_S dW_m.
\end{aligned} \tag{2.63}$$

Here, the first term on the right hand side of the above equation is analogous to terms appearing in the equation of motion for the mean values of the canonical operators (2.39), and is therefore equal to $A_{ij} \hat{\eta}_j$. For the other deterministic part, we used

$$\langle \hat{r}_i \hat{r}_j \rangle = \frac{1}{2} \langle [\hat{r}_i, \hat{r}_j]_+ + [\hat{r}_i, \hat{r}_j] \rangle = \frac{1}{2} (\Gamma_{ij}^c + 2x_i x_j + i\sigma_{ij}), \tag{2.64}$$

and $\hat{\rho} = \hat{\rho}_S \otimes \hat{\rho}_T$ to 0th order in ϵ . Finally, we defined $\hat{U}_{ij} = \text{tr}_T\{[\hat{r}_i - x_i, \hat{r}_j - x_j]_+ \hat{\rho}\}$. To solve equation (2.63), we also need an equation of motion for $x_i x_j \hat{\rho}_S$; since this quantity is a first order correction to $\hat{\eta}_i$ (which is a first order term in the equation for the reduced density matrix $\hat{\rho}_S$), it is sufficient to consider its deterministic part to 0th order in ϵ —the stochastic part would give rise to a stochastic contribution of second order for $\hat{\rho}_S$.

Using the Itô product rule, we have

$$\begin{aligned}
dx_i &= \text{tr}_S\{d\hat{\eta}_i\} \\
&= A_{ij} x_j dt + \epsilon \sigma_{ij} \langle \hat{s}_j \rangle dt + (\Gamma_{ij}^c c_{mj} - \sigma_{ij} m_{mj}) dW_m,
\end{aligned} \tag{2.65a}$$

$$\begin{aligned}
d(x_i \hat{\rho}_S) &= (dx_i) \hat{\rho}_S + x_i d\hat{\rho}_S + dx_i d\hat{\rho}_S \\
&= A_{ij} x_j \hat{\rho}_S dt + \epsilon \sigma_{ij} \langle \hat{s}_j \rangle \hat{\rho}_S dt + (\Gamma_{ij}^c c_{mj} - \sigma_{ij} m_{mj}) (2c_{mk} \hat{\mu}_k dt + \hat{\rho}_S dW_m) \\
&\quad - i x_i \epsilon [\hat{s}_j, \hat{\eta}_j] dt + 2x_i c_{mj} \hat{\mu}_j dW_m,
\end{aligned} \tag{2.65b}$$

$$\begin{aligned}
d(x_i x_j \hat{\rho}_S) &= A_{ik} x_k x_j \hat{\rho}_S dt + x_i x_k \hat{\rho}_S A_{kj}^T dt \\
&\quad + (\Gamma_{ik}^c c_{mk} - \sigma_{ik} m_{mk}) (\Gamma_{jl}^c c_{ml} - \sigma_{jl} m_{ml}) \hat{\rho}_S dt \\
&= A_{ik} x_k x_j \hat{\rho}_S dt + x_i x_k \hat{\rho}_S A_{kj}^T dt + \frac{1}{2} (A_{ik} \Gamma_{kj}^c + \Gamma_{ik}^c A_{kj}^T + 2N_{ij}) \hat{\rho}_S dt,
\end{aligned} \tag{2.65c}$$

where we used the Riccati equation (2.56) in the last equation; moreover, we used $\hat{\mu}_i = \hat{\eta}_i - x_i \hat{\rho}_S = O(\epsilon)$. Equation (2.65c) is a Lyapunov equation; generally, the steady-state solution of a Lyapunov equation $\mathbf{A}\mathbf{X} + \mathbf{X}\mathbf{A}^T + \mathbf{B} = \mathbf{0}$ can be written as

$$\mathbf{X} = \int_0^\infty dt e^{\mathbf{A}t} \mathbf{B} e^{\mathbf{A}^T t}. \tag{2.66}$$

A straightforward calculation shows that, in this case, this amounts to

$$x_i x_j \hat{\rho}_S = \frac{1}{2} (\Gamma_{ij}^u - \Gamma_{ij}^c) \hat{\rho}_S. \tag{2.67}$$

This result can be plugged into equation (2.63), which gets the form

$$\begin{aligned} d\hat{\eta}_i &= A_{ij}\hat{\eta}_j dt - \frac{i}{2}\epsilon\Gamma_{ij}^u[\hat{s}_j, \hat{\rho}_S]dt + \frac{1}{2}\epsilon\sigma_{ij}[\hat{s}_j, \hat{\rho}_S]_+ dt \\ &\quad + (\Gamma_{ij}^c c_{mj} - \sigma_{ij} m_{mj})\hat{\rho}_S dW_m; \end{aligned} \quad (2.68)$$

here we used $\hat{\rho} = \hat{\rho}_S \otimes \hat{\rho}_T + O(\epsilon)$ which gives, in leading order, $\text{tr}_T\{[\hat{r}_i, \hat{r}_j]_+ \hat{\rho}\} - 2\hat{\eta}_i x_j = \Gamma_{ij}^c \hat{\rho}_S$. We formally solve this equation; the solution is

$$\hat{\eta}_i = \frac{i}{2}\epsilon A_{ij}^{-1} \Gamma_{jk}^u[\hat{s}_k, \hat{\rho}_S] - \frac{1}{2}\epsilon A_{ij}^{-1} \sigma_{jk}[\hat{s}_k, \hat{\rho}_S]_+ - A_{ij}^{-1} (\Gamma_{jk}^c c_{mk} - \sigma_{jk} m_{mk}) \hat{\rho}_S \frac{dW_m}{dt}. \quad (2.69)$$

We can already see that the unconditional part of the reduced equation will not depend on the conditional state, as expected; since $\hat{\mu}_i$ enters equation (2.61) only in the stochastic term, the unconditional part of equation (2.69) gives the only contribution to the unconditional dynamics of the system density operator $\hat{\rho}_S$.

We proceed similarly to obtain an equation of motion for $\hat{\mu}_i$. Combining equations (2.63) and (2.65b) and keeping terms to first order in ϵ , we have

$$\begin{aligned} d\hat{\mu}_i &= d\hat{\eta}_i - d(x_i \hat{\rho}_S) \\ &= A_{ij}\hat{\mu}_j dt - 2(\Gamma_{ik}^c c_{mk} - \sigma_{ik} m_{mk})c_{mj}\hat{\mu}_j dt + \frac{1}{2}\epsilon\sigma_{ij}[\hat{s}_j - \langle \hat{s}_j \rangle, \hat{\rho}_S]_+ dt \\ &\quad - \frac{i}{2}\epsilon\Gamma_{ij}^c[\hat{s}_j, \hat{\rho}_S]dt + \hat{\Omega}_{ij}c_{mj}dW_m, \end{aligned} \quad (2.70)$$

where $\hat{\Omega}_{ij} = \hat{U}_{ij} - \Gamma_{ij}^c \hat{\rho}_S$. The quantities $\hat{\Omega}_{ij}$ can be interpreted in a similar way as the $\hat{\mu}_i$ in equation (2.62): $\hat{\Omega}_{ij}$ measure the deviation of the exact state $\hat{\rho}$ from the tensor product state $\hat{\rho}_S \otimes \hat{\rho}_T$ with respect to the second moments of the transducer's canonical variables \hat{r}_i . The equation of motion for $\hat{\Omega}_{ij}$ can be derived in a similar way as for $\hat{\mu}_i$, and shows that it is a second order quantity, $\hat{\Omega}_{ij} = O(\epsilon^2)$; refer to Appendix 2.C for more information about this quantity and the general structure of the equations of motion for the deviations of the exact and tensor states with respect to the statistical moments of the transducer. Since the deviations $\hat{\Omega}_{ij}$ are of second order, the stochastic term can be dropped in equation (2.70), and the solution is

$$\hat{\mu}_i = -\frac{1}{2}\epsilon Q_{ij}^{-1} \sigma_{jk}[\hat{s}_k - \langle \hat{s}_k \rangle, \hat{\rho}_S]_+ + \frac{i}{2}\epsilon Q_{ij}^{-1} \Gamma_{jk}^c[\hat{s}_k, \hat{\rho}_S], \quad (2.71a)$$

$$\mathbf{Q} = \mathbf{A} - 2(\Gamma^c \mathbf{c}_m - \sigma \mathbf{m}_m) \mathbf{c}_m^T. \quad (2.71b)$$

Plugging the results (2.69) and (2.71a) into the equation of motion for the system density operator, equation (2.61), we recover the effective equation

$$d\hat{\rho}_S = \frac{1}{2}A_{ij}^{-1} \Gamma_{jk}^u[\hat{s}_i, [\hat{s}_k, \hat{\rho}_S]]dt + \frac{i}{2}A_{ij}^{-1} \sigma_{jk}[\hat{s}_i, [\hat{s}_k, \hat{\rho}_S]_+]dt + \mathcal{H}[i\Lambda_{mi}\hat{s}_i]\hat{\rho}_S dW_m, \quad (2.72)$$

where we have the measurement term

$$\Lambda_m = (\Gamma^c - i\sigma)Q^{-T} \mathbf{c}_m + \mathbf{A}^{-1}(\Gamma^c \mathbf{c}_m - \sigma \mathbf{m}_m). \quad (2.73)$$

As expected, the deterministic part of the stochastic master equation [first two terms in equation (2.72)] depends only on the unconditional state of the transducer through its covariance matrix $\mathbf{\Gamma}^u$; the stochastic term, however, does depend on the conditional state $\mathbf{\Gamma}^c$.

The effective equation of motion (2.72) is not manifestly in Lindblad form. In order to bring it into the Lindblad form, we rewrite it as

$$d\hat{\rho}_S = -i[\hat{H}, \hat{\rho}_S]dt + P_{ij} \left[\hat{s}_i \hat{\rho}_S \hat{s}_j - \frac{1}{2}(\hat{s}_j \hat{s}_i \hat{\rho}_S + \hat{\rho}_S \hat{s}_j \hat{s}_i) \right] dt + \mathcal{H}[i\Lambda_{mi} \hat{s}_i] \hat{\rho}_S dW_m, \quad (2.74)$$

where

$$\hat{H} = \frac{i}{4} \hat{\mathbf{s}}^T [\mathbf{A}^{-1}(\mathbf{\Gamma}^u + i\boldsymbol{\sigma}) - (\mathbf{\Gamma}^u - i\boldsymbol{\sigma}^T)\mathbf{A}^{-T}] \hat{\mathbf{s}}, \quad (2.75a)$$

$$\mathbf{P} = -\frac{1}{2} [\mathbf{A}^{-1}(\mathbf{\Gamma}^u - i\boldsymbol{\sigma}) + (\mathbf{\Gamma}^u + i\boldsymbol{\sigma}^T)\mathbf{A}^{-T}]. \quad (2.75b)$$

The individual jump operators and corresponding decay rates are given by eigenvectors \mathbf{v}_i and eigenvalues $\omega_i > 0$ of the matrix \mathbf{P} , $\sum_i \omega_i \mathcal{D}[\mathbf{v}_i^T \hat{\mathbf{s}}] \hat{\rho}_S$. The decay matrix \mathbf{P} is indeed positive semidefinite, as shown in appendix 2.B. Finally, the effective equation of motion has to be appended with an equation relating the measured photocurrent to the system observables \hat{s}_i after elimination of the transducer degrees of freedom [replacing equation (2.60)],

$$I_m dt = \langle i\Lambda_m^T \hat{\mathbf{s}} - i\hat{\mathbf{s}}^\dagger \Lambda_m^* \rangle dt + dW_m. \quad (2.76)$$

2.4.2 Effective equation of motion for oscillating system–transducer interaction

When moving to the rotating frame with respect to the system Hamiltonian, the interaction stays time independent only for special cases. Generally, the system operators will become time-dependent. To go beyond the model presented in section 2.4.1, we now consider the simplest case of time-dependent operators—those oscillating at frequency $\pm\omega$. We write the interaction Hamiltonian as $\hat{H}_{\text{int}}(t) = \hat{\mathbf{s}}^T(t) \hat{\mathbf{t}}$, where $\hat{\mathbf{s}}(t) = \hat{\mathbf{s}}_+ e^{i\omega t} + \hat{\mathbf{s}}_- e^{-i\omega t}$, and the operators $\hat{\mathbf{s}}_\pm$ are time independent and Hermitian conjugate of each other, $(\hat{s}_\pm)_i^\dagger = (\hat{s}_\mp)_i$. Although this is not a completely general form of system–transducer coupling, together with the time-independent case, it can cover a large range of scenarios, including arbitrary qubit dynamics.

Since the system operators now oscillate at frequency ω , the essential part of the signal will be transmitted by the sidebands and not in the carrier frequency. To recover this signal, we perform the measurements with local oscillators that are detuned from the standard reference frame. Denoting the frequency of the standard reference frame (corresponding, e.g., to the frequency of the laser light used to drive the system) as ω_0 and the frequency of the local oscillator as ω_m , we can use the following description [233]: the adjustment results in time-dependent measurement operators $\hat{\lambda}_m(t) = (\mathbf{c}_m + i\mathbf{m}_m)^T \hat{\mathbf{t}}(t)$, where we have

$$\hat{q}_i = \frac{\hat{a}_i e^{-i\Delta_m t} + \hat{a}_i^\dagger e^{i\Delta_m t}}{\sqrt{2}}, \quad \hat{p}_i = i \frac{\hat{a}_i^\dagger e^{i\Delta_m t} - \hat{a}_i e^{-i\Delta_m t}}{\sqrt{2}} \quad (2.77)$$

with $\Delta_m = \omega_0 - \omega_m$. Alternatively, we can rewrite the measurement operators so that the time-dependence enters through the coefficients, $\hat{\lambda}_m(t) = [\mathbf{c}_m(t) + \mathbf{im}_m(t)]^T \hat{\mathbf{r}}$ (with the canonical operators $\hat{\mathbf{r}}$ time-independent), which will prove useful when adiabatically eliminating the transducer dynamics. Overall, the stochastic master equation takes the form

$$d\hat{\rho} = -i\epsilon[\hat{\mathbf{s}}^T(t)\hat{\mathbf{r}}, \hat{\rho}]dt + \mathcal{L}_T \hat{\rho} dt + \sum_m \mathcal{H}[\hat{\lambda}_m(t)]\hat{\rho}dW_m, \quad (2.78)$$

where we explicitly write the time dependence of the interaction Hamiltonian and the measurement operators.

Before proceeding with the adiabatic elimination, we have to pay attention to the conditional steady state of the Gaussian system. Since the measurement terms are now time-dependent, the Riccati equation (2.56) for this system is ill-defined. To circumvent this problem, we perform rotating wave approximation in the measurement terms by introducing the coarse-grained Wiener increments

$$dW_m^c = \int \sqrt{2} \cos(\Delta_m t) dW_m, \quad dW_m^s = \int \sqrt{2} \sin(\Delta_m t) dW_m. \quad (2.79)$$

For integration intervals long on the time scale of Δ_m^{-1} but short on all other time scales, this produces two independent Wiener increments, $dW_m^a dW_n^b = \delta_{mn} \delta_{ab} dt$; $a, b \in \{c, s\}$, effectively turning every measurement into two,

$$\mathcal{H}[\hat{\lambda}_m(t)]\hat{\rho}dW_m \rightarrow \frac{1}{\sqrt{2}}\mathcal{H}[\hat{\lambda}_m^c]\hat{\rho}dW_m^c + \frac{1}{\sqrt{2}}\mathcal{H}[\hat{\lambda}_m^s]\hat{\rho}dW_m^s, \quad (2.80)$$

where $\hat{\lambda}_m^a = (\mathbf{c}_m^a + \mathbf{im}_m^a)^T \hat{\mathbf{r}}$ and

$$\mathbf{c}_m(t) = \mathbf{c}_m^c \cos(\Delta_m t) + \mathbf{c}_m^s \sin(\Delta_m t), \quad (2.81a)$$

$$\mathbf{m}_m(t) = \mathbf{m}_m^c \cos(\Delta_m t) + \mathbf{m}_m^s \sin(\Delta_m t). \quad (2.81b)$$

These measurement operators are time-independent and thus give rise to a valid Riccati equation

$$\dot{\Gamma}^c = \mathbf{A}\Gamma^c + \Gamma^c \mathbf{A}^T + 2\mathbf{N} - \sum_m \sum_{a \in \{c, s\}} (\Gamma^c \mathbf{c}_m^a - \sigma \mathbf{m}_m^a)(\Gamma^c \mathbf{c}_m^a - \sigma \mathbf{m}_m^a)^T. \quad (2.82)$$

We treat the matrix \mathbf{Q} [equation (2.71b)], which now also becomes time-dependent, in a similar manner; it becomes

$$\mathbf{Q} = \mathbf{A} - \sum_m \sum_a (\Gamma^c \mathbf{c}_m^a - \sigma \mathbf{m}_m^a)(\mathbf{c}_m^a)^T. \quad (2.83)$$

With these adjustments, we are now ready to adiabatically eliminate the transducer dynamics and obtain an effective equation of motion for the system density matrix $\hat{\rho}_S$.

Since we made no assumptions about time-dependence of the system operators in deriving equations of motion for $\hat{\rho}_S$, $\hat{\eta}_i$, $x_i x_j \hat{\rho}_S$, and $\hat{\mu}_i$ in equations (2.61), (2.63), (2.65c), (2.70), these equations stay valid also in the present case. It is only their formal solution

where the time-dependence of the system and measurement operators starts to play a role. The solution is, nevertheless, analogous to the time-independent case, only with additional oscillation terms, $e^{\pm i\omega t}$. Solving the equations of motion for $x_i x_j \hat{\rho}_S$, $\hat{\eta}_i$, $\hat{\mu}_i$ formally and performing the rotating wave approximation, we arrive at the equation

$$d\hat{\rho}_S = \mathcal{L}\hat{\rho}_S dt + \mathcal{H}[\hat{\Lambda}_m]\hat{\rho}_S dW_m, \quad (2.84a)$$

$$I_m dt = \langle \hat{\Lambda}_m + \hat{\Lambda}_m^\dagger \rangle dt + dW_m. \quad (2.84b)$$

Here, the deterministic part is given by

$$\begin{aligned} \mathcal{L}\hat{\rho}_S = & \frac{1}{2}(A + i\omega)_{ij}^{-1} \{ \Gamma_{jk}^u [(\hat{s}_+)_i, [(\hat{s}_-)_k, \hat{\rho}_S]] + i\sigma_{jk} [(\hat{s}_+)_i, [(\hat{s}_-)_k, \hat{\rho}_S]_+] \} + \\ & + \frac{1}{2}(A - i\omega)_{ij}^{-1} \{ \Gamma_{jk}^u [(\hat{s}_-)_i, [(\hat{s}_+)_k, \hat{\rho}_S]] + i\sigma_{jk} [(\hat{s}_-)_i, [(\hat{s}_+)_k, \hat{\rho}_S]_+] \}, \end{aligned} \quad (2.85)$$

and the particular form of the measurement term depends on the choice of local oscillator detuning, for which one has to distinguish two relevant cases $\Delta_m = \pm\omega$,

$$\hat{\Lambda}_m = i\Theta_m^T \hat{s}_+ + i\Xi_m^T \hat{s}_-, \quad \Delta_m = -\omega, \quad (2.86a)$$

$$\hat{\Lambda}_m = i\Xi_m^T \hat{s}_+ + i\Theta_m^T \hat{s}_-, \quad \Delta_m = \omega, \quad (2.86b)$$

$$\Theta_m = (\Gamma^c - i\sigma)(\mathbf{Q} + i\Delta_m \mathbf{I})^{-T} \mathbf{c}_m^+ + (\mathbf{A} - i\Delta_m \mathbf{I})^{-1} (\Gamma^c \mathbf{c}_m^+ - \sigma \mathbf{m}_m^+), \quad (2.86c)$$

$$\Xi_m = (\Gamma^c - i\sigma)(\mathbf{Q} - i\Delta_m \mathbf{I})^{-T} \mathbf{c}_m^- + (\mathbf{A} + i\Delta_m \mathbf{I})^{-1} (\Gamma^c \mathbf{c}_m^- - \sigma \mathbf{m}_m^-), \quad (2.86d)$$

where we denote $\mathbf{c}_m(t) = \mathbf{c}_m^+ e^{i\Delta_m t} + \mathbf{c}_m^- e^{-i\Delta_m t}$ and \mathbf{m}_m^\pm are defined similarly.

To bring the deterministic part of this equation to Lindblad form, we can proceed similarly to the time-independent case. Since now the system operators $(\hat{s}_\pm)_i$ are non-Hermitian, we first need to express them using some Hermitian basis (in the case of qubits, for instance, that would be the set of the Pauli operators and the identity). We can then recover the Hamiltonian part and the dissipative part, the diagonalization of which reveals the individual decay channels.

2.5 EXAMPLES

In this section, I illustrate the use of the adiabatic elimination method presented in section 2.4 on a few simple examples. The model scenarios are taken from circuit quantum electrodynamics where small amounts of thermal noise—typically unaccounted for by other adiabatic elimination methods—can be present even in cryogenically cooled systems. I show that the adiabatic elimination of Gaussian systems (which I henceforth refer to as Gaussian adiabatic elimination) can provide significantly increased accuracy for thermal noise at the level of few quanta.

The examples are shown in figure 2.2. In section 2.5.1, I consider dispersive readout of a qubit using a cavity that is coupled to a thermal reservoir; see figure 2.2(a). I compare Gaussian adiabatic elimination with results obtained by density operator expansion (discussed in detail below) and show that significant qualitative and quantitative improvements can be achieved with the former method. I extend this system in section 2.5.2 [figure

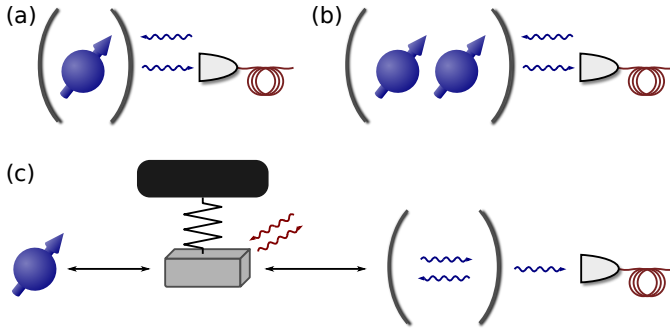


Figure 2.2: Schematic illustrations of the setups to exemplify Gaussian adiabatic elimination. In sections 2.5.1, 2.5.3, we analyse dynamics of a qubit coupled to a thermal cavity via dispersive and Jaynes–Cummings interaction, respectively, shown in (a). (b) Setup for entanglement generation by measurement as discussed in section 2.5.2. Here, two qubits interact dispersively with the same cavity but not with each other. With a suitable initial state and using the information obtained from the measurement record, it is then possible to postselect an entangled state of the two qubits. Finally, in section 2.5.4, I study a qubit coupled to the two-oscillator transducer shown in (c), where the first oscillator couples to a thermal bath; the second oscillator—which is used to read out the state of the first oscillator—is effectively at zero temperature.

2.2(b)] where I study the effect of thermal noise on generating two-qubit entanglement by measurement, following the approach of Hutchison et al. [91]. Next, I illustrate the use of Gaussian adiabatic elimination with time-dependent interaction in section 2.5.3 where I consider a single qubit coupled to a cavity field via Jaynes–Cummings Hamiltonian. Finally, in section 2.5.4, I consider the system shown in figure 2.2(c): a transducer consisting of two coupled oscillators, one of which is coupled to a thermal bath. This setup differs from all other scenarios considered here by having a different unconditional and conditional steady state of the transducer, and I show how the Gaussian adiabatic elimination fares in this case. All numerical calculations in this section are done in PYTHON using QUTIP [236–238].

2.5.1 Quantum nondemolition readout of a qubit

We consider the system shown in figure 2.2(a), where a qubit couples in a quantum nondemolition interaction to a cavity mode whose output field is subject to continuous homodyne detection. In such a system the cavity itself serves just as a transducer, and can be adiabatically eliminated if the cavity decay rate is sufficiently large (faster than the coupling). We start with the qubit–cavity Hamiltonian of the form

$$\hat{H} = \frac{\omega}{2} \hat{\sigma}_z + \Delta \hat{a}^\dagger \hat{a} + g \hat{a}^\dagger \hat{a} \hat{\sigma}_z + iE (\hat{a} e^{i\phi} + \hat{a}^\dagger e^{-i\phi}). \quad (2.87)$$

We move to the interaction picture with respect to the free qubit evolution, cancelling the first term. The second term shows the free cavity dynamics; we choose to drive the cavity mode at the centre frequency, $\Delta = 0$, maximising the measurement efficiency. The third term gives the standard dispersive interaction, and the last term describes the cavity drive.

To obtain interaction that is linear in the cavity quadrature operators, we linearize the Hamiltonian by moving to the displaced frame, $\hat{\rho} \rightarrow \hat{D}^\dagger(\alpha)\hat{\rho}\hat{D}(\alpha)$, where $\hat{D}(\alpha) = \exp(\alpha\hat{a}^\dagger - \alpha^*\hat{a})$ is the displacement operator and $\alpha = 2Ee^{-i\phi}/\kappa$ (with cavity decay rate κ) is the steady state cavity field. (The linearization also makes it possible to eliminate the cavity field using density operator expansion approach later.) This procedure brings the interaction Hamiltonian to the form $\hat{H}_{\text{int}} = g(\alpha^*\hat{a} + \alpha\hat{a}^\dagger)\hat{\sigma}_z + g\hat{a}^\dagger\hat{a}\hat{\sigma}_z$. If the driving field is strong enough, we can drop the second term, getting the interaction Hamiltonian $\hat{H}_{\text{int}} = \chi\hat{r}_\phi\hat{\sigma}_z$, where $\hat{r}_\phi = (\hat{a}e^{i\phi} + \hat{a}^\dagger e^{-i\phi})/\sqrt{2}$ and $\chi = \sqrt{2}g|\alpha|$. The phase ϕ is set by the field E driving the cavity.

Since the cavity field couples to a thermal bath (with average number of excitations \bar{n}), the measurement term takes the form $\sqrt{\kappa/(2\bar{n}+1)}\mathcal{H}[(\bar{n}+1)\hat{a} - \bar{n}\hat{a}^\dagger]\hat{\rho}$ [97]. The full dynamics of the qubit–cavity system is thus described by the equation

$$\begin{aligned} d\hat{\rho} = & -i\chi[\hat{\sigma}_z\hat{r}_\phi, \hat{\rho}]dt + \kappa\{(\bar{n}+1)\mathcal{D}[\hat{a}] + \bar{n}\mathcal{D}[\hat{a}^\dagger]\}\hat{\rho}dt \\ & + \sqrt{\frac{\kappa}{2\bar{n}+1}}\mathcal{H}[(\bar{n}+1)\hat{a} - \bar{n}\hat{a}^\dagger]\hat{\rho}dW. \end{aligned} \quad (2.88)$$

Here, we assume that the cavity leaks only through its output port at rate κ and the homodyne detector has unit efficiency; numerical simulations indicate that additional decay has little effect on the accuracy of the adiabatic elimination methods. The measurement signal has the form $I dt = \sqrt{2\kappa/(2\bar{n}+1)}\langle\hat{q}\rangle dt + dW$.

Following the recipe from section 2.4.1, we have the transducer Hamiltonian $\hat{H}_T = 0$, jump operators $\hat{j}_1 = \sqrt{\kappa(\bar{n}+1)}\hat{a}$, $\hat{j}_2 = \sqrt{\kappa\bar{n}}\hat{a}^\dagger$, and measurement operator $\hat{\lambda} = \sqrt{\kappa/(2\bar{n}+1)}[(\bar{n}+1)\hat{a} - \bar{n}\hat{a}^\dagger]$, or

$$\mathbf{R} = 0, \quad (2.89a)$$

$$\xi_1 = \sqrt{\frac{\kappa(\bar{n}+1)}{2}} \begin{pmatrix} 1 \\ i \end{pmatrix}, \quad \xi_2 = \sqrt{\frac{\kappa\bar{n}}{2}} \begin{pmatrix} 1 \\ -i \end{pmatrix}, \quad (2.89b)$$

$$\mathbf{c} = \sqrt{\frac{\kappa}{2(2\bar{n}+1)}} \begin{pmatrix} 1 \\ 0 \end{pmatrix}, \quad \mathbf{m} = \sqrt{\frac{\kappa(2\bar{n}+1)}{2}} \begin{pmatrix} 0 \\ 1 \end{pmatrix}. \quad (2.89c)$$

It then follows that $\mathbf{A} = -\frac{1}{2}\kappa\mathbf{I}_2$, $\mathbf{N} = (\bar{n} + \frac{1}{2})\mathbf{I}_2$ and both the unconditional and conditional steady states are the thermal state $\mathbf{\Gamma}^u = \mathbf{\Gamma}^c = (2\bar{n}+1)\mathbf{I}_2$. Furthermore, from the interaction Hamiltonian, we can read off $\hat{\mathbf{s}} = \chi\hat{\sigma}_z(\cos\phi, -\sin\phi)^T$. After plugging everything into equation (2.72), a straightforward calculation reveals the effective equation

$$d\hat{\rho}_S = \frac{2\chi^2}{\kappa}(2\bar{n}+1)\mathcal{D}[\hat{\sigma}_z]\hat{\rho}_S dt + \sqrt{\frac{2\chi^2}{\kappa(2\bar{n}+1)}}\mathcal{H}[-i(2\bar{n}\cos\phi + e^{-i\phi})\hat{\sigma}_z]\hat{\rho}_S dW, \quad (2.90a)$$

$$I dt = -\sqrt{\frac{8\chi^2}{\kappa(2\bar{n}+1)}}\sin\phi\langle\hat{\sigma}_z\rangle dt + dW. \quad (2.90b)$$

Obviously, the optimal phase for an efficient readout of the qubit state is $\phi = \pi/2$, which is not surprising—this phase choice corresponds to an interaction of the form $\hat{H}_{\text{int}} = \chi\hat{\sigma}_z\hat{p}$ accompanied by a \hat{q} measurement.

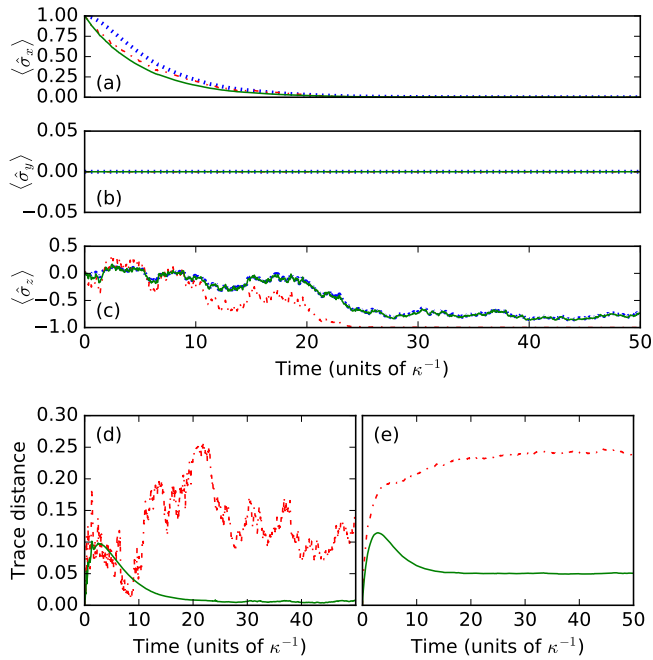


Figure 2.3: Determination of the average trace distance. Starting from a single quantum trajectory [expectation values of the Pauli matrices shown in plots (a–c)], we calculate the trace distance between the full model [dotted blue line, equation (2.88)], and the result obtained by Gaussian adiabatic elimination [full green line, equation (2.90)], or using the density operator expansion [dashed red line, equation (2.92)]. The resulting trace distances are shown in (d). We further average using 500 quantum trajectories in (e) to obtain an average trace distance. Using time averaging on this result, we further obtain a single figure of merit that determines quality of the two approaches. For the results shown here with $\bar{n} = 2$, $\chi = 0.1\kappa$, $\phi = \pi/2$ and initial qubit state $|\psi_0\rangle = (|0\rangle + |1\rangle)/\sqrt{2}$, we have the average trace distance $D \approx 0.05$ for Gaussian adiabatic elimination and $D \approx 0.22$ for density operator expansion (cf. figure 2.4).

I contrast the Gaussian adiabatic elimination with a more common approach based on expanding the density operator in the Fock basis of the cavity around its vacuum state assuming no thermal excitations in the cavity [91, 207],

$$\hat{\rho} = \hat{\rho}_{00}|0\rangle\langle 0| + \hat{\rho}_{10}|1\rangle\langle 0| + \hat{\rho}_{01}|0\rangle\langle 1| + \hat{\rho}_{11}|1\rangle\langle 1| + \dots, \quad (2.91)$$

where the elements $\hat{\rho}_{ij}$ are operators acting on the Hilbert space of the qubit, and are of the order $i + j$ in the small coupling parameter ϵ . Expanding up to second order, the reduced state of the qubit is given by $\hat{\rho}_S = \text{tr}_T\{\hat{\rho}\} = \hat{\rho}_{00} + \hat{\rho}_{11}$, and the elements $\hat{\rho}_{00}$, $\hat{\rho}_{11}$

depend on $\hat{\rho}_{ij}$ with $i + j \leq 2$. The qubit equation of motion takes the form

$$d\hat{\rho}_S = \frac{2\chi^2}{\kappa}(2\bar{n} + 1)\mathcal{D}[\hat{\sigma}_z]\hat{\rho}_S dt + \sqrt{\frac{2\chi^2}{\kappa}}\mathcal{H}[e^{-i(\phi+\pi/2)}\hat{\sigma}_z]\hat{\rho}_S dW, \quad (2.92a)$$

$$Idt = -\sqrt{\frac{8\chi^2}{\kappa}}\sin\phi\langle\hat{\sigma}_z\rangle dt + dW. \quad (2.92b)$$

Here we took into account the effect of thermal noise in the deterministic part (first term), which can be easily done using, for example, projection operator method [214]. The only difference between equations (2.90) and (2.92) is thus in the measurement term. Qualitatively speaking, the density operator expansion overestimates the effective strength of the measurement by a factor of $1/\sqrt{\bar{n}}$. The actual rate at which information about the qubit state is transferred to the output field does not depend on the temperature of the cavity (it is proportional to χ^2/κ) but, since the noise level increases with increasing temperature, the signal-to-noise ratio decreases, leading to a decrease of the effective measurement rate. For a zero temperature bath, both methods give the same results; in the presence of thermal excitations, however, this difference quickly starts to play a role.

To quantify the difference between the full model given by equation (2.88) and the effective qubit equation (2.90) or (2.92), we calculate the trace distance between the corresponding qubit states (I use $\hat{\rho}_1$ to denote state obtained from the exact dynamics and $\hat{\rho}_2$ for the approximation methods), $D(\hat{\rho}_1, \hat{\rho}_2) = \frac{1}{2}\text{tr}|\hat{\rho}_1 - \hat{\rho}_2|$ with $|\hat{X}| = \sqrt{\hat{X}^\dagger \hat{X}}$. Since the density matrices describe the state of a single qubit, the trace distance can be expressed using the expectation values of the Pauli matrices $\langle\hat{\sigma}_i^j\rangle = \text{tr}\{\hat{\rho}_j \hat{\sigma}_i\}$ as

$$D(\hat{\rho}_1, \hat{\rho}_2) = \frac{1}{2}\sqrt{\sum_{i \in \{x,y,z\}} (\langle\hat{\sigma}_i^1\rangle - \langle\hat{\sigma}_i^2\rangle)^2}. \quad (2.93)$$

To obtain an average trace distance between the full model and the reduced dynamics, we generate a large number of quantum trajectories. We are thus able to study how the average trace distance changes in time; in addition, upon time averaging, we obtain a single figure of merit quantifying the discrepancy between the full and reduced dynamics; the averaging process is illustrated in figure 2.3.

The results of the numerical investigations are shown in figure 2.4. In panel (a), I plot the average trace distance as a function of the interaction phase ϕ for Gaussian adiabatic elimination (green squares) and density operator expansion (black stars). Both methods provide best results for $\phi = \pi/2$, corresponding to an interaction of the form $\hat{H}_{\text{int}} = \chi\hat{p}\hat{\sigma}_z$. This feature is particularly beneficial since, as discussed before, this phase choice is optimal for nondemolition readout of the qubit state.

In panel (b) of figure 2.4, I plot the average trace distance versus thermal occupation number. While the average trace distance with Gaussian adiabatic elimination (green squares for $\phi = \pi/2$, blue circles for $\phi = 0$) eventually saturates (with the phase $\phi = 0$ this happens at $\bar{n} \approx 3$, which is not shown in the plot), the error with density operator expansion (black stars for $\phi = \pi/2$, red crosses for $\phi = 0$) grows with increasing temperature. Moreover, the Gaussian adiabatic elimination performs a factor of about 2 better than

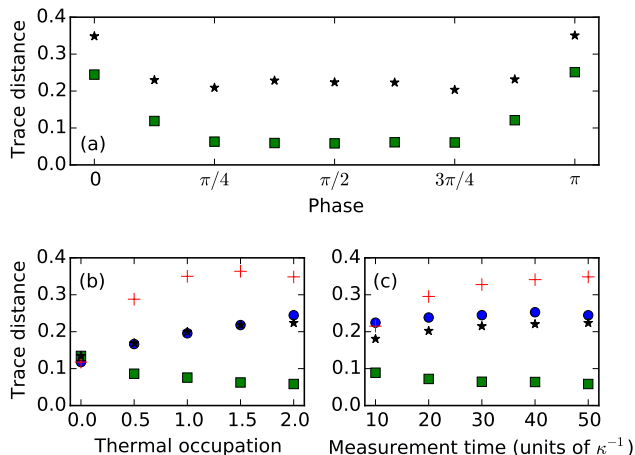


Figure 2.4: Average trace distance for Gaussian adiabatic elimination and density operator expansion as compared to the full model. (a) Trace distance as a function of the measurement phase with green squares showing results for the Gaussian adiabatic elimination and black stars for density operator expansion. The bottom panels show the trace distance versus thermal occupation number (b) and the overall measurement time (c) for two choices of phase: $\phi = \pi/2$ (green squares for Gaussian adiabatic elimination, black stars for density operator expansion), and $\phi = 0$ (blue circles for Gaussian adiabatic elimination, red crosses for density operator expansion). The parameters used for the simulations are $\chi = 0.1\kappa$, $\bar{n} = 2$ [for (a,c)], measurement time $T = 50$ [(a,b)], and initial qubit state $|\psi_0\rangle = (|0\rangle + |1\rangle)/\sqrt{2}$. The Fock space of the cavity field for the full model is cut off at $N_{\max} = 20$.

density operator expansion already for half a thermal excitation present in the bath; with the phase choice $\phi = \pi/2$, which corresponds to the optimal qubit readout, the difference between the two methods quickly grows.

Finally, in figure 2.4(c), I investigate how the measurement time affects the accuracy of the two methods. Gaussian adiabatic elimination remains unaffected by the length of the measurement ($\phi = 0$) or even slightly improves with time ($\phi = \pi/2$), whereas accuracy of the density operator expansion method slowly deteriorates over time. This feature can be seen already from the time-dependence of the trace distance [cf. figure 2.3(e)], where the trace distance with Gaussian adiabatic elimination reaches a maximum shortly after the begin of the evolution ($t \approx 5\kappa^{-1}$) and then settles at a smaller steady state value, while the trace distance with density operator expansion continues to grow throughout the evolution.

The choice of a single initial qubit state $|\psi_0\rangle = (|0\rangle + |1\rangle)/\sqrt{2}$ does not affect the completeness of our analysis. Since the evolution for eigenstates of the $\hat{\sigma}_z$ operator is trivial, the dynamics starting on the equator of the Bloch sphere is the most interesting from the point of view of solution accuracy. As there is no preferred phase for the qubit, the adiabatic elimination methods perform equally for all these states.

Additionally, generating quantum trajectories with the approximation methods is, due to smaller size of the Hilbert space, about four times faster than with the full model; in

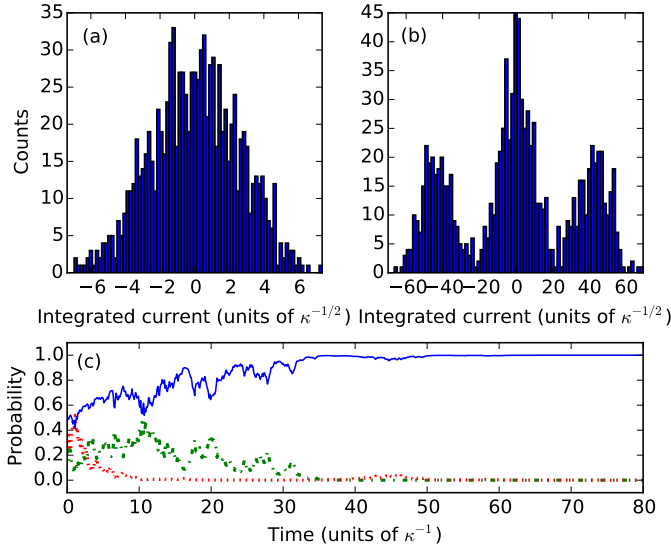


Figure 2.5: Example histograms of the integrated current at the beginning of the readout [$T = 5\kappa^{-1}$, (a)] and at a later time [$T = 100\kappa^{-1}$, (b)]. In panel (c), I plot the probability of the two qubits to be in the state $|00\rangle$ (dot-dashed green line), $|11\rangle$ (dotted red line), and $|\Psi_+\rangle$ (full blue line) for an example quantum trajectory. The simulations were run with the parameters $\chi = 0.1\kappa$, $\bar{n} = 0$, and 1000 trajectories were used for generating the histograms.

systems with larger thermal noise, this effect will be even larger. Moreover, as the qubit dynamics happen on a slower time scale than the evolution of the cavity field, it is possible to use larger time steps in the numerical solution, speeding the numerics up even more.

2.5.2 Two-qubit entanglement in presence of thermal noise

Extending the system presented in the previous section, we now consider two qubits dispersively coupled to a common cavity field, $\hat{H}_{\text{int}} = \sum_j \chi_j \hat{\gamma}_\phi \hat{\sigma}_z^j$, where $\hat{\sigma}_z^j$ acts on the j th qubit. Such a system is of particular interest as the joint measurement of the two qubits can generate entanglement between them [91, 92]. Indeed, a straightforward generalization of equation (2.90) (with $\phi = -\pi/2$) gives the effective dynamics

$$d\hat{\rho}_S = \frac{2}{\kappa}(2\bar{n} + 1)\mathcal{D}[\chi_1\hat{\sigma}_z^1 + \chi_2\hat{\sigma}_z^2]\hat{\rho}_S dt + \sqrt{\frac{2}{\kappa(2\bar{n} + 1)}}\mathcal{H}[\chi_1\hat{\sigma}_z^1 + \chi_2\hat{\sigma}_z^2]\hat{\rho}_S dW, \quad (2.94a)$$

$$Idt = \sqrt{\frac{8}{\kappa(2\bar{n} + 1)}}\langle\chi_1\hat{\sigma}_z^1 + \chi_2\hat{\sigma}_z^2\rangle dt + dW. \quad (2.94b)$$

We thus get an effective measurement of the total spin of the two qubits. If we prepare the qubits in the state $|\psi_0\rangle = \frac{1}{2}(|0\rangle + |1\rangle) \otimes (|0\rangle + |1\rangle)$, engineer the interaction so that $\chi_1 = \chi_2 = \chi$, and postselect only those trajectories with measurement outcome $\langle\hat{\sigma}_z^1 + \hat{\sigma}_z^2\rangle = 0$, the two-qubit state takes the form $|\Psi_+\rangle = (|01\rangle + |10\rangle)/\sqrt{2}$ since there is

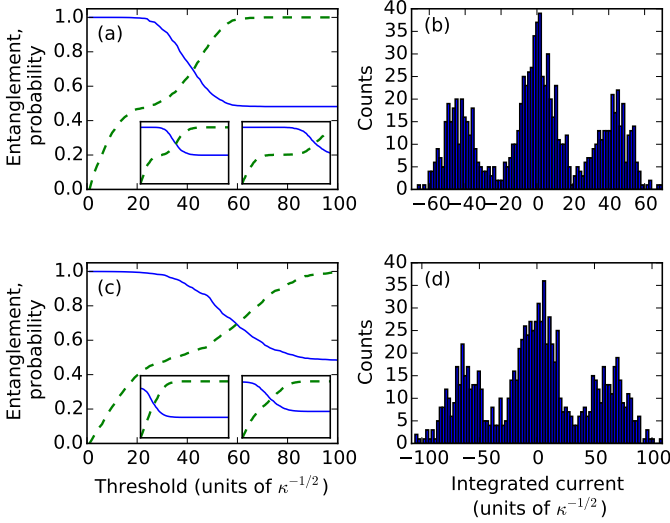


Figure 2.6: Logarithmic negativity (full blue line) and success probability (dashed green line) versus the postselection threshold ν for $\bar{n} = 0$ (a) and $\bar{n} = 2$ (c). The measurement time is $T = 100\kappa^{-1}$ in (a) and $T = 250\kappa^{-1}$ in (c); moreover, in the insets, I plot the logarithmic negativity and success probability for $T = 75\kappa^{-1}$ (left) and $T = 150\kappa^{-1}$ (right) for both (a) and (c). In addition, in panels (b,d), histograms of the integrated currents corresponding to the results in (a,c) are shown. I use the coupling $\chi = 0.1\kappa$ and average over 1000 quantum trajectories.

one excitation in the system but we have no information on which of the two qubits is excited. Moreover, this state is also a dark state of the Lindblad term $\mathcal{D}[\hat{\sigma}_z^1 + \hat{\sigma}_z^2]\hat{\rho}_S$ so it is a conditional steady state of the stochastic master equation (2.94).

In more detail, the entanglement is generated using the following protocol: first, the qubits interact with the cavity mode and the output field is measured, which is described by equation (2.94). After time T , we have accumulated the signal

$$J(T) = \int_0^T dt I(t); \quad (2.95)$$

if the integrated current is close to zero, the expectation value $\langle \hat{\sigma}_z^1 + \hat{\sigma}_z^2 \rangle = 0$ and the qubits are in the state $|\Psi_+\rangle$. The whole measurement is illustrated in figure 2.5. At an early time in the evolution [panel (a)], the distribution of the integrated current is Gaussian but at a later time [panel (b)] three distinct peaks form with the centre one corresponding to the qubits in the state $|\Psi_+\rangle$. Quantitatively, the postselection is performed by using a threshold ν and keeping the state if and only if $|J| \leq \nu$. A small threshold thus results in a pure entangled state, albeit with a small success probability; increasing the threshold value, in turn, results in a mixed state with reduced amount of entanglement.

I plot the results of the numerical simulations in figure 2.6. I analyse the logarithmic negativity [239] of the resulting postselected state (full blue line) and the corresponding success probability (dashed green line) for cavity coupled to a vacuum bath [panel (a)]

and a bath with $\bar{n} = 2$ [panel (c)]. Generally, in the presence of thermal photons, longer measurement times are needed to reach a maximally entangled state—I use the measurement times $T = 100\kappa^{-1}$ for zero temperature bath and $T = 250\kappa^{-1}$ in presence of thermal noise. This effect is due to the reduced signal-to-noise ratio, cf. figure 2.6(b,d). In the histograms, one can see that the local minima between peaks are slightly less pronounced for $\bar{n} = 2$ even with a measurement that is longer by a factor of 2.5.

These observations are further accentuated in the insets of figure 2.6(a,c), where I plot the logarithmic negativity and success probability for $T = 75\kappa^{-1}$ (left inset) and $T = 150\kappa^{-1}$ (right). With thermal photons present, the logarithmic negativity does not reach unity in the limit $\nu \rightarrow 0$ for the shorter time; at this point, a plateau of unit entanglement starts to form with vacuum bath. For the latter time, we reach a large plateau of success probability of 0.5 with zero temperature, making it possible to generate the $|\Psi_+\rangle$ Bell state in half the cases; a similar plateau with the thermal bath starts to form only around $T = 250\kappa^{-1}$. In any practical setting, this will present a problem since other decoherence mechanisms—such as intrinsic relaxation and dephasing of the qubits—will start to play a role.

2.5.3 Single-qubit measurement using Jaynes–Cummings interaction

To illustrate adiabatic elimination with oscillating system operators, I now consider an example of a single qubit coupled to a cavity mode via Jaynes–Cummings Hamiltonian,

$$\hat{H} = \frac{1}{2}\omega\hat{\sigma}_z + \Delta\hat{a}^\dagger\hat{a} + g(\hat{a}\hat{\sigma}_+e^{i\phi} + \hat{a}^\dagger\hat{\sigma}_-e^{-i\phi}). \quad (2.96)$$

In the rotating frame of the qubit, this interaction gives rise to the stochastic master equation

$$\begin{aligned} d\hat{\rho} = & -i[g(\hat{a}\hat{\sigma}_+e^{i(\omega t+\phi)} + \hat{a}^\dagger\hat{\sigma}_-e^{-i(\omega t+\phi)}) + \Delta\hat{a}^\dagger\hat{a}, \hat{\rho}]dt + \kappa\{(\bar{n}+1)\mathcal{D}[\hat{a}] + \bar{n}\mathcal{D}[\hat{a}^\dagger]\}\hat{\rho}dt \\ & + \sqrt{\frac{\kappa}{2\bar{n}+1}}\mathcal{H}[(\bar{n}+1)\hat{a}e^{-i\delta t} - \bar{n}\hat{a}^\dagger e^{i\delta t}]\hat{\rho}dW \end{aligned} \quad (2.97)$$

with homodyne detection performed with detuning δ . To obtain a full model without oscillating measurement operators, we choose the detunings $\Delta = \omega = -\delta$. Equation (2.97) simplifies to (in rotating frame with respect to the cavity Hamiltonian $\Delta\hat{a}^\dagger\hat{a}$)

$$\begin{aligned} d\hat{\rho} = & -ig[\hat{a}\hat{\sigma}_+e^{i\phi} + \hat{a}^\dagger\hat{\sigma}_-e^{-i\phi}, \hat{\rho}]dt + \kappa(\bar{n}+1)\mathcal{D}[\hat{a}]\hat{\rho}dt + \kappa\bar{n}\mathcal{D}[\hat{a}^\dagger]\hat{\rho}dt + \\ & + \sqrt{\frac{\kappa}{2\bar{n}+1}}\mathcal{H}[(\bar{n}+1)\hat{a} - \bar{n}\hat{a}^\dagger]\hat{\rho}dW, \end{aligned} \quad (2.98a)$$

$$Idt = \sqrt{\frac{2\kappa}{2\bar{n}+1}}\langle\hat{q}\rangle dt + dW. \quad (2.98b)$$

In the following, I use equation (2.98) for comparison with the adiabatic elimination methods; it is equation (2.97), however, that I use as a starting point for the elimination of the cavity dynamics. This choice enables us, in principle, to go beyond the scenario with $\Delta = \omega = -\delta$ in the adiabatic approximation; using the Gaussian adiabatic elimination

method, it is possible, for instance, to describe dynamics with measurement performed at the other sideband, $\delta = \omega$.

The transducer dynamics are given by the Hamiltonian $\hat{H}_T = \Delta \hat{a}^\dagger \hat{a}$, jump operators $\hat{J}_1 = \sqrt{\kappa(\bar{n}+1)} \hat{a}$, $\hat{J}_2 = \sqrt{\kappa \bar{n}} \hat{a}^\dagger$, and measurement operator $\hat{\lambda} = \sqrt{\kappa/(2\bar{n}+1)}[(\bar{n}+1)\hat{a}e^{-i\delta t} - \bar{n}\hat{a}^\dagger e^{i\delta t}]$, so we have $\mathbf{R} = \Delta \mathbf{I}_2$, $\xi_{1,2}$ the same as for the dispersive readout in equations (2.89b), and the measurement operator

$$\begin{aligned} \hat{\lambda} &= \sqrt{\frac{\kappa}{2(2\bar{n}+1)}} [\cos(\delta t) - i(2\bar{n}+1) \sin(\delta t)] \hat{q} \\ &+ \sqrt{\frac{\kappa}{2(2\bar{n}+1)}} [\sin(\delta t) + i(2\bar{n}+1) \cos(\delta t)] \hat{p}, \end{aligned} \quad (2.99a)$$

$$\mathbf{c}^- = \sqrt{\frac{\kappa}{2(2\bar{n}+1)}} \begin{pmatrix} 1 \\ 0 \end{pmatrix}, \quad \mathbf{m}^c = \sqrt{\frac{\kappa(2\bar{n}+1)}{2}} \begin{pmatrix} 0 \\ 1 \end{pmatrix}, \quad (2.99b)$$

$$\mathbf{c}^s = \sqrt{\frac{\kappa}{2(2\bar{n}+1)}} \begin{pmatrix} 0 \\ 1 \end{pmatrix}, \quad \mathbf{m}^s = \sqrt{\frac{\kappa(2\bar{n}+1)}{2}} \begin{pmatrix} 0 \\ -1 \end{pmatrix}, \quad (2.99c)$$

$$\mathbf{c}^+ = \sqrt{\frac{\kappa}{8(2\bar{n}+1)}} \begin{pmatrix} 1 \\ -i \end{pmatrix}, \quad \mathbf{m}^+ = \sqrt{\frac{\kappa(2\bar{n}+1)}{8}} \begin{pmatrix} i \\ 1 \end{pmatrix}, \quad (2.99d)$$

with $\mathbf{c}^- = (\mathbf{c}^+)^*$, $\mathbf{m}^- = (\mathbf{m}^+)^*$. We thus have $\mathbf{A} = -\frac{1}{2}\kappa \mathbf{I}_2 + \Delta \boldsymbol{\sigma}$, $\mathbf{N} = (\bar{n} + \frac{1}{2}) \mathbf{I}_2$, and the cavity steady state (both unconditional and conditional) is the thermal state $\mathbf{\Gamma}^u = \mathbf{\Gamma}^c = (2\bar{n}+1) \mathbf{I}_2$. Together with the system operators

$$\hat{\mathbf{s}}_- = \frac{g}{\sqrt{2}} e^{-i\phi} \hat{\sigma}_- \begin{pmatrix} 1 \\ -i \end{pmatrix}, \quad \hat{\mathbf{s}}_+ = \frac{g}{\sqrt{2}} e^{i\phi} \hat{\sigma}_+ \begin{pmatrix} 1 \\ i \end{pmatrix}, \quad (2.100)$$

and the choice of frequencies $\Delta = \omega = -\delta$, this gives the effective equation

$$\begin{aligned} d\hat{\rho}_S &= \frac{4g^2}{\kappa} \{(\bar{n}+1)\mathcal{D}[\hat{\sigma}_-] + \bar{n}\mathcal{D}[\hat{\sigma}_+]\} \hat{\rho}_S dt \\ &+ \frac{2g}{\sqrt{\kappa(2\bar{n}+1)}} \mathcal{H}[(\bar{n}+1)\hat{\sigma}_- e^{-i(\phi+\pi/2)} - \bar{n}\hat{\sigma}_+ e^{i(\phi+\pi/2)}] \hat{\rho}_S dW, \end{aligned} \quad (2.101a)$$

$$I dt = \frac{2g}{\sqrt{\kappa(2\bar{n}+1)}} (\hat{\sigma}_y \cos \phi - \hat{\sigma}_x \sin \phi) dt + dW. \quad (2.101b)$$

With density operator expansion (and a correction for thermal noise in the Lindblad terms), the qubit dynamics are described by the equation

$$d\hat{\rho}_S = \frac{4g^2}{\kappa} \{(\bar{n}+1)\mathcal{D}[\hat{\sigma}_-] + \bar{n}\mathcal{D}[\hat{\sigma}_+]\} \hat{\rho}_S dt + \frac{2g}{\sqrt{\kappa}} \mathcal{H}[\hat{\sigma}_- e^{-i(\phi+\pi/2)}] \hat{\rho}_S dW, \quad (2.102a)$$

$$I dt = \frac{2g}{\sqrt{\kappa}} (\hat{\sigma}_y \cos \phi - \hat{\sigma}_x \sin \phi) dt + dW. \quad (2.102b)$$

Both adiabatic elimination methods, equations (2.101), (2.102), give identical results for zero-temperature cavity bath.

The average trace distance for Gaussian adiabatic elimination and density operator expansion is analysed, in complete analogy with the dispersive readout, in figure 2.7. The

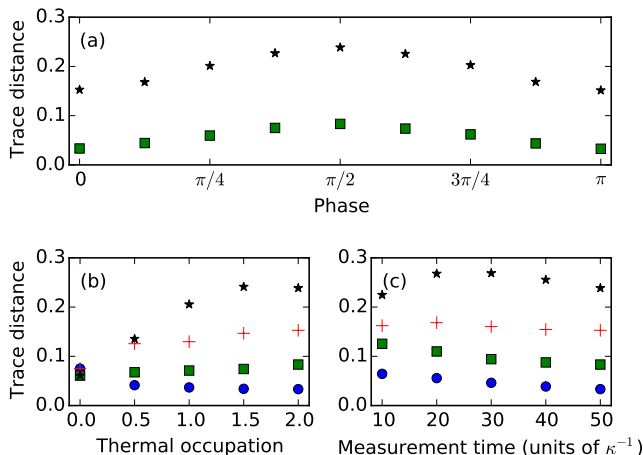


Figure 2.7: (a) Average trace distance for Gaussian adiabatic elimination (green squares) and density operator expansion (black stars) as a function of the interaction phase ϕ . In the bottom panels, I plot the average trace distance versus thermal occupation (b) and measurement time (c) for the choice of phase $\phi = 0$ (blue circles showing Gaussian adiabatic elimination and red crosses for density operator expansion) and $\phi = \pi/2$ (Gaussian adiabatic elimination shown in green squares, density operator expansion in black stars). The parameters used to run the simulations are $g = 0.1\kappa$, $\bar{n} = 2$ [for panels (a,c)], measurement time $T = 50$ [for (a,b)], and initial qubit state $|\psi_0\rangle = (|0\rangle + |1\rangle)/\sqrt{2}$. The cavity field for the full model has been cut off at the Fock number $N_{\max} = 20$.

error is minimised for phase $\phi = 0$ [panel (a)], which corresponds to a $\hat{\sigma}_y$ measurement; for a $\hat{\sigma}_x$ measurement (phase $\phi = \pi/2$), the average trace distance reaches its maximum. The error with the Jaynes–Cummings readout is, however, much less phase-sensitive than with the dispersive measurement. Performance of the Gaussian adiabatic elimination does not depend on the thermal occupation [panel (b)] while the average trace distance with the density operator expansion increases with temperature. Finally, for long measurement times [panel (c)], the average trace distance for both methods gradually decreases as the measurement approaches a projective readout and the qubit approaches one of its conditional steady states.

2.5.4 Qubit readout with a two-oscillator transducer

All examples considered so far had one special property in common: the unconditional and conditional steady states of the transducer were equal. To show how Gaussian adiabatic elimination can be applied to systems where this is not the case, I now consider the following example [see figure 2.2(c)]: A qubit, our system of interest, couples to a harmonic oscillator by means of a quantum nondemolition interaction, similar to the example in section 2.5.1. This oscillator decays into a thermal bath and, at the same time, couples to another oscillator of much higher frequency so its reservoir is effectively in the ground state. Finally, we measure the output of the second oscillator.

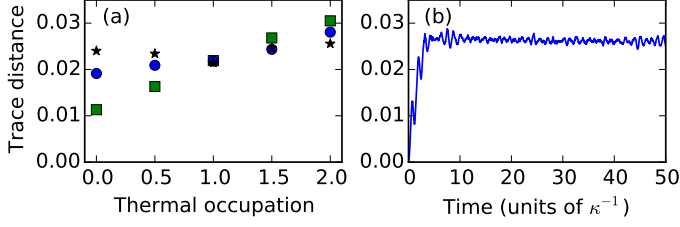


Figure 2.8: (a) Average trace distance as a function of thermal occupation for three regimes: weak coupling ($g = 0.2\kappa$, green squares), intermediate coupling ($g = 0.5\kappa$, blue circles), and strong coupling ($g = \kappa$, black stars). In (b), I show the average trace distance versus time for $\bar{n} = 2$, $g = \kappa$. Other parameters used in the simulations are $\chi = 0.2\kappa$, $\omega = 5\kappa$, $\gamma = 0.1\kappa$, initial qubit state $|\psi_0\rangle = (|0\rangle + |1\rangle)/\sqrt{2}$, and we averaged over 100 quantum trajectories.

The conditional master equation of the overall system has the form

$$d\hat{\rho} = -i[\chi\hat{\sigma}_z\hat{r}_\phi + \omega_1\hat{a}^\dagger\hat{a} + \omega_2\hat{b}^\dagger\hat{b} + g\hat{q}_1\hat{q}_2, \hat{\rho}]dt + \gamma\{(\bar{n} + 1)\mathcal{D}[\hat{a}] + \bar{n}\mathcal{D}[\hat{a}^\dagger]\}\hat{\rho}dt + \kappa\mathcal{D}[\hat{b}]\hat{\rho}dt + \sqrt{\kappa}\mathcal{H}[\hat{b}e^{i\varphi}]\hat{\rho}dW, \quad (2.103a)$$

$$Idt = \sqrt{\kappa}\langle\hat{b}e^{i\varphi} + \hat{b}^\dagger e^{-i\varphi}\rangle dt + dW. \quad (2.103b)$$

Here, \hat{a} describes the first (i.e., thermal) oscillator, \hat{b} is used for the second, readout oscillator, and $\hat{r}_\phi = (\hat{a}e^{i\phi} + \hat{a}^\dagger e^{-i\phi})/\sqrt{2}$ denotes a general quadrature operator of the thermal oscillator. Such a system can be realised by coupling superconducting qubit to a mechanical oscillator [173, 184] and reading out the signal in the mechanical oscillator optically. The oscillator coupling has the form of standard linearized optomechanical interaction [18], $\hat{H}_{\text{osc}} = g\hat{q}_1\hat{q}_2$, and I consider the scenario where the optomechanical system is driven on the red sideband, $\omega_1 = \omega_2 = \omega$; in this case, the states of the mechanical oscillator and the optical cavity field are swapped. The readout efficiency can further be maximized by letting the qubit couple to the phase quadrature of the thermal oscillator and measuring the phase quadrature of the readout oscillator. The stochastic master equation then takes the form

$$d\hat{\rho} = -i[\chi\hat{\sigma}_z\hat{p}_1 + \omega(\hat{a}^\dagger\hat{a} + \hat{b}^\dagger\hat{b}) + g\hat{q}_1\hat{q}_2, \hat{\rho}]dt + \gamma\{(\bar{n} + 1)\mathcal{D}[\hat{a}] + \bar{n}\mathcal{D}[\hat{a}^\dagger]\}\hat{\rho}dt + \kappa\mathcal{D}[\hat{b}]\hat{\rho}dt + \sqrt{\kappa}\mathcal{H}[i\hat{b}]\hat{\rho}dW. \quad (2.104)$$

As the transducer dynamics are more complex than for the simple transducers considered in the previous sections, I perform the whole adiabatic elimination numerically; see the simulation files [238] for details. The results of the numerical simulations are shown in figure 2.8. In panel (a), I investigate how the bath temperature for the thermal oscillator affects the average trace distance in three distinct regimes: for weak ($g = 0.2\kappa$, green squares), intermediate ($g = 0.5\kappa$, blue circles), and strong ($g = \kappa$, black stars) coupling. As the strength of the coupling between the two oscillators grows, the trace distance becomes less temperature sensitive. This effect is a natural consequence of the

optomechanical coupling which effectively cools the mechanical oscillator so that its steady state occupation is lower for stronger coupling. The error of the adiabatic elimination is, however, for all three values of coupling an order of magnitude smaller than for the readout using simple transducer in sections 2.5.1, 2.5.3. In figure 2.8(b), I plot an example trace distance as a function of time. This plot illustrates that the time dependence has features similar to simpler transducers considered in the previous sections: after a short initial transient time, the trace distance saturates and stays constant for the rest of the evolution.

These small errors in accuracy come with drastically reduced computational requirements. With only two thermal excitations in the heat bath, the full model needs 700 times longer time to be simulated compared to the adiabatic elimination; this difference can be further increased by using larger time steps for the approximate dynamics since the qubit evolution happens at longer time scales. The main limitation in the numerical analysis, however, are the memory requirements. With two thermal excitations (and corresponding Fock space cutoffs at 20 and 10 excitations for the thermal and readout oscillator, respectively), the storing of the full density matrix for the whole time evolution requires several gigabytes of working memory. Since the cutoff energy grows superlinearly with increasing temperature and the size of the density matrix grows quadratically with the cutoff, it is not possible to perform reliable numerical simulations for larger bath temperatures. Nevertheless, the results presented in this section strongly suggest that Gaussian adiabatic elimination can be used for systems with tens or hundreds thermal excitations present.

2.6 SUMMARY

In this chapter, I showed how the unavoidable interaction of quantum systems with their environment can be used to measure and control them and how such dynamics can be described. Afterwards, I discussed how the description using a stochastic master equation can be simplified for Gaussian systems and for systems consisting of both Gaussian and non-Gaussian elements.

Gaussian systems can be efficiently described using the statistical moments of their quasi-probability distribution; equations of motion for the mean vector and the covariance matrix can be derived from the stochastic master equation. Remarkably, the covariance matrix obeys a deterministic Riccati equation, which can be efficiently solved. Since the exact mean value is often irrelevant, this approach represents a very powerful tool for describing Gaussian systems under continuous measurements.

This description of Gaussian systems enables their efficient adiabatic elimination from dynamics containing both Gaussian and non-Gaussian elements. Adopting the formalism of the covariance matrix, we are able to treat Gaussian transducers coupled to thermal bath or consisting of multiple bosonic modes. While eliminating several modes using the approach based on density operator expansion or polaron transformation quickly becomes tedious, this method requires only basic linear-algebraic tools and can be easily applied numerically.

Since the procedure relies on the fact that the system of interest itself has no free evolution, I did not present a completely general treatment; instead, I focused on the most relevant scenarios. In the first case, moving to the rotating frame with respect to the system Hamiltonian leaves its interaction with the transducer time independent, corresponding, in particular, to a quantum nondemolition interaction. Second, I considered a scenario, where the interaction has terms oscillating at the frequency $\pm\omega$. Adapting the method for other forms of coupling is straightforward.

Further improvements can be achieved with ideas borrowed from adiabatic elimination using polaron transformation; for strong coupling between the system and the transducer, one has to consider different steady states of the transducer for individual states of the system and perform adiabatic elimination with respect to these conditional states. Using similar tools, it should be possible to eliminate any Gaussian transducer with respect to several conditional steady states. In addition, one should be able to generalize the method for system–transducer coupling that is quadratic in the canonical transducer operators; one could, for instance, use such a result to analyse a full dispersive readout of a superconducting qubit, described by the Hamiltonian $\hat{H}_{\text{int}} = g\hat{\sigma}_z\hat{a}^\dagger\hat{a}$.

The results can find applications in circuit quantum electrodynamics and cavity optomechanics. Compared to the method of expanding the density operator around the vacuum state of the readout cavity, the new method provides significantly better results already for a few thermal excitations present and is thus relevant to qubit readout in superconducting systems. Typical frequencies of mechanical oscillations, on the other hand, correspond to thermal noise of a few hundred quanta even with cryogenic cooling. Such systems cannot be eliminated from stochastic master equations using present methods; the toy model in the last example shows how similar tasks can be achieved.

2.A PROPERTIES OF GAUSSIAN CHARACTERISTIC FUNCTIONS

The characteristic function of an arbitrary state $\hat{\rho}$ is defined as

$$\chi(\mathbf{z}) = \text{tr}\{\hat{D}(\mathbf{z})\hat{\rho}\}; \quad (2.105)$$

here, $\mathbf{z} \in \mathbb{R}^{2N}$ and $\hat{D}(\mathbf{z}) = \exp(-i\mathbf{z}^T\boldsymbol{\sigma}\hat{\mathbf{r}})$ (with the symplectic matrix $\boldsymbol{\sigma}$ and vector of canonical operators $\hat{\mathbf{r}}$) is the displacement operator. For a single-mode system ($N = 1$), we have $\hat{\mathbf{r}} = (\hat{q}, \hat{p})^T$ and the displacement operator can be expressed using the following two expressions:

$$\hat{D}(\mathbf{z}) = \exp\left(-\frac{i\mathbf{z}_1\mathbf{z}_2}{2}\right) \exp(i\mathbf{z}_2\hat{q}) \exp(-i\mathbf{z}_1\hat{p}) \quad (2.106a)$$

$$= \exp\left(\frac{i\mathbf{z}_1\mathbf{z}_2}{2}\right) \exp(-i\mathbf{z}_1\hat{p}) \exp(i\mathbf{z}_2\hat{q}). \quad (2.106b)$$

From these formulas, it follows that the derivative of the displacement operator can be expressed as

$$\frac{\partial\hat{D}(\mathbf{z})}{\partial\mathbf{z}_i} = -\frac{i}{2}[\sigma_{ij}\hat{r}_j\hat{D}(\mathbf{z}) + \hat{D}(\mathbf{z})\sigma_{ij}\hat{r}_j]. \quad (2.107)$$

With the definition (2.105) and identity (2.107), we can evaluate the first, second, and third derivative of the characteristic function,

$$\left. \frac{\partial \chi(\mathbf{z})}{\partial z_i} \right|_{\mathbf{z}=0} = \text{tr} \left\{ \left. \frac{\partial \hat{D}(\mathbf{z})}{\partial z_1} \right|_{\mathbf{z}=0} \hat{\rho} \right\} = -i\sigma_{ij} \langle \hat{r}_j \rangle, \quad (2.108a)$$

$$\left. \frac{\partial^2 \chi(\mathbf{z})}{\partial z_i \partial z_j} \right|_{\mathbf{z}=0} = -\frac{1}{2} \sigma_{ik} \sigma_{jl} \langle [\hat{r}_k, \hat{r}_l]_+ \rangle, \quad (2.108b)$$

$$\left. \frac{\partial^3 \chi(\mathbf{z})}{\partial z_i \partial z_j \partial z_k} \right|_{\mathbf{z}=0} = \frac{i}{4} \sigma_{il} \sigma_{jm} \sigma_{kn} \langle [\hat{r}_l, [\hat{r}_m, \hat{r}_n]_+]_+ \rangle. \quad (2.108c)$$

The characteristic function of a general Gaussian state can be written as

$$\chi(\mathbf{z}) = \exp \left(-i\mathbf{z}^T \boldsymbol{\mu} - \frac{1}{4} \mathbf{z}^T \mathbf{V} \mathbf{z} \right) \quad (2.109)$$

with some mean vector $\boldsymbol{\mu}$ and covariance matrix $\mathbf{V} = \mathbf{V}^T$. We can evaluate the derivatives also for this Gaussian characteristic function,

$$\left. \frac{\partial \chi(\mathbf{z})}{\partial z_i} \right|_{\mathbf{z}=0} = \left(-i\mu_i - \frac{1}{2} V_{ij} z_j \right) \chi(\mathbf{z}) \Big|_{\mathbf{z}=0} = -i\mu_i, \quad (2.110a)$$

$$\left. \frac{\partial^2 \chi(\mathbf{z})}{\partial z_i \partial z_j} \right|_{\mathbf{z}=0} = -\frac{1}{2} V_{ij} - \mu_i \mu_j, \quad (2.110b)$$

$$\left. \frac{\partial^3 \chi(\mathbf{z})}{\partial z_i \partial z_j \partial z_k} \right|_{\mathbf{z}=0} = \frac{i}{2} (\mu_i V_{jk} + \mu_j V_{ki} \mu_k V_{ij} + 2\mu_i \mu_j \mu_k); \quad (2.110c)$$

by direct comparison with equations (2.108), we identify

$$\boldsymbol{\mu} = \boldsymbol{\sigma} \mathbf{x}, \quad \mathbf{V} = -\boldsymbol{\sigma} \boldsymbol{\Gamma} \boldsymbol{\sigma}^T = -\boldsymbol{\sigma}^T \boldsymbol{\Gamma} \boldsymbol{\sigma}. \quad (2.111)$$

Equations (2.108c) and (2.110c) now yield

$$\langle [\hat{r}_i, [\hat{r}_j, \hat{r}_k]_+]_+ \rangle = 2(\Gamma_{ij} x_k + \Gamma_{jk} x_i + \Gamma_{ki} x_j + 2x_i x_j x_k), \quad (2.112)$$

which is the identity (2.54) that we used in section 2.3.

2.B POSITIVE-SEMIDEFINITENESS OF DECAY

In order to give rise to valid Markovian dynamics, the decay rates in a quantum-optical master equation have to be positive. For the effective dynamics after adiabatic elimination of the transducer, this means that the eigenvalues of the decay matrix \mathbf{P} [equation (2.75b)] have all to be non-negative. Using its definition, equation (2.75b), together with the Lyapunov equation (2.47), and the definitions given in equations (2.39) and (2.48), we can write

$$\mathbf{P} = \mathbf{A}^{-1} \left[\mathbf{N} + \frac{i}{2} (\mathbf{A} \boldsymbol{\sigma} - \boldsymbol{\sigma}^T \mathbf{A}^T) \right] \mathbf{A}^{-T} = \mathbf{A}^{-1} \boldsymbol{\sigma} \sum_n \boldsymbol{\xi}_n^T \boldsymbol{\xi}_n^* \boldsymbol{\sigma}^T \mathbf{A}^{-T}. \quad (2.113)$$

The decay matrix \mathbf{P} is thus positive semidefinite and gives rise to a valid master equation.

Next, each measurement channel in the stochastic master equation has to have a corresponding decay process. Quantitatively, matrix \mathbf{P} in equation (2.75b) describing all decay terms needs to be larger than the matrix $\sum_m \Lambda_m \Lambda_m^\dagger$ characterizing all measurement channels; the matrix

$$\mathbf{P}' = \mathbf{P} - \sum_m \Lambda_m \Lambda_m^\dagger \quad (2.114)$$

has to be positive semidefinite. In words, all information we obtain from the measurement comes from the system and not its environment. I did not prove this statement in the general case but checked it for all of the cases treated in section 2.5.

2.C HIERARCHY OF DYNAMICAL EQUATIONS FOR TRANSDUCER CUMULANTS

To understand the adiabatic elimination [in particular, deriving equation (2.71a)], we need to understand the hierarchy of equations of motion for deviations of the exact and tensor-product state with respect to the cumulants of the transducer and their general structure. (In the following, I will, for simplicity, refer to these quantities as cumulants.) I use the term cumulant here since, as we will see, the cumulants are more fundamental for the expansion than statistical moments. The distinction is, nevertheless, important only for higher order cumulants and moments—the first cumulant is equal to the mean value, and the second and third cumulant are equal to the second and third central moment, respectively.

We start by writing the equation of motion for the second cumulant $\hat{\Omega}_{ij} = \text{tr}_T\{[\hat{r}_i - x_i, \hat{r}_j - x_j]_+(\hat{\rho} - \hat{\rho}_S \otimes \hat{\rho}_T)\}$, which can be derived in complete analogy with section 2.4.1,

$$\begin{aligned} d\hat{\Omega}_{ij} = & \epsilon(\sigma_{ik}[\hat{s}_k - \langle \hat{s}_k \rangle, \hat{\mu}_j]_+ + \sigma_{jk}[\hat{s}_k - \langle \hat{s}_k \rangle, \hat{\mu}_i]_+)dt + (A_{ik}\hat{\Omega}_{kj} + A_{jk}\hat{\Omega}_{ki})dt \\ & + \hat{v}_{ijk}c_{mk}dW_m, \end{aligned} \quad (2.115)$$

where

$$\hat{v}_{ijk} = \text{tr}_T\{[[\hat{r}_i - x_i, \hat{r}_j - x_j]_+, \hat{r}_k - x_k]_+\hat{\rho}\} - 2(\Gamma_{ij}^c\hat{\mu}_k + \Gamma_{jk}^c\hat{\mu}_i + \Gamma_{ki}^c\hat{\mu}_j) \quad (2.116)$$

is the third cumulant. We can now see from the deterministic part of the equation that the second cumulant $\hat{\Omega}_{ij}$ is of second order in ϵ since it couples to the first cumulant $\hat{\mu}_i = \text{tr}_T\{\hat{r}_i(\hat{\rho} - \hat{\rho}_S \otimes \hat{\rho}_T)\}$ (which is a first order quantity) via ϵ . I further conjecture that the third cumulant is of higher order, $\hat{v}_{ijk} = O(\epsilon^3)$. In the rest of this section, I justify this assumption by presenting the expected hierarchy of the cumulants.

We start by defining the deviation of the exact state from the tensor-product state

$$\hat{\omega} = \hat{\rho} - \hat{\rho}_S \otimes \hat{\rho}_T. \quad (2.117)$$

The equation of motion for the reduced state now describes the evolution of the reduced deviation $\hat{\omega}_S = \text{tr}_T\{\hat{\omega}\}$; note that the tensor-product state (a zero-order quantity) does not evolve since there is no free evolution of $\hat{\rho}_S$ and the equilibration of $\hat{\rho}_T$ is effectively instantaneous. The reduced deviation $\hat{\omega}_S$ can then be viewed as the zero-order cumulant.

With this observation, we can now rewrite the equations of motion for the zeroth, first, and second cumulant,

$$d\hat{\omega}_S = -i\epsilon[\hat{s}_i, \hat{\eta}_i]dt + 2c_{mi}\hat{\mu}_i dW_m, \quad (2.118a)$$

$$d\hat{\mu}_i = Q_{ij}\hat{\mu}_j dt + \frac{1}{2}\epsilon\sigma_{ij}[\hat{s}_j - \langle\hat{s}_j\rangle, \hat{\rho}_S]_+ dt - \frac{i}{2}\epsilon\Gamma_{ij}^c[\hat{s}_j, \hat{\rho}_S]dt + \hat{\Omega}_{ij}c_{mj}dW_m, \quad (2.118b)$$

$$d\hat{\Omega}_{ij} = \epsilon(\sigma_{ik}[\hat{s}_k - \langle\hat{s}_k\rangle, \hat{\mu}_j]_+ + \sigma_{jk}[\hat{s}_k - \langle\hat{s}_k\rangle, \hat{\mu}_i]_+)dt + (A_{ik}\hat{\Omega}_{kj} + A_{jk}\hat{\Omega}_{ki})dt + \hat{v}_{ijk}c_{mk}dW_m; \quad (2.118c)$$

moreover, the cumulants can be written as

$$\hat{\omega}_S = \text{tr}_T\{\hat{\omega}\}, \quad (2.119a)$$

$$\hat{\mu}_i = \text{tr}_T\{\hat{r}_i\hat{\omega}\}, \quad (2.119b)$$

$$\hat{\Omega}_{ij} = \text{tr}_T\{[[\hat{r}_i, \hat{r}_j]_+ - 2(x_i\hat{r}_j + x_j\hat{r}_i)]\hat{\omega}\}, \quad (2.119c)$$

$$\hat{v}_{ijk} = \text{tr}_T\{[[[\hat{r}_i, \hat{r}_j]_+, \hat{r}_k]_+ - 2(x_i[\hat{r}_j, \hat{r}_k]_+ + x_j[\hat{r}_k, \hat{r}_i]_+ + x_k[\hat{r}_i, \hat{r}_j]_+) - 2(V_{ij}\hat{r}_k + V_{jk}\hat{r}_i + V_{ki}\hat{r}_j) + 8(x_i x_j \hat{r}_k + x_j x_k \hat{r}_i + x_k x_i \hat{r}_j)]\hat{\omega}\}, \quad (2.119d)$$

where $V_{ij} = \text{tr}_T\{[[\hat{r}_i, \hat{r}_j]_+ \hat{\rho}_T]\}$ is the second raw moment of the transducer.

The cumulants are now clearly generalizations of regular cumulants that include the effect of the partial trace, such as $x_i x_j \rightarrow x_i \text{tr}_T\{\hat{r}_j\hat{\omega}\} + x_j \text{tr}_T\{\hat{r}_i\hat{\omega}\}$, etc. Furthermore, the equations of motion have a clear structure; for the n th cumulant, denoted $\hat{\mathbf{k}}^{(n)}$, we can symbolically write

$$d\hat{\mathbf{k}}^{(n)} = \mathcal{R}^{(n)}\hat{\mathbf{k}}^{(n)} dt + \epsilon\mathcal{S}^{(n)}\hat{\mathbf{k}}^{(n-1)} dt + \epsilon\mathcal{T}^{(n)}\mathbf{M}^{(n+1)} dt + \mathcal{V}^{(n)}\hat{\mathbf{k}}^{(n+1)} dW_m \quad (2.120)$$

with $\mathbf{M}^{(n)}$ denoting n th central moment of the transducer and some superoperators $\mathcal{R}^{(n)}$, $\mathcal{S}^{(n)}$, $\mathcal{T}^{(n)}$, $\mathcal{V}^{(n)}$. In words, the n th cumulant (apart from its own free evolution) couples to the $(n-1)$ th cumulant via ϵ in the deterministic part and to the $(n+1)$ th cumulant in the stochastic part. In addition, there is also coupling to a higher order central moment of the transducer which is, nevertheless, present only for the first order deviation because the transducer is Gaussian so that $\mathbf{M}^{(n)} = \mathbf{0}$ for $n > 2$. Finally, the deterministic part of the equation of motion for the zeroth cumulant $\hat{\omega}_S$ has a somewhat different structure since it cannot couple to a lower order cumulant; as a result, there is coupling to $\hat{\eta}_i = \text{tr}_T\{\hat{r}_i\hat{\rho}\}$ instead of the first moment of the transducer. The moments appear for $\hat{\rho} = \hat{\rho}_S \otimes \hat{\rho}_T$ which is correct to leading order only for the first cumulant; as there is no -1 st cumulant in the equation for the zeroth cumulant, this approximation is not valid for $\hat{\omega}_S$.

The hierarchy (constructed explicitly for $n \leq 2$ and conjectured for $n > 2$) is related to the cumulant expansion method of van Kampen [240–242]. With this method, the effect of a bath is expressed via a series of cumulants of the bath operators in which the n th cumulant is of the order ϵ^n in the system–bath coupling. For Markovian systems, it is sufficient to consider the first and second cumulants (i.e., the mean and the covariance); for a general non-Markovian bath, represented by coloured noise, higher orders have to be considered [243]. In our treatment, the role of the bath is played by the transducer which

can, in the most general case, act as a non-Markovian medium. For a short correlation time, which corresponds to a quickly decaying transducer and is thus relevant to adiabatic elimination methods, the Markovian approximation is valid and only the first and second cumulants play a role. Since we are interested in the deviation of the exact and tensor product state, which is a small quantity already, $\hat{\omega} = \hat{\rho} - \hat{\rho}_S \otimes \hat{\rho}_T = O(\epsilon)$, it is sufficient to consider the contributions of the first cumulant $\hat{\mu}_i$ in the effective equation of motion for the system density matrix.

CHAPTER 3

QUANTUM FORCE SENSING WITH OPTOMECHANICAL TRANSDUCERS

Optomechanical force sensing is a well-established measurement technique that can reach remarkable precision. The core of the setup is a mechanical oscillator which serves to translate an external force into mechanical motion. The main advantage of mechanical oscillators in this context lies in their large susceptibility to external influences: micromechanical oscillators quickly and strongly respond to electric and magnetic fields, and to mechanical effects. Radiation pressure interaction is then used to transfer the information about the force onto the phase of a light field, which can be measured with high precision using interferometric techniques.

Such measurements are subject to the standard quantum limit as discussed in chapter 1: if the optomechanical interaction is too weak, we cannot successfully resolve the resulting phase shift; a strong coupling leads to measurement backaction since the fluctuations of the light beam strongly affect the mechanical motion. With an intermediate coupling strength, the measurement sensitivity is maximized. The sensitivity can be further increased if we use—instead of a coherent state, for which the standard quantum limit is formulated—an entangled state of light or more sophisticated readout schemes where the measurement backaction can be avoided [101, 124, 133, 244]. Quantum physics can thus be used to improve the measurement sensitivity.

The opposite situation—where the force acting on the mechanical oscillator is quantum-mechanical—received no attention so far. After all, such a scenario is of little or no interest for most applications. Whether the force is exerted by a quantum object or not, the force estimate will be a single figure; if the source of the force was in a quantum superposition at the beginning, it will have collapsed into one particular eigenstate of the measurement.

Quantum coherence of the source starts to play a role when several such systems are read out using a single beam of light. Owing to interference effects, different states of the system can give rise to the same measurement outcome. For example, in a measurement of the spin of two qubits, the information about which qubit is excited can be erased when they are measured with a single probe. Several questions then arise: Can quantum coherence of the force source survive the optomechanical measurement? And can it be used for interesting applications?

In this chapter, I answer both questions in the affirmative. I consider a scheme where an optomechanical system is used to read out the state of a superconducting transmon qubit; cascading two such systems results in the measurement of the total spin of the two qubits (see figure 3.1) [95]. Generation of entanglement by spin measurement has been demonstrated in a purely microwave system [91, 92, 245]; here, I show that such a measurement is possible with optomechanical transducers under realistic conditions. The advantage of using light instead of microwaves for the measurement lies in the possibility of bridging room-temperature environment between the qubits; the approach can thus be used to generate entanglement between distant superconducting qubits, thus solving a long-standing open problem of building quantum networks with superconducting circuits.

I describe the system theoretically in section 3.1 and consider possible experimental implementations in section 3.2; the latter include transmon qubits, flux qubits, and magnetic sublevels of nitrogen–vacancy centres. In section 3.3, I consider two extensions of the scheme: quantum nondemolition measurements to measure one quadrature of the force and the use of a microwave cavity, which serves as a filter for the qubit-state-dependent force. Technical details—derivation of the effective equations of motion and their analysis—are delegated to sections 3.4 and 3.5.

In section 3.6, I apply the effective equation of motion on quantum nondemolition detection of the photon number [117, 246, 247]. Instead of the state of a superconducting qubit, the force felt by the mechanical oscillator is coming from a nonlinearly coupled cavity and thus depends on the number of photons in this cavity. If the photons arrive into the cavity from an external source, the measurement performance is limited by quantum Zeno effect [209, 220, 246], which gives rise to a variant of the standard quantum limit. I then briefly discuss a few strategies that can be used to combat the quantum Zeno effect and, finally, address fundamental limits on photon counting with optomechanical transducers.

3.1 GENERATION OF ENTANGLEMENT BETWEEN TWO SUPERCONDUCTING QUBITS

3.1.1 Measuring qubit-state-dependent forces

To get a simple, intuitive understanding of the system shown in figure 3.1, we start by considering a single node of the system. Here, a superconducting qubit interacts capacitively with a mechanical oscillator so that the position of the oscillator determines the transition frequency of the qubit, $\hat{H}_{\text{int}} = \hbar\chi\hat{\sigma}_z(\hat{b} + \hat{b}^\dagger)$, as shown, for example, in references [172, 173]. The qubit thus exerts a state-dependent force $F = \pm\hbar\chi/\sqrt{2}x_{\text{zpf}}$ on the oscillator with position operator $\hat{x} = \sqrt{2}x_{\text{zpf}}(\hat{b} + \hat{b}^\dagger)$ and zero-point fluctuation $x_{\text{zpf}} = \sqrt{\hbar/2m\omega_m}$.

In order to determine the force (and thus the state of the qubit), we measure the mechanical position using a resonantly driven optical cavity. Via the optomechanical interaction $\hat{H}_{\text{om}} = \hbar g(\hat{a} + \hat{a}^\dagger)(\hat{b} + \hat{b}^\dagger)$, the mechanical position determines a phase shift on the light field which can be measured with homodyne detection. Assuming the measurement is shot-noise limited, the sensitivity of the readout at Fourier frequency ω is

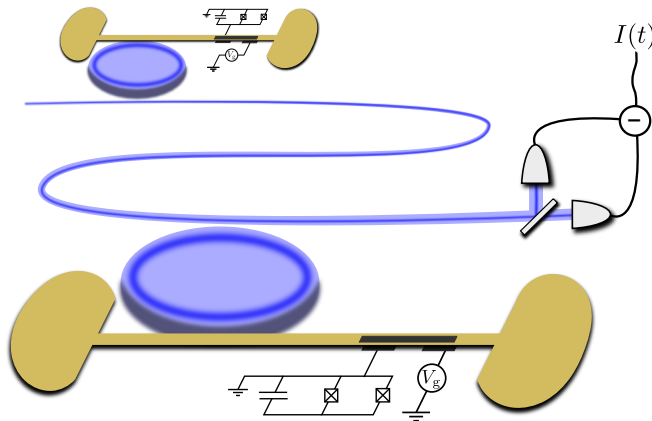


Figure 3.1: Schematic depiction of the setup for generation of entanglement between two superconducting qubits. Each of two superconducting transmon qubits (shown as black circuits) interacts with a mechanical oscillator (here in the form of nanobeams, shown in yellow). The position of the oscillators is read out optically using microdisk resonators supporting whispering-gallery modes (shown in blue). The two systems are unidirectionally coupled using an optical fibre; homodyne measurement at the output provides information about the joint state of the qubits, making it possible to postselect an entangled state.

given by the spectral density of the added noise

$$S_F^2(\omega) = \frac{\kappa x_{\text{zpf}}^2}{8g^2 \chi_m^2(\omega)}, \quad (3.1)$$

where $\chi_m(\omega) = [m(\omega_m^2 - \omega^2) - im\gamma\omega]^{-1}$ is the mechanical susceptibility and κ, γ are the optical and mechanical linewidth.

The force sensitivity of the optomechanical system and the qubit force together determine the measurement time needed to successfully distinguish the qubit states $|0\rangle, |1\rangle$, namely,

$$\tau_{\text{meas}} = \frac{S_F^2(\omega)}{F^2} = \frac{\kappa\omega_m^2}{16\chi^2 g^2}. \quad (3.2)$$

Here, we used the fact that the qubit force is quasi-static so the Fourier frequencies we are interested in are smaller than the mechanical frequency, $\omega \ll \omega_m$, and the susceptibility can be approximated as $\chi_m(\omega) \simeq 1/m\omega_m^2$. For an efficient readout, the measurement time τ_{meas} has to be shorter than the lifetime of the qubit which is characterised by its intrinsic decoherence (quantified by the intrinsic relaxation and dephasing lifetimes $T_{1,2}$) and decoherence due to the interaction with the transducer.

For the intrinsic decoherence, we consider a superconducting transmon qubit with $T_{1,2} \approx 20 \mu\text{s}$ and coupling $\chi/2\pi = 5 \text{ MHz}$ to the mechanical oscillator [172, 173]. The required force sensitivity is then $S_F = F \sqrt{\tau_{\text{meas}}} \sim 0.5 \text{ fN}/\sqrt{\text{Hz}}$ which can be achieved with state-of-the-art optomechanical systems. To compare the measurement time with the decoherence due to the interaction with the transducer, we analyse the force the oscillator

exerts on the qubit, $\hat{f}(\omega) = \chi \hat{x}(\omega)/\sqrt{2}x_{\text{zpf}}$; here, $\hat{x}(\omega) = \chi_m(\omega)\hat{f}_{\text{th}}(\omega)$ is the noisy mechanical position driven by the thermal force \hat{f}_{th} with spectrum $S_{\text{th}}(\omega) = 2\gamma m\hbar\omega_m\bar{n}$ and $\bar{n} \simeq k_{\text{B}}T/\hbar\omega_m$ is the mean occupation number of the oscillator at temperature T . This random, thermal force results in dephasing of the qubit at a rate that is given by the spectral density of the force $\hat{f}(\omega)$ for $\omega \ll \omega_m$,

$$\Gamma_{\text{mech}} = S_f^2(\omega) = \frac{2\chi^2}{\omega_m^2}\gamma\bar{n}. \quad (3.3)$$

Comparing the dephasing time $\tau_{\text{mech}} = 1/\Gamma_{\text{mech}}$ with the measurement time τ_{meas} , we see that the former is longer than the latter for strong optomechanical cooperativity,

$$\bar{C} = 4g^2/\kappa\gamma\bar{n} > \frac{1}{2}. \quad (3.4)$$

3.1.2 Equation of motion

With a clear picture for the action of the protocol, we now turn to the full system comprising two nodes connected by a unidirectional optical link as shown in figure 3.1. To rigorously include all decoherence channels and to accommodate for the finite duration of the measurement, we describe the system using the stochastic master equation (with $\hbar = 1$ in the following)

$$\begin{aligned} d\hat{\rho} = & -i[\hat{H}, \hat{\rho}]dt + \mathcal{L}_q\hat{\rho}dt + \sum_{j=1}^2 \gamma\{(\bar{n}+1)\mathcal{D}[\hat{b}_j] + \bar{n}\mathcal{D}[\hat{b}_j^\dagger]\}\hat{\rho}dt \\ & + \kappa\mathcal{D}[\hat{a}_1 - \hat{a}_2]\hat{\rho}dt + \sqrt{\kappa}\mathcal{H}[(\hat{a}_1 - \hat{a}_2)e^{i\phi}]\hat{\rho}dW. \end{aligned} \quad (3.5)$$

The Hamiltonian describes the coherent evolution of the system,

$$\hat{H} = \sum_{j=1}^2 [\chi\hat{\sigma}_z^j(\hat{b}_j + \hat{b}_j^\dagger) + \omega_m\hat{b}_j^\dagger\hat{b}_j + g(\hat{a}_j + \hat{a}_j^\dagger)(\hat{b}_j + \hat{b}_j^\dagger)] + \frac{i\kappa}{2}(\hat{a}_1\hat{a}_2^\dagger - \hat{a}_2\hat{a}_1^\dagger), \quad (3.6)$$

with terms corresponding (from left to right) to the interaction between the qubits and the mechanical oscillators, the free mechanical evolution, and the optomechanical coupling. The last term in the Hamiltonian (3.6) together with the Lindblad term $\kappa\mathcal{D}[\hat{a}_1 - \hat{a}_2]\hat{\rho}$ describes the joint decay of the cascaded optical cavities [214]. Next, the Liouvillian

$$\mathcal{L}_q\hat{\rho} = \sum_{j=1}^2 \left(\frac{1}{T_1}\mathcal{D}[\hat{\sigma}_-^j] + \frac{1}{T_2}\mathcal{D}[\hat{\sigma}_z^j] \right) \hat{\rho} \quad (3.7)$$

describes the intrinsic decoherence of the qubits, characterised by their relaxation and dephasing lifetimes $T_{1,2}$. The Lindblad terms on the first line of equation (3.5) describe the thermal noise of the mechanical oscillators and the last term on the second line describes the effect of homodyne measurement of the outgoing light field. To remind the reader, $\mathcal{D}[\hat{O}]\hat{\rho} = \hat{O}\hat{\rho}\hat{O}^\dagger - \frac{1}{2}(\hat{O}^\dagger\hat{O}\hat{\rho} + \hat{\rho}\hat{O}^\dagger\hat{O})$, $\mathcal{H}[\hat{O}]\hat{\rho} = (\hat{O} - \langle\hat{O}\rangle)\hat{\rho} + \hat{\rho}(\hat{O}^\dagger - \langle\hat{O}^\dagger\rangle)$, and dW

is Wiener increment with mean value $\langle dW \rangle = 0$ and variance $\langle dW^2 \rangle = dt$. Finally, the measurement gives rise to a classical measurement signal that obeys the equation

$$I dt = \sqrt{\kappa} \langle (\hat{a}_1 - \hat{a}_2) e^{i\phi} + \text{H.c.} \rangle dt + dW. \quad (3.8)$$

The conditional master equation (3.5) is too complicated to be integrated analytically or numerically. Simulating the dynamics using Monte Carlo trajectories would need to take into account the thermal baths of the mechanical oscillators, which can easily contain several hundreds or thousands of phonons on average. Instead, since the dynamics of the transducer is Gaussian, we adiabatically eliminate the optical and mechanical degrees of freedom following the approach presented in chapter 2. If we assume that the qubit coupling rate χ is smaller than the rate of the transducer dynamics (in the examples considered in the next section, this timescale is of the order of the cavity decay rate κ), the effective equation for the state of the two qubits $\hat{\rho}_q$ is

$$\begin{aligned} d\hat{\rho}_q = & \mathcal{L}_q \hat{\rho}_q dt + \sum_{j=1}^2 \Gamma_{\text{mech}} \mathcal{D}[\hat{\sigma}_z^j] \hat{\rho}_q dt + \Gamma_{\text{meas}} \mathcal{D}[\hat{\sigma}_z^1 + \hat{\sigma}_z^2] \hat{\rho}_q dt \\ & + \sqrt{\Gamma_{\text{meas}}} \mathcal{H}[\hat{\sigma}_z^1 + \hat{\sigma}_z^2] \hat{\rho}_q dW; \end{aligned} \quad (3.9)$$

see section 3.4 for detailed derivation. The measurement and dephasing rates are given by

$$\Gamma_{\text{meas}} = 16 \frac{\chi^2 g^2}{\kappa \omega_m^2}, \quad \Gamma_{\text{mech}} = \frac{\chi^2 \gamma}{\omega_m^2} (2\bar{n} + 1), \quad (3.10)$$

in perfect agreement with the argument of force sensing presented in the previous section. Finally, the classical measurement signal corresponding to the conditional master equation (3.9) is given by

$$I dt = 2\sqrt{\Gamma_{\text{meas}}} \langle \hat{\sigma}_z^1 + \hat{\sigma}_z^2 \rangle dt + dW. \quad (3.11)$$

So far, we assumed that all light leaving the cavities arrives at the detector. In any practical realization of the measurement, however, part of the light will necessarily be lost via absorption in optical fibres, transmission through imperfect mirrors, or other processes. All these effects can be modelled by adding a beam splitter into an otherwise perfect system. First, we characterize the losses between the two nodes by transmissivity τ ; we modify the dynamics of the cascaded optical cavities as follows [214]:

$$\begin{aligned} \mathcal{L}_{\text{casc}} \hat{\rho} = & \frac{\kappa}{2} [\hat{a}_1 \hat{a}_2^\dagger - \hat{a}_2 \hat{a}_1^\dagger, \hat{\rho}] + \kappa \mathcal{D}[\hat{a}_1 - \hat{a}_2] \hat{\rho} \\ \rightarrow & \frac{\kappa \sqrt{\tau}}{2} [\hat{a}_1 \hat{a}_2^\dagger - \hat{a}_2 \hat{a}_1^\dagger, \hat{\rho}] + \kappa (1 - \tau) \mathcal{D}[\hat{a}_1] \hat{\rho} + \kappa \mathcal{D}[\sqrt{\tau} \hat{a}_1 - \hat{a}_2] \hat{\rho}. \end{aligned} \quad (3.12)$$

Second, optical loss after the second node results in a limited detection efficiency $\eta \in (0, 1)$. Thus, it does not directly introduce additional decoherence but necessitates the use of longer measurement times during which other decoherence processes degrade the state.

Before we discuss the resulting effective equation governing the dynamics of the two qubits, we have to address one more point: the protocol for entanglement generation relies

on equal measurement rates for both qubits which guarantee that the states $|01\rangle$, $|10\rangle$ give rise to the same signal and are thus indistinguishable. Since part of the signal from the first qubit is lost due to the limited transmission between the systems, its effective measurement rate is reduced. We compensate this effect by reducing the coupling rate of the second qubit with respect to the coupling of the first qubit, $\chi_2 = \sqrt{\tau}\chi_1$; see section 3.4 for an in-depth discussion. With this adjustment, the effective conditional master equation reads

$$\begin{aligned} d\hat{\rho}_q = & \mathcal{L}_q\hat{\rho}_q dt + [(1-\tau)\Gamma_{\text{meas}} + \Gamma_{\text{mech}}]\mathcal{D}[\hat{\sigma}_z^1]\hat{\rho}_q dt + \tau\Gamma_{\text{mech}}\mathcal{D}[\hat{\sigma}_z^2]\hat{\rho}_q dt \\ & + \tau\Gamma_{\text{meas}}\mathcal{D}[\hat{\sigma}_z^1 + \hat{\sigma}_z^2]\hat{\rho}_q dt + \sqrt{\tau\eta\Gamma_{\text{meas}}}\mathcal{H}[\hat{\sigma}_z^1 + \hat{\sigma}_z^2]\hat{\rho}_q dW \end{aligned} \quad (3.13)$$

with Γ_{meas} and Γ_{mech} given in equation (3.10) and the measurement signal

$$Idt = 2\sqrt{\tau\eta\Gamma_{\text{meas}}}\langle\hat{\sigma}_z^1 + \hat{\sigma}_z^2\rangle dt + dW. \quad (3.14)$$

We see that optical loss between the two systems presents an additional dephasing channel for the first qubit and losses after the second system limit the detection efficiency.

3.2 EXPERIMENTAL REALIZATIONS

The discussion so far was completely general and did not assume any specific experimental realization. In this section, we consider several possible implementations as shown in figure 3.2: the most promising platform is provided by superconducting transmon qubits coupled to mechanical motion using a mechanically compliant gate capacitor [172, 180]. We further consider flux qubits where, following the proposal by Xue et al. [170], the mechanical oscillator forms a part of the qubit loop and experiences a qubit-state-dependent Lorentz force. Finally, solid-state spin qubits—such as magnetic levels of nitrogen–vacancy centres—can interact with mechanical oscillators via magnetic fields [192, 194, 248, 249]. Experimental parameters of the systems are summarized in table 3.1.

3.2.1 Transmon qubits

The first implementation uses superconducting transmon qubits that interact with mechanical oscillators via mechanically compliant gate capacitors, $C_g = C_g(\hat{x})$ [171, 172, 180]; see also chapter 1. The Hamiltonian for the qubit–mechanical system,

$$\hat{H} = \omega_m \hat{b}^\dagger \hat{b} + 4E_c(\hat{n} - n_0)^2 - E_J(\Phi_{\text{ext}}) \cos \hat{\varphi} - E_-(\Phi_{\text{ext}}) \sin \hat{\varphi} + \chi(\hat{n} - n_0)(\hat{b} + \hat{b}^\dagger), \quad (3.15)$$

has a nonzero transversal interaction in the diagonal basis of the qubit. To see how we can limit its contribution, we can rewrite the Josephson energy using the sum and difference of the Josephson energies of the two junctions $E_{J1,2}$; the Josephson energy is controlled using an external flux Φ_{ext} ,

$$E_J(\Phi_{\text{ext}}) = (E_{J1} + E_{J2}) \cos\left(\pi \frac{\Phi_{\text{ext}}}{\Phi_0}\right), \quad E_-(\Phi_{\text{ext}}) = (E_{J1} - E_{J2}) \sin\left(\pi \frac{\Phi_{\text{ext}}}{\Phi_0}\right), \quad (3.16)$$

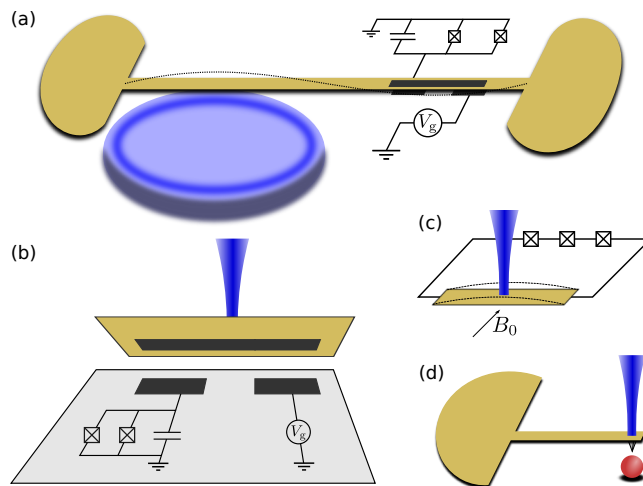


Figure 3.2: Illustrations of possible experimental realizations of the proposed scheme for entanglement generation. Transmon qubits can interact with mechanical oscillators via position-dependent gate capacitance; the mechanical oscillator can take the form of a nanobeam, which interacts with the near field of a toroidal optical resonator (a), or a membrane, which forms one end of a Fabry-Perot cavity or is placed in the middle of an optical cavity (b). Mechanical oscillators can further be integrated into the circuit of a flux qubit and, at the same time, form an end mirror of an optical cavity (c). The setups are not limited to superconducting systems; the qubit can also be formed by magnetic sublevels of a nitrogen-vacancy centre that interacts with the magnetic field of a cantilever with a magnetic tip (d). Superconducting circuits are indicated in black, nitrogen-vacancy centre in red, mechanical oscillators in yellow, and optical modes in blue.

where Φ_0 is the flux quantum. For flux $\Phi_{\text{ext}} = \Phi_0/2$ and equal Josephson energies $E_{J1} = E_{J2}$, the potential energy of the qubit in the Hamiltonian (3.15) is identically zero and the qubit Hamiltonian has only the longitudinal component,

$$H = \frac{\omega_q}{2} \hat{\sigma}_z + \omega_m \hat{b}^\dagger \hat{b} + \chi (\hat{b} + \hat{b}^\dagger) \hat{\sigma}_z. \quad (3.17)$$

Small discrepancies between the Josephson energies do not pose a problem; the resulting transversal coupling is weak and can be neglected in the rotating wave approximation.

The mechanical oscillator can take the form of a nanobeam interacting with an evanescent field of a microtoroidal cavity [122, 232]; see figure 3.2(a). In such a system, the opto- and electromechanical parts of the system are well spatially separated and photon absorption will not heat up the superconducting circuit. Alternatively, the mechanical oscillator can be a membrane forming an end of a Fabry-Perot cavity or placed in the middle of such an optical resonator as has been used in recent experimental demonstrations of microwave-to-optical conversion [82, 83]; cf. figure 3.2(b). Particularly the system of Andrews et al. [82], which uses a second harmonic mode of a membrane-in-the-middle setup with optical and microwave field interacting with different antinodes of motion, is well suited for the interface since it minimises optical heating of the superconducting circuit.

Quantity	Symbol	Transmon qubit			
		Nanobeam	Membrane	Flux qubit	NV centre
Qubit-mechanical coupling	$\chi/2\pi$	5.8 MHz	3.7 MHz	2.4 MHz	50 kHz
Mechanical frequency	$\omega_m/2\pi$	8.7 MHz	1.0 MHz	2.3 MHz	2.0 MHz
Effective mass	m	3.8 pg	30 ng	10 pg	25 pg
Mechanical quality factor	Q_m	5×10^4	5×10^5	10^5	10^4
Mechanical linewidth	$\gamma/2\pi$	170 Hz	2 Hz	22 Hz	200 Hz
Thermal occupation	\bar{n}	48	420	185	210
Optical quality factor	Q_{opt}	5×10^6	10^7	10^7	2×10^8
Optical decay rate	$\kappa/2\pi$	39 MHz	19 MHz	19 MHz	1 MHz
Single-photon optomechanical coupling	$g_0/2\pi$	300 Hz	25 Hz	65 Hz	20 Hz
Linearized optomechanical coupling	$g/2\pi$	900 kHz	140 kHz	450 kHz	300 kHz
Driving optical power	P	138 μW	300 μW	370 μW	90 μW
Optomechanical cooperativity	\bar{C}	10	5	10	8.5
Measurement rate	$\Gamma_{\text{meas}}/2\pi$	150 kHz	230 kHz	190 kHz	900 Hz
Measurement time	$1/\Gamma_{\text{meas}}$	1.1 μs	0.7 μs	0.8 μs	177 μs
Force sensitivity	S_F	130 aN/ $\sqrt{\text{Hz}}$	1.9 aN/ $\sqrt{\text{Hz}}$	38 aN/ $\sqrt{\text{Hz}}$	18 aN/ $\sqrt{\text{Hz}}$
Displacement sensitivity	S_x	11 am/ $\sqrt{\text{Hz}}$	1.6 am/ $\sqrt{\text{Hz}}$	18 am/ $\sqrt{\text{Hz}}$	4.1 am/ $\sqrt{\text{Hz}}$
Schematic figure		3.2(a)	3.2(b)	3.2(c)	3.2(d)

Table 3.1: Suggested experimental parameters for systems realizing the measurement of the total spin of two qubits. I consider transmon qubits (section 3.2.1) coupled to either nanobeams or vibrating membranes, flux qubits (section 3.2.2), and nitrogen-vacancy centres (section 3.2.3). For the thermal occupation of the mechanical bath, I assume that each system is cooled to 20 mK temperature. All setups are schematically depicted in figure 3.2.

Nanobeam mechanical oscillators We consider a silicon nitride beam of length $l = 70 \mu\text{m}$ that is $w = 400 \text{ nm}$ wide and $t = 100 \text{ nm}$ thick. The gate capacitor and the microtoroid are placed so that they both lie at the antinode of the second harmonic mode of frequency $\omega_m/2\pi \approx 8.7 \text{ MHz}$ with effective mass $m = 3.8 \text{ pg}$ and zero-point motion $x_{zpf} = 16 \text{ fm}$. If one third of the beam is covered by a superconductor, the gate capacitance $C_g = 275 \text{ aF}$ for a beam–circuit distance $d_q = 75 \text{ nm}$. Considering typical charging energy $E_c = 5 \text{ GHz}$ and gate voltage $V_g = 10 \text{ V}$, the qubit coupling $\chi/2\pi \approx 5.8 \text{ MHz}$. Our values of qubit coupling and mechanical frequency are somewhat lower than in a recent experiment by Pirkkalainen et al. [173] since our mechanical oscillator is smaller; reaching a coupling rate comparable with the mechanical frequency has, nevertheless, been demonstrated in their system.

The bare optomechanical coupling between an oscillating nanobeam and a toroidal optical cavity can reach values up to $g_0/2\pi = 20 \text{ kHz}$ [232]. Here, we consider a beam–toroid distance of $d_{om} = 50 \text{ nm}$ and a toroid with radius $r = 30 \mu\text{m}$ supporting optical resonance for the wavelength $\lambda = 1550 \text{ nm}$. These parameters result in moderate coupling of about $g_0/2\pi \approx 300 \text{ Hz}$. Driving the optical resonator with the power

$$P = \frac{1}{2} \hbar \frac{2\pi c}{\lambda} \kappa \left(\frac{g}{g_0} \right)^2 \approx 138 \mu\text{W} \quad (3.18)$$

for linewidth $\kappa/2\pi = 39 \text{ MHz}$ (toroidal whispering gallery resonators can reach decay rates an order of magnitude smaller [122]), we can reach the optomechanical coupling rate $g/2\pi \approx 900 \text{ kHz}$ and a measurement rate $\Gamma_{\text{meas}}/2\pi \approx 150 \text{ kHz}$, corresponding to a measurement time of about $1 \mu\text{s}$. Such a measurement is strong enough to be performed within the coherence time of transmon qubits, which is typically around $10 \mu\text{s}$ to $20 \mu\text{s}$ [92, 162].

Entanglement generation with nanobeam oscillators We study entanglement generation with the nanobeam mechanical oscillators in figure 3.3. To this end, we consider the following protocol for entanglement generation: measuring for time T , we accumulate the total signal $J(T) = \int_0^T dt I(t)$. We then compare this signal with a predefined postselection cutoff ν and keep the state if and only if $|J(T)| < \nu$. Two parameters are of interest to us—the entanglement of the resulting state and the success probability, that is, the probability of the signal being smaller than the cutoff. I discuss the protocol in more detail in section 3.5 and derive a simplified model that enables us to find the resulting state analytically without generating quantum trajectories.

In figure 3.3(a), I plot the concurrence [250] of the final state as a function of time: at early times, $t < \tau_{\text{meas}}/2$, the entanglement is limited by indistinguishability of the measurement outcomes resulting in an inconclusive measurement and a strongly mixed postselected state of the qubits. Next, the concurrence reaches its maximum around $t \sim \tau_{\text{meas}}$ and then steadily decays owing to dephasing and relaxation of the qubits. In the following, I consider the optimum value as a figure of merit characterizing the system.

In panel (b), I analyse how optical losses affect the concurrence. I consider the transmission losses between the two nodes (horizontal axis), as well as finite detection

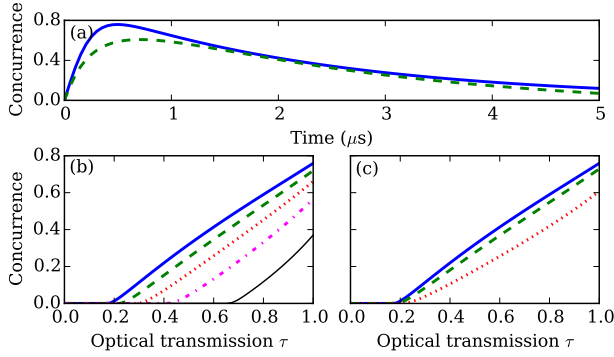


Figure 3.3: Entanglement generation with the nanobeam optomechanical transducer of figure 3.2(a). In panel (a), I show the time dependence of the concurrence for success probability $P_{\text{succ}} = 0.1$ (solid blue line) and $P_{\text{succ}} = 0.5$ (dashed green line). In the bottom panels, I plot the concurrence (optimized over the measurement time) versus optical transmission τ between the two nodes; in (b), the concurrence is shown for various detection efficiencies [$\eta = 1$ (solid blue line), $\eta = 0.8$ (dashed green line), $\eta = 0.6$ (dotted red line), $\eta = 0.4$ (dot-dashed magenta line), and $\eta = 0.2$ (thin black line)]; in (c), the plotted curves represent different success probabilities [$P_{\text{succ}} = 0.1$ (solid blue line), $P_{\text{succ}} = 0.3$ (dashed green line), and $P_{\text{succ}} = 0.5$ (dotted red line)]. I consider the qubit coupling $\chi/2\pi = 5.8$ MHz, mechanical frequency $\omega_m/2\pi = 8.7$ MHz and quality $Q_m = 5 \times 10^4$, optical decay rate $\kappa/2\pi = 39$ MHz, optomechanical coupling $g/2\pi = 900$ kHz, and temperature 20 mK (corresponding to thermal occupation $\bar{n} = 48$); I further assume the intrinsic relaxation and coherence lifetimes of the qubits $T_{1,2} = 20$ μs . Finally, I use the values $\tau = \eta = 1$ for panel (a), $P_{\text{succ}} = 0.1$ for (b), and $\eta = 1$ for (c).

efficiency (individual curves in the plot, see figure caption for more details). Remarkably, entanglement can be generated with up to 80 % transmission loss; with increased qubit lifetime and optomechanical cooperativity, it is possible to generate entanglement with even higher losses. Finally, in figure 3.3(c), the effect of transmission losses is investigated in combination with success probability of the postselection. While larger success probability generally leads to a smaller concurrence, it has little effect on the transmission loss for which the concurrence reaches zero.

Oscillating membranes For a system using a vibrating membrane, we consider a membrane-in-the-middle optomechanical system, similar to the recent experiment by Andrews et al. [82] with membrane dimensions $1 \text{ mm} \times 1 \text{ mm}$ and second harmonic frequency of $\omega_m/2\pi = 1$ MHz placed $d_q = 500$ nm from the gate capacitor with capacitance $C_g = 60$ fF. In such a system, qubit–mechanical coupling $\chi/2\pi = 3.7$ MHz can be achieved. (A similar value has been obtained in a recent experiment with significantly smaller oscillator [172].) With optomechanical coupling $g/2\pi = 140$ kHz and decay rate $\kappa/2\pi = 19$ MHz, the effective measurement rate can reach value of 230 kHz.

3.2.2 Flux qubits

For measurements with flux qubits, we consider the magnetomechanical qubit coupling proposed by Xue et al. [170]; see figure 3.2(c). The mechanical oscillator forms a part of the qubit loop and its fundamental out-of-plane mode is excited by applying an external magnetic field B_0 . The current in the qubit loop results in a Lorentz force in the suspended part of the loop (i.e., the mechanical oscillator); the direction of the force depends on the direction in which the current is running. The coupling rate is given by

$$\chi = B_0 I_p l_{\text{eff}} x_{\text{zpf}}, \quad (3.19)$$

where I_p is the persistent current in the qubit loop (typically 500 nA) and l_{eff} is the effective length of the mechanical oscillator.

We consider a 12 μm -long bridge resulting in mechanical frequency $\omega_m/2\pi = 2.3$ MHz, effective mass $m = 10$ pg, and coupling rate $\chi/2\pi = 2.3$ MHz, which is somewhat smaller than in the proposal of Xue et al. [170]. The bridge can form one end of a Fabry-Perot cavity; with coupling rate $g/2\pi = 450$ kHz and optical decay rate $\kappa/2\pi = 19$ MHz, the effective measurement rate is $\Gamma_{\text{meas}}/2\pi = 190$ kHz. Since lifetimes of flux qubits are shorter than those of transmons (typically around 5 μs), weaker entanglement will be generated with such a system. Moreover, due to the integration of the mechanical oscillator into the superconducting circuit as well as the optomechanical Fabry-Perot cavity, optical absorption will lead to unwanted heating of the circuit.

3.2.3 Nitrogen-vacancy centres

The protocol for entanglement generation is not limited to superconducting systems. Here, we consider entanglement of the magnetic sublevels of electron spins in nitrogen-vacancy centres using the transducer schematically depicted in figure 3.2(d). Each qubit interacts with a cantilever with a magnetic tip and, at the same time, the cantilever works as an end mirror in a Fabry-Perot optical cavity.

In such a system, magnetomechanical coupling $\chi/2\pi = 50$ kHz can be reached [194, 248]. For mechanical frequency $\omega_m/2\pi = 2$ MHz, optomechanical coupling $g/2\pi = 300$ kHz, and optical linewidth $\kappa/2\pi = 1$ MHz (thus requiring extremely high-quality Fabry-Perot resonator), the effective measurement rate is about $\Gamma_{\text{meas}}/2\pi = 0.9$ kHz, requiring qubit lifetime on the order of milliseconds; such values of the magnetomechanical coupling, cavity decay rate, and nitrogen-vacancy centre dephasing time put very strong requirements on the fabrication of the system.

Alternatively, other kinds of solid-state spins can be used. For instance, the coherence lifetime of phosphorus donors in silicon can reach several seconds [251]. With such systems, the requirements on the magnetomechanical coupling and the optical decay can be somewhat relaxed. If we consider the values $\chi/2\pi = 10$ kHz, $\kappa/2\pi = 10$ MHz (with other parameters same as before), the qubit measurement rate $\Gamma_{\text{meas}}/2\pi = 3$ Hz, corresponding to a measurement time of about 50 ms.

Strategy	Measurement rate	Dephasing rate	Conditions for efficient readout
Basic approach	$16 \frac{\chi^2 g^2}{\kappa \omega_m^2}$	$\frac{\chi^2 \gamma}{\omega_m^2} (2\bar{n} + 1)$	$\frac{4g^2}{\kappa \gamma \bar{n}} > \frac{1}{2}$
Modulated coupling	$16 \frac{\chi^2 g^2}{\kappa \gamma^2}$	$\frac{\chi^2}{\gamma} (2\bar{n} + 1)$	$\frac{4g^2}{\kappa \gamma (2\bar{n} + 1)} > \frac{1}{4}$
Modulated coupling with squeezing	$16 \frac{\chi^2 g_1^2}{\kappa \gamma^2}$	$\frac{\chi^2}{\gamma} \left(1 - 32 \frac{g_1 g_2}{\gamma \kappa} \right) (2\bar{n} + 1)$	$\frac{4g_1^2}{\kappa \gamma (2\bar{n} + 1)} + 2 \frac{4g_1 g_2}{\kappa \gamma} > \frac{1}{4}$
Microwave cavity	$256 \frac{\chi^2 g_a^2 g_c^2}{\kappa_a^2 \omega_m^2 \kappa_c}$	$4 \frac{\chi^2}{\kappa_a} + 256 \frac{\chi^2 g_a^4}{\kappa_a^3 \omega_m^2} + 16 \frac{\chi^2 g_a^2 \gamma}{\kappa_a^2 \omega_m^2} (2\bar{n} + 1)$	$\frac{4g_c^2}{\kappa_c \gamma \bar{n}} > \frac{1}{2}$, $\frac{g_c^2}{\kappa_c} > \frac{g_a^2}{\kappa_a}$, $\frac{4g_a^2}{\kappa_a \gamma} \frac{4g_c^2}{\kappa_c \gamma} > \frac{1}{4} Q_m^2$
Microwave cavity and modulated coupling	$1024 \frac{\chi^2 g_a^2 g_c^2}{\kappa_a^2 \gamma^2 \kappa_c}$	$4 \frac{\chi^2}{\kappa_a} + 64 \frac{\chi^2 g_a^2}{\kappa_a^2 \gamma} (2\bar{n} + 1)$	$\frac{4g_c^2}{\kappa_c \gamma (2\bar{n} + 1)} > \frac{1}{4}$, $\frac{4g_a^2}{\kappa_a \gamma} \frac{4g_c^2}{\kappa_c \gamma} > \frac{1}{16}$

Table 3.2: A summary of the measurement rates, dephasing rates, and conditions for efficient readout for the various strategies for entanglement generation. I compare the basic scheme (described in section 3.1) with the approach using modulated coupling (section 3.3.1), protocol where the coupling between the qubit and the mechanical oscillator is mediated by a microwave resonator (section 3.3.2), and a strategy that combines modulated coupling and the use of a microwave cavity (section 3.3.3). On top of the conditions listed here, the measurement rate has to exceed the intrinsic qubit lifetime for each of the strategies.

3.3 ALTERNATIVE SCHEMES

Coupling superconducting qubits directly to mechanical oscillators comes with a significant disadvantage: the readout is slow because the quasi-static force the qubit exerts on the mechanical oscillator is not resonant with the natural frequency of the mechanical motion. This problem can be alleviated by modulating the coupling at the mechanical frequency. In the rotating frame of the mechanical oscillator, such modulation results in a resonant interaction between the qubit, mechanical oscillator, and cavity field; this modification greatly enhances the speed of the qubit readout.

Second, placing the qubit in free space—thus coupling it to a continuum of electromagnetic modes—significantly decreases its lifetime. If the qubit were placed in a cavity with a different resonance frequency, the lifetime would be enhanced by the Purcell effect. The output of the microwave resonator will, however, serve as an additional dephasing channel for the qubit. An important question arises whether efficient entanglement generation is possible in this case.

I analyse these alternative schemes in this section. I start by the scheme where the coupling is modulated at the mechanical frequency, leading to quantum nondemolition coupling. Next, I analyse the strategy where the qubit is first coupled to a microwave resonator which then interacts with the mechanical oscillator and show that qubit dephasing associated with the decay of the microwave cavity dominates the dynamics. Finally, to avoid the resonantly enhanced dephasing of the qubit through the microwave output, I consider an approach where the coupling is modulated to achieve a quantum nondemolition interaction between the qubit, microwave resonator, mechanical oscillator, and optical cavity. The main parameters of the protocols (i.e., the measurement rates, dephasing rates, and conditions for efficient optical readout of the qubit state) are summarized in table 3.2.

3.3.1 Quantum nondemolition interaction

We start with a scheme where the coupling of the optical cavity and the qubit to the mechanical oscillator is modulated at the mechanical frequency. In an optomechanical system, such modulation can be introduced by driving the cavity (which is in the resolved-sideband regime, $\omega_m > \kappa$) at both mechanical sidebands. If the sidebands are driven with the same amplitude, backaction-evading measurement of a single mechanical quadrature can be performed [101, 124, 125]; the use of unequal driving amplitudes leads to squeezing of the light field [103] or of the mechanical oscillator [102, 252]. Additionally, modulation of the qubit coupling is achieved by driving the qubit with time-dependent gate voltage [176].

When the optical cavity is driven on both sidebands with equal amplitudes, the linearized optomechanical coupling rate in the laboratory frame is given by $g(t) = -2g \sin(\omega_m t)$. Similarly, modulating the gate voltage of the qubit, $V_g(t) = V_0 + V_1 \cos(\omega_m t)$, results in qubit-mechanical coupling

$$\chi(t) = 2E_c \frac{C_g V_0}{e} \frac{x_{zpf}}{d} + 2E_c \frac{C_g V_1}{e} \frac{x_{zpf}}{d} \cos(\omega_m t) = \chi_0 + \chi \cos(\omega_m t). \quad (3.20)$$

The overall Hamiltonian for a single system is

$$\hat{H} = \frac{\omega_q}{2} \hat{\sigma}_z + \omega_m \hat{b}^\dagger \hat{b} + \chi(t) \hat{\sigma}_z (\hat{b} + \hat{b}^\dagger) + g(t) (\hat{a} + \hat{a}^\dagger) (\hat{b} + \hat{b}^\dagger). \quad (3.21)$$

Moving to the rotating frame with respect to the free Hamiltonian $\hat{H}_0 = \frac{1}{2} \omega_q \hat{\sigma}_z + \omega_m \hat{b}^\dagger \hat{b}$ and applying the rotating wave approximation, we get the interaction-picture Hamiltonian

$$\hat{H} = \frac{\chi}{2} \hat{\sigma}_z (\hat{b} + \hat{b}^\dagger) - ig (\hat{a} + \hat{a}^\dagger) (\hat{b} - \hat{b}^\dagger). \quad (3.22)$$

Here, the relative phase between the optical drives and the voltage modulation is chosen such that the qubit and cavity field couple to orthogonal mechanical quadratures. The information about the qubit state is thus imprinted on the momentum quadrature of the mechanical oscillator which is then read out optically; homodyne detection of the output phase quadrature reveals this state.

We can adiabatically eliminate the mechanical and optical degrees of freedom in analogy with the previous case; the resulting two-qubit equation reads

$$\begin{aligned} d\hat{\rho}_q = & \mathcal{L}_q \hat{\rho}_q dt + \frac{\chi^2}{\gamma} (2\bar{n} + 1) \{ \mathcal{D}[\hat{\sigma}_z^1] + \mathcal{D}[\hat{\sigma}_z^2] \} \hat{\rho}_q dt \\ & + 16 \frac{\chi^2 g^2}{\gamma^2 \kappa} \mathcal{D}[\hat{\sigma}_z^1 + \hat{\sigma}_z^2] \hat{\rho}_q dt + \sqrt{16 \frac{\chi^2 g^2}{\gamma^2 \kappa}} \mathcal{H}[\hat{\sigma}_z^1 + \hat{\sigma}_z^2] \hat{\rho}_q dW. \end{aligned} \quad (3.23)$$

The measurement and dephasing rates differ from the previous case by a factor of Q_m^2 . The measurement is thus significantly faster while keeping the dephasing induced by the mechanical bath low; the measurement rate dominates over the dephasing for strong optomechanical cooperativity, $4g^2/[\kappa\gamma(2\bar{n} + 1)] > \frac{1}{4}$.

When the mechanical sidebands of the cavity are not driven with the same amplitude, the cavity field couples, in the rotating frame, to both mechanical quadratures,

$$\hat{H}_{\text{om}} = -g_1 (\hat{a} + \hat{a}^\dagger) (\hat{b} + \hat{b}^\dagger) + g_2 (\hat{a} - \hat{a}^\dagger) (\hat{b} - \hat{b}^\dagger). \quad (3.24)$$

The coupling rates depend on the coupling of the sidebands; we have $g_1 = g_+ + g_-$, $g_2 = g_- - g_+$, where, g_- (g_+) is the coupling of the lower (upper) motional sideband to the mechanical oscillator and we assume $g_- > g_+$ to ensure stability. Furthermore, we assume $g_{1,2} > 0$ without loss of generality. Such interaction can be used to squeeze the mechanical motion [102]; it is natural to expect that if the qubit couples to the squeezed mechanical quadratures, its readout will be improved compared to the unsqueezed motion.

To check this expectation, we write the Hamiltonian for a single system,

$$\hat{H} = -\frac{i\chi}{2} \hat{\sigma}_z (\hat{b} - \hat{b}^\dagger) - g_1 (\hat{a} + \hat{a}^\dagger) (\hat{b} + \hat{b}^\dagger) + g_2 (\hat{a} - \hat{a}^\dagger) (\hat{b} - \hat{b}^\dagger), \quad (3.25)$$

and adiabatically eliminate the optomechanical transducer. The resulting stochastic master equation reads

$$\begin{aligned} d\hat{\rho}_q = & \mathcal{L}_q \hat{\rho}_q dt + \frac{\chi^2}{\gamma} \left(1 - 32 \frac{g_1 g_2}{\gamma \kappa} \right) (2\bar{n} + 1) \{ \mathcal{D}[\hat{\sigma}_z^2] + \mathcal{D}[\hat{\sigma}_z^2] \} \hat{\rho}_q dt \\ & + 16 \frac{\chi^2 g_1^2}{\gamma^2 \kappa} \mathcal{D}[\hat{\sigma}_z^1 + \hat{\sigma}_z^2] \hat{\rho}_q dt + \sqrt{16 \frac{\chi^2 g_1^2}{\gamma^2 \kappa}} \mathcal{H}[\hat{\sigma}_z^1 + \hat{\sigma}_z^2] \hat{\rho}_q dW. \end{aligned} \quad (3.26)$$

The optomechanical interaction described by the Hamiltonian (3.24) indeed reduces noise in the mechanical momentum quadrature which, in turn, reduces dephasing of the qubits; the measurement rate is not affected by the squeezing since it depends on the first term in equation (3.24) only. Equation (3.26) is valid only for weak optomechanical coupling, $g_1 g_2 < \gamma \kappa$, which can be fulfilled since g_2 is given by the difference of the coupling rates of the sidebands.

3.3.2 Coupling via a microwave cavity

When the coupling between the qubit and mechanical oscillator is mediated by a microwave resonator, the Hamiltonian takes the form

$$\hat{H} = \chi \hat{\sigma}_z (\hat{a} + \hat{a}^\dagger) - i g_a (\hat{a} - \hat{a}^\dagger) (\hat{b} + \hat{b}^\dagger) + \omega_m \hat{b}^\dagger \hat{b} + g_c (\hat{c} + \hat{c}^\dagger) (\hat{b} + \hat{b}^\dagger); \quad (3.27)$$

now, \hat{a} is the annihilation operator for the microwave field and the annihilation operator for the optical cavity is denoted by \hat{c} . Interaction of the qubit and the mechanical oscillator with orthogonal microwave quadratures can be achieved if the qubit couples longitudinally to the microwave resonator in the laboratory frame, $\hat{H}_{\text{int}} = \chi \hat{\sigma}_z (\hat{a} + \hat{a}^\dagger)$ [163, 164]. If we now strongly drive the cavity and move to the displaced frame, $\hat{a} \rightarrow \alpha + \hat{a}$, the coupling is unchanged since the drive results merely in a constant energy offset for the qubit, $\delta\omega_q = \chi(\alpha + \alpha^*)$. The microwave quadrature which interacts with the mechanical oscillator, on the other hand, is determined by the phase of the driving field; it is thus possible for the qubit and the mechanical oscillator to couple to orthogonal microwave quadratures. Finally, the longitudinal interaction between the qubit and microwave field can be made resonant in the rotating frame if suitable modulation of the coupling rate is used [165].

After adiabatic elimination of the optomechanical transducers (now consisting of the microwave, optical, and mechanical modes; we also assume that each microwave resonator couples to a vacuum bath), the effective equation of motion for the qubits reads

$$\begin{aligned} d\hat{\rho}_q = & \mathcal{L}_q \hat{\rho}_q dt + \left[4 \frac{\chi^2}{\kappa_a} + 256 \frac{\chi^2 g_a^4}{\kappa_a^3 \omega_m^2} + 16 \frac{\chi^2 g_a^2 \gamma}{\kappa_a^2 \omega_m^2} (2\bar{n} + 1) \right] \{ \mathcal{D}[\hat{\sigma}_z^1] + \mathcal{D}[\hat{\sigma}_z^2] \} \hat{\rho}_q dt \\ & + 256 \frac{\chi^2 g_a^2 g_c^2}{\kappa_a^2 \omega_m^2 \kappa_c} \mathcal{D}[\hat{\sigma}_z^1 + \hat{\sigma}_z^2] \hat{\rho}_q dt + \sqrt{256 \frac{\chi^2 g_a^2 g_c^2}{\kappa_a^2 \omega_m^2 \kappa_c}} \mathcal{H}[\hat{\sigma}_z^1 + \hat{\sigma}_z^2] \hat{\rho}_q dW. \end{aligned} \quad (3.28)$$

The presence of the microwave cavity results in two additional dephasing channels for the qubit (described by the first two terms in the square bracket): the first dephasing process

corresponds to the signal from the qubit leaving directly through the microwave output port; the second channel describes the signal reflected by the mechanical oscillator. It travels to the mechanical oscillator where it is converted back to microwaves, which then decay to the microwave bath.

The latter process can be suppressed if the mechanical oscillator couples more strongly to the optical output than to the microwave output, $g_c^2/\kappa_c > g_a^2/\kappa_a$. The former channel presents a more considerable challenge—it is the only dephasing process that is resonant (i.e., independent of the mechanical frequency). If the measurement is to dominate over this dephasing, the condition

$$\frac{4g_a^2}{\kappa_a\gamma} \frac{4g_c^2}{\kappa_c\gamma} > \frac{1}{4} Q_m^2 \quad (3.29)$$

has to be satisfied. With current experimental technology, this condition is virtually impossible to fulfil.

3.3.3 Combining microwave cavity and modulated coupling

Finally, we can combine the two approaches discussed above in a single system—the qubit interacts with a microwave cavity which is driven on both sidebands to realize nondemolition coupling to the mechanical oscillator. The optical cavity is driven the same way so we obtain a quantum nondemolition interaction of the qubit, microwave resonator, mechanical oscillator, and optical cavity. In the ideal case (i.e., within validity of the rotating wave approximation, $\kappa_{a,c} < \omega_m$), the interaction is described by the Hamiltonian

$$\hat{H} = \chi \hat{\sigma}_z (\hat{a} + \hat{a}^\dagger) - i g_a (\hat{a} - \hat{a}^\dagger) (\hat{b} + \hat{b}^\dagger) - i g_c (\hat{c} + \hat{c}^\dagger) (\hat{b} - \hat{b}^\dagger). \quad (3.30)$$

Adiabatic elimination of the microwave, optical, and mechanical degrees of freedom results in the stochastic master equation

$$\begin{aligned} d\hat{\rho}_q = & \mathcal{L}_q \hat{\rho}_q dt + \left[4 \frac{\chi^2}{\kappa_a} + 64 \frac{\chi^2 g_a^2}{\kappa_a^2 \gamma} (2\bar{n} + 1) \right] \{ \mathcal{D}[\hat{\sigma}_z^1] + \mathcal{D}[\hat{\sigma}_z^2] \} \hat{\rho}_q dt \\ & + 1024 \frac{\chi^2 g_a^2 g_c^2}{\kappa_a^2 \gamma^2 \kappa_c} \mathcal{D}[\hat{\sigma}_z^1 + \hat{\sigma}_z^2] \hat{\rho}_q dt + \sqrt{1024 \frac{\chi^2 g_a^2 g_c^2}{\kappa_a^2 \gamma^2 \kappa_c}} \mathcal{H}[\hat{\sigma}_z^1 + \hat{\sigma}_z^2] \hat{\rho}_q dW. \end{aligned} \quad (3.31)$$

There is now one dephasing channel less than in the previous case, equation (3.28), since the signal that enters the mechanical oscillator leaves through either the mechanical bath or the optical cavity and cannot be reflected back to the microwave resonator. The dephasing through the measurement channel dominates over the mechanical and microwave dephasing if

$$\frac{4g_c^2}{\kappa_c\gamma(2\bar{n}+1)} > \frac{1}{4}, \quad \frac{4g_a^2}{\kappa_a\gamma} \frac{4g_c^2}{\kappa_c\gamma} > \frac{1}{16}. \quad (3.32)$$

Additionally, the measurement rate also has to be larger than the intrinsic relaxation and dephasing rates of the qubits; this condition can be fulfilled more easily since the measurement rate is increased by a factor of Q_m^2 compared to the case of non-resonant qubit and mechanical oscillator.

3.4 DERIVATION OF EFFECTIVE EQUATIONS OF MOTION

In this section, I derive the effective equation (3.13) governing the dynamics of two qubits under continuous measurement by optomechanical transducers. To this end, I start by considering a single node and show how to adiabatically eliminate the mechanical and optical degrees of freedom. Then, I discuss the case of two such systems connected by a directional optical link; after treating the case of an ideal system without optical losses, I analyse the role of imperfections, specifically the presence of optical loss and asymmetry in the parameters of the two transducers.

3.4.1 Single-qubit readout

To derive an effective equation of motion for a single qubit, we start from the stochastic master equation for the qubit coupled to a transducer,

$$d\hat{\rho} = -i[\hat{H}, \hat{\rho}]dt + \mathcal{L}_q \hat{\rho} dt + \gamma\{(\bar{n} + 1)\mathcal{D}[\hat{b}] + \bar{n}\mathcal{D}[\hat{b}^\dagger]\}\hat{\rho} dt + \kappa\mathcal{D}[\hat{a}]\hat{\rho} dt + \sqrt{\kappa}\mathcal{H}[\hat{a}e^{i\phi}]\hat{\rho} dW \quad (3.33)$$

with the Hamiltonian $\hat{H} = \chi(\hat{b} + \hat{b}^\dagger)\hat{\sigma}_z + \omega_m\hat{b}^\dagger\hat{b} + g(\hat{a} + \hat{a}^\dagger)(\hat{b} + \hat{b}^\dagger)$. To adiabatically eliminate the mechanical and optical degrees of freedom, we consider the equation governing the dynamics of the transducer

$$d\hat{\rho}_T = -i[\omega_m\hat{b}^\dagger\hat{b} + g(\hat{a} + \hat{a}^\dagger)(\hat{b} + \hat{b}^\dagger), \hat{\rho}_T]dt + \gamma\{(\bar{n} + 1)\mathcal{D}[\hat{b}] + \bar{n}\mathcal{D}[\hat{b}^\dagger]\}\hat{\rho}_T dt + \kappa\mathcal{D}[\hat{a}]\hat{\rho}_T dt + \sqrt{\kappa}\mathcal{H}[\hat{a}e^{i\phi}]\hat{\rho}_T dW, \quad (3.34)$$

where I use the subscript T to remind us that the density matrix $\hat{\rho}_T$ describes the state of the transducer. Since the dynamics are linear, the state is fully described by the first and second statistical moments of the canonical operators which we collect in the vector

$$\hat{\mathbf{r}} = \frac{1}{\sqrt{2}}[\hat{a} + \hat{a}^\dagger, -i(\hat{a} - \hat{a}^\dagger), \hat{b} + \hat{b}^\dagger, -i(\hat{b} - \hat{b}^\dagger)]^T. \quad (3.35)$$

The covariance matrix of the conditional state of the transducer obeys the Riccati equation

$$\dot{\mathbf{\Gamma}}^c = \mathbf{A}\mathbf{\Gamma}^c + \mathbf{\Gamma}^c\mathbf{A}^T + 2\mathbf{N} - 2(\mathbf{\Gamma}^c\mathbf{c} - \mathbf{\sigma m})(\mathbf{\Gamma}^c\mathbf{c} - \mathbf{\sigma m})^T, \quad (3.36a)$$

$$\mathbf{A} = \begin{pmatrix} -\frac{\kappa}{2} & 0 & 0 & 0 \\ 0 & -\frac{\kappa}{2} & -2g & 0 \\ 0 & 0 & -\frac{\gamma}{2} & \omega_m \\ -2g & 0 & -\omega_m & -\frac{\gamma}{2} \end{pmatrix}, \quad (3.36b)$$

$$\mathbf{N} = \text{diag}\left[\frac{\kappa}{2}, \frac{\kappa}{2}, \gamma\left(\bar{n} + \frac{1}{2}\right), \gamma\left(\bar{n} + \frac{1}{2}\right)\right], \quad (3.36c)$$

$$\mathbf{c} = \frac{\kappa}{\sqrt{2}}(\cos\phi, -\sin\phi, 0, 0)^T, \quad (3.36d)$$

$$\mathbf{m} = \frac{\kappa}{\sqrt{2}}(\sin\phi, \cos\phi, 0, 0)^T; \quad (3.36e)$$

see also chapter 2. On the other hand, the unconditional state of the transducer follows the deterministic master equation

$$\begin{aligned} \frac{d\hat{\rho}_T^u}{dt} = & -i[\omega_m \hat{b}^\dagger \hat{b} + g(\hat{a} + \hat{a}^\dagger)(\hat{b} + \hat{b}^\dagger), \hat{\rho}_T^u] + \gamma\{(\bar{n} + 1)\mathcal{D}[\hat{b}] + \bar{n}\mathcal{D}[\hat{b}^\dagger]\}\hat{\rho}_T^u \\ & + \kappa\mathcal{D}[\hat{a}]\hat{\rho}_T^u; \end{aligned} \quad (3.37)$$

the corresponding covariance matrix obeys the Lyapunov equation

$$\dot{\mathbf{\Gamma}}^u = \mathbf{A}\mathbf{\Gamma}^u + \mathbf{\Gamma}^u\mathbf{A}^T + 2\mathbf{N}. \quad (3.38)$$

The Riccati and Lyapunov equations, (3.36a), (3.38), can be solved analytically in the limit of weak optomechanical coupling, $g < \kappa$, but I omit the resulting expressions since they are too cumbersome. The solution, together with the general expression for the effective equation presented in chapter 2 gives the equation

$$d\hat{\rho}_q = \mathcal{L}_q\hat{\rho}_q dt + (\Gamma_{\text{meas}} + \Gamma_{\text{mech}})\mathcal{D}[\hat{\sigma}_z]\hat{\rho}_q dt + \sqrt{\Gamma_{\text{meas}}}\mathcal{H}[\hat{\sigma}_z]\hat{\rho}_q dW, \quad (3.39)$$

where the measurement and dephasing rates Γ_{meas} , Γ_{mech} are given by equations (3.10).

3.4.2 Two-qubit measurement

When two such systems are cascaded, the dynamics are described by the equation

$$\begin{aligned} d\hat{\rho} = & -i[\hat{H}, \hat{\rho}]dt + \mathcal{L}_q\hat{\rho}dt + \sum_{j=1}^2 \gamma\{(\bar{n} + 1)\mathcal{D}[\hat{b}_j] + \bar{n}\mathcal{D}[\hat{b}_j^\dagger]\}\hat{\rho}dt \\ & + \kappa\mathcal{D}[\hat{a}_1 - \hat{a}_2]\hat{\rho}dt + \sqrt{\kappa}\mathcal{H}[(\hat{a}_1 - \hat{a}_2)e^{i\phi}]\hat{\rho}dW \end{aligned} \quad (3.40)$$

with the Hamiltonian

$$\hat{H} = \sum_{j=1}^2 [\chi\hat{\sigma}_z^j(\hat{b}_j + \hat{b}_j^\dagger) + \omega_m \hat{b}_j^\dagger \hat{b}_j + g(\hat{a}_j + \hat{a}_j^\dagger)(\hat{b}_j + \hat{b}_j^\dagger)] + \frac{i\kappa}{2}(\hat{a}_1\hat{a}_2^\dagger - \hat{a}_2\hat{a}_1^\dagger). \quad (3.41)$$

Apart from the local dynamics of the two nodes—given by the square bracket in the Hamiltonian (3.41) and by the dissipation of the qubits and the mechanical oscillators—there is the unidirectional coupling of the optical cavities. This effect appears in the form of the last term in the Hamiltonian (3.41) and in the Lindblad and measurement terms which now describe the joint decay and measurement of the two cavity modes [214]. (The minus sign in the Lindblad and measurement terms is due to our choice of the relative phase between the two cavity fields; see the discussion below.) For the moment, we assume that the two qubit–oscillator–cavity systems are identical and can be described by the same frequencies, coupling constants, and decoherence rates.

After adiabatically eliminating the mechanical and optical degrees of freedom (in complete analogy with the single-qubit readout), the effective two-qubit equation takes the form

$$\begin{aligned} d\hat{\rho}_q = & \mathcal{L}_q\hat{\rho}_q dt + \Gamma_{\text{mech}}\{\mathcal{D}[\hat{\sigma}_z^1] + \mathcal{D}[\hat{\sigma}_z^2]\}\hat{\rho}_q dt + \Gamma_{\text{meas}}\mathcal{D}[\hat{\sigma}_z^1 + \hat{\sigma}_z^2]\hat{\rho}_q dt \\ & + \sqrt{\Gamma_{\text{meas}}}\mathcal{H}[\hat{\sigma}_z^1 + \hat{\sigma}_z^2]\hat{\rho}_q dW. \end{aligned} \quad (3.42)$$

Here, the relative phase between the two qubits in the measurement and two-qubit dephasing terms is set by the phase between the two cavities in the Hamiltonian $\hat{H}_{\text{casc}} = \frac{1}{2}i\kappa(\hat{a}_1\hat{a}_2^\dagger - \hat{a}_2\hat{a}_1^\dagger)$ and the Lindblad term $\mathcal{D}[\hat{a}_1 - \hat{a}_2]\hat{\rho}$; this phase can be controlled by applying an additional phase shift to the light field between the cavities. The relevant choices are $\hat{\sigma}_z^1 + \hat{\sigma}_z^2$ [which can be used to generate the entangled state $|\Psi_+\rangle = (|01\rangle + |10\rangle)/\sqrt{2}$] and $\hat{\sigma}_z^1 - \hat{\sigma}_z^2$ [with which the state $|\Phi_+\rangle = (|00\rangle + |11\rangle)/\sqrt{2}$ can be prepared]; the latter measurement can be obtained from the former one by applying a π phase shift between the cavities, $\hat{a}_2 \rightarrow -\hat{a}_2$. Any other phase results in the signals from the two qubits appearing in different quadratures.

With optical losses in the channel between the cavities and limited detection efficiency, the overall dynamics are described by the equation

$$\begin{aligned} d\hat{\rho} = & -i[\hat{H}, \hat{\rho}]dt + \mathcal{L}_q\hat{\rho}dt + \sum_{j=1}^2 \gamma_j \{(\bar{n}_j + 1)\mathcal{D}[\hat{b}_j] + \bar{n}_j\mathcal{D}[\hat{b}_j^\dagger]\}\hat{\rho}dt \\ & + \kappa_1(1 - \tau)\mathcal{D}[\hat{a}_1]\hat{\rho}dt + \mathcal{D}[\sqrt{\kappa_1\tau}\hat{a}_1 - \sqrt{\kappa_2}\hat{a}_2]\hat{\rho}dt \\ & + \sqrt{\eta}\mathcal{H}[(\sqrt{\kappa_1\tau}\hat{a}_1 - \sqrt{\kappa_2}\hat{a}_2)e^{i\phi}]\hat{\rho}dW \end{aligned} \quad (3.43)$$

where the Hamiltonian takes the form

$$\begin{aligned} \hat{H} = & \sum_{j=1}^2 [\chi_j \hat{\sigma}_z^j (\hat{b}_j + \hat{b}_j^\dagger) + \omega_{m,j} \hat{b}_j^\dagger \hat{b}_j + g_j (\hat{a}_j + \hat{a}_j^\dagger) (\hat{b}_j + \hat{b}_j^\dagger)] \\ & - \frac{i}{2} \sqrt{\kappa_1 \kappa_2 \tau} (\hat{a}_1^\dagger \hat{a}_2 - \hat{a}_2^\dagger \hat{a}_1). \end{aligned} \quad (3.44)$$

Here, $\tau \in (0, 1]$ is the transmittance of the channel between the two cavities (including optical losses in the first cavity) and $\eta \in (0, 1]$ is the detection efficiency (it includes any optical losses in and after the second cavity). Furthermore, I now assume different parameters for the two qubits, mechanical oscillators, and optical cavities. The effective two-qubit equation of motion takes the form

$$\begin{aligned} d\hat{\rho}_q = & \mathcal{L}_q\hat{\rho}_qdt + 16(1 - \tau) \frac{\chi_1^2 g_1^2}{\kappa_1 \omega_{m,1}^2} \mathcal{D}[\hat{\sigma}_z^1]\hat{\rho}_qdt + \sum_{j=1}^2 \frac{\chi_j^2 \gamma_j (2\bar{n}_j + 1)}{\omega_{m,j}^2} \mathcal{D}[\hat{\sigma}_z^j]\hat{\rho}_qdt \\ & + \mathcal{D} \left[\sqrt{16\tau \frac{\chi_1^2 g_1^2}{\kappa_1 \omega_{m,1}^2}} \hat{\sigma}_z^1 + \sqrt{16 \frac{\chi_2^2 g_2^2}{\kappa_2 \omega_{m,2}^2}} \hat{\sigma}_z^2 \right] \hat{\rho}_qdt \\ & + \sqrt{\eta}\mathcal{H} \left[\sqrt{16\tau \frac{\chi_1^2 g_1^2}{\kappa_1 \omega_{m,1}^2}} \hat{\sigma}_z^1 + \sqrt{16 \frac{\chi_2^2 g_2^2}{\kappa_2 \omega_{m,2}^2}} \hat{\sigma}_z^2 \right] \hat{\rho}_qdW. \end{aligned} \quad (3.45)$$

For a total-spin measurement, we require that both qubits be measured at the same rate, $\tau \chi_1^2 g_1^2 / \kappa_1 \omega_{m,1}^2 = \chi_2^2 g_2^2 / \kappa_2 \omega_{m,2}^2$. For most implementations, the easiest way to fulfil this condition is to tune the coupling (the qubit–mechanical coupling can usually be tuned using external fields, similar to the optomechanical coupling). I consider tuning the coupling of the second qubit, $\chi_2 = \sqrt{\tau} \chi_1$, since enhancing any of the coupling strengths

in the first node would increase the dephasing rate of the first qubit; furthermore, the reduction of the qubit coupling (compared to reducing the optomechanical coupling) also reduces the dephasing of the second qubit. The resulting equation of motion is

$$\begin{aligned}
d\hat{\rho}_q &= \mathcal{L}_q \hat{\rho}_q dt + \left[16(1-\tau) \frac{\chi^2 g^2}{\kappa \omega_m^2} + \frac{\chi^2 \gamma (2\bar{n} + 1)}{\omega_m^2} \right] \mathcal{D}[\hat{\sigma}_z^1] \hat{\rho}_q dt \\
&+ \frac{\tau \chi^2 \gamma (2\bar{n} + 1)}{\omega_m^2} \mathcal{D}[\hat{\sigma}_z^2] \hat{\rho}_q dt + 16\tau \frac{\chi^2 g^2}{\kappa \omega_m^2} \mathcal{D}[\hat{\sigma}_z^1 + \hat{\sigma}_z^2] \hat{\rho}_q dt \\
&+ \sqrt{16\tau\eta} \frac{\chi^2 g^2}{\kappa \omega_m^2} \mathcal{H}[\hat{\sigma}_z^1 + \hat{\sigma}_z^2] \hat{\rho}_q dW \\
&= \mathcal{L}_q \hat{\rho}_q dt + [(1-\tau)\Gamma_{\text{meas}} + \Gamma_{\text{mech}}] \mathcal{D}[\hat{\sigma}_z^1] \hat{\rho}_q dt + \tau \Gamma_{\text{mech}} \mathcal{D}[\hat{\sigma}_z^2] \hat{\rho}_q dt \\
&+ \tau \Gamma_{\text{meas}} \mathcal{D}[\hat{\sigma}_z^1 + \hat{\sigma}_z^2] \hat{\rho}_q dt + \sqrt{\tau\eta\Gamma_{\text{meas}}} \mathcal{H}[\hat{\sigma}_z^1 + \hat{\sigma}_z^2] \hat{\rho}_q dW, \tag{3.46}
\end{aligned}$$

where the mechanical coupling rate of the first and second qubit is χ , $\sqrt{\tau}\chi$, respectively, and Γ_{meas} , Γ_{mech} are given in equations (3.10). Finally, individual tuning of the coupling rates (both χ and g) can also be used to compensate other differences between the systems arising during manufacture, such as the difference in optical decay rates or mechanical frequencies.

3.5 ANALYSIS OF STOCHASTIC MASTER EQUATIONS

Conditional master equations are usually solved using Monte Carlo techniques. When used with postselection, however, stochastic dynamics can be approximated using an analytical approach. This treatment is possible since we are interested only in the final state and not the precise evolution during the measurement. We start from the conditional master equation which we write as

$$\begin{aligned}
d\hat{\rho} &= \gamma_- \{ \mathcal{D}[\hat{\sigma}_z^1] + \mathcal{D}[\hat{\sigma}_z^2] \} \hat{\rho} dt + \gamma_1 \mathcal{D}[\hat{\sigma}_z^1] \hat{\rho} dt + \gamma_2 \mathcal{D}[\hat{\sigma}_z^2] \hat{\rho} dt \\
&+ \Gamma \mathcal{D}[\hat{\sigma}_z^1 + \hat{\sigma}_z^2] \hat{\rho} dt + \sqrt{\eta\Gamma} \mathcal{H}[\hat{\sigma}_z^1 + \hat{\sigma}_z^2] \hat{\rho} dW, \tag{3.47}
\end{aligned}$$

$$Idt = 2\sqrt{\eta\Gamma} \langle \hat{\sigma}_z^1 + \hat{\sigma}_z^2 \rangle dt + dW. \tag{3.48}$$

We assume that both qubits relax at the same rate γ_- while their dephasing rates $\gamma_{1,2}$ can, in principle, differ. (This situation describes two identical qubits coupled to light via optomechanical transducers with optical losses between them.) Now, we prepare the qubits in the state $|\psi_0\rangle = \frac{1}{2}(|0\rangle + |1\rangle) \otimes (|0\rangle + |1\rangle)$ and measure for time T , accumulating the signal

$$J(T) = \int_0^T Idt. \tag{3.49}$$

Clearly, if $J(T) \approx 0$, the expectation value $\langle \hat{\sigma}_z^1 + \hat{\sigma}_z^2 \rangle = 0$ and the qubits are in the entangled state $|\Psi_+\rangle = (|01\rangle + |10\rangle)/\sqrt{2}$ (assuming all decoherence channels are negligible compared with the measurement) while for $J(T) \ll 0$ they are in the state $|11\rangle$ [$|00\rangle$ for $J(T) \gg 0$]. Choosing a suitable postselection cutoff ν , we keep the state if $|J(T)| \leq \nu$ and discard it otherwise.

To get a deeper understanding of the system dynamics, we can adopt the following simplified approach: first, we assume that the system evolves according to the unconditional master equation

$$\frac{d\hat{\rho}}{dt} = \gamma_- \{ \mathcal{D}[\hat{\sigma}_-^1] + \mathcal{D}[\hat{\sigma}_-^2] \} \hat{\rho} + \gamma_1 \mathcal{D}[\hat{\sigma}_z^1] \hat{\rho} + \gamma_2 \mathcal{D}[\hat{\sigma}_z^2] \hat{\rho} + \Gamma \mathcal{D}[\hat{\sigma}_z^1 + \hat{\sigma}_z^2] \hat{\rho} \quad (3.50)$$

from time $t = 0$ to time $t = T$. Afterwards, a fast, strong measurement is applied, returning the result $J(T)$. Finally, using the cutoff ν , we either keep or discard the state; we are interested in the entanglement of the state we keep. This approach is generally not valid since nonlinearity in the measurement term $\mathcal{H}[\hat{\sigma}_z^1 + \hat{\sigma}_z^2] \hat{\rho} = (\hat{\sigma}_z^1 + \hat{\sigma}_z^2) \hat{\rho} - \text{tr}\{(\hat{\sigma}_z^1 + \hat{\sigma}_z^2) \hat{\rho}\} \hat{\rho} + \text{H.c.}$ mixes the subspaces corresponding to the three measurement outcomes, $\langle \hat{\sigma}_z^1 + \hat{\sigma}_z^2 \rangle = 2$ (spanned by the state $|00\rangle$), $\langle \hat{\sigma}_z^1 + \hat{\sigma}_z^2 \rangle = 0$ (spanned by $|01\rangle$, $|10\rangle$), and $\langle \hat{\sigma}_z^1 + \hat{\sigma}_z^2 \rangle = -2$ (spanned by $|11\rangle$), which can be considered independent in the unconditional dynamics under weak relaxation, $\gamma_- < \gamma_{1,2}, \Gamma$. Nevertheless, if the measurement is strong enough (so that the inter-subspace coherences quickly decay), this treatment is a good approximation of the true stochastic dynamics which can otherwise be studied only using quantum trajectories.

Formally, we start by solving the deterministic master equation (3.50) with the initial condition $\hat{\rho}(t=0) = |\psi_0\rangle\langle\psi_0|$; although this equation can be solved analytically, I omit the solution for brevity. The qubits then interact with the measurement apparatus (initially in the vacuum state), which we then project on an eigenstate of the measurement operator, resulting in the unnormalized state

$$\hat{\varrho}_x = \langle x | \exp(-i\mu \hat{S}_z \hat{p}) \hat{\rho}(T) \otimes |0\rangle\langle 0| \exp(i\mu \hat{S}_z \hat{p}) |x\rangle. \quad (3.51)$$

Here, $\hat{S}_z = \frac{1}{2}(\hat{\sigma}_z^1 + \hat{\sigma}_z^2)$, \hat{p} is the phase quadrature of the measurement apparatus, and μ is the measurement strength which can be evaluated from the classical signal (3.49): each of the projections $\langle \hat{S}_z \rangle = 0, \pm 1$ gives rise to normally distributed signals $J(T)$ with mean value $4\sqrt{\eta\Gamma} \langle \hat{S}_z \rangle T$ and variance T . Considering we want to treat the measurement apparatus as a bosonic mode and the interaction with the two qubits as a conditional displacement, the measurement strength is given by the mean (for $\langle \hat{S}_z \rangle = 1$) renormalized by the square root of the variance so that $\mu = 2\sqrt{\eta\Gamma T}$ [a factor of $\frac{1}{2}$ appears due to the used definition of the amplitude quadrature $\hat{x} = (\hat{a} + \hat{a}^\dagger)/\sqrt{2}$].

We can express the unnormalized projected state $\hat{\varrho}_x$ using phase-quadrature representation for the measurement apparatus

$$\begin{aligned} \hat{\varrho}_x &= \frac{1}{(2\pi)^{3/2}} \int dp \exp\left[-\frac{p^2}{4} + i(x - \mu \hat{S}_z)p\right] \hat{\rho}(T) \int dp' \exp\left[-\frac{p'^2}{4} - i(x - \mu \hat{S}_z)p'\right] \\ &= \sqrt{\frac{2}{\pi}} \sum_{S, S'=-1}^1 e^{-(x-\mu S)^2} \hat{\mathbb{P}}_S \hat{\rho}(T) \hat{\mathbb{P}}_{S'} e^{-(x-\mu S')^2} \\ &= \hat{D}(x) \hat{\rho}(T) \hat{D}(x). \end{aligned} \quad (3.52)$$

Here, $\hat{\mathbb{P}}_S$ is projector onto the subspace with $\langle \hat{S}_z \rangle = S$ and

$$\hat{D}(x) = \sqrt{\frac{2}{\pi}} \text{diag}\{\exp[-(x-\mu)^2], \exp(-x^2), \exp(-x^2), \exp[-(x+\mu)^2]\}. \quad (3.53)$$

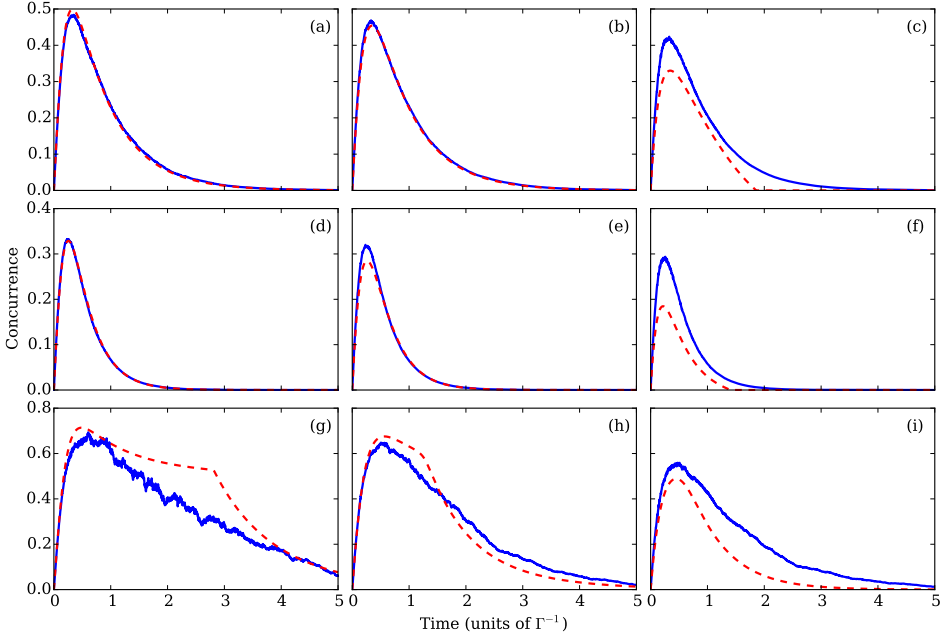


Figure 3.4: Comparison of the analytical model (dashed red line) to numerical simulations (solid blue line). In the first row [panels (a–c)], we consider system with parameters $\gamma_- = 0.1\Gamma$, $\gamma_1 = \gamma_2 = 0.2\Gamma$, $\eta = 0.6$; in the second row [panels (d–f)], the parameters are $\gamma_- = 0.1\Gamma$, $\gamma_1 = \Gamma$, $\gamma_2 = 0.3\Gamma$, $\eta = 1$; for the last row [panels (g–i)], we use the parameters $\gamma_- = 0.8\Gamma$, $\gamma_1 = \gamma_2 = 0$, $\eta = 1$. The success probability is $P_{\text{succ}} = 0.1$ for the first column [panels (a,d,g)], $P_{\text{succ}} = 0.3$ for the second column [panels (b,e,h)], and $P_{\text{succ}} = 0.5$ for the last column [panels (c,f,i)].

Integrating over the interval $x \in (-\nu, \nu)$, we obtain the final postselected state

$$\hat{\rho}_f = \frac{\int_{-\nu}^{\nu} dx \hat{\rho}_x}{\text{tr}\{\int_{-\nu}^{\nu} dx \hat{\rho}_x\}}; \quad (3.54)$$

the normalization factor gives the success probability of the postselection procedure, $P_{\text{succ}} = \text{tr}\{\int_{-\nu}^{\nu} dx \hat{\rho}_x\}$. It is possible to express the final density matrix analytically but the resulting expression is too cumbersome to be presented here.

I compare the analytical model with numerical simulations in figure 3.4. As expected, the analytical model breaks down when the qubit relaxation rate becomes large so that the nonlinearity of the measurement term in the stochastic master equation starts to play a role [panels (g–i)]. Furthermore, the analytical model and the numerical simulations start to deviate when the success probability is increased [panels (c,f,i)]. This behaviour is, however, merely a result of different data analysis procedure—while the analytical model evaluates entanglement of the average state obtained by postselection, the numerical simulations reveal the average entanglement that can be obtained. In the extreme case of a perfect measurement (i.e., dynamics described by the stochastic master equation $d\hat{\rho} = \Gamma\mathcal{D}[\hat{\sigma}_z^1 + \hat{\sigma}_z^2]\hat{\rho}dt + \sqrt{\Gamma}\mathcal{H}[\hat{\sigma}_z^1 + \hat{\sigma}_z^2]\hat{\rho}dW$) and success probability 100 % (corresponding

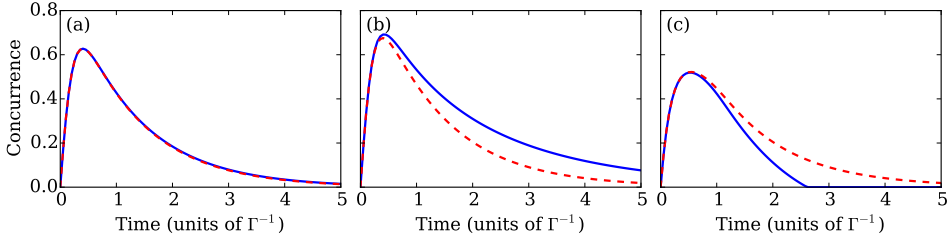


Figure 3.5: Comparison of the total-spin measurement (solid blue line) with the measurement of the spin difference (dashed red line). (a) Decoherence dominated by dephasing, $\gamma_1 = \gamma_2 = 0.2\Gamma$, $\gamma_- = 0.05\Gamma$, $P_{\text{succ}} = 0.2$. (b,c) Comparable dephasing and relaxation, $\gamma_1 = \gamma_2 = 0.1\Gamma$, $\gamma_- = 0.3\Gamma$, $P_{\text{succ}} = 0.1$ (b), $P_{\text{succ}} = 0.5$ (c). For all plots, the detection efficiency $\eta = 1$.

to simply disregarding the measurement record), the average state is a statistical mixture of all possible measurement outcomes,

$$\hat{\rho} = \frac{1}{4}|00\rangle\langle 00| + \frac{1}{2}|\Psi_+\rangle\langle\Psi_+| + \frac{1}{4}|11\rangle\langle 11| = \frac{1}{4} \begin{pmatrix} 1 & 0 & 0 & 0 \\ 0 & 1 & 1 & 0 \\ 0 & 1 & 1 & 0 \\ 0 & 0 & 0 & 1 \end{pmatrix}, \quad (3.55)$$

which is a separable state. Simulating individual quantum trajectories, on the other hand, we obtain the maximally entangled state $|\Psi_+\rangle$ with 50 % probability and the average entanglement equals 0.5 ebit.

We can treat the measurement of the spin difference $\hat{\sigma}_z^1 - \hat{\sigma}_z^2$ in a similar manner. This time, the entangled state $|\Phi_+\rangle = (|00\rangle + |11\rangle)/\sqrt{2}$ can be generated from the initial state $|\psi_0\rangle = \frac{1}{2}(|0\rangle + |1\rangle) \otimes (|0\rangle + |1\rangle)$. The two measurements, of the total spin $\hat{\sigma}_z^1 + \hat{\sigma}_z^2$ and of the spin difference $\hat{\sigma}_z^1 - \hat{\sigma}_z^2$, are compared in figure 3.5. When the decoherence of the qubits is dominated by their dephasing [panel (a)], there is no difference between the two strategies since dephasing affects both cases equally. When the qubit relaxation cannot be neglected, the success probability decides which measurement ought to be used. For small success probabilities [panel (b)], it is beneficial to measure the total spin $\hat{\sigma}_z^1 + \hat{\sigma}_z^2$; with this measurement, only states in the relevant subspace (spanned by the states $|01\rangle, |10\rangle$) are postselected. While this is the case also for the spin difference measurement (where the preferred subspace is spanned by $|00\rangle, |11\rangle$), the ground state population contains also contributions from the decayed odd-parity states $|01\rangle, |10\rangle$, which leads to a reduction of concurrence. The measurement of the spin difference is, however, a better choice if the success probability is large [panel (c)]; in such a situation, the total-spin measurement results in a state that is a mixture of all three subspaces and its entanglement is thus reduced. There is, nevertheless, a little difference between the two strategies for times up to the optimal measurement time, independent of the chosen success probability.

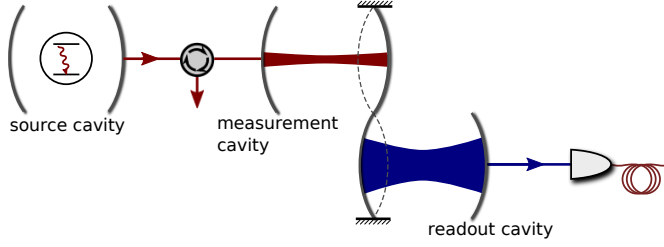


Figure 3.6: Scheme for optomechanical quantum nondemolition detection of single photons. A photon in the measurement cavity transfers part of its momentum to a mechanical oscillator; this momentum is then measured using a second, readout cavity mode. An incoming photon can be modelled with a third, source cavity (left) with an embedded photon source (e.g., an atom).

3.6 PHOTOCOUNTING WITH OPTOMECHANICAL TRANSDUCERS

Generation of entanglement is but a single possible application of optomechanical transducers for quantum force sensing. The purpose of the device is to measure a force that, in this case, comes from a superconducting qubit. The source of this force, however, can be another object. For instance, using a nonlinearly coupled optomechanical cavity, we can use the transducer to count photons.

The scheme is depicted in figure 3.6. An optical cavity (which I will refer to as the measurement cavity) interacts with a mechanical oscillator via the nonlinear optomechanical coupling $g_0 \hat{a}^\dagger \hat{a} (\hat{b} + \hat{b}^\dagger)$. The mechanical oscillator thus feels a force $F_n = n g_0 / \sqrt{2} x_{\text{zpf}}$ that depends on the number of photons $n = \langle \hat{a}^\dagger \hat{a} \rangle$ in the measurement cavity. We use another, readout cavity to estimate this force and determine the number of photons in the measurement cavity. The dynamics of the measurement cavity are, in full analogy with the qubit readout, described by the conditional master equation

$$d\hat{\rho} = \kappa \mathcal{D}[\hat{a}] \hat{\rho} dt + (\Gamma_{\text{meas}} + \Gamma_{\text{mech}}) \mathcal{D}[\hat{a}^\dagger \hat{a}] \hat{\rho} dt + \sqrt{\Gamma_{\text{meas}}} \mathcal{H}[\hat{a}^\dagger \hat{a}] \hat{\rho} dW; \quad (3.56)$$

the first term on the right-hand side accounts for the cavity decay, the terms proportional to Γ_{meas} describe the measurement, and the term with Γ_{mech} gives the mechanically induced dephasing; the rates are given by

$$\Gamma_{\text{meas}} = 16 \frac{g_0^2 g^2}{\kappa_r \omega_m^2}, \quad \Gamma_{\text{mech}} = \frac{g_0^2 \gamma}{\omega_m^2} (2\bar{n} + 1). \quad (3.57)$$

Here, κ_r is the linewidth of the readout cavity and g is its linearized coupling to the mechanical oscillator.

In the following, I will focus on the simplest scenario: distinguishing between the presence and absence of a single photon. The transducer allows a quantum nondemolition detection of the photon—it is not absorbed by the detector but imparts a momentum kick to the mechanical oscillator that can be measured using a second cavity mode. To fully exploit the possibilities this measurement offers, I will consider a situation where the photon arrives in the measurement cavity from some outer source, is measured, and

decays from the cavity. I will show that the sensitivity of such a measurement is limited by the quantum Zeno effect [209, 220, 246]: the measurement prevents the photon from entering the measurement cavity. I will then argue that basic evasion of the measurement backaction is possible if the arrival time of the photon is known; the sensitivity in such a case is limited by imperfect coupling of the photon into the measurement cavity. Finally, I will briefly discuss a scenario where the photon is coupled perfectly into the cavity and the technical requirements to successfully detect its presence in this setting.

3.6.1 Measurement strategy

The basic model for sending the photon to the detector from an outside source is the following (see figure 3.6): we consider a third, source cavity, which is prepared in the single photon state. The source cavity is cascaded with the measurement cavity so that the photon decaying from the source enters the detector where its presence is measured. Finally, the photon decays from the measurement cavity and is available for further operations. The detector can thus be used to improve the efficiency of the source.

Formally, we introduce the annihilation operator of the source cavity \hat{a}_s and describe the source and measurement cavity using the conditional master equation

$$\begin{aligned} d\hat{\rho} = & \sqrt{\kappa_s\kappa}[\hat{a}_s^\dagger\hat{a} - \hat{a}^\dagger\hat{a}_s, \hat{\rho}]dt + \mathcal{D}[\sqrt{\kappa_s}\hat{a}_s + \sqrt{\kappa}\hat{a}]\hat{\rho}dt + \Gamma\mathcal{D}[\hat{a}^\dagger\hat{a}]\hat{\rho}dt \\ & + \sqrt{\Gamma}\mathcal{H}[\hat{a}^\dagger\hat{a}]\hat{\rho}dW. \end{aligned} \quad (3.58)$$

Here, κ_s is the linewidth of the source cavity and we neglect mechanically induced dephasing of the measurement cavity; for the simple task of distinguishing the presence and absence of a photon, this dephasing effect is irrelevant. The initial state is a single photon in the source cavity and vacuum in the measurement cavity, $\hat{\rho}_1(t=0) = |1_s, 0\rangle\langle 1_s, 0|$ [or the vacuum $\hat{\rho}_0(t=0) = |0_s, 0\rangle\langle 0_s, 0|$], and the measurement gives rise to the classical signal

$$I dt = 2\sqrt{\Gamma}\langle\hat{a}^\dagger\hat{a}\rangle dt + dW. \quad (3.59)$$

The distinguishability of the vacuum and single-photon states can be maximized by using an appropriate filter $F(t)$,

$$J = \int_0^T dt F(t)I(t); \quad (3.60)$$

the filter is optimized by taking $F(t) \propto I_1(t)$; we assume the filter function to be normalized $\int dt F^2(t) = 1$. Here $I_1(t) = 2\sqrt{\Gamma}n_1(t)$ is the signal we expect from a single photon and $n_1(t)$ is the unconditional population of the measurement cavity. The population can be found by solving the master equation

$$\frac{d\hat{\rho}}{dt} = \frac{\sqrt{\kappa_s\kappa}}{2}[\hat{a}_s^\dagger\hat{a} - \hat{a}^\dagger\hat{a}_s, \hat{\rho}] + \mathcal{D}[\sqrt{\kappa_s}\hat{a}_s + \sqrt{\kappa}\hat{a}]\hat{\rho} + \Gamma\mathcal{D}[\hat{a}^\dagger\hat{a}]\hat{\rho} \quad (3.61)$$

with the initial state $\hat{\rho}_1$; we obtain

$$n_1(t) = \frac{4\kappa_s\kappa e^{-\kappa t}}{\Gamma + \kappa - \kappa_s} \left(\frac{1 - e^{-(\kappa_s - \kappa)t}}{\kappa_s - \kappa} + 2 \frac{e^{-\frac{1}{2}(\Gamma - \kappa + \kappa_s)t} - 1}{\Gamma - \kappa + \kappa_s} \right). \quad (3.62)$$

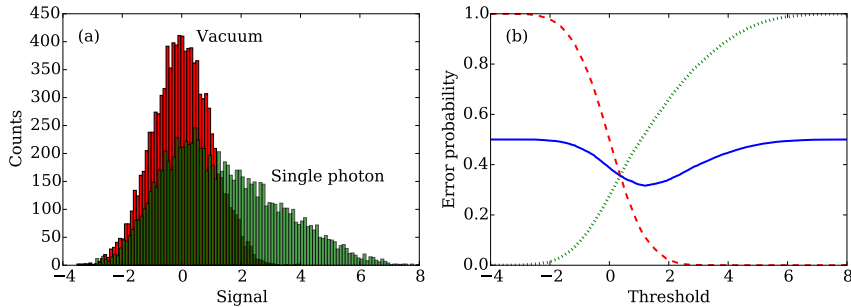


Figure 3.7: (a) Histograms of signals coming from the vacuum (red) and single-photon states (green). (b) Error probabilities versus the discrimination threshold. The plot shows the dark-count probability (dashed red line), false detection (dotted green line), and their average (solid blue line).

This choice of filter maximizes, on average, the signal from the single photon since the filtered signal J is given by the scalar product of the photon population with itself; any other (normalized) filter must necessarily give rise to a smaller filtered signal. At the same time, unfiltered signals from the vacuum state fluctuate around zero; the expected signal is thus $n_0(t) = 0$ and the expected filtered signal is zero.

Under these conditions, vacuum gives rise to normally distributed signals with zero mean and unit variance. The mean signal for the single-photon state is $J_1 = \int dt F(t) I_1(t) = 2\sqrt{\Gamma} \sqrt{\int dt n_1^2(t)}$. The signals due to a single photon do not have a Gaussian distribution. We can, nevertheless, still use the mean signal J_1 as an approximation of the signal-to-noise ratio; unlike the exact signal-to-noise ratio or any other measure of distinguishability of the two states, this quantity can be calculated analytically. For long measurement times, $T > 1/\kappa$, we can take the limit $T \rightarrow \infty$ and the single-photon signal becomes

$$J_1 = 4\sqrt{\frac{2\Gamma\kappa_s\kappa[\Gamma + 3(\kappa + \kappa_s)]}{(\kappa + \kappa_s)(\Gamma + \kappa + \kappa_s)(\Gamma + 3\kappa + \kappa_s)(\Gamma + \kappa + 3\kappa_s)}}. \quad (3.63)$$

This quantity can be numerically maximized: for $\kappa_s = \kappa$, $\Gamma = 2.355\kappa$, we get $J_1 = 1.34$.

Results of numerical simulations for these parameters are shown in figure 3.7. From panel (a), we see that the histograms of signals corresponding to the vacuum and single-photon state are largely overlapping. This result is further illustrated in panel (b), where the measurement error is plotted as a function of the discrimination threshold. In this setting, a threshold ν is picked and the signal is interpreted as coming from a single photon if and only if $J > \nu$; we ask what the probability of a wrong determination of the cavity state is. The best performance in this case reaches measurement infidelity of about 31%.

3.6.2 Quantum Zeno effect and the standard quantum limit

We can understand the limitations of the measurement scheme by introducing Stokes operators for the source and measurement cavity,

$$\hat{S}_0 = \frac{1}{2}(\hat{a}_s^\dagger \hat{a}_s + \hat{a}^\dagger \hat{a}), \quad (3.64a)$$

$$\hat{S}_1 = \frac{1}{2}(\hat{a}_s^\dagger \hat{a} + \hat{a}^\dagger \hat{a}_s), \quad (3.64b)$$

$$\hat{S}_2 = -\frac{i}{2}(\hat{a}_s^\dagger \hat{a} - \hat{a}^\dagger \hat{a}_s), \quad (3.64c)$$

$$\hat{S}_3 = \frac{1}{2}(\hat{a}_s^\dagger \hat{a}_s - \hat{a}^\dagger \hat{a}). \quad (3.64d)$$

The interaction of the two cavities (up to the Lindblad term $\mathcal{D}[\sqrt{\kappa_s}\hat{a}_s + \sqrt{\kappa}\hat{a}]\hat{\rho}$) is given by the Stokes operator \hat{S}_2 . The transducer measures, on the other hand, the combination $\hat{S}_0 - \hat{S}_3$. Owing to the commutation relation $[\hat{S}_i, \hat{S}_j] = i\epsilon_{ijk}\hat{S}_k$, $i, j, k = 1, 2, 3$, the measurement of the Stokes operator \hat{S}_3 necessarily disturbs the second Stokes operator \hat{S}_2 ; this disturbance is then reflected in the measurement of \hat{S}_3 at a later time.

We can get a deeper understanding of this phenomenon from circuit quantum electrodynamics [209, 220]: a qubit under a Rabi drive and continuous measurement of its population exhibits quantum Zeno effect. The coupling of the cavities (analogous to the Rabi drive) and the measurement are two competing processes; while the former leads to a change of the cavity population, the latter freezes the dynamics and prevents any population change. With a weak measurement, the driving is stronger and the cavity becomes populated by the photon; the measurement is, however, too weak to observe it. A strong measurement, which dominates over the drive, prevents this effect and the measurement cavity remains empty, giving a false negative in the detection. Similar effect has been observed also for quantum nondemolition detection with two nonlinearly coupled cavity fields [246].

The solution to this problem and a way to improve the detection efficiency is to turn the measurement on after the photon entered the measurement cavity. This adaptation leads to a less general measurement than the one we started with—we now need to know when the photon arrives so we know when to start the measurement. In its simplest form, this can be modelled with the time-dependent measurement rate

$$\Gamma(t) = \Gamma\Theta(t - t_0), \quad (3.65)$$

where $\Theta(t)$ is the Heaviside step function; the measurement is switched on at time t_0 , which is achieved by turning on the driving of the readout cavity. The photon thus enters the measurement cavity without any backaction, and only then do we switch the measurement on.

The off-on measurement is compared with the simple approach in figure 3.8(a). The time-dependent measurement can outperform the simplest strategy already for moderate measurement rates ($\Gamma \lesssim 3\kappa$). The performance of both approaches is further analysed in

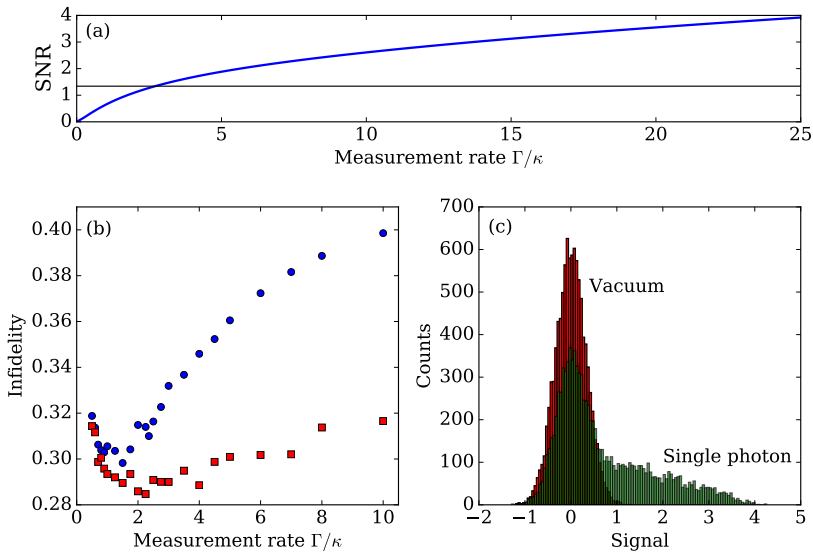


Figure 3.8: (a) Signal-to-noise ratio (SNR) as a function of the measurement rate. The curve shows results for the off-on measurement numerically optimized over the switching time t_0 . The black horizontal line represents the standard quantum limit obtained for time-independent measurement. (b) Measurement infidelity for the simple measurement scheme (blue circles) and the time-dependent measurement (red squares) versus the measurement rate. (c) Sample histograms for vacuum (red) and single-photon states (green) for the off-on measurement with $\Gamma = 10\kappa$.

panel (b). The off-on measurement indeed outperforms the basic scheme; its performance, however, does not improve with increasing measurement rate beyond $\Gamma \sim 2.5\kappa$.

We can understand this behaviour from figure 3.8(c), which shows the histograms for vacuum and single-photon states with the time-dependent measurement for $\Gamma = 10\kappa$. Owing to the non-Gaussianity of the single photon, the corresponding histogram has a long tail with strong measurement signals that skews the signal-to-noise-ratio. A significant number of the single-photon trajectories do not result in a click due to imperfect coupling of the photon to the measurement cavity. Since the cavity population reaches a maximum of about 50 %, the photon can be detected only with the same efficiency.

3.6.3 Fundamental limits on measurement precision

To maximize the detection efficiency, we need to improve the coupling of the photon into the measurement cavity. We can achieve this goal if we have control over the pulse shape of the photon. With an inverted-exponential profile, the photon will couple perfectly into the measurement cavity. If we now turn the measurement on, measurement backaction will not limit the distinguishability of the vacuum and single photon states. This scheme is, however, the most problematic to implement—apart from knowledge of the arrival time of the photon, we also need to be able to control its pulse shape.

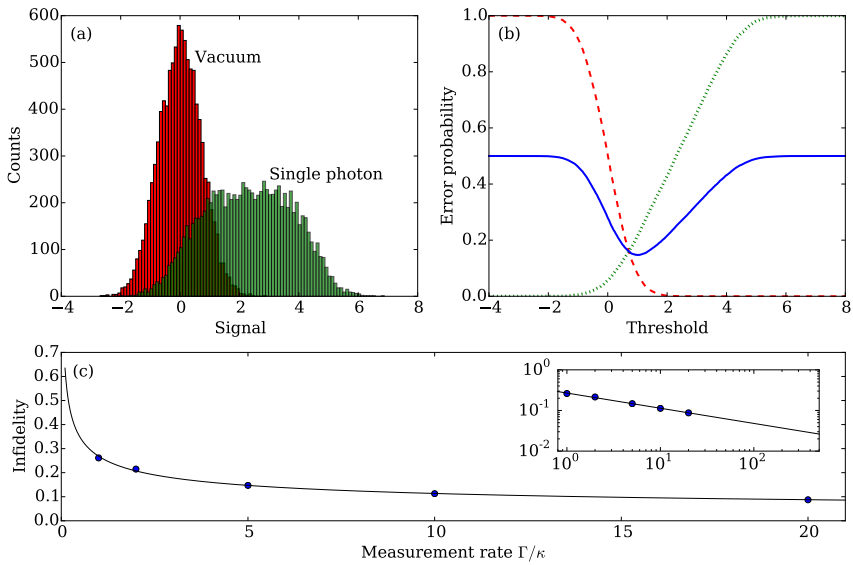


Figure 3.9: (a) Histograms for vacuum (red) and single-photon (green) states for scheme with a single cavity and $\Gamma = \kappa$. (b) Corresponding error probabilities versus the discrimination threshold. The plot shows the dark count probability (dashed red line), false detection (dotted green line), and their average (solid blue line). (c) Scaling of the measurement infidelity with measurement rate. The blue points represent simulation data, the line is a polynomial fit. The inset shows the same data on a logarithmic scale.

The dynamics are now described by the conditional master equation

$$d\hat{\rho} = \kappa\mathcal{D}[\hat{a}]\hat{\rho}dt + \Gamma\mathcal{D}[\hat{a}^\dagger\hat{a}]\hat{\rho}dt + \sqrt{\Gamma}\mathcal{H}[\hat{a}^\dagger\hat{a}]\hat{\rho}dW. \quad (3.66)$$

For an efficient measurement, the measurement rate has to be larger than the cavity decay rate, $\Gamma > \kappa$. Using the expression for the measurement rate, equation (3.57), we can rewrite this condition as

$$\frac{4g_0^2}{\kappa\gamma} \frac{4g^2}{\kappa_r\gamma} > Q_m^2. \quad (3.67)$$

We can also estimate the resulting signal-to-noise ratio: the expected measurement signal is now an exponential, $n(t) = e^{-\kappa t}$, so we have

$$\text{SNR} = 2\sqrt{\Gamma} \sqrt{\int dt n^2(t)} = \sqrt{\frac{2\Gamma}{\kappa}}. \quad (3.68)$$

Results of numerical simulations are shown in figure 3.9. Panel (a) shows signal histograms for $\Gamma = 5\kappa$ and in panel (b), the corresponding error rates are plotted versus the discrimination threshold. The performance is greatly improved compared to the previous strategies but there still is a finite overlap between the histograms corresponding to the vacuum and single-photon states.

To investigate how this overlap depends on the measurement rate, figure 3.9(c) shows the measurement infidelity as a function of the measurement rate. Polynomial fit (black line) to the simulated data (blue points) shows that the infidelity scales approximately as $\Gamma^{-0.37}$. From the signal-to-noise ratio in equation (3.68), we would expect the infidelity to scale as $\Gamma^{-1/2}$; the discrepancy is caused by the non-Gaussian character of the distribution of the single-photon signals; cf. figure 3.9(a).

To analyse experimental feasibility of this scheme, let us consider the following parameters: in recent experiments, the ratio $g_0/\omega_m \sim 10^{-2}$ can be expected. Together with a readout rate $g^2/\kappa_r \sim 1$ MHz, this value gives a measurement rate of about 1 kHz, which is significantly smaller than typical cavity decay rates. The single-photon coupling can be enhanced by mediating the optomechanical coupling by a two-level system [173, 180] or by parametrically driving the mechanical motion [253]. With current technology, however, these strategies improve the measurement rate only by one or two orders of magnitude; the scheme thus remains extremely challenging to implement.

3.7 SUMMARY

Optomechanical force sensing is a measurement method that can reach remarkable precision. In a typical scenario, the object exerting the force on the oscillator is treated classically. Here, I showed on two examples that treating the source of the force quantum mechanically can bring useful practical applications and interesting new effects.

First, I considered using two optomechanical transducers for joint readout of two superconducting qubits. The optomechanical system is used to measure the qubit-state-dependent force on the mechanical oscillator; the topology of the system results in an effective measurement of the total spin and can thus be used for generation of entanglement between the qubits, following recent experimental efforts in microwave systems [92]. An important open question was whether the coherence of the qubits can survive the measurement; the transducer introduces a dephasing channel for the qubit so this question is highly nontrivial. I demonstrated that the qubit coherence is well preserved during the measurement if the transducer has large cooperativity; moreover, the system tolerates a substantial optical loss. The strategy builds on existing experimental techniques and can thus be readily implemented.

Second, I considered using an optomechanical transducer for quantum nondemolition detection of single photons. In this case, a single photon—a highly nonclassical object—imparts a momentum kick to the mechanical oscillator, which can be detected using a second, strongly driven cavity mode. We saw that a continuous measurement gives rise to backaction that limits the population of the measurement cavity. We can avoid the resulting quantum Zeno effect with a time-dependent measurement setting for which, however, knowledge of the arrival time of the photon is necessary. The detection performance is then limited by the natural imperfection of the coupling of the incoming photon to the measurement cavity. The solution to this problem is a manipulation of the temporal profile of the photon; the resulting measurement, nevertheless, puts very strong requirements on the system parameters and is far from being feasible with current technology.

CHAPTER 4

SPATIALLY ADIABATIC FREQUENCY CONVERSION IN TRANSDUCER ARRAYS

An optomechanical transducer formed by an optical and a microwave cavity coupled to a common mechanical oscillator [figure 4.1(a)] is a conceptually simple, yet versatile device. Frequency conversion of propagating fields is possible with time-independent control using optomechanically induced transparency [254]; arbitrary input signals in one mode can be converted into the output of the other mode. The main limitation of this scheme is its small bandwidth, given by the optomechanically broadened mechanical linewidth, which is, for typical experimental parameters, much smaller than the linewidth of the cavity modes [134].

Conversion bandwidth can be improved by using adiabatic passage with intracavity fields [79, 80]; in this case, the bandwidth is equal to the cavity linewidth. This approach requires complicated time-control schemes to store incoming signals inside one of the cavities and for efficient conversion. The main limitation, however, is the requirement for strong coupling, which is not available with current opto- and electromechanical systems. Although the process can be sped up using shortcuts to adiabaticity [255, 256] (which relax the conditions on the coupling strength), the correction Hamiltonian that compensates nonadiabatic transitions results in more complex time-control schemes.

A solution to this conundrum lies in developing new strategies for frequency conversion in optoelectromechanical systems. In this chapter, I take this approach and show that the conversion bandwidth can be increased in an array of optomechanical transducers [96]; see figure 4.1(b). Two propagating fields (one optical and one microwave) form two normal modes, one of which is decoupled from the mechanical motion. Varying the opto- and electromechanical coupling rates within the array, we can change the nature of the mechanically dark mode from purely microwave to purely optical. This variation, which needs to be sufficiently slow so the orthogonal normal mode is not excited in the process, adiabatically converts any signal initially in the microwave field to light (or vice versa). The conversion bandwidth can be improved by increasing the array size and is limited only by the frequency of the mechanical oscillations.

Using a mechanically dark mode also leads to a strongly suppressed added noise. Even though the total noise that enters the propagating fields scales with the array size, it gets added predominantly to the mechanically bright mode. This effect is more pronounced as the array size increases and the adiabaticity improves. Added noise is thus suppressed in

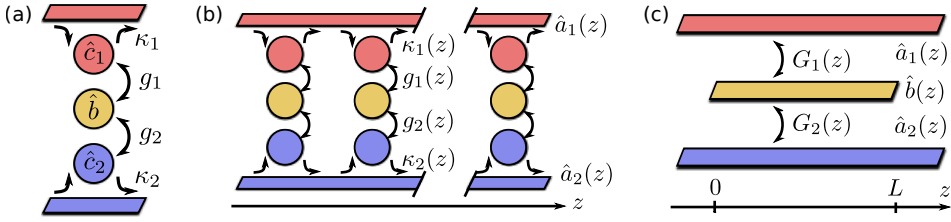


Figure 4.1: (a) Schematic representation of a basic optomechanical transducer. Conversion between a microwave mode \hat{c}_1 (red circle) and an optical mode \hat{c}_2 (blue) via the mechanical mode \hat{b} (yellow) is possible using a mechanically dark mode. (b) Transducer array for spatially adiabatic frequency conversion. The opto- and electromechanical coupling rates are varied throughout the array so that a mechanically dark mode of the propagating fields $\hat{a}_{1,2}(z)$ changes from a purely microwave mode to a purely optical mode. The transducers are directionally coupled; signals propagate from left to right. (c) Continuous model for spatially adiabatic frequency conversion where the propagating fields are coupled via a spatially extended phonon mode $\hat{b}(z)$.

the regime where the collectively enhanced optomechanical cooperativity is strong; we do not need each transducer to be in the strong-cooperativity regime.

I start by describing existing strategies of optomechanical transduction, namely conversion of propagating fields and conversion of intracavity fields by adiabatic passage in section 4.1. I describe both approaches in detail and outline their limitations for practical applications. I then briefly outline how frequency conversion of propagating fields via adiabatic passage could be implemented in a continuous optoelectromechanical system [figure 4.1(c)].

Next, I show how spatially adiabatic dynamics can be effectively achieved in an array of optomechanical transducers. An array is only an approximation of the continuous dynamics; as the array size grows, however, the dynamics are closer to the continuous model. I find a simple analytical expression for the conversion bandwidth and provide an intuitive explanation for its scaling with system parameters.

In section 4.3, I address losses and noise in the system and show that efficient frequency conversion is possible even in presence of imperfections. I identify the main sources of decoherence and find regimes in which these imperfections can be neglected. Particularly, I show that the mechanical noise is suppressed in large arrays by the adiabatic parameter. I also identify a loss mechanism—backscattering of electromagnetic signals—that has no analogue in temporal adiabatic dynamics and analyse its role in spatially adiabatic frequency conversion.

Finally, I discuss possible implementations and summarize the chapter in section 4.4. Apart from implementations in optoelectromechanical nanostructures, I also briefly discuss the main hurdles in implementing direct conversion between propagating fields in the spirit of the continuous model discussed in section 4.1.

4.1 SINGLE OPTOMECHANICAL TRANSDUCER

4.1.1 Transduction of itinerant fields

The most versatile approach to optomechanical transduction uses time-independent control and is capable of converting arbitrary input fields [79, 80, 82]. In this transducer [see figure 4.1(a)], a single mechanical oscillator (annihilation operator \hat{b}) is coupled to a microwave and an optical cavity (annihilation operators $\hat{c}_{1,2}$) via a beam splitter-like Hamiltonian

$$\hat{H} = g_1(\hat{c}_1^\dagger \hat{b} + \hat{b}^\dagger \hat{c}_1) + g_2(\hat{c}_2^\dagger \hat{b} + \hat{b}^\dagger \hat{c}_2). \quad (4.1)$$

To understand how input fields are converted by the transducer, we solve its state-space model (see also chapter 1): we start by writing the Heisenberg–Langevin equations and the input–output relations in the vector form

$$\frac{d\hat{\mathbf{a}}}{dt} = \mathbf{A}\hat{\mathbf{a}} + \mathbf{B}\hat{\mathbf{a}}_{\text{in}}, \quad (4.2a)$$

$$\hat{\mathbf{a}}_{\text{out}} = \mathbf{C}\hat{\mathbf{a}} + \mathbf{D}\hat{\mathbf{a}}_{\text{in}} \quad (4.2b)$$

with the vector $\hat{\mathbf{a}} = (\hat{c}_1, \hat{b}, \hat{c}_2)^T$ (and similar vectors for the input and output fields). For the matrices, we have

$$\mathbf{A} = \begin{pmatrix} -\frac{\kappa_1}{2} & -ig_1 & 0 \\ -ig_1 & -\frac{\gamma}{2} & -ig_2 \\ 0 & -ig_2 & -\frac{\kappa_2}{2} \end{pmatrix}, \quad (4.3a)$$

$$\mathbf{B} = \mathbf{C} = \text{diag}(\sqrt{\kappa_1}, \sqrt{\gamma}, \sqrt{\kappa_2}), \quad (4.3b)$$

$$\mathbf{D} = -\mathbf{I}_3; \quad (4.3c)$$

here, $\kappa_{1,2}$, γ are the decay rates of the cavity fields $\hat{a}_{1,2}$ and the mechanical mode \hat{b} .

The Heisenberg–Langevin equations (4.2) can be solved in the frequency domain; the relation between the input and output fields is described by the scattering matrix

$$\hat{\mathbf{a}}_{\text{out}}(\omega) = \mathbf{S}(\omega)\hat{\mathbf{a}}_{\text{in}}(\omega) = [\mathbf{D} - \mathbf{C}(\mathbf{A} + i\omega\mathbf{I}_3)^{-1}\mathbf{B}]\hat{\mathbf{a}}_{\text{in}}(\omega). \quad (4.4)$$

For the optomechanical transducer, the scattering matrix is

$$\mathbf{S}(\omega) = \begin{pmatrix} t_1 & n_1 & c \\ n_1 & m & n_2 \\ c & n_2 & t_2 \end{pmatrix}; \quad (4.5)$$

the coefficients are, close to cavity resonance, $\omega \approx 0$, given by

$$t_i = \frac{-C_i + C_{i\oplus 1} + 1}{C_1 + C_2 + 1}, \quad (4.6a)$$

$$c = -\frac{2\sqrt{C_1 C_2}}{C_1 + C_2 + 1}, \quad (4.6b)$$

$$m = -\frac{C_1 + C_2 - 1}{C_1 + C_2 + 1}, \quad (4.6c)$$

$$n_i = -\frac{2i\sqrt{C_i}}{C_1 + C_2 + 1}; \quad (4.6d)$$

here, $C_i = 4g_i^2/\kappa_i\gamma$ is the classical cooperativity and \oplus denotes addition modulo 2.

Efficient conversion requires $|c| \approx 1$; this condition is fulfilled if the opto- and electromechanical systems are impedance matched, $C_1 = C_2 = C > 1$. In this case, the conversion coefficient simplifies to $c = -2C/(2C + 1) \approx -1$, while direct transmission is strongly suppressed, $t_i = 1/(2C + 1) \approx 0$. Impedance matching thus results in destructive interference between signal reflected off the input mirror and from inside the cavity [80].

To fully characterize transduction of quantum signals, we must further determine the added noise. To this end, we compare the conversion coefficient [given by equation (4.6b)] with the coefficient quantifying the noise that enters the same output mode from the thermal mechanical bath [equation (4.6d)]. For an impedance-matched system, we have

$$\frac{n_i}{c} = \frac{i}{\sqrt{C}}. \quad (4.7)$$

Since the average occupation of the thermal mechanical bath is \bar{n} , the total noise compared to the signal is $|n_i/c|^2\bar{n} = \bar{n}/C = 1/\bar{C}$; to successfully limit thermal noise, we thus need to operate in the regime of strong optomechanical cooperativity,

$$\bar{C} = \frac{4g^2}{\kappa\gamma\bar{n}} > 1. \quad (4.8)$$

This condition is similar to the requirement on efficient generation of entanglement between two qubits presented in the previous chapter; both results illustrate the important of the cooperativity as a figure of merit for optomechanical systems.

The final figure of merit we are interested in is the transducer bandwidth, that is, the frequency range across which efficient transduction is possible. To evaluate the bandwidth, we need to find the scattering coefficients away from resonance; we can proceed as follows: we write the Heisenberg–Langevin equation for the mechanical oscillator with adiabatically eliminated cavity fields,

$$\frac{d\hat{b}}{dt} = -\left(\frac{\gamma}{2} + \frac{4g_1^2}{\kappa_1} + \frac{4g_2^2}{\kappa_2}\right)\hat{b} - \frac{2ig_1}{\sqrt{\kappa_1}}\hat{c}_{1,\text{in}} - \frac{2ig_2}{\sqrt{\kappa_2}}\hat{c}_{2,\text{in}} + \sqrt{\gamma}\hat{b}_{\text{in}}, \quad (4.9)$$

and solve it in frequency space. After plugging the result into the input–output relation

$$\hat{c}_{2,\text{out}} = -\frac{2ig_2}{\sqrt{\kappa_2}}\hat{b} + \hat{c}_{2,\text{in}}, \quad (4.10)$$

we can identify the conversion coefficient in the term containing $\hat{c}_{1,\text{in}}$. We obtain

$$c = -\frac{8g_1g_2}{\sqrt{\kappa_1\kappa_2}} \frac{1}{\Gamma - 2i\omega}, \quad \Gamma = \gamma + \frac{8g_1^2}{\kappa_1} + \frac{8g_2^2}{\kappa_2}. \quad (4.11)$$

Equation (4.11) reveals that the conversion coefficient has a Lorentzian profile with width given by the optically broadened mechanical linewidth Γ . We thus have the conversion bandwidth $\Delta\omega = \Gamma$. Together, the conversion bandwidth and added noise fully characterize the optomechanical transducer [257].

4.1.2 Frequency conversion by adiabatic passage

Efficient conversion of cavity fields is possible using adiabatic state transfer [79, 80]. The two cavity fields interact with a mechanical oscillator via the time-dependent Hamiltonian

$$\hat{H}_{\text{int}}(t) = g_1(t)(\hat{c}_1^\dagger \hat{b} + \hat{b}^\dagger \hat{c}_1) + g_2(t)(\hat{c}_2^\dagger \hat{b} + \hat{b}^\dagger \hat{c}_2). \quad (4.12)$$

In the strong-coupling regime, $g_i > \kappa_i$, the cavity fields hybridize into two normal modes,

$$\hat{d}_1 = \frac{g_1(t)\hat{c}_1 + g_2(t)\hat{c}_2}{g(t)}, \quad \hat{d}_2 = \frac{g_2(t)\hat{c}_1 - g_1(t)\hat{c}_2}{g(t)}, \quad (4.13)$$

where $g^2(t) = g_1^2(t) + g_2^2(t)$. The normal mode \hat{d}_2 is mechanically dark; it does not appear in the interaction Hamiltonian $\hat{H}_{\text{int}} = g(t)(\hat{d}_1^\dagger \hat{b} + \hat{b}^\dagger \hat{d}_1)$ and is thus insensitive to mechanical losses and associated noise.

Frequency conversion between the two cavity fields can be achieved by adiabatically varying the two coupling rates. In this process, the nature of the dark mode is changed from purely microwave at $t = 0$ [achieved for $g_1(0) \ll g_2(0)$] to purely optical at a later time $t = T$ [now, $g_1(T) \gg g_2(T)$]. Adiabaticity is ensured if the conversion is slow and does not lead to excitation of the bright mode \hat{d}_1 . This condition is fulfilled whenever the rate of change of the coupling rates is smaller than the frequency spacing of the normal modes [79]; mathematically, we can write

$$|\dot{g}_i(t)| < g_1^2(t) + g_2^2(t). \quad (4.14)$$

This requirement bounds the duration of the process from below, $T > 1/g$. On the other hand, the conversion has to be fast compared to the lifetime of the cavity fields. We thus get a hierarchy of time scales $1/\kappa_i > T > 1/g$; this hierarchy cannot be fulfilled with current systems.

Imagine now that we perform the conversion in a spatially extended structure, in which the coupling rates can be varied in space, rather than in time; cf. figure 4.1(c). The two fields (now with annihilation operators $\hat{a}_{1,2}(z)$ and propagating with velocity $v_{1,2}$) are coupled to a phonon mode $\hat{b}(z)$ extended over length L via beam splitter interaction. The Hamiltonian of the full system now has to take into account the propagation of the

fields; we have $\hat{H} = \hat{H}_0 + \hat{H}_{\text{int}}$ with the free propagation Hamiltonian and interaction

$$\hat{H}_0 = \int_{-\infty}^{\infty} dz \sum_{i=1}^2 v_i \left[\hat{a}_i^\dagger(z) \frac{\partial}{\partial z} \hat{a}_i(z) + \frac{\partial \hat{a}_i^\dagger}{\partial z} \hat{a}_i \right], \quad (4.15a)$$

$$\begin{aligned} \hat{H}_{\text{int}} &= \int_0^L dz [G_1(z) \hat{a}_1^\dagger(z) + G_2(z) \hat{a}_2^\dagger(z)] \hat{b}(z) + \text{H.c.} \\ &= \int_0^L dz G [\hat{d}_1^\dagger(z) \hat{b}(z) + \hat{b}^\dagger(z) \hat{d}_1(z)]; \end{aligned} \quad (4.15b)$$

in the interaction Hamiltonian, I introduced the propagating normal mode $\hat{d}_1(z) = [G_1(z) \hat{a}_1(z) + G_2(z) \hat{a}_2(z)]/G(z)$ with $G^2(z) = G_1^2(z) + G_2^2(z)$. The orthogonal normal mode $\hat{d}_2(z) = [G_2(z) \hat{a}_1(z) - G_1(z) \hat{a}_2(z)]/G(z)$ is not directly coupled to the mechanical mode. To ensure that the mode \hat{d}_2 is mechanically dark, however, we have to ensure that the normal modes are not coupled in the free Hamiltonian \hat{H}_0 .

To derive conditions under which the normal modes stay decoupled, we collect the propagating fields in a vector $\hat{\mathbf{a}}(z) = [\hat{a}_1(z), \hat{a}_2(z)]^T$ [the normal modes are collected in a similar vector $\hat{\mathbf{d}}(z)$]. The transformation between the propagating fields and normal modes can be described by the orthogonal matrix $\mathbf{O}(z)$,

$$\hat{\mathbf{a}}(z) = \mathbf{O}(z) \hat{\mathbf{d}}(z) = G^{-1} \begin{pmatrix} G_1 & G_2 \\ G_2 & -G_1 \end{pmatrix} \begin{pmatrix} \hat{d}_1 \\ \hat{d}_2 \end{pmatrix}. \quad (4.16)$$

Plugging this expression into the free Hamiltonian (4.15a) [which we write in the matrix form $\hat{H}_0 = \int dz \hat{\mathbf{a}}^\dagger \mathbf{v} \partial_z \hat{\mathbf{a}} + \text{H.c.}$ with $\mathbf{v} = \text{diag}(v_1, v_2)$], we find that the normal modes remain decoupled if the matrices $\mathbf{O}^T \mathbf{v} \mathbf{O}$ and $\mathbf{O}^T \mathbf{v} \partial_z \mathbf{O} + (\partial_z \mathbf{O}^T) \mathbf{v} \mathbf{O}$ are diagonal. The matrix $\mathbf{O}^T \mathbf{v} \mathbf{O}$ is diagonal if both fields propagate at the same velocity, $v_1 = v_2 = v$; the other matrix is, under this condition, identically zero. The normal modes thus remain decoupled and the mode \hat{d}_2 is a dark mode of the mechanical oscillator.

Adiabatic frequency conversion between the propagating fields $\hat{a}_{1,2}$ is now possible by slowly varying the coupling rates $G_{1,2}(z)$. To ensure that the conversion stays adiabatic, the change of the coupling rates has to be slow so that we do not excite the orthogonal normal mode \hat{d}_1 . From equation (4.14), we can express the time derivative using the spatial derivative and get the condition $|dG_i/dz| < G^2/v$.

4.2 TRANSDUCER ARRAY

The continuous dynamics can be approximated in an array of optomechanical transducers; see figure 4.1(b). Each transducer is formed by a mechanical oscillator coupled to an optical and a microwave cavity; the interaction is described by the interaction Hamiltonian $\hat{H}_{\text{int}} = g_1(\hat{c}_1^\dagger \hat{b} + \hat{b}^\dagger \hat{c}_1) + g_2(\hat{c}_2^\dagger \hat{b} + \hat{b}^\dagger \hat{c}_2)$. The dynamics are governed by the Heisenberg-

Langevin equations

$$\frac{d\hat{c}_i}{dt} = -\frac{\kappa_i}{2}\hat{c}_i - ig_i\hat{b} + \sqrt{\kappa_i}\hat{a}_i(z^-), \quad (4.17a)$$

$$\frac{d\hat{b}}{dt} = -\frac{\gamma}{2}\hat{b} - ig_1\hat{c}_1 - ig_2\hat{c}_2 + \sqrt{\gamma}\hat{b}_{\text{in}} \quad (4.17b)$$

with the input–output relations, for a transducer at position z , $\hat{a}_i(z^+) = \sqrt{\kappa_i}\hat{c}_i - \hat{a}_i(z^-)$; the input fields are denoted $\hat{a}_i(z^-)$ and the outputs are $\hat{a}_i(z^+)$.

Conversion via the mechanically dark mode is achieved by varying the coupling rates from $g_1(0) \approx 0$, $g_2(0) = \bar{g}_2$ at the beginning of the array to $g_1(L) = \bar{g}_1$, $g_2(L) \approx 0$ at its end; this ensures that the mode varies from $\hat{d}_2(0) = \hat{a}_1$ to $\hat{d}_2(L) = \hat{a}_2$. The condition of equal propagation velocities implies that the two fields have to acquire the same phase in propagation between two sites. (In the following, I set this phase to 0 without loss of generality.) The adiabatic condition is fulfilled for $\bar{g}_i\sqrt{N} > \kappa_i$; this result follows from eliminating the cavity fields, from which we obtain $G_i = 4g_i^2/\kappa_i$.

4.2.1 Transfer matrix formalism

The Heisenberg–Langevin equations (4.17) can be solved in frequency domain, which enables us to describe the relation between the input and output fields by the scattering matrix, $\hat{\mathbf{a}}_{\text{out}}(\omega) = \hat{\mathbf{a}}(z^+, \omega) = \mathbf{S}(\omega)\hat{\mathbf{a}}(z^-, \omega) = \mathbf{S}(\omega)\hat{\mathbf{a}}_{\text{in}}(\omega)$. We write the equations of motion in the matrix form

$$-i\omega\hat{\mathbf{a}}(\omega) = \mathbf{A}\hat{\mathbf{a}}(\omega) + \mathbf{B}\hat{\mathbf{a}}_{\text{in}}(\omega), \quad (4.18a)$$

$$\hat{\mathbf{a}}_{\text{out}}(\omega) = \mathbf{C}\hat{\mathbf{a}}(\omega) + \mathbf{D}\hat{\mathbf{a}}_{\text{in}}(\omega), \quad (4.18b)$$

where $\hat{\mathbf{a}} = (\hat{c}_1, \hat{c}_2, \hat{b})^T$, $\hat{\mathbf{a}}_{\text{in}} = [\hat{a}_1(z^-), \hat{a}_2(z^-)]^T$, and $\hat{\mathbf{a}}_{\text{out}} = [\hat{a}_1(z^+), \hat{a}_2(z^+)]^T$. The matrices are given by

$$\mathbf{A} = \begin{pmatrix} -\frac{\kappa_1}{2} & 0 & -ig_1 \\ 0 & -\frac{\kappa_2}{2} & -ig_2 \\ -ig_1 & -ig_2 & -\frac{\gamma}{2} \end{pmatrix}, \quad (4.19a)$$

$$\mathbf{B}^T = \mathbf{C} = \begin{pmatrix} \sqrt{\kappa_1} & 0 & 0 \\ 0 & \sqrt{\kappa_2} & 0 \end{pmatrix}, \quad (4.19b)$$

$$\mathbf{D} = -\mathbf{I}_2; \quad (4.19c)$$

here, \mathbf{I}_2 is the 2×2 identity matrix. With these matrices, the scattering matrix can be expressed as

$$\mathbf{S}(\omega) = \mathbf{D} - \mathbf{C}(\mathbf{A} + i\omega\mathbf{I}_2)\mathbf{B}. \quad (4.20)$$

In this description, I intentionally dropped the effect of thermal noise on the propagating fields (which was included in the scattering matrix derived in section 4.1); its role is discussed in section 4.3.1.

The state-space model can be solved analytically; we obtain the scattering matrix

$$\mathbf{S} = \begin{pmatrix} \frac{8g_2^2\kappa_1 + 2\kappa_1(\kappa_2 - 2i\omega)(\gamma - 2i\omega)}{D} - 1 & -\frac{8g_1g_2\sqrt{\kappa_1\kappa_2}}{D} \\ -\frac{8g_1g_2\sqrt{\kappa_1\kappa_2}}{D} & \frac{8g_1^2\kappa_2 + 2\kappa_2(\kappa_1 - 2i\omega)(\gamma - 2i\omega)}{D} - 1 \end{pmatrix} \\ \approx \begin{pmatrix} \frac{\kappa_1 + 2i\omega}{\kappa_1 - 2i\omega} - \frac{8g_1^2\kappa_1}{(\kappa_1 - 2i\omega)^2(\gamma - 2i\omega)} & -\frac{8g_1g_2\sqrt{\kappa_1\kappa_2}}{(\kappa_1 - 2i\omega)(\kappa_2 - 2i\omega)(\gamma - 2i\omega)} \\ -\frac{8g_1g_2\sqrt{\kappa_1\kappa_2}}{(\kappa_1 - 2i\omega)(\kappa_2 - 2i\omega)(\gamma - 2i\omega)} & \frac{\kappa_2 + 2i\omega}{\kappa_2 - 2i\omega} - \frac{8g_2^2\kappa_2}{(\kappa_2 - 2i\omega)^2(\gamma - 2i\omega)} \end{pmatrix}. \quad (4.21)$$

Here, $D = 4g_1^2(\kappa_2 - 2i\omega) + 4g_2^2(\kappa_1 - 2i\omega) + (\kappa_1 - 2i\omega)(\kappa_2 - 2i\omega)(\gamma - 2i\omega)$ and the second line approximates the scattering matrix in the weak-coupling regime, $g_i < \kappa_i$. This approximation is not valid close to resonance, $\omega \approx 0$; on resonance, we can express the scattering matrix using the classical cooperativities $C_i = 4g_i^2/\kappa_i\gamma$,

$$\mathbf{S}(0) = \frac{1}{C_1 + C_2 + 1} \begin{pmatrix} -C_1 + C_2 + 1 & -2\sqrt{C_1C_2} \\ -2\sqrt{C_1C_2} & C_1 - C_2 + 1 \end{pmatrix}. \quad (4.22)$$

For one-sided cavities, the scattering matrix is identical with the transfer matrix. We can now describe the transfer of signals through the array by the transfer matrix of the array, which we obtain by multiplying the scattering matrices of the transducers,

$$\mathbf{T} = \mathbf{S}_N \mathbf{S}_{N-1} \dots \mathbf{S}_1; \quad (4.23)$$

in this expression, \mathbf{S}_j is the scattering matrix of the j th transducer in the array. Frequency conversion from microwaves to light is characterized by the matrix element $T_{21}(\omega)$ of the resulting scattering matrix $\mathbf{T}(\omega)$.

4.2.2 Conversion bandwidth

Far off resonance, the probability of conversion in a single transducer is small owing to the large frequency detuning, $p_1 = |S_{21}(\omega)|^2 \propto g_1g_2\kappa/\omega^3 \ll 1$. (Here, I assume equal cavity linewidths, $\kappa_1 = \kappa_2 = \kappa$.) In an array, the probability is enhanced by sending the photon through many transducers so that $p_N \approx Np_1 = g_1g_2\kappa N/\omega^3$. We can therefore expect the bandwidth to grow with the cubic root of the array size, $\Delta\omega \propto (g_1g_2\kappa N)^{1/3}$.

We can check this expectation rigorously using the transfer matrix formalism. For equal linewidths of the microwave and optical cavities, $\kappa_1 = \kappa_2 = \kappa$, we can write the transfer matrix of the j th transducer as

$$\mathbf{S}_j = \begin{pmatrix} t & c_j \\ c_j & t \end{pmatrix}; \quad (4.24)$$

the transmission and conversion coefficients can be written as

$$t \approx \frac{\kappa + 2i\omega}{\kappa - 2i\omega}, \quad c_j \approx -\frac{8g_{1j}g_{2j}\kappa}{(\kappa - 2i\omega)^2(\gamma - 2i\omega)}. \quad (4.25)$$

In the transmission coefficients, we dropped the effect of the opto- and electromechanical interaction, which is, for off-resonant signals, small compared to direct transmission. Equations (4.25) do not hold on resonance and thus cannot give us the proper spectrum; when estimating the bandwidth of large arrays, we are, however, interested only in frequencies far off resonance where this approximation of the scattering matrix is valid.

Although the transfer matrices differ from site to site, they can all be diagonalized simultaneously. Using the transformation $\mathbf{U}^{-1}\mathbf{S}_j\mathbf{U}$ with

$$\mathbf{U} = \frac{1}{\sqrt{2}} \begin{pmatrix} 1 & 1 \\ 1 & -1 \end{pmatrix}, \quad (4.26)$$

we obtain the diagonal form

$$\mathbf{S}_j^{\text{diag}} = \text{diag}(t + c_j, t - c_j). \quad (4.27)$$

In the diagonal form, we can multiply all scattering matrices and obtain the diagonal form of the transfer matrix of the array,

$$\mathbf{T}_{\text{diag}} = \prod_{j=1}^N \mathbf{S}_j^{\text{diag}} = \text{diag} \left[\prod_{j=1}^N (t + c_j), \prod_{j=1}^N (t - c_j) \right]. \quad (4.28)$$

For weak coupling and far off resonance, $|c_j| \ll 1$, we can keep only terms linear in c_j ,

$$\prod_{j=1}^N (t \pm c_j) \approx t^N \pm t^{N-1} \sum_{j=1}^N c_j. \quad (4.29)$$

The conversion coefficient of the array can be found by transforming \mathbf{T}_{diag} back to the laboratory frame, $\mathbf{T} = \mathbf{U}\mathbf{T}_{\text{diag}}\mathbf{U}^{-1}$, which yields the conversion coefficient

$$T_{21}(\omega) = t^{N-1} \sum_{j=1}^N c_j. \quad (4.30)$$

Next, we assume that the coupling rates are varied linearly across the array, $g_{1j} = jg/N$, $g_{2j} = g(1 - j/N)$. We can now perform the sum in equation (4.30) and obtain the conversion coefficient

$$T_{21}(\omega) = \left(\frac{\kappa + 2i\omega}{\kappa - 2i\omega} \right)^2 \frac{8g^2\kappa}{(\kappa - 2i\omega)^2(\gamma - 2i\omega)} \frac{1 - N^2}{6N}. \quad (4.31)$$

To find the bandwidth [the full-width half-maximum of the energy conversion coefficient $|T_{21}(\omega)|^2$], we put $|T_{21}(\omega)|^2 = \frac{1}{2}$ and solve for frequency. We obtain a cubic equation in ω^2 with two complex roots; from the third, real root, we get

$$\omega_{\pm} = \pm \frac{-3^{2/3}\kappa^2 + 3^{1/3} \left(6\sqrt{2}g^2\kappa \frac{N^2 - 1}{N} + \kappa \sqrt{72g^4 \frac{(N^2 - 1)^2}{N^2} + 3\kappa^4} \right)^{2/3}}{6 \left(6\sqrt{2}g^2\kappa \frac{N^2 - 1}{N} + \kappa \sqrt{72g^4 \frac{(N^2 - 1)^2}{N^2} + 3\kappa^4} \right)^{1/3}}. \quad (4.32)$$

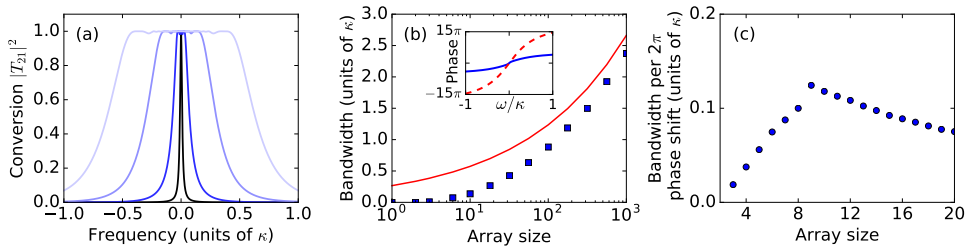


Figure 4.2: (a) Energy conversion spectrum $|T_{21}(\omega)|^2$ for different array sizes. From dark colours to light, the array size is $N = 3, 10, 50, 200$. (b) Transducer bandwidth (full-width half-maximum of the energy conversion coefficient $|T_{21}|^2$) versus array size. Blue squares show results of numerical simulations; the red line represents the analytical result (4.33). The inset shows the phase of the conversion coefficient for array sizes $N = 5$ (solid blue line) and $N = 20$ (dashed red line). (c) Bandwidth per phase shift of 2π as a function of the array size. For all panels (and following figures), I use $g = 0.1\kappa$.

The frequency ω_+ is always positive (and ω_- is always negative): the negative term in the numerator is compensated by the last term under the square root in the numerator. The conversion bandwidth is $\Delta\omega = \omega_+ - \omega_- = 2\omega_+$. In the large-array limit, $g\sqrt{N} > \kappa$, the bandwidth can be further simplified to

$$\Delta\omega = \left(\frac{4\sqrt{2}}{3} g^2 \kappa N \right)^{1/3}. \quad (4.33)$$

For symmetric transducer arrays, the bandwidth depends only on the maximum coupling rate, the cavity linewidth, and the array size. If the maximum coupling rates are not equal for the two fields, i.e., if the coupling rates vary as $g_{1j} = j\bar{g}_1/N$, $g_{2j} = \bar{g}_2(1 - j/N)$, we can replace the g^2 term in the bandwidth by the product of the maximum coupling rates $\bar{g}_1\bar{g}_2$.

4.2.3 Numerical simulations

Results of the transfer matrix analysis are plotted in figure 4.2. Panel (a) shows the energy conversion coefficient $|T_{21}(\omega)|^2$ as a function of frequency for an increasing array size (from dark to light). As the array size increases, the dynamics better approximate the continuous adiabatic state transfer, resulting in larger conversion bandwidth. Remarkably, frequency conversion with unit efficiency is possible even when the adiabatic condition is not fulfilled. The bandwidth is further analysed in panel (b), where it is shown versus array size. In the large-array limit, the bandwidth (blue squares showing results of the numerical simulations) indeed scales with cubic root of the array size and approaches the analytical formula given by equation (4.33) (shown as the red line). The converted signal acquires a large phase shift (inset) owing to reflection from a large number of cavities; the phase across the whole frequency spectrum grows linearly with array size and is equal to $2\pi N$. In practical applications, this phase shift has to be taken into account in postprocessing or compensated by a suitable phase shift on the input or output field.

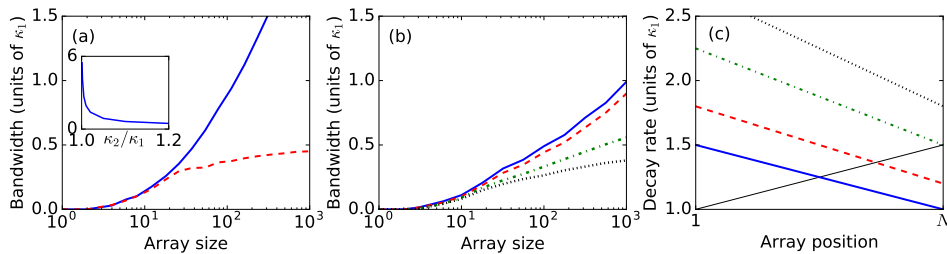


Figure 4.3: (a) Conversion bandwidth versus array size for symmetric (solid blue line) and asymmetric (dashed red line, $\kappa_2 = 1.2\kappa_1$) array. The inset shows bandwidth (in units of κ_1) with $N = 10^5$ transducers as a function of the linewidth imbalance κ_2/κ_1 . (b) Bandwidth with variable cavity decay rates. Throughout the array, the microwave decay rate changes from κ_1 to $1.5\kappa_1$; the optical linewidth varies in the opposite direction from $1.5\kappa_2$ to κ_2 . The curves show bandwidth for $\kappa_2 = \kappa_1$ (solid blue line), $\kappa_2 = 1.2\kappa_1$ (dashed red line), $\kappa_2 = 1.5\kappa_1$ (dot-dashed green line), and $\kappa_2 = 1.8\kappa_1$ (dotted black line). (c) Variation of the decay rates throughout the array used to obtain the results in panel (b). For all curves, the variation of the decay rate of the microwave cavity κ_1 is the same (thin black line); the colour coding for the optical decay rates κ_2 corresponds to the colours used in (b).

Alternatively, if the phase shift cannot be compensated, we might want to find strategies that can limit it. In figure 4.2(c), I demonstrate that a small transducer array can still provide an advantage in this situation. I plot the conversion bandwidth over which the total phase shift is within 2π . For very small arrays, the total phase shift across the bandwidth is smaller than 2π and, therefore, the bandwidth grows with increasing array size. Once the phase shift across the bandwidth reaches 2π , the bandwidth per 2π phase shift starts to drop; the total bandwidth grows with cubic root of the array size while the phase shift across the whole frequency spectrum grows linearly.

In figure 4.3, I study conversion bandwidth with asymmetric transducer arrays (i.e., with $\kappa_1 \neq \kappa_2$). One could naïvely expect that this imbalance can be compensated by changing the coupling rates since adiabatic elimination of the cavity fields gives $G_i = 4g_i^2/\kappa_i$; this statement is, however, true only close to cavity resonance. From panel (a), we see that any imbalance between the decay rates quickly kills the cubic-root scaling and leads to saturation of the bandwidth. Interestingly, this scaling can be recovered if we vary the cavity linewidth across the array. We vary the decay rates in the same direction as the coupling rates—the microwave cavity linewidth κ_1 increases while the linewidth of the optical cavities κ_2 decreases—and observe that, as long as the linewidths are equal at one site in the array, the bandwidth monotonically increases with array size; see panel (b) for the bandwidth and panel (c) for the variation of the decay rates. This variation can be moderate and does not require the decay rate to approach zero at the edges of the array.

4.3 LOSSES AND NOISE

So far, the only imperfection we considered was mechanical loss; we did not include the associated noise or losses related to the propagation of the electromagnetic fields. These

factors are, however, important for any experimental implementation. Electromagnetic losses will reduce conversion efficiency which is, together with added noise, an important figure of merit characterizing transducer performance [257].

Apart from the thermal mechanical noise (discussed below), noise comes from heating due to Stokes scattering associated with the opto- and electromechanical interaction. The full interaction between a cavity field and a mechanical oscillator under a classical drive is described by the Hamiltonian $\hat{H}_{\text{int}} = g_i(\hat{c}_i + \hat{c}_i^\dagger)(\hat{b} + \hat{b}^\dagger)$. If the cavity is driven on the lower mechanical sideband, we can apply the rotating wave approximation and obtain the beam splitter interaction necessary for state transfer. This approximation (which neglects the heating associated with the two-mode squeezing part of the interaction) is valid if the device operates in the resolved-sideband regime, $\kappa_i < \omega_m$. Furthermore, the approximation implies that Fourier frequencies of interest follow the same rule, $\omega < \omega_m$; the mechanical frequency thus provides a limit on conversion bandwidth in practical realizations.

4.3.1 Mechanical noise

For optomechanical transducers, the main source of noise is the thermal bath of mechanical oscillators. The noise that enters the signal from this bath can be suppressed in the strong-cooperativity regime, $\bar{C} = 4g^2/\kappa\gamma\bar{n} > 1$ (here, \bar{n} is the average thermal occupation). In an array, we can expect the noise to be enhanced by the array size N . On the other hand, conversion via a mechanically dark mode is protected from mechanical noise. The noise amplitude is suppressed by the adiabatic parameter $1/N$ (we obtain this result from the expression $(dg/dz)/g$ with linear variation of coupling rates). The noise spectral density is then suppressed by the square of the adiabatic parameter and the total added noise scales as $(\bar{C}N)^{-1}$. For frequency conversion in a transducer array with low added noise, we thus need only the collectively enhanced optomechanical cooperativity to be strong; the cooperativity of individual transducers does not have to be.

To prove this expectation, we start by introducing a source term describing the mechanical noise into the scattering process,

$$\hat{\mathbf{a}}(z_j^+, \omega) = \mathbf{S}_j(\omega)\hat{\mathbf{a}}(z_j^-, \omega) + \mathbf{V}_j(\omega)\hat{f}_j. \quad (4.34)$$

Here, \hat{f}_j is the noise operator of the mechanical bath of the j th transducer and $\mathbf{V}_j(\omega)$ describes the coupling of the bath to the propagating fields; we have

$$\mathbf{V}_j(\omega) = -\frac{4ig\sqrt{\kappa\gamma}}{4(g/N)^2(N^2 - 2jN + 2j^2) + (\kappa - 2i\omega)(\gamma - 2i\omega)} \left(\frac{j}{N}, 1 - \frac{j}{N} \right)^T; \quad (4.35)$$

for a symmetric transducer ($\kappa_1 = \kappa_2 = \kappa$, $\bar{g}_1 = \bar{g}_2 = g$) with linear variation of coupling rates.

We can obtain the total added noise by incoherently summing the noise contributions from each transducer in the array,

$$\mathbf{S}_{\text{add}}^2(\omega) = \sum_{j=1}^N |\chi_j(\omega)|^2 S_j^2(\omega); \quad (4.36)$$

here, $S_f^2(\omega) = 2\bar{n} + 1$ is the noise spectral density of the thermal force \hat{f}_j (we assume that all mechanical reservoirs have the same temperature). Moreover,

$$\chi_j(\omega) = \prod_{k=j+1}^N \mathbf{S}_k(\omega) \mathbf{V}_j(\omega) \quad (4.37)$$

is the noise susceptibility of the j th transducer. In equation (4.36), the absolute value of the noise susceptibility is taken element-wise, $|\chi_j(\omega)|^2 = [|\chi_{1j}(\omega)|^2, |\chi_{2j}(\omega)|^2]^T$; we can thus describe noise added to both normal modes.

In the following, I will consider two different regimes for evaluating the added noise: in the first one, we operate close to resonance and use the scattering matrix given by equation (4.22). Alternatively, we consider off-resonant signals and use approach similar to the one we employed to find the conversion bandwidth.

Added noise on resonance On cavity resonance, the scattering matrix of a single transducer is real and given by equation (4.22). It can be diagonalized by the orthogonal transformation $\mathbf{O}_j \mathbf{S}_j \mathbf{O}_j^T$ where

$$\mathbf{O}_j = \frac{1}{\sqrt{C_1 + C_2}} \begin{pmatrix} \sqrt{C_1} & \sqrt{C_2} \\ -\sqrt{C_2} & \sqrt{C_1} \end{pmatrix}; \quad (4.38)$$

with strong total cooperativity, $C_1 + C_2 > 1$, the diagonal form of the scattering matrix is $\mathbf{S}_j^{\text{diag}} = \text{diag}(-1, 1)$. The matrix \mathbf{O}_j describes a rotation with rotation angle $\tan \theta_j = \sqrt{C_2/C_1}$. In a large array, the rotation angles for two neighbouring transducers are almost identical; we therefore have $\mathbf{O}_{j+1}^T \mathbf{O}_j = \mathbf{I}_2 + \epsilon$ with

$$\epsilon = \frac{1}{N} \begin{pmatrix} 0 & 1 \\ -1 & 0 \end{pmatrix}. \quad (4.39)$$

When evaluating the noise susceptibility, we can diagonalize all scattering matrices simultaneously; to first order in the small correction ϵ , we obtain the expression

$$\begin{aligned} \chi_j(0) &= \prod_{k=j+1}^N \mathbf{S}_k(0) \mathbf{V}_j(0) = \mathbf{O}_N^T \left(\prod_{k=j+1}^N \mathbf{S}_j^{\text{diag}} + \sum_{k=j+1}^N \prod_{m=k+1}^N \mathbf{S}_m^{\text{diag}} \epsilon \prod_{n=j+1}^k \mathbf{S}_n^{\text{diag}} \right) \mathbf{O}_{j+1} \mathbf{V}_j(0) \\ &= -2i \frac{\sqrt{C}}{C+1} \left((-1)^{N+j}, \frac{1}{2N} [-1 + (-1)^{N+j}] \right)^T \end{aligned} \quad (4.40)$$

with $C = 4g^2/\kappa\gamma$. For the total added noise, we now have

$$\mathbf{S}_{\text{add}}^2(0) = \frac{4C(2\bar{n} + 1)}{(C + 1)^2} \left(N, \frac{1}{2N} \right)^T. \quad (4.41)$$

This expression clearly reveals the advantage of using the dark mode for frequency conversion: with the dark mode, the noise is suppressed for $CN > \bar{n}$ (second component of the noise spectral density) and larger array thus helps to reduce the noise. The noise in the bright mode, on the other hand, grows with array size; we would need $C > \bar{n}N$ to suppress the noise.

Off-resonant noise In estimating the added noise off resonance, we proceed similar to evaluating the conversion bandwidth. We assume that the scattering matrix of a single transducer is given by equation (4.24) which enables us to simultaneously diagonalize the scattering matrices of all transducers. We then transform the added noise $\mathbf{V}_j(\omega)\hat{f}_j$ by the same transformation and thus obtain the total added noise. The result of this calculation (which I omit here for brevity) is the same as for noise on resonance, namely, that thermal noise is suppressed for $CN > \bar{n}$.

4.3.2 Optical and microwave losses

Loss of signal in propagation comes in two different processes: first, electromagnetic fields decay directly during propagation in waveguides and via intrinsic loss in cavities. These losses are similar to cavity loss in temporal adiabatic dynamics; for efficient conversion, they have to be smaller than the effective coupling of the propagating fields to the mechanical oscillators. Second, part of the signal can be reflected off a cavity and propagate backwards, interfering with the incoming field. This process is not present in temporal adiabatic conversion since it would imply the backscattered signal propagates backwards in time.

Direct losses To model optical and microwave losses, we modify the state-space model describing the transducers. In the Heisenberg–Langevin equations for the cavity modes, we consider two decay channels, the waveguide and an intrinsic loss channel,

$$\frac{d\hat{c}_i}{dt} = -\frac{\kappa_i + \kappa_{i,\text{int}}}{2}\hat{c}_i - ig_i\hat{b} + \sqrt{\kappa_i}\hat{a}_i(z^-) + \sqrt{\kappa_{i,\text{int}}}\hat{c}_{i,\text{in}}; \quad (4.42)$$

here, $\kappa_{i,\text{int}}$ is the intrinsic decay rate and $\hat{c}_{i,\text{in}}$ the associated input field.

Propagation loss can be described by a transfer matrix for free propagation. Generally, the propagating fields will acquire a phase shift and decay when travelling between two transducers. Denoting the propagation distance between neighbouring transducers d , we can write the free propagation transfer matrix

$$\begin{aligned} \mathbf{T}_{\text{free}}(\omega) &= \text{diag} \left[\exp \left(-\zeta_1 d + i\omega \frac{d}{v_1} + ik_1 d \right), \exp \left(-\zeta_2 d + i\omega \frac{d}{v_2} + ik_2 d \right) \right] \\ &\approx \text{diag} [\exp (-\zeta_1 d + ik_1 d), \exp (-\zeta_2 d + ik_2 d)]. \end{aligned} \quad (4.43)$$

The parameters $\zeta_i > 0$ describe decay of the signals and k_i is the resonant wavenumber for field i ; moreover, in the second line, we dropped the dispersion, which can be neglected for propagation distances smaller than the wavelength associated with the frequency detuning, $d \ll v_i/\omega$. The requirement of both fields propagating with the same acquired phase implies $k_1 d = k_2 d \pmod{2\pi}$. (In principle, the two fields can propagate different distances; in this case, the condition would change to $k_1 d_1 = k_2 d_2 \pmod{2\pi}$.) Without loss of generality, we can set $k_1 d = k_2 d = 2m\pi$ with $m \in \mathbb{Z}$; the transfer matrix then contains only two parameters, $\mathbf{T}_{\text{free}} = \text{diag}(\tau_1, \tau_2)$, where $\tau_i = e^{-\zeta_i d}$.

The total transfer matrix is now obtained from scattering on the transducers and free propagation. For the j th unit cell of the array, we obtain the transfer matrix by multiplying

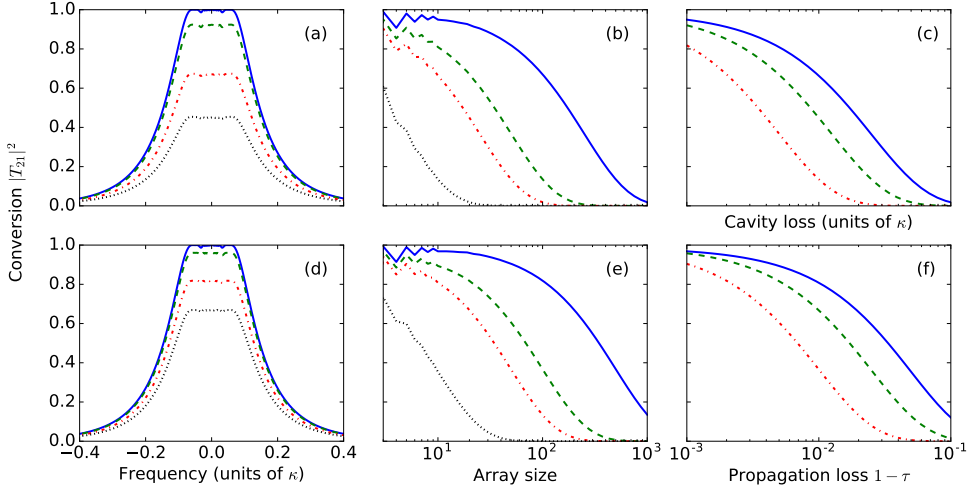


Figure 4.4: Conversion efficiency in presence of intrinsic cavity loss (top row) and propagation loss (bottom). (a) Conversion spectrum with $\kappa_{i,\text{int}} = 0$ (solid blue line), $\kappa_{i,\text{int}} = 0.001\kappa$ (dashed green line), $\kappa_{i,\text{int}} = 0.005\kappa$ (dot-dashed red line), and $\kappa_{i,\text{int}} = 0.01\kappa$ (dotted black line). (b) Conversion efficiency on resonance as a function of array size for $\kappa_{i,\text{int}} = 0.001\kappa$ (solid blue line), $\kappa_{i,\text{int}} = 0.005\kappa$ (dashed green line), $\kappa_{i,\text{int}} = 0.01\kappa$ (dot-dashed red line), and $\kappa_{i,\text{int}} = 0.05\kappa$ (dotted black line). (c) Conversion efficiency versus cavity loss for array size $N = 10$ (solid blue line), $N = 20$ (dashed green line), and $N = 50$ (dot-dashed red line). Panels (d–f) show the same for various propagation losses instead of cavity loss; the values are (in the same order as above) $\epsilon = 1 - \tau = 0, 0.001, 0.005, 0.01$ for panel (d) and $\epsilon = 0.001, 0.005, 0.01, 0.05$ for panel (e); the array sizes in panel (f) are identical with sizes used in (b). For all plots, the loss rates are equal for both fields, $\kappa_{1,\text{int}} = \kappa_{2,\text{int}}$, $\tau_1 = \tau_2 = \tau$.

the scattering matrix for the j th transducer with transfer matrix for free propagation,

$$\mathbf{T}_{j,\text{cell}}(\omega) = \mathbf{T}_{\text{free}}\mathbf{S}_j(\omega). \quad (4.44)$$

We can now find the total transfer matrix by multiplying the transfer matrices of individual unit cells,

$$\mathbf{T}(\omega) = \prod_{j=1}^N \mathbf{T}_{j,\text{cell}}(\omega). \quad (4.45)$$

The effect of direct losses on frequency conversion is analysed in figure 4.4. For both intrinsic cavity loss (top row) and propagation loss (bottom), the behaviour is qualitatively the same; cavity loss is, generally, more detrimental than propagation loss. From the conversion spectra [panels (a,d)], we can see that losses limit the overall conversion efficiency without changing the bandwidth or spectral profile. The following plots [conversion efficiency versus array size in panels (b,e) and versus cavity and propagation loss in panels (c,f)] show the efficiency on resonance.

Backscattering Backscattering of propagating fields on the transducers can also be included in the state-space model. With the cavities driven by and decaying into left- and

right-propagating fields, the Heisenberg–Langevin equations become

$$\frac{d\hat{c}_i}{dt} = -\frac{\kappa_{i,R} + \kappa_{i,L}}{2}\hat{c}_i - ig_i\hat{b} + \sqrt{\kappa_{i,R}}\hat{a}_{i,R}(z^-) + \sqrt{\kappa_{i,L}}\hat{a}_{i,L}(z^+). \quad (4.46)$$

Moreover, we have the input–output relations

$$\hat{a}_{i,R}(z^+) = \sqrt{\kappa_{i,R}}\hat{c}_i - \hat{a}_{i,R}(z^-), \quad \hat{a}_{i,L}(z^-) = \sqrt{\kappa_{i,L}}\hat{c}_i - \hat{a}_{i,L}(z^+) \quad (4.47)$$

with input fields $\hat{a}_{i,R}(z^-)$, $\hat{a}_{i,L}(z^+)$ and outputs $\hat{a}_{i,R}(z^+)$, $\hat{a}_{i,L}(z^-)$; note the different position argument for the right- and left-propagating fields.

Next, we collect the localized modes in the vector $\hat{\mathbf{a}} = (\hat{c}_1, \hat{c}_2, \hat{b})^T$ and the propagating fields in the vector $\hat{\mathbf{a}}_{\text{in}} = [\hat{a}_{1,R}(z^-), \hat{a}_{2,R}(z^-), \hat{a}_{1,L}(z^+), \hat{a}_{2,L}(z^+)]^T$ (and similar for $\hat{\mathbf{a}}_{\text{out}}$); we group the propagating fields by their direction of propagation. We can now write the scattering matrix in the block form

$$\mathbf{S} = \begin{pmatrix} \mathbf{S}_R & \mathbf{S}_{RL} \\ \mathbf{S}_{LR} & \mathbf{S}_L \end{pmatrix}. \quad (4.48)$$

Here, the diagonal elements describe scattering processes, in which the field does not change direction of propagation; the off-diagonal terms describe scattering processes, in which the propagation direction is changed.

The scattering matrix describes the relation between input and output fields. To describe propagation of signals through the array, we need to convert it to a transfer matrix which describes the relation between fields at z^- and z^+ via $\hat{\mathbf{a}}(z^+) = \mathbf{T}_{\text{trans}}\hat{\mathbf{a}}(z^-)$; we find (see also reference [258])

$$\mathbf{T}_{\text{trans}} = \begin{pmatrix} \mathbf{S}_R - \mathbf{S}_{RL}\mathbf{S}_L^{-1}\mathbf{S}_{LR} & \mathbf{S}_{RL}\mathbf{S}_L^{-1} \\ -\mathbf{S}_L^{-1}\mathbf{S}_{LR} & \mathbf{S}_L^{-1} \end{pmatrix}. \quad (4.49)$$

Additionally, propagation of the fields between two transducers is described by the transfer matrix

$$\mathbf{T}_{\text{free}} = \text{diag}(e^{ik_1d}, e^{ik_2d}, e^{-ik_1d}, e^{-ik_2d}); \quad (4.50)$$

propagation through a unit cell of the array is now described by a product of the transfer matrices for the transducer and free propagation, $\mathbf{T}_{j,\text{cell}} = \mathbf{T}_{\text{free}}\mathbf{T}_{j,\text{trans}}$ and propagation through the whole array by the product of transfer matrices over all unit cells, $\mathbf{T} = \mathbf{T}_{N,\text{cell}}\mathbf{T}_{N-1,\text{cell}} \dots \mathbf{T}_{1,\text{cell}}$. We can convert the transfer matrix \mathbf{T} into a scattering matrix using a formula analogous to equation (4.50); the resulting matrix characterizes scattering of arbitrary signals by the array.

Conversion spectra in presence of backscattering are plotted in figure 4.5 for arrays with (a) $N = 10$ and (b) $N = 50$ transducers. The backscattering rate $\kappa_{i,L}/\kappa_{i,R}$ reduces the overall conversion efficiency; this decrease is independent of the array size. Additionally, owing to the large phase shift the signal acquires during propagation through the array, the forward- and backward-propagating signals partially interfere. This interference manifests as oscillation of the conversion efficiency with frequency. The modulation depth depends on the backscattering rate while its frequency depends on the acquired phase shift and thus on the array size.

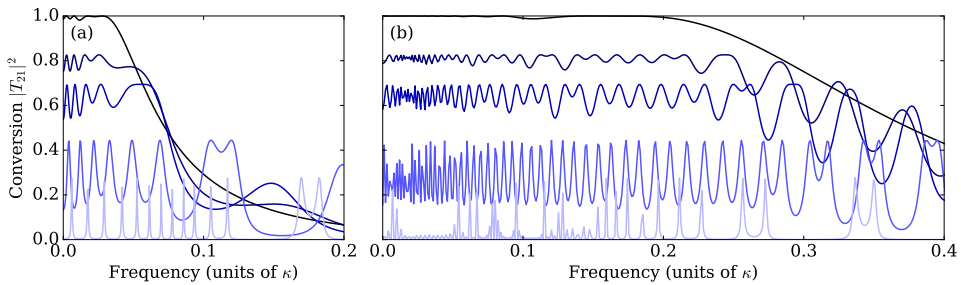


Figure 4.5: Conversion spectra with (a) $N = 10$ and (b) $N = 50$ transducers in presence of backscattering. For both panels, the backscattering rate increases from dark colours to light; we have $\kappa_{i,L}/\kappa_{i,R} = 0, 0.1, 0.2, 0.5, 0.9$.

4.4 DISCUSSION

Optoelectromechanical arrays for frequency conversion can be implemented in integrated systems such as optomechanical crystals or microdisk optical resonators. Both opto- and electromechanical interactions have been demonstrated in the former [259, 260]; additionally, optomechanical arrays (albeit with photon hopping between sites and not directional propagation) have been constructed with the latter system [261]. Variation of the coupling rates can be achieved by varying the single-photon coupling rates across the array; a single driving field can then be used for each type of cavities (i.e., one drive for microwaves and one for light). Building a large array would be extremely challenging, but even a moderate size is sufficient to significantly improve the conversion bandwidth and reduce added noise. Since the strategy uses adiabatic passage for state transfer, it is insensitive to small variations (compared to the adiabatic requirements) in system parameters across the array that are bound to arise in the fabrication process.

Going beyond implementations in transducer arrays, it would be interesting to investigate whether direct conversion of propagating fields is possible in continuum systems [262, 263]. Interaction between propagating light and acoustic κ waves is well understood, but coupling of propagating microwave fields to mechanical vibrations has received no attention so far. With efficient interaction of both propagating fields to mechanical vibrations, the most important issue would be finding ways in which the coupling rates can vary throughout the device to achieve adiabatic state transfer. Finally, an important question would be how to couple propagating optical and microwave fields to the same mechanical mode without disturbing the microwave mode (probably guided in a superconducting transmission line) by optical absorption.

In summary, I showed that efficient frequency conversion is possible in one-dimensional optoelectromechanical arrays. The strategy uses a mechanically dark mode formed by two propagating fields; by varying the opto- and electromechanical coupling rates throughout the array, we can change the nature of the dark mode and achieve adiabatic conversion of signals between the two fields. This approach thus combines the advantages of existing conversion strategies based on the mechanically dark mode: large bandwidth (achievable

with adiabatic conversion of intracavity fields) and multimode operation (possible between propagating fields via optomechanically induced transparency).

In the adiabatic limit, $g\sqrt{N} > \kappa$, the conversion bandwidth grows with array size and is limited only by the mechanical frequency. This condition corresponds to the strong-coupling regime with respect to the collectively enhanced optomechanical interaction. In this sense, the system is similar to existing proposals for enhancing optomechanical interaction by coupling a cavity field to an array of dielectric membranes [264, 265]. In a membrane array, strong interaction of the collective motion to the cavity field is possible even though each membrane couples only weakly to the cavity. Similar effect can be observed here; at each transducer, the opto- and electromechanical interaction (and thus the effective coupling between the two fields) is weak but the overall interaction is enhanced by the array, resulting in an overall strong coupling and large conversion bandwidth. The collective enhancement also helps to reduce the added noise—we saw that the relevant figure of merit for quantifying mechanical noise is the collectively enhanced optomechanical cooperativity.

Surprisingly, a transducer array offers an advantage also far away from the adiabatic regime; a small array possesses a larger bandwidth than a single transducer. This regime will be of interest for quantum networks with superconducting circuits in the near future. Since a small array has a larger bandwidth than a single transducer, it enables higher communication rates between nodes of a network. At the same time, it will be easier to implement than a large array.

CONCLUSION

Optomechanical transducers are a versatile platform for frequency conversion between microwaves and light. Various strategies have been proposed and implemented: some protocols enable conversion of arbitrary input signals, either using quantum state transfer between the two fields [79, 80, 82, 96] or via generation of entanglement and teleportation [99]; other schemes focus on specific tasks, such as detection of weak microwave and radio signals [83, 87, 138] or quantum networks with superconducting systems [78, 95]. Each of these approaches has its own advantages and limitations. State transfer methods based on adiabatic dynamics require time-dependent control; time-independent schemes often provide only a limited bandwidth.

The strategies for optomechanical transduction I presented in this dissertation avoid one of the pitfalls: they work with time-independent control. This limitation—which might appear critical at first—does not preclude us from achieving crucial tasks needed for quantum networking with superconducting circuits. In particular, generation of entanglement between two superconducting qubits is possible with a conceptually simple system inspired by existing experimental techniques [95]. Additionally, frequency conversion in a transducer array goes beyond near-future applications and shows that efficient transduction across a large bandwidth is possible with low added noise [96].

Consider the proposal for generation of entanglement between two superconducting qubits presented in chapter 3. The main strength of this scheme lies in its similarity to existing experimental techniques: parity (or half-parity) measurements are commonly employed in circuit quantum electrodynamics for generation of entanglement on a chip [92, 162] and optomechanical force sensing is a strategy with broad range of applications from measuring the force from individual spins [93] to detecting gravitational waves [19]. Together, these techniques represent a simple and beautiful method for connecting superconducting circuits into quantum networks.

On a more fundamental note, a rigorous mathematical description of the optomechanical measurement required the development of new mathematical methods. An interesting side result of this problem is the method of adiabatic elimination of Gaussian subsystems from conditional dynamics containing both Gaussian and non-Gaussian elements [98] that I discussed in chapter 2. This approach is, to the best of my knowledge, the only elimination procedure for systems including both a continuous measurement and a thermal reservoir. As such, it can find applications with other hybrid systems that combine Gaussian and non-Gaussian elements with homodyne measurements. With this approach, many

systems might be mapped onto simple systems known from different context, similar to mapping the protocol for entanglement generation onto total-spin measurement.

Looking forward, frequency conversion in an array of optomechanical transducers discussed in chapter 4 is an interesting and feasible strategy for advanced superconducting quantum processors and complex quantum networks. For more sophisticated devices, current transducers [73, 74, 82] do not offer sufficient bandwidth to allow fast and efficient quantum communication between individual chips. These devices will require transducers capable of multimode conversion over a large frequency range; these converters will enable efficient transmission of frequency-multiplexed quantum signals between the nodes of a large quantum network. An optoelectromechanical transducer array falls precisely in this category. From the perspective of current technological progress, such a device is extremely challenging to build. But state of the art in experimental quantum science evolves at a remarkable pace; tasks that now seem impossible might soon become reality just as experiments that seemed unfeasible twenty years ago are routinely performed nowadays.

All in all, optomechanical transducers have earned their place in the growing field of hybrid quantum systems. But mechanical motion plays a pivotal role in many other interesting applications in quantum information processing: mechanical oscillators can serve as engineered reservoirs for optical and microwave fields [266, 267], form nonreciprocal devices for controlling the propagation of electromagnetic fields [268–270], be used as quantum memories [271–274], or mediate interactions between various quantum systems [200]. On a more fundamental note, hybrid systems with mechanical oscillators enable us to observe well-known effects in novel settings, providing us with a deeper insight into similarities and differences between various quantum systems [172, 193]. All these results show the importance of opto- and electromechanical systems for future quantum technologies; I can only hope that the work I presented here will play an important role in these developments.

REFERENCES

- [1] J. P. Dowling and G. J. Milburn, ‘Quantum technology: the second quantum revolution,’ *Philosophical Transactions of the Royal Society A: Mathematical, Physical and Engineering Sciences* **361**, 1655 (2003).
- [2] P. Ball, ‘Google moves closer to a universal quantum computer,’ *Nature* (2016), 10.1038/nature.2016.20032.
- [3] D. Castelvecchi, ‘Quantum computers ready to leap out of the lab in 2017,’ *Nature* **541**, 9 (2017).
- [4] D. Castelvecchi, ‘IBM’s quantum cloud computer goes commercial,’ *Nature* **543**, 159 (2017).
- [5] ‘UK national quantum technologies programme,’ <uknqt.epsrc.ac.uk>, accessed 24 June 2017.
- [6] ‘QUTEGA – die nationale Initiative zur Förderung von Quantentechnologien,’ <www.qutega.de>, accessed 24 June 2017.
- [7] ‘Quantum manifesto,’ <qurope.eu/manifesto>, accessed 24 June 2017.
- [8] ‘European commission will launch €1 billion quantum technologies flagship,’ <ec.europa.eu/digital-single-market/en/news/european-commission-will-launch-eu1-billion-quantum-technologies-flagship>, accessed 24 June 2017.
- [9] E. Gibney, ‘Europe plans giant billion-euro quantum technologies project,’ *Nature* **532**, 426 (2016).
- [10] K. Kupferschmidt, ‘Europe to bet up to €1 billion on quantum technology,’ *Science* (2016), 10.1126/science.aaf9969.
- [11] A. A. Clerk, M. H. Devoret, S. M. Girvin, F. Marquardt, and R. J. Schoelkopf, ‘Introduction to quantum noise, measurement, and amplification,’ *Reviews of Modern Physics* **82**, 1155 (2010).
- [12] C. L. Degen, F. Reinhard, and P. Cappellaro, ‘Quantum sensing,’ *Reviews of Modern Physics* **89**, 035002 (2017).

- [13] H. J. Kimble, ‘The quantum internet,’ *Nature* **453**, 1023 (2008).
- [14] V. Scarani, H. Bechmann-Pasquinucci, N. J. Cerf, et al., ‘The security of practical quantum key distribution,’ *Reviews of Modern Physics* **81**, 1301 (2009).
- [15] I. M. Georgescu, S. Ashhab, and F. Nori, ‘Quantum simulation,’ *Reviews of Modern Physics* **86**, 153 (2014).
- [16] H. Weimer, ‘Lecture notes on quantum simulation,’ arXiv:1704.07260.
- [17] M. A. Nielsen and I. L. Chuang, *Quantum Computation and Quantum Information* (Cambridge University Press, Cambridge, 2010).
- [18] M. Aspelmeyer, T. J. Kippenberg, and F. Marquardt, ‘Cavity optomechanics,’ *Reviews of Modern Physics* **86**, 1391 (2014).
- [19] B. P. Abbott, R. Abbott, T. D. Abbott, et al., ‘Observation of gravitational waves from a binary black hole merger,’ *Physical Review Letters* **116**, 061102 (2016).
- [20] L. Rondin, J.-P. Tetienne, T. Hingant, et al., ‘Magnetometry with nitrogen–vacancy defects in diamond,’ *Reports on Progress in Physics* **77**, 056503 (2014).
- [21] R. Schirhagl, K. Chang, M. Loretz, and C. L. Degen, ‘Nitrogen–vacancy centers in diamond: nanoscale sensors for physics and biology,’ *Annual Review of Physical Chemistry* **65**, 83 (2014).
- [22] H. Weinfurter, in *Lectures on Quantum Information*, edited by D. Bruß and G. Leuchs (Wiley-VCH Verlag GmbH, Weinheim, Germany, 2008).
- [23] S. L. Braunstein and P. van Loock, ‘Quantum information with continuous variables,’ *Reviews of Modern Physics* **77**, 513 (2005).
- [24] C. Weedbrook, S. Pirandola, R. García-Patrón, et al., ‘Gaussian quantum information,’ *Reviews of Modern Physics* **84**, 621 (2012).
- [25] F. Grosshans, G. Van Assche, J. Wenger, et al., ‘Quantum key distribution using Gaussian-modulated coherent states,’ *Nature* **421**, 238 (2003).
- [26] T. Schmitt-Manderbach, H. Weier, M. Fürst, et al., ‘Experimental demonstration of free-space decoy-state quantum key distribution over 144 km,’ *Physical Review Letters* **98**, 010504 (2007).
- [27] H.-L. Yin, T.-Y. Chen, Z.-W. Yu, et al., ‘Measurement-device-independent quantum key distribution over a 404 km optical fiber,’ *Physical Review Letters* **117**, 190501 (2016).
- [28] D. Bouwmeester, J.-W. Pan, K. Mattle, et al., ‘Experimental quantum teleportation,’ *Nature* **390**, 575 (1997).

-
- [29] A. Furusawa, J. L. Sørensen, S. L. Braunstein, et al., ‘Unconditional quantum teleportation,’ *Science* **282**, 706 (1998).
- [30] H. Yonezawa, T. Aoki, and A. Furusawa, ‘Demonstration of a quantum teleportation network for continuous variables,’ *Nature* **431**, 430 (2004).
- [31] M. Giustina, M. A. M. Versteegh, S. Wengerowsky, et al., ‘Significant-loophole-free test of Bell’s theorem with entangled photons,’ *Physical Review Letters* **115**, 250401 (2015).
- [32] B. Hensen, H. Bernien, A. E. Dréau, et al., ‘Loophole-free Bell inequality violation using electron spins separated by 1.3 kilometres,’ *Nature* **526**, 682 (2015).
- [33] L. K. Shalm, E. Meyer-Scott, B. G. Christensen, et al., ‘Strong loophole-free test of local realism,’ *Physical Review Letters* **115**, 250402 (2015).
- [34] J. Yin, Y. Cao, Y.-H. Li, et al., ‘Satellite-based entanglement distribution over 1200 kilometers,’ *Science* **356**, 1140 (2017).
- [35] K. Hammerer, A. S. Sørensen, and E. S. Polzik, ‘Quantum interface between light and atomic ensembles,’ *Reviews of Modern Physics* **82**, 1041 (2010).
- [36] N. Sangouard, C. Simon, H. de Riedmatten, and N. Gisin, ‘Quantum repeaters based on atomic ensembles and linear optics,’ *Reviews of Modern Physics* **83**, 33 (2011).
- [37] P. Lodahl, S. Mahmoodian, and S. Stobbe, ‘Interfacing single photons and single quantum dots with photonic nanostructures,’ *Reviews of Modern Physics* **87**, 347 (2015).
- [38] A. Reiserer and G. Rempe, ‘Cavity-based quantum networks with single atoms and optical photons,’ *Reviews of Modern Physics* **87**, 1379 (2015).
- [39] A. A. Houck, H. E. Türeci, and J. Koch, ‘On-chip quantum simulation with superconducting circuits,’ *Nature Physics* **8**, 292 (2012).
- [40] S. Schmidt and J. Koch, ‘Circuit QED lattices: towards quantum simulation with superconducting circuits,’ *Annalen der Physik* **525**, 395 (2013).
- [41] R. Blatt and C. F. Roos, ‘Quantum simulations with trapped ions,’ *Nature Physics* **8**, 277 (2012).
- [42] A. Aspuru-Guzik and P. Walther, ‘Photonic quantum simulators,’ *Nature Physics* **8**, 285 (2012).
- [43] P. Schindler, D. Nigg, T. Monz, et al., ‘A quantum information processor with trapped ions,’ *New Journal of Physics* **15**, 123012 (2013).
- [44] A. Bermudez, X. Xu, R. Nigmatullin, et al., ‘Assessing the progress of trapped-ion processors towards fault-tolerant quantum computation,’ *arXiv:1705.02771*.

- [45] W. K. Hensinger, S. Olmschenk, D. Stick, et al., ‘T-junction ion trap array for two-dimensional ion shuttling, storage, and manipulation,’ *Applied Physics Letters* **88**, 034101 (2006).
- [46] R. Bowler, J. Gaebler, Y. Lin, et al., ‘Coherent diabatic ion transport and separation in a multizone trap array,’ *Physical Review Letters* **109**, 080502 (2012).
- [47] M. H. Devoret, A. Wallraff, and J. M. Martinis, ‘Superconducting qubits: a short review,’ *cond-mat/0411174*.
- [48] M. H. Devoret and R. J. Schoelkopf, ‘Superconducting circuits for quantum information: an outlook.’ *Science* **339**, 1169 (2013).
- [49] U. Vool and M. Devoret, ‘Introduction to quantum electromagnetic circuits,’ *International Journal of Circuit Theory and Applications* **45**, 897(2017).
- [50] J. Majer, J. M. Chow, J. M. Gambetta, et al., ‘Coupling superconducting qubits via a cavity bus,’ *Nature* **449**, 443 (2007).
- [51] M. A. Sillanpää, J. I. Park, and R. W. Simmonds, ‘Coherent quantum state storage and transfer between two phase qubits via a resonant cavity,’ *Nature* **449**, 438 (2007).
- [52] M. Mariantoni, H. Wang, T. Yamamoto, et al., ‘Implementing the quantum von Neumann architecture with superconducting circuits,’ *Science* **334**, 61 (2011).
- [53] R. Barends, J. Kelly, A. Megrant, et al., ‘Superconducting quantum circuits at the surface code threshold for fault tolerance.’ *Nature* **508**, 500 (2014).
- [54] L. DiCarlo, J. M. Chow, J. M. Gambetta, et al., ‘Demonstration of two-qubit algorithms with a superconducting quantum processor,’ *Nature* **460**, 240 (2009).
- [55] L. DiCarlo, M. D. Reed, L. Sun, et al., ‘Preparation and measurement of three-qubit entanglement in a superconducting circuit,’ *Nature* **467**, 574 (2010).
- [56] A. Fedorov, L. Steffen, M. Baur, M. P. da Silva, and A. Wallraff, ‘Implementation of a Toffoli gate with superconducting circuits,’ *Nature* **481**, 170 (2011).
- [57] M. D. Reed, L. DiCarlo, S. E. Nigg, et al., ‘Realization of three-qubit quantum error correction with superconducting circuits,’ *Nature* **482**, 382 (2012).
- [58] A. Córcoles, E. Magesan, S. J. Srinivasan, et al., ‘Demonstration of a quantum error detection code using a square lattice of four superconducting qubits,’ *Nature Communications* **6**, 6979 (2015).
- [59] J. Kelly, R. Barends, A. G. Fowler, et al., ‘State preservation by repetitive error detection in a superconducting quantum circuit,’ *Nature* **519**, 66 (2015).
- [60] D. Ristè, S. Poletto, M.-Z. Huang, et al., ‘Detecting bit-flip errors in a logical qubit using stabilizer measurements,’ *Nature Communications* **6**, 6983 (2015).

-
- [61] B. Vermersch, P.-O. Guimond, H. Pichler, and P. Zoller, ‘Quantum state transfer via noisy photonic and phononic waveguides,’ *Physical Review Letters* **118**, 133601 (2017).
- [62] Z.-L. Xiang, M. Zhang, L. Jiang, and P. Rabl, ‘Intra-city quantum communication via thermal microwave networks,’ *Physical Review X* **7**, 011035 (2017).
- [63] Z.-L. Xiang, S. Ashhab, J. Q. You, and F. Nori, ‘Hybrid quantum circuits: superconducting circuits interacting with other quantum systems,’ *Reviews of Modern Physics* **85**, 623 (2013).
- [64] P. Treutlein, C. Genes, K. Hammerer, M. Poggio, and P. Rabl, in *Cavity optomechanics: Nano- and micromechanical resonators interacting with light*, edited by M. Aspelmeyer, T. J. Kippenberg, and F. Marquardt (Springer, Berlin, 2014).
- [65] G. Kurizki, P. Bertet, Y. Kubo, et al., ‘Quantum technologies with hybrid systems,’ *Proceedings of the National Academy of Sciences* **112**, 3866 (2015).
- [66] A. S. Sørensen, C. H. van der Wal, L. I. Childress, and M. D. Lukin, ‘Capacitive coupling of atomic systems to mesoscopic conductors,’ *Physical Review Letters* **92**, 063601 (2004).
- [67] L. Tian, P. Rabl, R. Blatt, and P. Zoller, ‘Interfacing quantum-optical and solid-state qubits,’ *Physical Review Letters* **92**, 247902 (2004).
- [68] P. Rabl, D. DeMille, J. M. Doyle, et al., ‘Hybrid quantum processors: molecular ensembles as quantum memory for solid state circuits,’ *Physical Review Letters* **97**, 033003 (2006).
- [69] C. O’Brien, N. Lauk, S. Blum, G. Morigi, and M. Fleischhauer, ‘Interfacing superconducting qubits and telecom photons via a rare-earth-doped crystal,’ *Physical Review Letters* **113**, 063603 (2014).
- [70] K. Xia and J. Twamley, ‘Solid-state optical interconnect between distant superconducting quantum chips,’ *Physical Review A* **91**, 042307 (2015).
- [71] S. Das, V. E. Elfving, S. Faez, and A. S. Sørensen, ‘Interfacing superconducting qubits and single optical photons using molecules in waveguides,’ *Physical Review Letters* **118**, 140501 (2017).
- [72] B. T. Gard, K. Jacobs, R. McDermot, and M. Saffman, ‘Microwave-to-optical frequency conversion using a cesium atom coupled to a superconducting resonator,’ *Physical Review A* **96**, 013833 (2017).
- [73] I. Lekavicius, D. A. Golter, T. Oo, and H. Wang, ‘Transfer of phase information between microwave and optical fields via an electron spin,’ *Physical Review Letters* **119**, 063601 (2017).

- [74] R. Hisatomi, A. Osada, Y. Tabuchi, et al., ‘Bidirectional conversion between microwave and light via ferromagnetic magnons,’ *Physical Review B* **93**, 174427 (2016).
- [75] M. Tsang, ‘Cavity quantum electro-optics. II. Input–output relations between traveling optical and microwave fields,’ *Physical Review A* **84**, 043845 (2011).
- [76] C. Javerzac-Galy, K. Plekhanov, N. R. Bernier, et al., ‘On-chip microwave-to-optical quantum coherent converter based on a superconducting resonator coupled to an electro–optic microresonator,’ *Physical Review A* **94**, 053815 (2016).
- [77] A. Rueda, F. Sedlmeir, M. C. Collodo, et al., ‘Efficient microwave to optical photon conversion: an electro–optical realization,’ *Optica* **3**, 597 (2016).
- [78] K. Stannigel, P. Rabl, A. S. Sørensen, P. Zoller, and M. D. Lukin, ‘Optomechanical transducers for long-distance quantum communication,’ *Physical Review Letters* **105**, 220501 (2010).
- [79] L. Tian, ‘Adiabatic state conversion and pulse transmission in optomechanical systems,’ *Physical Review Letters* **108**, 153604 (2012).
- [80] Y.-D. Wang and A. A. Clerk, ‘Using interference for high fidelity quantum state transfer in optomechanics,’ *Physical Review Letters* **108**, 153603 (2012).
- [81] J. Bochmann, A. Vainsencher, D. D. Awschalom, and A. N. Cleland, ‘Nanomechanical coupling between microwave and optical photons,’ *Nature Physics* **9**, 712 (2013).
- [82] R. W. Andrews, R. W. Peterson, T. P. Purdy, et al., ‘Bidirectional and efficient conversion between microwave and optical light,’ *Nature Physics* **10**, 321 (2014).
- [83] T. Bagci, A. Simonsen, S. Schmid, et al., ‘Optical detection of radio waves through a nanomechanical transducer,’ *Nature* **507**, 81 (2014).
- [84] K. C. Balram, M. I. Davanço, J. D. Song, and K. Srinivasan, ‘Coherent coupling between radiofrequency, optical and acoustic waves in piezo–optomechanical circuits,’ *Nature Photonics* **10**, 346 (2016).
- [85] V. S. Shumeiko, ‘Quantum acousto–optic transducer for superconducting qubits,’ *Physical Review A* **93**, 023838 (2016).
- [86] A. Okada, F. Oguro, A. Noguchi, et al., ‘Cavity optomechanics with surface acoustic waves,’ arXiv:1705.04593.
- [87] K. Takeda, K. Nagasaka, A. Noguchi, et al., ‘Electro–mechano–optical NMR detection,’ arXiv:1706.00532.
- [88] A. H. Safavi-Naeini and O. Painter, ‘Proposal for an optomechanical traveling wave phonon–photon translator,’ *New Journal of Physics* **13**, 013017 (2011).

-
- [89] B. D. Clader, ‘Quantum networking of microwave photons using optical fibers,’ *Physical Review A* **90**, 012324 (2014).
- [90] Z.-q. Yin, W. L. Yang, L. Sun, and L. M. Duan, ‘Quantum network of superconducting qubits through an optomechanical interface,’ *Physical Review A* **91**, 012333 (2015).
- [91] C. L. Hutchison, J. Gambetta, A. Blais, and F. K. Wilhelm, ‘Quantum trajectory equation for multiple qubits in circuit QED: generating entanglement by measurement,’ *Canadian Journal of Physics* **87**, 225 (2009).
- [92] N. Roch, M. E. Schwartz, F. Motzoi, et al., ‘Observation of measurement-induced entanglement and quantum trajectories of remote superconducting qubits,’ *Physical Review Letters* **112**, 170501 (2014).
- [93] D. Rugar, R. Budakian, H. J. Mamin, and B. W. Chui, ‘Single spin detection by magnetic resonance force microscopy.’ *Nature* **430**, 329 (2004).
- [94] S. Schreppler, N. Spethmann, N. Brahms, et al., ‘Optically measuring force near the standard quantum limit,’ *Science* **344**, 1486 (2014).
- [95] O. Černotík and K. Hammerer, ‘Measurement-induced long-distance entanglement of superconducting qubits using optomechanical transducers,’ *Physical Review A* **94**, 012340 (2016).
- [96] O. Černotík, S. Mahmoodian, and K. Hammerer, ‘Spatially adiabatic frequency conversion in optoelectromechanical arrays,’ arXiv:1707.03339.
- [97] H. M. Wiseman and G. J. Milburn, *Quantum Measurement and Control* (Cambridge University Press, Cambridge, 2010).
- [98] O. Černotík, D. V. Vasilyev, and K. Hammerer, ‘Adiabatic elimination of Gaussian subsystems from quantum dynamics under continuous measurement,’ *Physical Review A* **92**, 012124 (2015).
- [99] S. Barzanjeh, M. Abdi, G. J. Milburn, P. Tombesi, and D. Vitali, ‘Reversible optical-to-microwave quantum interface,’ *Physical Review Letters* **109**, 130503 (2012).
- [100] C. Genes, A. Mari, D. Vitali, and P. Tombesi, ‘Quantum effects in optomechanical systems,’ *Advances In Atomic, Molecular, and Optical Physics* **57**, 33 (2009).
- [101] A. A. Clerk, F. Marquardt, and K. Jacobs, ‘Back-action evasion and squeezing of a mechanical resonator using a cavity detector,’ *New Journal of Physics* **10**, 095010 (2008).
- [102] A. Kronwald, F. Marquardt, and A. A. Clerk, ‘Arbitrarily large steady-state bosonic squeezing via dissipation,’ *Physical Review A* **88**, 063833 (2013).

- [103] A. Kronwald, F. Marquardt, and A. A. Clerk, ‘Dissipative optomechanical squeezing of light,’ *New Journal of Physics* **16**, 063058 (2014).
- [104] F. Marquardt, J. Chen, A. A. Clerk, and S. M. Girvin, ‘Quantum theory of cavity-assisted sideband cooling of mechanical motion,’ *Physical Review Letters* **99**, 093902 (2007).
- [105] I. Wilson-Rae, N. Nooshi, W. Zwerger, and T. J. Kippenberg, ‘Theory of ground state cooling of a mechanical oscillator using dynamical backaction,’ *Physical Review Letters* **99**, 093901 (2007).
- [106] J. Chan, T. P. M. Alegre, A. H. Safavi-Naeini, et al., ‘Laser cooling of a nanomechanical oscillator into its quantum ground state,’ *Nature* **478**, 89 (2011).
- [107] J. D. Teufel, T. Donner, D. Li, et al., ‘Sideband cooling of micromechanical motion to the quantum ground state.’ *Nature* **475**, 359 (2011).
- [108] R. Riedinger, S. Hong, R. A. Norte, et al., ‘Non-classical correlations between single photons and phonons from a mechanical oscillator,’ *Nature* **530**, 313 (2016).
- [109] C. F. Ockeloen-Korppi, T. T. Heikkilä, M. A. Sillanpää, and F. Massel, ‘Theory of phase-mixing amplification in an optomechanical system,’ *Quantum Science and Technology* **2**, 035002 (2017).
- [110] C. F. Ockeloen-Korppi, E. Damskägg, J.-M. Pirkkalainen, et al., ‘Low-noise amplification and frequency conversion with a multiport microwave optomechanical device,’ *Physical Review X* **6**, 041024 (2016).
- [111] J. Qian, A. A. Clerk, K. Hammerer, and F. Marquardt, ‘Quantum signatures of the optomechanical instability,’ *Physical Review Letters* **109**, 253601 (2012).
- [112] N. Lörch, J. Qian, A. A. Clerk, F. Marquardt, and K. Hammerer, ‘Laser theory for optomechanics: limit cycles in the quantum regime,’ *Physical Review X* **4**, 011015 (2014).
- [113] C. A. Regal, J. D. Teufel, and K. W. Lehnert, ‘Measuring nanomechanical motion with a microwave cavity interferometer,’ *Nature Physics* **4**, 555 (2008).
- [114] A. Sawadsky, H. Kaufer, R. M. Nia, et al., ‘Observation of generalized optomechanical coupling and cooling on cavity resonance,’ *Physical Review Letters* **114**, 043601 (2015).
- [115] J. D. Thompson, B. M. Zwickl, A. M. Jayich, et al., ‘Strong dispersive coupling of a high-finesse cavity to a micromechanical membrane,’ *Nature* **452**, 72 (2008).
- [116] J. C. Sankey, C. Yang, B. M. Zwickl, A. M. Jayich, and J. G. E. Harris, ‘Strong and tunable nonlinear optomechanical coupling in a low-loss system,’ *Nature Physics* **6**, 707 (2010).

-
- [117] M. Ludwig, A. H. Safavi-Naeini, O. Painter, and F. Marquardt, ‘Enhanced quantum nonlinearities in a two-mode optomechanical system,’ *Physical Review Letters* **109**, 063601 (2012).
- [118] Y. Yanay and A. A. Clerk, ‘Shelving-style QND phonon-number detection in quantum optomechanics,’ *New Journal of Physics* **19**, 033014 (2017).
- [119] M. Eichenfield, R. Camacho, J. Chan, K. J. Vahala, and O. Painter, ‘A picogram- and nanometre-scale photonic-crystal optomechanical cavity,’ *Nature* **459**, 550 (2009).
- [120] M. Eichenfield, J. Chan, R. M. Camacho, K. J. Vahala, and O. Painter, ‘Optomechanical crystals,’ *Nature* **462**, 78 (2009).
- [121] E. Verhagen, S. Deléglise, S. Weis, A. Schliesser, and T. J. Kippenberg, ‘Quantum-coherent coupling of a mechanical oscillator to an optical cavity mode.’ *Nature* **482**, 63 (2012).
- [122] G. Anetsberger, O. Arcizet, Q. P. Unterreithmeier, et al., ‘Near-field cavity optomechanics with nanomechanical oscillators,’ *Nature Physics* **5**, 909 (2009).
- [123] T. Rocheleau, T. Ndukum, C. Macklin, et al., ‘Preparation and detection of a mechanical resonator near the ground state of motion,’ *Nature* **463**, 72 (2010).
- [124] J. B. Hertzberg, T. Rocheleau, T. Ndukum, et al., ‘Back-action-evading measurements of nanomechanical motion,’ *Nature Physics* **6**, 213 (2009).
- [125] J. Suh, A. J. Weinstein, C. U. Lei, et al., ‘Mechanically detecting and avoiding the quantum fluctuations of a microwave field,’ *Science* **344**, 1262 (2014).
- [126] C. Schäfermeier, H. Kerdoncuff, U. B. Hoff, et al., ‘Quantum enhanced feedback cooling of a mechanical oscillator using nonclassical light,’ *Nature Communications* **7**, 13628 (2016).
- [127] J. Aasi, J. Abadie, B. P. Abbott, et al., ‘Enhanced sensitivity of the LIGO gravitational wave detector by using squeezed states of light,’ *Nature Photonics* **7**, 613 (2013).
- [128] H. J. Kimble, Y. Levin, A. B. Matsko, K. S. Thorne, and S. P. Vyatchanin, ‘Conversion of conventional gravitational-wave interferometers into quantum nondemolition interferometers by modifying their input and/or output optics,’ *Physical Review D* **65**, 022002 (2001).
- [129] H. Habibi, E. Zeuthen, M. Ghanaatshoar, and K. Hammerer, ‘Quantum feedback cooling of a mechanical oscillator using variational measurements: tweaking Heisenberg’s microscope,’ *Journal of Optics* **18**, 084004 (2016).
- [130] M. Tsang and C. M. Caves, ‘Coherent quantum-noise cancellation for optomechanical sensors,’ *Physical Review Letters* **105**, 123601 (2010).

- [131] E. S. Polzik and K. Hammerer, ‘Trajectories without quantum uncertainties,’ *Annalen der Physik* **527**, A15 (2015).
- [132] M. H. Wimmer, D. Steinmeyer, K. Hammerer, and M. Heurs, ‘Coherent cancellation of backaction noise in optomechanical force measurements,’ *Physical Review A* **89**, 053836 (2014).
- [133] C. B. Møller, R. A. Thomas, G. Vasilakis, et al., ‘Quantum back-action-evading measurement of motion in a negative mass reference frame,’ *Nature* **547**, 191 (2017).
- [134] J. T. Hill, A. H. Safavi-Naeini, J. Chan, and O. Painter, ‘Coherent optical wavelength conversion via cavity optomechanics.’ *Nature Communications* **3**, 1196 (2012).
- [135] M. Abdi, P. Tombesi, and D. Vitali, ‘Entangling two distant non-interacting microwave modes,’ *Annalen der Physik* **527**, 139 (2015).
- [136] S. Barzanjeh, S. Guha, C. Weedbrook, et al., ‘Microwave quantum illumination,’ *Physical Review Letters* **114**, 080503 (2015).
- [137] P.-C. Ma, J.-Q. Zhang, M. Feng, and Z.-M. Zhang, ‘Bidirectional and tunable single-photons multi-channel quantum router between microwave and optical light,’ arXiv:1410.4371.
- [138] J. Taylor, A. S. Sørensen, C. M. Marcus, and E. S. Polzik, ‘Laser cooling and optical detection of excitations in a LC electrical circuit,’ *Physical Review Letters* **107**, 273601 (2011).
- [139] S. Barzanjeh, M. C. de Oliveira, and S. Pirandola, ‘Microwave photodetection with electro-opto-mechanical systems,’ arXiv:1410.4024.
- [140] S. Lloyd and S. L. Braunstein, ‘Quantum computation over continuous variables,’ *Physical Review Letters* **82**, 1784 (1999).
- [141] D. Walls and G. J. Milburn, *Quantum Optics* (Springer, Berlin, 2008).
- [142] M. R. Geller, E. J. Pritchett, A. T. Sornborger, and F. K. Wilhelm, in *Manipulating Quantum Coherence in Solid State Systems*, edited by M. E. Flatté and I. Tifrea (Springer, Dordrecht, 2007).
- [143] J. Koch, T. M. Yu, J. Gambetta, et al., ‘Charge-insensitive qubit design derived from the Cooper pair box,’ *Physical Review A* **76**, 042319 (2007).
- [144] I. Chiorescu, P. Bertet, K. Semba, et al., ‘Coherent dynamics of a flux qubit coupled to a harmonic oscillator,’ *Nature* **431**, 159 (2004).
- [145] A. Wallraff, D. I. Schuster, A. Blais, et al., ‘Strong coupling of a single photon to a superconducting qubit using circuit quantum electrodynamics,’ *Nature* **431**, 162 (2004).

-
- [146] F. Deppe, M. Mariani, E. P. Menzel, et al., ‘Two-photon probe of the Jaynes–Cummings model and controlled symmetry breaking in circuit QED,’ *Nature Physics* **4**, 686 (2008).
- [147] J. M. Fink, M. Göppl, M. Baur, et al., ‘Climbing the Jaynes–Cummings ladder and observing its nonlinearity in a cavity QED system,’ *Nature* **454**, 315 (2008).
- [148] L. S. Bishop, J. M. Chow, J. Koch, et al., ‘Nonlinear response of the vacuum Rabi resonance,’ *Nature Physics* **5**, 105 (2009).
- [149] G. Kirchmair, B. Vlastakis, Z. Leghtas, et al., ‘Observation of quantum state collapse and revival due to the single-photon Kerr effect,’ *Nature* **495**, 205 (2013).
- [150] M. A. Castellanos-Beltran, K. D. Irwin, G. C. Hilton, L. R. Vale, and K. W. Lehnert, ‘Amplification and squeezing of quantum noise with a tunable Josephson metamaterial,’ *Nature Physics* **4**, 929 (2008).
- [151] M. Hofheinz, E. M. Weig, M. Ansmann, et al., ‘Generation of Fock states in a superconducting quantum circuit.’ *Nature* **454**, 310 (2008).
- [152] M. Hofheinz, H. Wang, M. Ansmann, et al., ‘Synthesizing arbitrary quantum states in a superconducting resonator.’ *Nature* **459**, 546 (2009).
- [153] B. Vlastakis, G. Kirchmair, Z. Leghtas, et al., ‘Deterministically encoding quantum information using 100-photon Schrödinger cat states,’ *Science* **342**, 607 (2013).
- [154] S. J. Bosman, M. F. Gely, V. Singh, et al., ‘Multi-mode ultra-strong coupling in circuit quantum electrodynamics,’ arXiv:1704.06208.
- [155] P. Forn-Díaz, J. J. García-Ripoll, B. Peropadre, et al., ‘Ultrastrong coupling of a single artificial atom to an electromagnetic continuum in the nonperturbative regime,’ *Nature Physics* **13**, 39 (2017).
- [156] F. Yoshihara, T. Fuse, S. Ashhab, et al., ‘Superconducting qubit–oscillator circuit beyond the ultrastrong-coupling regime,’ *Nature Physics* **13**, 44 (2017).
- [157] C. Leroux, L. C. G. Govia, and A. A. Clerk, ‘Simple variational ground state and pure cat state generation in the quantum rabi model,’ arXiv:1704.02937.
- [158] D. I. Schuster, A. A. Houck, J. A. Schreier, et al., ‘Resolving photon number states in a superconducting circuit,’ *Nature* **445**, 515 (2007).
- [159] R. Vijay, D. H. Slichter, and I. Siddiqi, ‘Observation of quantum jumps in a superconducting artificial atom,’ *Physical Review Letters* **106**, 110502 (2011).
- [160] D. Ristè, J. G. van Leeuwen, H.-S. Ku, K. W. Lehnert, and L. DiCarlo, ‘Initialization by measurement of a superconducting quantum bit circuit,’ *Physical Review Letters* **109**, 050507 (2012).

- [161] D. Ristè, C. C. Bultink, K. W. Lehnert, and L. DiCarlo, ‘Feedback control of a solid-state qubit using high-fidelity projective measurement,’ *Physical Review Letters* **109**, 240502 (2012).
- [162] D. Ristè, M. Dukalski, C. A. Watson, et al., ‘Deterministic entanglement of superconducting qubits by parity measurement and feedback.’ *Nature* **502**, 350 (2013).
- [163] A. J. Kerman, ‘Quantum information processing using quasiclassical electromagnetic interactions between qubits and electrical resonators,’ *New Journal of Physics* **15**, 123011 (2013).
- [164] P.-M. Billangeon, J. S. Tsai, and Y. Nakamura, ‘Circuit-QED-based scalable architectures for quantum information processing with superconducting qubits,’ *Physical Review B* **91**, 094517 (2015).
- [165] N. Didier, J. Bourassa, and A. Blais, ‘Fast quantum nondemolition readout by parametric modulation of longitudinal qubit–oscillator interaction,’ *Physical Review Letters* **115**, 203601 (2015).
- [166] M. Neeley, R. C. Bialczak, M. Lenander, et al., ‘Generation of three-qubit entangled states using superconducting phase qubits,’ *Nature* **467**, 570 (2010).
- [167] M. Baur, A. Fedorov, L. Steffen, et al., ‘Benchmarking a quantum teleportation protocol in superconducting circuits using tomography and an entanglement witness,’ *Physical Review Letters* **108**, 040502 (2012).
- [168] L. Steffen, Y. Salathe, M. Oppliger, et al., ‘Deterministic quantum teleportation with feed-forward in a solid state system,’ *Nature* **500**, 319 (2013).
- [169] A. N. Cleland and M. Geller, ‘Superconducting qubit storage and entanglement with nanomechanical resonators,’ *Physical Review Letters* **93**, 070501 (2004).
- [170] F. Xue, Y. D. Wang, C. P. Sun, et al., ‘Controllable coupling between flux qubit and nanomechanical resonator by magnetic field,’ *New Journal of Physics* **9**, 35 (2007).
- [171] A. D. Armour, M. P. Blencowe, and K. C. Schwab, ‘Entanglement and decoherence of a micromechanical resonator via coupling to a Cooper-pair box,’ *Physical Review Letters* **88**, 148301 (2002).
- [172] J.-M. Pirkkalainen, S. U. Cho, J. Li, et al., ‘Hybrid circuit cavity quantum electrodynamics with a micromechanical resonator.’ *Nature* **494**, 211 (2013).
- [173] J.-M. Pirkkalainen, S. Cho, F. Massel, et al., ‘Cavity optomechanics mediated by a quantum two-level system,’ *Nature Communications* **6**, 6981 (2015).
- [174] E. K. Irish and K. C. Schwab, ‘Quantum measurement of a coupled nanomechanical resonator–Cooper-pair box system,’ *Physical Review B* **68**, 155311 (2003).

-
- [175] A. D. O’Connell, M. Hofheinz, M. Ansmann, et al., ‘Quantum ground state and single-phonon control of a mechanical resonator.’ *Nature* **464**, 697 (2010).
- [176] P. Rabl, A. Shnirman, and P. Zoller, ‘Generation of squeezed states of nanomechanical resonators by reservoir engineering,’ *Physical Review B* **70**, 205304 (2004).
- [177] J. Suh, M. D. LaHaye, P. M. Echternach, K. C. Schwab, and M. L. Roukes, ‘Parametric amplification and back-action noise squeezing by a qubit-coupled nanoresonator.’ *Nano letters* **10**, 3990 (2010).
- [178] J.-Q. Zhang, W. Xiong, S. Zhang, Y. Li, and M. Feng, ‘Generating the Schrödinger cat state in a nanomechanical resonator coupled to a charge qubit,’ *Annalen der Physik* **527**, 180 (2014).
- [179] A. Asadian and M. Abdi, ‘Heralded entangled coherent states between spatially separated massive resonators,’ *Physical Review A* **93**, 052315 (2016).
- [180] T. T. Heikkilä, F. Massel, J. Tuorila, R. Khan, and M. Sillanpää, ‘Enhancing optomechanical coupling via the Josephson effect,’ *Physical Review Letters* **112**, 203603 (2014).
- [181] A. J. Rimberg, M. P. Blencowe, A. D. Armour, and P. D. Nation, ‘A cavity–Cooper pair transistor scheme for investigating quantum optomechanics in the ultra-strong coupling regime,’ *New Journal of Physics* **16**, 055008 (2014).
- [182] E. A. Sete and H. Eleuch, ‘Strong squeezing and robust entanglement in cavity electromechanics,’ *Physical Review A* **89**, 013841 (2014).
- [183] F.-Y. Hong, Y. Xiang, W. H. Tang, et al., ‘Theory of control of optomechanical transducers for quantum networks,’ *Physical Review A* **85**, 012309 (2012).
- [184] K. Xia, M. R. Vanner, and J. Twamley, ‘An opto–magneto–mechanical quantum interface between distant superconducting qubits.’ *Scientific reports* **4**, 5571 (2014).
- [185] D. Kafri, P. Adhikari, and J. M. Taylor, ‘Dynamics of an ion coupled to a parametric superconducting circuit,’ *Physical Review A* **93**, 013412 (2016).
- [186] K. Hammerer, M. Aspelmeyer, E. S. Polzik, and P. Zoller, ‘Establishing Einstein–Podolsky–Rosen channels between nanomechanics and atomic ensembles,’ *Physical Review Letters* **102**, 020501 (2009).
- [187] S. Camerer, M. Korppi, A. Jöckel, et al., ‘Realization of an optomechanical interface between ultracold atoms and a membrane,’ *Physical Review Letters* **107**, 223001 (2011).
- [188] J. S. Bennett, L. S. Madsen, M. Baker, H. Rubinsztein-Dunlop, and W. P. Bowen, ‘Coherent control and feedback cooling in a remotely coupled hybrid atom–optomechanical system,’ *New Journal of Physics* **16**, 083036 (2014).

- [189] A. Jöckel, A. Faber, T. Kampschulte, et al., ‘Sympathetic cooling of a membrane oscillator in a hybrid mechanical–atomic system,’ *Nature Nanotechnology* **10**, 55 (2015).
- [190] F. Bariani, H. Seok, S. Singh, M. Vengalattore, and P. Meystre, ‘Atom-based coherent quantum-noise cancellation in optomechanics,’ *Physical Review A* **92**, 043817 (2015).
- [191] S. D. Bennett, S. Kolkowitz, Q. P. Unterreithmeier, et al., ‘Measuring mechanical motion with a single spin,’ *New Journal of Physics* **14**, 125004 (2012).
- [192] S. Kolkowitz, A. C. B. Jayich, Q. P. Unterreithmeier, et al., ‘Coherent sensing of a mechanical resonator with a single-spin qubit.’ *Science* **335**, 1603 (2012).
- [193] B. Pigeau, S. Rohr, L. Mercier de Lépinay, et al., ‘Observation of a phononic Mollow triplet in a multimode hybrid spin–nanomechanical system,’ *Nature Communications* **6**, 8603 (2015).
- [194] P. Rabl, S. J. Kolkowitz, F. H. L. Koppens, et al., ‘A quantum spin transducer based on nanoelectromechanical resonator arrays,’ *Nature Physics* **6**, 602 (2010).
- [195] O. Arcizet, V. Jacques, A. Siria, et al., ‘A single nitrogen–vacancy defect coupled to a nanomechanical oscillator,’ *Nature Physics* **7**, 879 (2011).
- [196] L. P. Neukirch, E. von Haartman, J. M. Rosenholm, and A. Nick Vamivakas, ‘Multi-dimensional single-spin nano-optomechanics with a levitated nanodiamond,’ *Nature Photonics* **9**, 653 (2015).
- [197] P. Ouartchaiyapong, K. W. Lee, B. A. Myers, and A. C. B. Jayich, ‘Dynamic strain-mediated coupling of a single diamond spin to a mechanical resonator,’ *Nature Communications* **5**, 4429 (2014).
- [198] A. Barfuss, J. Teissier, E. Neu, A. Nunnenkamp, and P. Maletinsky, ‘Strong mechanical driving of a single electron spin,’ *Nature Physics* **11**, 820 (2015).
- [199] K. C. Balram, M. I. Davanço, B. R. Ilic, et al., ‘Acousto–optic modulation and optoacoustic gating in piezo–optomechanical circuits,’ *Physical Review Applied* **7**, 024008 (2017).
- [200] M. J. A. Schuetz, E. M. Kessler, G. Giedke, et al., ‘Universal quantum transducers based on surface acoustic waves,’ *Physical Review X* **5**, 031031 (2015).
- [201] D. A. Golter, T. Oo, M. Amezcua, K. A. Stewart, and H. Wang, ‘Optomechanical quantum control of a nitrogen–vacancy center in diamond,’ *Physical Review Letters* **116**, 143602 (2016).
- [202] M. V. Gustafsson, T. Aref, A. F. Kockum, et al., ‘Propagating phonons coupled to an artificial atom,’ *Science* **346**, 207 (2014).

-
- [203] P. Arrangoiz-Arriola and A. H. Safavi-Naeini, ‘Engineering interactions between superconducting qubits and phononic nanostructures,’ *Physical Review A* **94**, 063864 (2016).
- [204] D. Gottesman and I. L. Chuang, ‘Demonstrating the viability of universal quantum computation using teleportation and single-qubit operations,’ *Nature* **402**, 390 (1999).
- [205] S. J. Weber, K. W. Murch, M. E. Kimchi-Schwartz, N. Roch, and I. Siddiqi, ‘Quantum trajectories of superconducting qubits,’ *Comptes Rendus Physique* **17**, 766 (2016).
- [206] J. Zhang, Y.-x. Liu, R.-B. Wu, K. Jacobs, and F. Nori, ‘Quantum feedback: theory, experiments, and applications,’ *Physics Reports* **679**, 1 (2017).
- [207] A. Doherty and K. Jacobs, ‘Feedback control of quantum systems using continuous state estimation,’ *Physical Review A* **60**, 2700 (1999).
- [208] J. Gough and R. van Handel, ‘Singular perturbation of quantum stochastic differential equations with coupling through an oscillator mode,’ *Journal of Statistical Physics* **127**, 575 (2007).
- [209] J. Gambetta, A. Blais, M. Boissonneault, et al., ‘Quantum trajectory approach to circuit QED: quantum jumps and the Zeno effect,’ *Physical Review A* **77**, 012112 (2008).
- [210] L. Bouten and A. Silberfarb, ‘Adiabatic elimination in quantum stochastic models,’ *Communications in Mathematical Physics* **283**, 491 (2008).
- [211] L. Bouten, R. van Handel, and A. Silberfarb, ‘Approximation and limit theorems for quantum stochastic models with unbounded coefficients,’ *Journal of Functional Analysis* **254**, 3123 (2008).
- [212] K. Lalumière, J. Gambetta, and A. Blais, ‘Tunable joint measurements in the dispersive regime of cavity QED,’ *Physical Review A* **81**, 040301 (2010).
- [213] H. Yang, H. Miao, and Y. Chen, ‘Nonadiabatic elimination of auxiliary modes in continuous quantum measurements,’ *Physical Review A* **85**, 040101 (2012).
- [214] C. Gardiner and P. Zoller, *Quantum Noise: A Handbook of Markovian and Non-Markovian Quantum Stochastic Methods with Applications to Quantum Optics* (Springer, Berlin, 2004).
- [215] J. Dalibard, Y. Castin, and K. Mølmer, ‘Wave-function approach to dissipative processes in quantum optics,’ *Physical Review Letters* **68**, 580 (1992).
- [216] S. Gleyzes, S. Kuhr, C. Guerlin, et al., ‘Quantum jumps of light recording the birth and death of a photon in a cavity,’ *Nature* **446**, 297 (2007).

- [217] C. Guerlin, J. Bernu, S. Deléglise, et al., ‘Progressive field-state collapse and quantum non-demolition photon counting.’ *Nature* **448**, 889 (2007).
- [218] C. Sayrin, I. Dotsenko, X. Zhou, et al., ‘Real-time quantum feedback prepares and stabilizes photon number states,’ *Nature* **477**, 73 (2011).
- [219] K. W. Murch, S. J. Weber, C. Macklin, and I. Siddiqi, ‘Observing single quantum trajectories of a superconducting quantum bit.’ *Nature* **502**, 211 (2013).
- [220] D. H. Slichter, C. Müller, R. Vijay, et al., ‘Quantum Zeno effect in the strong measurement regime of circuit quantum electrodynamics,’ *New Journal of Physics* **18**, 053031 (2016).
- [221] S. Hacothen-Gourgy, L. S. Martin, E. Flurin, et al., ‘Quantum dynamics of simultaneously measured non-commuting observables,’ *Nature* **538**, 491 (2016).
- [222] U. Vool, S. Shankar, S. O. Mundhada, et al., ‘Continuous quantum nondemolition measurement of the transverse component of a qubit,’ *Physical Review Letters* **117**, 133601 (2016).
- [223] J. E. Johnson, C. Macklin, D. H. Slichter, et al., ‘Heralded state preparation in a superconducting qubit,’ *Physical Review Letters* **109**, 050506 (2012).
- [224] M. Boissonneault, J. Gambetta, and A. Blais, ‘Dispersive regime of circuit QED: photon-dependent qubit dephasing and relaxation rates,’ *Physical Review A* **79**, 013819 (2009).
- [225] M. Boissonneault, A. C. Doherty, F. R. Ong, et al., ‘Back-action of a driven nonlinear resonator on a superconducting qubit,’ *Physical Review A* **85**, 022305 (2012).
- [226] R. Vijay, C. Macklin, D. H. Slichter, et al., ‘Stabilizing Rabi oscillations in a superconducting qubit using quantum feedback.’ *Nature* **490**, 77 (2012).
- [227] G. de Lange, D. Ristè, M. J. Tiggelman, et al., ‘Reversing quantum trajectories with analog feedback,’ *Physical Review Letters* **112**, 080501 (2014).
- [228] P. Campagne-Ibarcq, S. Jezouin, N. Cottet, et al., ‘Using spontaneous emission of a qubit as a resource for feedback control,’ *Physical Review Letters* **117**, 060502 (2016).
- [229] P. Campagne-Ibarcq, E. Flurin, N. Roch, et al., ‘Persistent control of a superconducting qubit by stroboscopic measurement feedback,’ *Physical Review X* **3**, 021008 (2013).
- [230] S. Mancini, D. Vitali, and P. Tombesi, ‘Optomechanical cooling of a macroscopic oscillator by homodyne feedback,’ *Physical Review Letters* **80**, 688 (1998).

-
- [231] P. Bushev, D. Rotter, A. Wilson, et al., ‘Feedback cooling of a single trapped ion,’ *Physical Review Letters* **96**, 043003 (2006).
- [232] D. J. Wilson, V. Sudhir, N. Piro, et al., ‘Measurement-based control of a mechanical oscillator at its thermal decoherence rate,’ *Nature* **524**, 325 (2015).
- [233] S. G. Hofer and K. Hammerer, ‘Entanglement-enhanced time-continuous quantum control in optomechanics,’ *Physical Review A* **91**, 033822 (2015).
- [234] S. G. Hofer, D. V. Vasilyev, M. Aspelmeyer, and K. Hammerer, ‘Time-continuous Bell measurements,’ *Physical Review Letters* **111**, 170404 (2013).
- [235] S. C. Edwards and V. P. Belavkin, ‘Optimal quantum filtering and quantum feedback control,’ [quant-ph/0506018](https://arxiv.org/abs/quant-ph/0506018).
- [236] J. R. Johansson, P. D. Nation, and F. Nori, ‘QUTIP: an open-source PYTHON framework for the dynamics of open quantum systems,’ *Computer Physics Communications* **183**, 1760 (2012).
- [237] J. R. Johansson, P. D. Nation, and F. Nori, ‘QUTIP 2: a PYTHON framework for the dynamics of open quantum systems,’ *Computer Physics Communications* **184**, 1234 (2013).
- [238] O. Černotík, ‘Adiabatic elimination of Gaussian subsystems in stochastic quantum dynamics,’ [Zenodo](https://zenodo.org/record/105281) (2015), 10.5281/zenodo.15855.
- [239] G. Vidal and R. F. Werner, ‘Computable measure of entanglement,’ *Physical Review A* **65**, 032314 (2002).
- [240] N. G. van Kampen, ‘A cumulant expansion for stochastic linear differential equations. I,’ *Physica* **74**, 215 (1974).
- [241] N. G. van Kampen, ‘A cumulant expansion for stochastic linear differential equations. II,’ *Physica* **74**, 239 (1974).
- [242] N. G. van Kampen, ‘Stochastic differential equations,’ *Physics Reports* **24**, 171 (1976).
- [243] N. G. van Kampen, ‘Langevin-like equation with colored noise,’ *Journal of Statistical Physics* **54**, 1289 (1989).
- [244] V. Giovannetti, S. Lloyd, and L. Maccone, ‘Quantum-enhanced measurements: beating the standard quantum limit,’ *Science* **306**, 1330 (2004).
- [245] F. Motzoi, K. B. Whaley, and M. Sarovar, ‘Continuous joint measurement and entanglement of qubits in remote cavities,’ *Physical Review A* **92**, 032308 (2015).
- [246] F. Helmer, M. Mariani, E. Solano, and F. Marquardt, ‘Quantum nondemolition photon detection in circuit QED and the quantum Zeno effect,’ *Physical Review A* **79**, 052115 (2009).

- [247] B. Fan, G. Johansson, J. Combes, G. J. Milburn, and T. M. Stace, ‘Nonabsorbing high-efficiency counter for itinerant microwave photons,’ *Physical Review B* **90**, 035132 (2014).
- [248] P. Rabl, P. Cappellaro, M. V. G. Dutt, et al., ‘Strong magnetic coupling between an electronic spin qubit and a mechanical resonator,’ *Physical Review B* **79**, 041302 (2009).
- [249] S. Hong, M. S. Grinolds, P. Maletinsky, et al., ‘Coherent, mechanical control of a single electronic spin.’ *Nano letters* **12**, 3920 (2012).
- [250] W. K. Wootters, ‘Entanglement of formation of an arbitrary state of two qubits,’ *Physical Review Letters* **80**, 2245 (1998).
- [251] A. M. Tyryshkin, S. Tojo, J. J. L. Morton, et al., ‘Electron spin coherence exceeding seconds in high-purity silicon,’ *Nature Materials* **11**, 143 (2011).
- [252] F. Lecocq, J. B. Clark, R. W. Simmonds, J. Aumentado, and J. D. Teufel, ‘Quantum nondemolition measurement of a nonclassical state of a massive object,’ *Physical Review X* **5**, 041037 (2015).
- [253] M.-A. Lemonde, N. Didier, and A. A. Clerk, ‘Enhanced nonlinear interactions in quantum optomechanics via mechanical amplification,’ *Nature Communications* **7**, 11338 (2016).
- [254] S. Weis, R. Rivière, S. Deléglise, et al., ‘Optomechanically induced transparency,’ *Science* **330**, 1520 (2010).
- [255] X. Zhou, B.-J. Liu, L.-B. Shao, X.-D. Zhang, and Z.-Y. Xue, ‘Quantum state conversion in opto–electro–mechanical systems via shortcut to adiabaticity,’ arXiv:1612.05927.
- [256] A. Baksic, R. Belyansky, H. Ribeiro, and A. A. Clerk, ‘Shortcuts to adiabaticity in the presence of a continuum: applications to itinerant quantum state transfer,’ arXiv:1705.04239.
- [257] E. Zeuthen, A. Schliesser, A. S. Sørensen, and J. M. Taylor, ‘Figures of merit for quantum transducers,’ arXiv:1610.01099.
- [258] I. Iakoupov, J. R. Ott, D. E. Chang, and A. S. Sørensen, ‘Dispersion relations for stationary light in one-dimensional atomic ensembles,’ *Physical Review A* **94**, 053824 (2016).
- [259] A. Pitanti, J. M. Fink, A. H. Safavi-Naeini, et al., ‘Strong opto–electro–mechanical coupling in a silicon photonic crystal cavity,’ *Optics Express* **23**, 3196 (2015).
- [260] J. M. Fink, M. Kalae, A. Pitanti, et al., ‘Quantum electromechanics on silicon nitride nanomembranes,’ *Nature Communications* **7**, 12396 (2016).

-
- [261] M. Zhang, S. Shah, J. Cardenas, and M. Lipson, ‘Synchronization and phase noise reduction in micromechanical oscillator arrays coupled through light,’ *Physical Review Letters* **115**, 163902 (2015).
- [262] P. Rakich and F. Marquardt, ‘Quantum theory of continuum optomechanics,’ arXiv:1610.03012.
- [263] H. Zoubi and K. Hammerer, ‘Optomechanical multimode Hamiltonian for nanophotonic waveguides,’ *Physical Review A* **94**, 053827 (2016).
- [264] A. Xuereb, C. Genes, and A. Dantan, ‘Strong coupling and long-range collective interactions in optomechanical arrays,’ *Physical Review Letters* **109**, 223601 (2012).
- [265] A. Xuereb, C. Genes, and A. Dantan, ‘Collectively enhanced optomechanical coupling in periodic arrays of scatterers,’ *Physical Review A* **88**, 053803 (2013).
- [266] A. Nunnenkamp, V. Sudhir, A. K. Feofanov, A. Roulet, and T. J. Kippenberg, ‘Quantum-limited amplification and parametric instability in the reversed dissipation regime of cavity optomechanics,’ *Physical Review Letters* **113**, 023604 (2014).
- [267] L. D. Tóth, N. R. Bernier, A. Nunnenkamp, et al., ‘Engineered dissipative reservoir for microwave light using circuit optomechanics,’ *Nature Physics* **13**, 787 (2017).
- [268] A. Metelmann and A. A. Clerk, ‘Nonreciprocal photon transmission and amplification via reservoir engineering,’ *Physical Review X* **5**, 021025 (2015).
- [269] N. R. Bernier, L. D. Tóth, A. Koottandavida, et al., ‘Nonreciprocal reconfigurable microwave optomechanical circuit,’ arXiv:1612.08223.
- [270] S. Barzanjeh, M. Wulf, M. Peruzzo, et al., ‘Mechanical on-chip microwave circulator,’ arXiv:1706.00376.
- [271] D. E. Chang, A. H. Safavi-Naeini, M. Hafezi, and O. Painter, ‘Slowing and stopping light using an optomechanical crystal array,’ *New Journal of Physics* **13**, 023003 (2011).
- [272] T. A. Palomaki, J. W. Harlow, J. D. Teufel, R. W. Simmonds, and K. W. Lehnert, ‘Coherent state transfer between itinerant microwave fields and a mechanical oscillator.’ *Nature* **495**, 210 (2013).
- [273] E. Damskägg, J.-M. Pirkkalainen, and M. A. Sillanpää, ‘Dynamically creating tripartite resonance and dark modes in a multimode optomechanical system,’ *Journal of Optics* **18**, 104003 (2016).
- [274] A. P. Reed, K. H. Mayer, J. D. Teufel, et al., ‘Faithful conversion of propagating quantum information to mechanical motion,’ arXiv:1703.02548.

CURRICULUM VITAE

PERSONAL DATA

Name Ondřej Černotík
Date of birth June 6, 1989
Place of birth Příbram, Czech Republic
Nationality Czech
Address Innersteweg 10, 30419 Hannover

EDUCATION

- Since 2013 PhD studies at Leibniz Universität Hannover
Institute for Theoretical Physics
Supervisor: Klemens Hammerer
Thesis: *Novel approaches to optomechanical transduction*
- 2011–2013 MSc studies at Palacký University Olomouc
Department of Optics
Supervisor: Jaromír Fiurášek
Thesis: *Transformations of continuous-variable entangled states of light*
- 2011–2012 Exchange studies at Umeå University
Department of Physics
- 2008–2011 BSc studies at Palacký University Olomouc
Department of Optics
Supervisor: Jaromír Fiurášek
Thesis: *Numerical simulations of dynamics of quantum systems using stochastic wavefunction method*
- 2004–2008 Gymnázium Zlín - Lesní čtvrť

PUBLICATIONS

- [1] O. Černotík, S. Mahmoodian, and K. Hammerer, ‘Spatially adiabatic frequency conversion in optoelectromechanical arrays,’ arXiv:1707.03339.*
- [2] O. Černotík and K. Hammerer, ‘Measurement-induced long-distance entanglement of superconducting qubits using optomechanical transducers,’ *Physical Review A* **94**, 012340 (2016).*
- [3] O. Černotík, D. V. Vasilyev, and K. Hammerer, ‘Adiabatic elimination of Gaussian subsystems from quantum dynamics under continuous measurement,’ *Physical Review A* **92**, 012124 (2015).*
- [4] O. Černotík and J. Fiurášek, ‘Transformations of symmetric multipartite Gaussian states by Gaussian local operations and classical communication,’ *Physical Review A* **89**, 042331 (2014).
- [5] O. Černotík and J. Fiurášek, ‘Displacement-enhanced continuous-variable entanglement concentration,’ *Physical Review A* **86**, 052339 (2012).

* These publication form the basis of the dissertation.



Dissertation angefertigt am
Institut für Theoretische Physik
Leibniz Universität Hannover

2017